Fakultät für Mathematik, Informatik und Naturwissenschaften | RWTH AACHEN UNIVERSITY

3D artificial extracellular matrices for directed in vitro cell growth

Von der Fakultät für Mathematik, Informatik und Naturwissenschaften der RWTH Aachen University zur Erlangung des akademischen Grades einer Doktorin der Naturwissenschaften genehmigte Dissertation

vorgelegt von

Sitara Vedaraman, M.Sc

aus

New Delhi, India

Berichter: Universitätsprofessorin Dr.-Ing. Laura De Laporte

Universitätsprofessor Dr. rer. nat. Martin Möller

Tag der mündlichen Prüfung: 16.01.2023

Dedicated to my Appa,

Declaration

The work presented in this thesis was conducted at the DWI - Leibniz Institute for Interactive Materials in Aachen and Advanced Materials for Biomedicine, RWTH Aachen, from June 2016 until May 2022, under the supervision of Prof. Dr. Laura De Laporte.

Declaration of Authorship

I declare that this thesis and the work presented in it are my own and have been generated by me as the result of my original research. I do solemnly swear that:

1. This work was done wholly or mainly while in candidature for the doctoral degree at this faculty and university.

2. Where any part of this thesis has previously been submitted for a degree or any other qualification at this university or any other institution, this has been clearly stated.

3. Where I have consulted the published work of others or this, myself is always clearly attributed.

4. Where I have quoted from the work of others or myself, the source is always given. This thesis is entirely my work, with the exception o such quotations.

5. I have acknowledged all major sources of assistance.

6. Where the thesis is based on work done by myself jointly with others, I have made clear exactly what was done by others and what I have contributed myself.

7. Parts of this work have been published before as:

1. S.Vedaraman, A. Perez-Tirado, T. Haraszti, J. Gerardo-Nava, L. De Laporte. Adv. Healthcare Mater. 2021, 10, 2100874.

2. S.Vedaraman, D. Bernhagen, T. Haraszti, C. Licht, A. Castro Nava, A. Omidinia Anarkoli P. Timmerman, L. De Laporte. Biomaterial Science, Biomater. Sci., 2021, 9, 4329-4342.

Sitara Vedaraman, 18.02.2023

Author's contributions

1. Publication (incorporated into Chapter 3): I developed and conducted the substrate fabrication protocol to produce microelement array substrates, performed cell experiments, and characterized the platform. A. Perez-Tirado, S.Vedaraman optimized the platform as a high throughput array, and T. Haraszti, S.Vedaraman developed a protocol to analyze cell orientation using computational algorithms. J. Gerardo-Nava provided intellectual contributions to the development of the project. L. De Laporte developed the concept together with A. Nishiguchi, and L. De Laporte supervised the project. I wrote the manuscript, which was corrected by L. De Laporte and All authors finalized the manuscript.

2. Publication (incorporated into Chapter 4): I developed the in vitro hydrogels incorporating bicyclic RGD peptides, characterized the hydrogels, translated them into ANISOGELs, and analyzed fiber orientation in ANISOGELS and its influence on cells. Dr. D. Bernhagen and P. Timmerman designed the bicyclic peptides in PEPSCAN, Lelystad, NL. C. Licht and A. Castro Nava developed PEG Q-K hydrogels and produced degradable peptide domains, respectively. PCL fibers for the ANISOGELS were provided by A. Omidinia Anarkoli and T. Harasti developed the computational quantification for ANISOGELS. L. De Laporte designed the concept and supervised the project. I and LDL wrote the manuscript together and finalized the article together with the co-authors.

3. Manuscript in preparation (incorporated in Chapter 5): I adapted the concept of interpenetrating networks and designed the experiments. A. Kirschner performed the experiments and analyzed data. S.Vedaraman, M. Schüler and S. Babu fabricated ANISOGELS with PIC hydrogels. K.Liu and P.Kouwer designed the PIC poylmers at RU, Netherlands. L. De Laporte supervised the project.

4. Manuscript in preparation (incorporated in Chapter 6): I designed the experiments and optimized the protocol for the development of PEG hydrogels for photopatterning for nerve cells, especially with caged Q platform. S. Ramakrishna performed experiments with Caged K and Q peptides for nerve and fibroblast growth. J. Hüffel performed experiments to optimize gels for fibroblast growth. A. Farrukh and M. A. Del Campo Bécares provided caged RGD and Caged IKVAV peptides. D. Blondel and M. Lutolf provided the protocols for photopatterning. L. De Laporte supervised the project and provided intellectual contribution.

Eidesstattliche Erklärung

Hiermit erkläre ich, Sitara Vedaraman, an Eid statt, dass ich die vorliegende Dissertation selbstständig verfasst habe und keine anderen als die angegebenen Quellen und Hilfsmittel verwendet habe.

Sitara Vedaraman, 18.02.2023

Table of Contents

Chapter 1. Motivation and overview of the thesis

1.1 Introduction

Over several decades, tremendous advancement in the field of tissue engineering and regenerative medicine has been achieved to improve the quality and longevity of human life. Systematic solutions are engineered by combining multiple scientific faculties with biological systems to develop functional tissue or organ substitutes using tissue engineering. The principal focus of tissue engineering involves designing, controlling, and tuning microenvironments that imitate natural, healthy, and diseased tissue/organs. This can be achieved by a combination of materials, cells, and bioactive molecules. The resulting constructs can function as implants, used for therapeutic applications, or employed *ex vivo* to generate quantitative knowledge of biological processes.[1] One of the earliest achievable applications includes regenerating skin epidermal tissue using hydrogel-based scaffolds[2]. Other non-regenerative methods to improve tissue function are metallic support inserts to support damaged bone tissue[3] or more recent bionics, which establish synaptic connections between prosthetic limbs and functional nerves[4]. The latter aims to bypass an injured or diseases tissue site with machinery, while regenerative medicine has the goal of regrowing functional tissue. *Ex vivo* tissue constructs are developed to understand and comprehend cellular mechanisms, test pathological conditions, and reduce the need for animal experiments.[5] Organoid models are developed *in vitro* to mimic the microanatomy and physiology of organs in great detail. These present simplified versions of healthy tissues and disease models, such as genetic disorders, infectious diseases, or even cancer.[6] Organ-on-a-chip technology is now combined with patient-derived cells to develop personalized treatment.[7] The potential of culturing patient-derived cells/tissues *in vitro* in combination with biomaterials is developed to later

implant/inject the same scaffold into the patient *in vivo,* minimizing immune response and improving the recovery phase.[8] In this thesis, I investigated the influence of different cues from the cells' microenvironment to design suitable biomaterials for tissue regeneration. Hence, scaffolds supporting cell growth and invasion without triggering immune responses are essential. Several combinations of materials derived from natural or synthetic origin and cells are used to recreate the extracellular matrix (ECM) and achieve a profound understanding of cell-material interactions.[9]

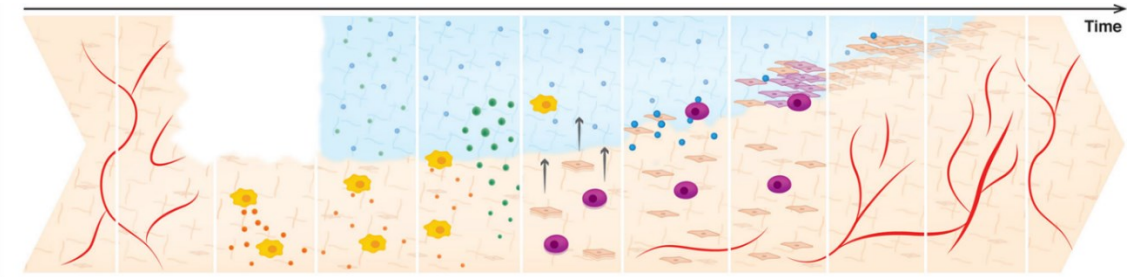

Rice, De Laporte et al. 2013 Adv. Healthcare

Figure 1: Schematic representation of tissue regeneration assisted by hydrogels to form fully functional tissues over time. Adapted from reference[9] with kind permission from John Wiley and Sons.

Extensive research in biomaterials is performed either *in vitro*, in combination with cells grown on two-dimensional (2D) substrates or in three-dimensional (3D) matrices, imparting physical or mechanical and biochemical cues, or *in vivo* with animal models. While 2D models do not envisage the dynamic complexity and hierarchy of native ECM, the animal models only partly recapitulate the clinical features of human diseases. Furthermore, minimizing the scale of animal testing is desired which often involve high costs and work effort.[10] Hence, to achieve plausible clinical success, a translation from 2D substrate-based models to 3D models is desired, where the cells experience signals and forces from all directions.[11] *In vitro,* 3D models offer an alternative to animal testing involving multiple testing groups for preliminary biomaterial screening and in addition, act as an intermediate screening platform, reducing the number of animals required.

1.2 Recapturing ECM components and their functions in tissue engineering

Biomaterials developed from natural or naturally-derived ECM scaffolds vary in their properties based on their conformation, containing proteinaceous (collagen, elastin, laminin, fibronectin) and non-proteinaceous (glycosaminoglycans or alginate) components.[12] The proteinaceous scaffolds offer fibrous topography that supports cell adhesion, migration, and direct tissue reorganization while providing structural, architectural, and chemical cues.[13] Whereas, the non-proteinaceous components, such as glycosaminoglycans, mainly fill up the extra interstitial spaces while supporting the scaffold in hydration to regulate swelling pressure and endure external compressional forces.[14] Capturing the functional properties of ECM components include response to cell interaction and signal transmission, including chemical, mechanical or electrical signals (**Figure 1**).[9,15] Loss or damage in one or several components of ECM results in pathological conditions in these tissues.[16] Scaffolds made of decellularized tissues display several advantages of biocompatibility and retain native architectures compared to synthetic scaffolds.[17] Although natural proteins and biopolymers are the most sought-after biomaterials, they often offer immunogenic responses with batch-to-batch variability that vastly affects reproducible outcomes. Hence synthetic matrices with high reproducibility and controllability are desired. We can envisage the complex hierarchical ECM as a chemically defined model by simplifying its composition using a modular approach, using a soft synthetic hydrogel network with appropriate spatial and temporal cues. To render this artificial ECM (aECM) functional and hierarchical, three major stimuli: mechanical, biochemical, and architectural, that vastly influence cell fate inside an aECM need to be controlled with suitable assemblies (**Figure 2**). The close interdependence of these parameters offers a limitation to decoupling them one from another (**Figure 3**).

Among the synthetic matrices, polymeric scaffolds are the most sought-after materials for fabricating hydrogels with highly controlled and tunable properties.[18] These

scaffolds swell in an aqueous environment to form hydrogels composed of > 90% water. Though they lack the native biochemical and architectural cues, these properties can be easily tuned to mimic cellular micro-environments and control cellular responses.[19] The different synthetic scaffolds are discussed in detail in **Chapter 2**. The major advantage is that they are predominantly a solution as a precursor enabling encapsulation of cells inside the hydrogel to render them injectable or implantable.

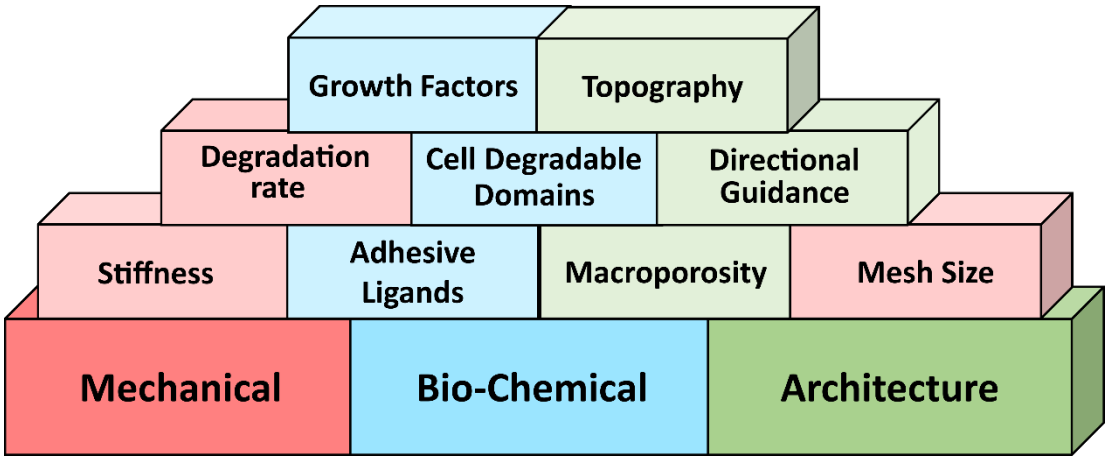

Figure 2. Schematic representation of 3 fundamental cues influencing cell fate: Mechanical, Biochemical, and Architectural cues. Derived from these cues are different parameters that affect the viability, growth, proliferation, and invasion of cells inside an artificial ECM.

1.2.1 Bio-Mechanical cues

Mechanical properties of a hydrogel, such as mesh size, degree of swelling, elastic modulus, viscoelasticity, strain stiffening, and degradation, impart mechanical forces on the cells and can be easily controlled by tuning the hydrogel composition, crosslinking type and kinetics, and degradation domains. The physical cues in aECM are provided by the polymeric networks that form either covalent or non-covalent bonds resulting in matrices that are either permanently altered due to degradable domains or remodeled locally with reversible bonds.[20] The degree of crosslinking determines the stiffness, which is inversely proportional to the mesh size and swelling (**Figure 3**). Among the synthetic scaffolds, medically (FDA) approved polyethylene glycol (PEG)-based hydrogels offer a bioinert blank slate that can be easily rendered

bioactive and biodegradable. While facile synthesis of PEG polymer is possible with different functional groups that determine the crosslinking method and kinetics, the degradation kinetics depends on the number and type of cleavable sites, such as esters[21] or enzyme sensitive domains[22], thus imparting unique hydrogel properties for every system. Unlike linear polymers, the multi-arm or star-PEG (sPEG) polymers allow for simultaneous crosslinking and biofunctionalization using the same sPEG polymer.

Additionally, these gels are crosslinked at concentrations lower than their critical concentration, resulting in heterogeneous pores suitable for nutrient transport and perfusion.[23] Two unique sPEG hydrogel systems with different arm lengths, crosslinking mechanisms, and the number of PEG arms are investigated in **Chapter 4** and **Chapter 6** in detail. The first system involves enzymatic crosslinking of two 8-arm sPEG-VS coupled with lysine-bearing peptides or glutamine-bearing peptides. These gels mimic the fibrin crosslinking mechanism using transglutaminase, making them biocompatible and highly specific.[24,25] The second PEG system involves a 4 arm sPEG vinyl sulphone (sPEG-VS) crosslinked with a linear di-cysteine crosslinker bearing a degradable domain sensitive to matrix metalloproteases (MMP) produced by the cells. The polymers are crosslinked by Michael type addition at physiological conditions.[26] Biofunctionalization in both systems is achieved using mono functionalized pendant-like adhesive ligands coupled using their respective crosslinking mechanisms. Such gels are often applied in wound models where their ability to fill the irregular shape of the cavity in the injury site makes them ideal for non-invasive therapies.

1.2.2 Bio-Chemical cues

The biochemical properties are often incorporated inside aECM by tethering cell adhesive domains or growth factors to the backbone of the polymer network.[27] The cell viability and growth depend on the concentration of cell adhesion ligands and rate of growth factor perfusion.[28] The cell-ECM interaction is regulated via the cell

membrane, which consists of transmembrane proteins called integrins involved in bidirectional cell-ECM signaling, regulating physiological processes such as adhesion, migration, proliferation, and apoptosis. The adhesive ligands to enable integrin-mediated cell adhesion are covalently incorporated into scaffolds to promote cell-matrix interaction.[26] Several known domains are endogenous proteins, their fragments, or derived peptides. For example, fibronectin, laminin, and collagen are the most applied proteins in tissue engineering for adherent cells, with RGD peptide as the most common ligand for integrin binding. Engineered protein fragments can assemble specific functions, like FNIII 9*-10/12- 14 derived from fibronectin, which consists of domains FNIII 9*-10 responsible for cell adhesion[29] and FNIII 12-14 for growth factor binding[30]. Such protein fragments offer synergistic sites where the adhesion occurs adjacent to the growth factor site.[31] Integrin binding sites in proteins like fibronectin and laminin were decoded, revealing the role of small peptide ligands responsible for cell adhesion. Peptides such as Arg–Gly–Asp (RGD)[32], Tyr–Ile–Gly–Ser–Arg (YIGSR)[33], Ile-Lys-Val-ala-Val (IKVAV)[34], Arg-Asn-Ile-Ala-Glu-Ile-Ile-Lys-Asp-Ile (RNIAEIIKDI)[35], Pro–His–Ser–Arg–Asn (PHSRN)[36] are some of the most explored integrin-binding domains. Peptides are easily synthesized in high purity using peptide synthesizers that are either semi or wholly automated to produce in large-scale with high reproducibility.

Being synthetic, these peptides do not trigger an immune response, thereby facilitating scaffold compatibility for in vivo application. A combination of YIGSR and RGD peptides that were covalently immobilized inside PEG acrylate gels with endothelial cells induced greater tubule length and diameter *in vitro,* resulting in greater vessel density and branching *in vivo*.[37] Similarly, a combination of equal molar ratios of RGD, IKVAV, YIGSR, and RNIAEIIKDI in fibrin gels showed a synergistic effect, improving the neurite out growth. The highest level of regeneration was observed during *in vivo* experiments when the optimized fibrin was injected inside a tube used to bridge the gap between nerve disconnected stumps in adult male rats.[38] Another class of synthetic molecules emerged to replicate the docking site of integrin

heterodimers, called peptidomimetics, which impart high selectivity and affinity.[39] These chemically defined ligands adhere to integrin proteins on the cell surface. The extent of adhesion depends on the conformation and structure of the ligand, thus imparting selectivity and affinity to integrins. For example, the integrin selectivity of a protein fragment from fibronectin FNIII 9*-10 is inclined more toward $\alpha_5\beta_1$, promoting MSCs proliferation and differentiation[29] while I observed that bicyclic RGD peptides developed to bind $\alpha_v\beta_3$.[40] In Ligands, the integrin affinity and selectivity can be improved by adding amino acids before and after the adhesive peptides as suitable spacers[41] or by cyclization of the peptides. For example, monocyclic RGD peptides known for their high cell binding affinity lacked selectivity. Hence, I investigated the effect of a new class of cyclic peptides bearing two cyclic loops containing an integrin binding site like RGD peptide and a tri amino acid sequence which promotes integrin selectivity. This has been discussed in detail in **Chapter 4**. Two bicyclic peptides were coupled to PEG hydrogels and I investigated their influence on cell growth, and alignment for L929 cells and primary sensory nerve cells.

1.2.3 Architectural cues

Hierarchical tissues, such as muscles, heart, cartilage, spinal cord, bone, and tendons have oriented tissues, and the design of such aECM demands anisotropy to achieve functional tissue regeneration.[42] The anisotropy is often induced by incorporating cues developed by micro and nanofabrication techniques that create patterns inside the scaffold to impart chemical or mechanical gradients.[42,43] Physical gradients in the 3D microenvironment are often created by orienting the intrinsic hydrogel fibers by layer by layer patterning, extrusion, movement of magnetic particles, or flow imparting directional cues.[43–45] For example, spherical microgels particles are annealed to form a packed bulk scaffold with pores between for cell infiltration,[46] and tethering these microgels with biomolecules enabled spatial patterning inside the 3D porous scaffolds.[47] In the case of monolithic hydrogels, where the porosity is accounted only

from the mesh size created by the molecular crosslinks, spatial cell patterning was achieved with magnetically labeled cardiomyocytes in the presence of an external magnetic field. This resulted in magnetic patterning of cells to obtain biomimetic cardiac cell alignment.[48] However, direct contact between magnetic micro/nanoparticles and cells is discouraged for *in vivo* applications.[49] Magnetic nanoparticles dispersed in a collagen matrix in the presence of low magnetic fields resulted in the aggregation of particles to form magnetic strings. During gelation, the orientation of the collagen fibers was influenced by the oriented magnetic strings. In vitro experiments with neurons showed elongated morphology along the direction of the magnetic string.[50] Though the magnetic strings provide directional cues, they are less controllable in dimensions and require more magnetic materials (~ 3 mg/mL). Moving iron nanoparticles were employed during bioprinting with collagen to avoid direct contact with magnetic particles and cells.[43] Here, the magnetic materials migrated to an edge which can be removed easily, however, this system may be unsuitable for in vivo experiments. Hence, a system employing the magnetic nanoparticles embedded in PEG microgels or fibers was developed.[51,52] While the magnetic nanoparticles are used in low concentrations and help orient the microgels, the aspect ratio of microgels plays a critical role in influencing anisotropy. The microgels/fibers are anisometric in dimension, enabling them to orient along the direction of the external magnetic field lines. Encapsulating these microgels/fibers inside a bulk crosslinking PEG hydrogel creates a spatial distribution of oriented microgels/fibers.[25] These gels, also referred to as ANISOGELS, impart anisometric material properties to promote cell growth in an oriented manner and are investigated in **Chapters 3 and 5**.[52,53] Biofunctionalization of such microgels with ligands, such as RGD, enable ANISOGELS to present a combination of mechanical, architectural, and biochemical cues for the cells.[54] Alternatively, exclusive bio-chemical gradients in 3D hydrogels are often desired to understand the role of biochemical gradients in determining cell fate by decoupling the biophysical cues. Such interactions mimic native tissues responses where the cells grow and mature without altering the

mechanical properties. Such microenvironments can be artificially developed by applying photo-patterning techniques to enabling spatial and temporal control, where multiple biomolecules can be tethered to synthetic hydrogels using orthogonal chemistry.[55,56] In **chapter 6,** such biochemical patterns are fabricated in 3D, at high spatial resolution using confocal and two photon lithography microscopes. I was able to fabricate biochemical gradients without altering the biomechanical properties and bind specific cell adhesive and growth factor binding sites like RGD, IKVAV and FN 9*-10/12-14 create spatial biochemical pattern/gradients. Since the spinal niche is one of the most highly ordered tissue, understanding the fundamentals of axonal viability, growth, and steering is essential. Throughout my thesis, I investigate the influence of several aECM cues in distinct modules on nerve cells from dorsal root ganglions extracted from chick embryo.

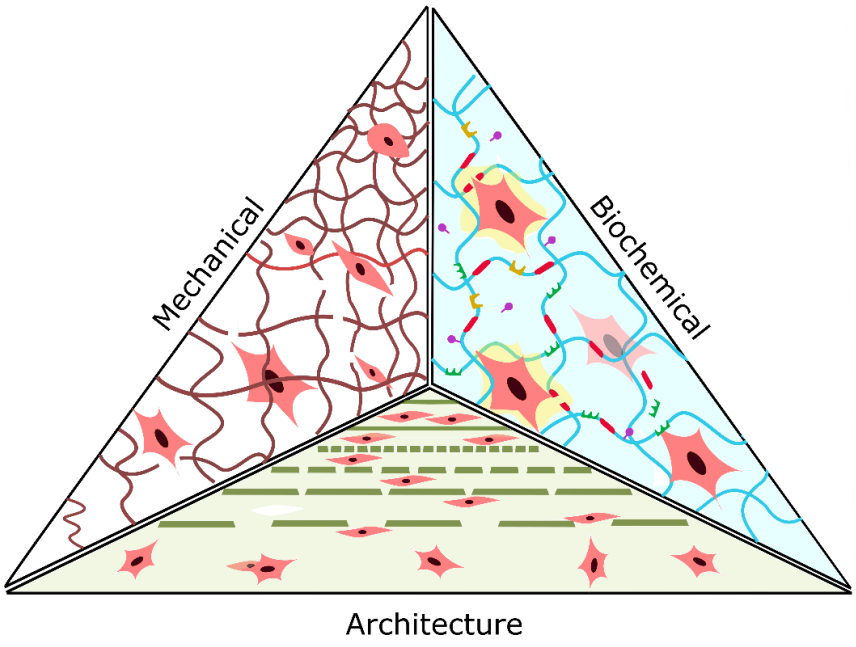

Figure 3. Schematic representation of interdependence between physical/ mechanical, biochemical and architectural cues influencing cell growth and proliferation, forming a triad. In mechanical cues, the stiffness is directly proportional to the degree of crosslinking and inversely proportional to mesh size and swelling. In biochemical cues, trans-membrane integrin receptors and its sub-units engage in the interaction with ECM and docking on ligands and growth factors. Different architectural cues, either physical or biochemical, responsible for cell guidance and orientation.

1.3 Role of physical cues in determining cell fate

Among the several stimuli affecting cell growth and proliferation, the physical guidance cues play a prominent role in determining cell fate, especially for hierarchical tissues imparting anisotropic tissue morphology. In an attempt to mimic *in vivo* neuronal niches, synthetic substrates, such as fibers and surfaces with isotropic and anisotropic features, are used as 2D scaffolds to emulate the features of ECM (**Figure 4**).[57,58] The cytoskeleton (microtubules, actin, intermediate filaments) of cells undergoes morphological changes due to interaction with scaffold with the help of cellular protrusions (lamellipodia and filopodia).[59] Other cellular mechanisms, including cellular attachment, migration, polarization, and growth, are also coordinated by these flat membranous lamellipodia and the thin finger-like projections of the filopodia that also sense chemical gradients.[60]

In the case of nerve cells, the growth cone (GC) is the motile structure at the tip of a polarized neuron that explores the ECM, is receptive to external cues, and reacts via signal cascades.[61 62] The growth of axons involves three distinct peripheral domains in the GC: filipodia and lamellipodia at the tip of the growth cone, the transition zone, and the central domain that consists of microtubules connecting to the axon. Axon growth is initiated as the GC advances, changing the outermost peripheral domain to become the central domain, subsequently becoming part of the axon.[63] As the GC advances, the filipodia and lamellipodia probe the ECM by forming temporary attachments, which detect chemical and mechanical cues. Reports reveal that GC is capable of detecting attractive and repulsive molecular cues.[64 65]

In the presence of linear physical cues, two distinct populations of filipodia are formed in the GC. While one population senses the environment's anisotropy, the other behave stochastically. The cytoskeleton of the first population of filopodia is rich in F-actin, while the latter population consists of non-aligned and unstable filopodia, suggesting crosstalk between both filopodia populations. Long filopodia are observed on flat substrates and cannot be stabilized by a robust F-actin cytoskeleton, resulting

in neurite collapse events.[66] As the GC advances, an alternate exchange between deterministic and stochastic behavior occurs with a transition in between where the external cues influence axonal steering.[67] The GC responds to the external stimuli by turning to a side of the GC when microtubules invade the side of the peripheral domain resulting in directional polarization.[61,63] Filipodia and lamellipodia in the GC act as cytoskeletal sensors that sense topographical or biochemical (for example, laminin, tenascin, fibronectin) cues in the cellular ECM using transmembrane receptors, such as integrins. The integrins bind to ECM ligands by signaling cascades[68], which impart cues and guidance achieved by physical contact. This is popularly known as 'contact guidance' and plays a significant role in axonal steering and cell migration in, for example, nerve regeneration and cancer propagation models. Especially in neurons, ECM topographies are known to induce changes in morphology and affect growth direction. [69]

The ECM in an oriented nervous tissue niche contains microstructures imparting physical cues, such as fibrils, and anisotropic features, which the GC senses during the morphogenesis of the neurites.[70] Peripheral nerve regeneration vastly depends on the extent of aligned Schwann cells paving a path for axonal myelination.[71] Hence replicating and understanding neuronal growth on Schwann cell topographies allow us to understand nerve regeneration better. The artificial topographies influence the rate of cell motility and the direction of the growth cone.[72] Mimicking such surfaces is now possible by advanced micro- and nanofabrication techniques that can imitate parts of the native topography, such as dimensions or structure.[57] Techniques, such as photolithography, soft lithography, electrospinning, and etching, are developed to study *in vitro* cell interactions.[73] To understand neurites' interactions with bio-active environments, *in vitro* experiments were predominantly performed on 2D substrates, revealing faster and straighter axonal growth on stiffer substrates[74] with topographies classified as isotropic or anisotropic based on their aspect ratios. Isotropic topographies have uniform features along all directions, while anisotropic topographies have a preferential direction along single or multiple axes.

Similarly, discreet geometrical features[57,73,75] are tailored to guide cells and promote migration.[76] Though these topographies offer linear cell guidance, they failed to create one primary direction, especially with an isotropic micropillar array, where the micropillars' shape determines the neurites' growth direction. For example, the primary nerve cells from rat dorsal root ganglia (DRG) grew longer axons in 6 directions (60° between each other) along the hexagon's sides.[77,78] Similar discontinuous isotropic pillar arrays cultured with primary hippocampal neurons demonstrated that optimal spacing between the pillars enables neurites to grow longer along one primary direction, indicating that the gaps between pillars are preferred over high frequency of the pillars to achieve growth in one direction.[79]

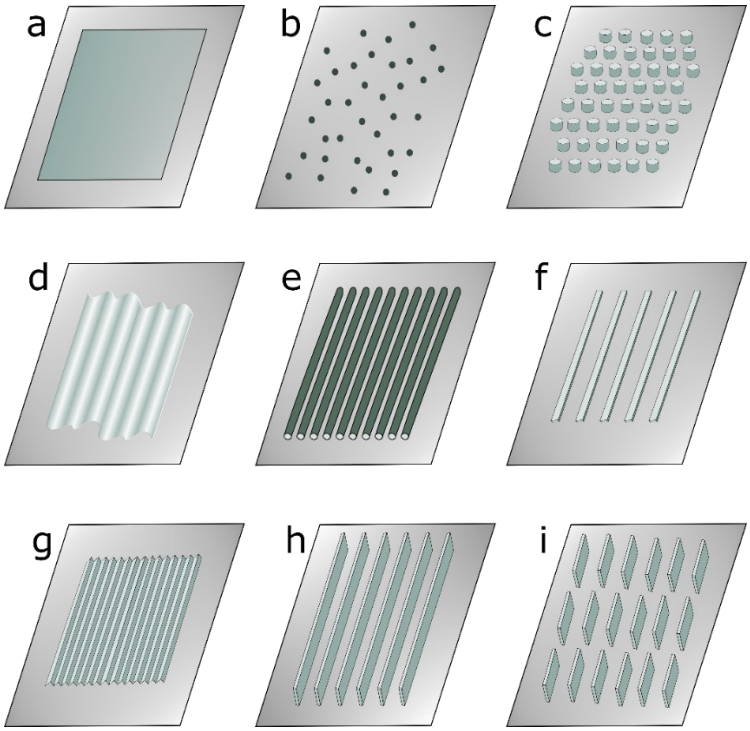

Figure 4. 2D *in vitro* substrate topography. a) Flat Surface, b) Micro/nanodots, c) Micropillars, d) Wrinkles, e) Fiber topography, f) Grooves and ridges, g) Micro cones/zig-zag, h) Continuous anisometric microelements, i) Discreet anisometric microelements.

Discontinuous micron-scale topographies with anisotropic geometries, such as linear, circular, angular gratings, triangles, or rectangles, are reported to influence the length of the axons and dendrites more than isotropic geometries, such as dots, grids, squares.[80] Further, femtosecond pulsed laser on silicon wafer produced pseudo discreet

elliptical micro cones that linearly guided DRG axonal growth, shedding light on the influence of an anisotropic surface in nanoscale.[75]

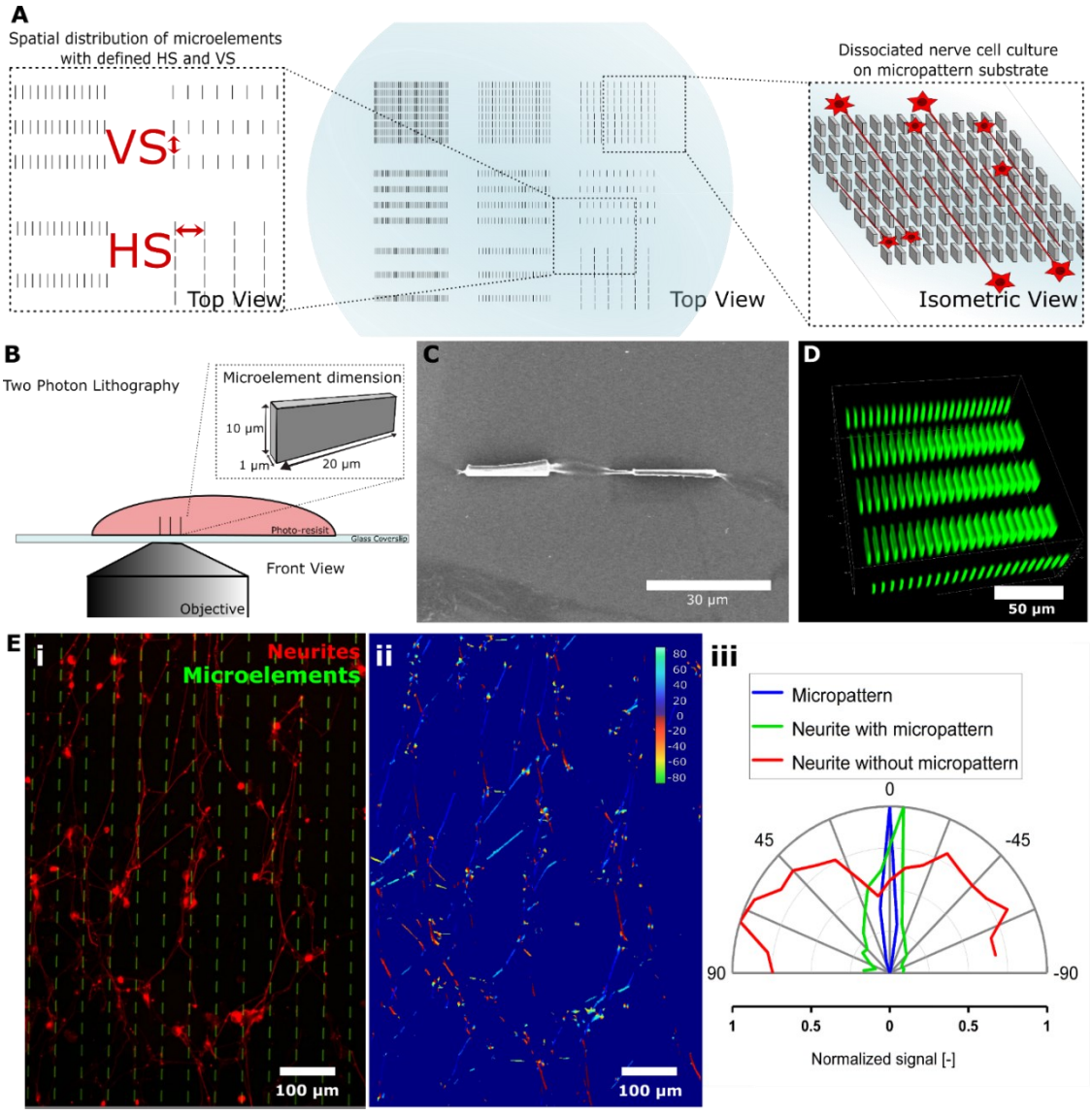

Figure 5. a) Schematic representation of the spatial distribution of microelements with defined horizontal and vertical spacing on a glass substrate printed using b) a two-photon lithography machine and a photoresist. The dimensions of the microelements are fixed to 20x 1x 10 µm. C) The FE-SEM images reveal that the cells follow the auto-fluorescent microelements, as shown in d). The beta-tubulin stained microelements are analyzed using an elliptical kernel, revealing the maximum orientation at 0° for microelements and narrow distribution of neurites around 0°.

Although both isotropic and anisotropic topographies influence directed axonal growth, the anisotropic elements direct cells in a linear manner imparting greater

control in the primary growth direction of axons. Physical parameters, such as dimensions of the features, widths, slopes, and depths, generate different effects on cells at the macroscale, microscale, and nanoscale. While subcellular structures influence the sensitivity of cellular filopodia, integrin-mediated adhesion involves clustering primarily at the nanoscale, and micro-scale topographies regulate changes in the direction, morphology, and polarity. [70,76,81]

Externally triggered orientation of directional cues is essential for the spatial distribution of physical cues, especially in injectable systems, to create *in situ* anisotropic microenvironments. As described before, incorporating magnetically orientable anisometric elements inside ANISOGELS provides a directed ECM architecture allowing neurons to grow in a highly oriented and linear manner.[52,82,83] The ANISOGELS initially containing fibrin as surrounding gel and magnetically orientable microelements (microgels/fibers) enabled linear growth of axons inside the fibrin with one primary direction. The microgels were further coated with bio-adhesive molecules, such as RGD, to provide biochemical cues in addition to physical cues.[54] Such matrices led to oriented cell growth yet reduced native aligned fibronectin production to further direct cells in a positive feedback cycle. This demonstrated that overstimulation could make the cells 'lazy', resulting in reduced biological healing. Switching from fibrin to fully synthetic PEG hydrogels enabled higher control in scaffold development, for example, to incorporate engineered fibronectin fragments, which possess both integrins and growth factor binding sites.[25] Some of the parameters of the orienting microelements that influence directed cell growth are size, aspect ratio, and distance. When tested inside fibrin matrices, variation of these parameters revealed superior growth for long microgels (50 μm) with shorter cross-sections (2.5 μm).[53] Though this works covers a wide range of microgel parameters, it lacks control to study the effect of the distance between the microelements to guide unidirectional cell growth.

In **Chapter 3**, I developed a more controlled, high-throughput 2.5 D platform with two-photon lithography (TPL) to study varying interelement spaces (vertical and horizontal) and elucidate the role of physical guidance cues required to steer neurite growth linearly. Here, short, anisometric discreet microelements with varying interelement spaces are fabricated (**Figure 5a, 5b**) to obtain a deeper understanding of the minimal physical guidance cues required for axonal navigation in primary sensory nerve cells. A comparative study with continuous guidance cues shows that similar nerve alignment can be achieved with discreet/discontinuous anisotropic microelements (**Figure 5c, 5d**). The incremental increase in horizontal spacing (HS) and vertical spacing (VS) is used to analyze the behavior of cell-material interaction, and neurite orientation is quantified using an anisometric orientation kernel that measures the influence of neurite growth direction with reference to the direction of the microelements (**Figure 5e**).[84] This is plotted in polar coordinates, revealing most orientation kernels occupying the same direction resulting in a sharp peak for microelements (blue), a blunter yet narrow peak for neurites influenced by the microelements (green), and finally, a broad distribution of neurite orientation for neurites without physical guidance cues from the microelements (red).

A discreet anisometric microelement array (VS = 5 μm, HS = 10 μm) resulted in the highest physical guidance for directed neurite growth, with over 55% of neurites orienting parallel to the guiding direction and only < 5% in the direction perpendicular with an interquartile range (IQR) ~ 24° (**Figure 6**). On the other hand, similar levels of neurite alignment are achieved for different HS and VS combinations, resulting in different total areas occupied by the guiding elements on the substrate. Interdependence between HS and VS is reported where even at large VS up to 100 μm between the discrete elements, linear nerve growth was still achieved for HS: 20 μm. Hence, we can reduce the total volume of the required guidance cues to obtain cell alignment by altering the vertical or horizontal spaces between the microelements. We also report an increase in the neurite orientation perpendicular to the microelements when VS: 200 μm (at HS: 20 μm), demonstrating a maximum vertical

distance at which the long axis of the anisometric microelements is still dominating the directionality of nerve growth.

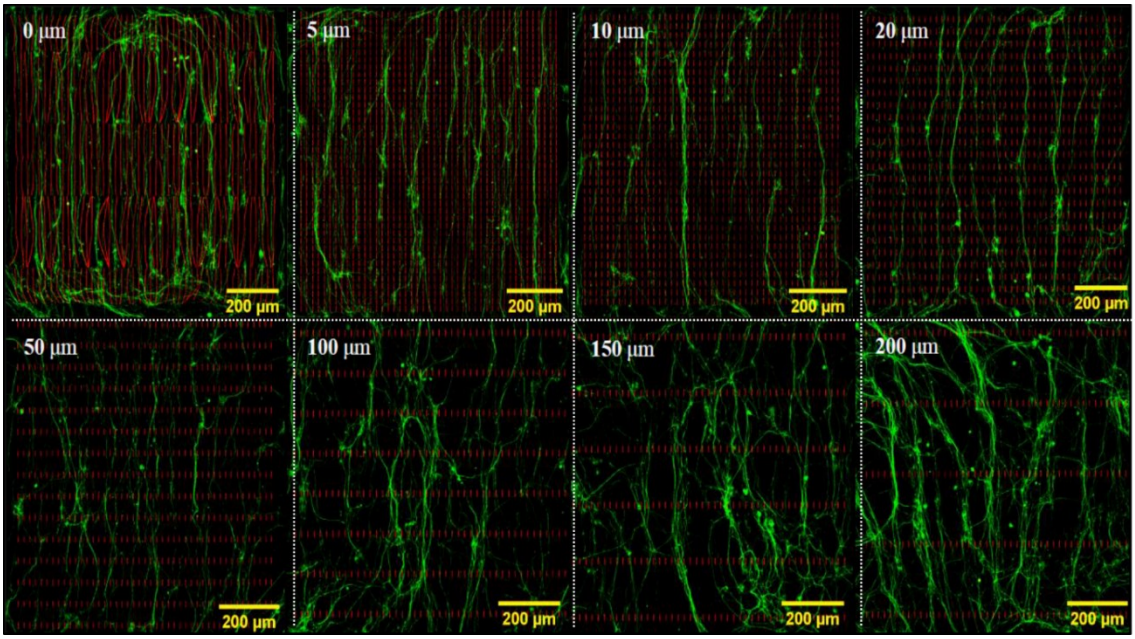

Figure 6. An array of anisometric microelements of dimension 20 x 1 x 10 µm with defined horizontal spacing (HS) of 10 µm and variable vertical spacing (VS) of 0 to 200 µm shows a decrease in neurite alignment along the microelements with an increase in VS.

1.4 The transition from 2D models to 3D models

Cells grown on flat substrates experience forces only from the surface, unlike native 3D tissue (**Figure 7a**), where cells experience forces from all directions (**Figure 7b)**. These forces come from interaction with their surrounding ECM or their neighboring cells. Haptotatic signals (biochemical signals attached to the substrate) determine how cells interact with their surroundings, and this often occurs in the form of gradients to direct cells in a specific direction.[85,86] In addition, cells respond to different stimuli, such as and shear forces that are transmitted through the bulk of the tissue or bulk resistance that is drastically different from traditional 2D *in vitro* culture.[85] In the case of 2D cell monolayer formation, the cells spread horizontally in one plane, and no control in the vertical plane is feasible. Control in bulk is essential, especially to steer cells in the direction of biochemical and mechanical gradients.

In contrast to 2D substrates where integrin-mediated cell adhesion occurs in a short period due to the restraint-free, unrestricted access to adhesion sites, cells inside 3D are dependent on degradable domains or physical remodeling of the microenvironment to spread, which usually takes a longer period.[87] Hence, 2D substrates do not faithfully reflect the complexities of the ECM, and the spreading morphologies of the cells are vastly different on 2D than in 3D scaffolds. To recapitulate the native ECM, a transition from 2D to 3D *in vitro* is desired. The 3D scaffolds are one step closer to mimicking the native ECM and act as an intermediate between 2D models and animal testing by playing a pivotal role in reducing the number of animal experiments, especially when screening a biomaterial for its cytocompatibility and toxicity, drug testing, and understanding cellular mechanisms. Another advantage of a 3D system is its versatility in imparting material architecture with cell models to mimic hierarchical tissue niches. Fabrication of ANISOGELS is one such example of creating spatially distributed mechanical cues imparting an anisotropic microenvironment for cells[51] (**Figure 7c**) (**Chapter 4**). Similarly, biomolecules can be spatially incorporated inside 3D gels to create a chemical gradient for controlling cell fate[88] (**Figure 7d**) (**Chapter 6**).

1.5 Strategy and need for hierarchical ECM mimicking scaffolds

Hierarchical tissues are complex, with architectures specific to their function. They are usually vascularised and/or innervated with nerve cells from the peripheral nervous system. The peripheral nervous system includes the nerves from and to the spinal cord. Both are composed of highly oriented neural tissue enclosed in long tubular structures.[89] After a spinal cord injury (SCI), the tissue architecture is damaged due to compression, laceration, stretching, or shearing, which is followed by secondary injuries that aggravate neurological deficit, impede axonal growth, induce further scar formation around the lesion, resulting in a loss in cell-cell communication, leading to impairment of sensory and motor functions as the

connection from the brain to the peripheral nervous system is interrupted.[90–94] Regeneration of such oriented nerve tissues after trauma involves designing a biocompatible environment for the injured neurons to regrow. This is achieved with either topographical cues to guide damaged axons to reach their target[92] or pharmacological neuroprotective drugs to reduce further damage. The former can promote tissue engineering-based strategies to promote self-regeneration of cells and their native ECM production to bridge the injury gap by filling the cavity created at the site of the injury[95] and creating a passageway[93,96].

For recovery of such injury sites, bio-instructive scaffolds need to provide an ambiance for cellular adhesion for neurites, reduce glial scar formation, and provide directional cues for the regenerating axons to cross the injury site to regain partial or complete functionality.[95,97] Implant technology allows for the incorporation of artificial conduits or scaffolds that often involve removing damaged tissues, which may cause plausible damage to any spared functional tissue.[52,98] Transition from implantable to injectable scaffolds paved the way to minimally invasive tissue engineering. Although injectable scaffolds developed from exogenous (agarose, chitin), endogenous (fibrin, collagen), or synthetic (PEG, PLGA) biomaterials provide microenvironments with chemical and physical cues, they usually do not create directional guidance for axons to cross the site of injury.[99] Understanding the process of neuronal circuits, their regeneration, and axonal navigation is primordial for developing functional biomaterial scaffolds.[100] Axonal regeneration is primarily influenced by the architecture of the scaffold, adhesive chemical cues, supporting cells, and growth factors.[101] In the following sections, we will address these components to develop hydrogels imparting oriented cell growth.

1.6 Integrin binding domains improve cell adhesion

In addition to the diverse bio-physical cues discussed in **section 1.3**, biochemical cues in the form of ligands are either soluble in media and diffusible for cell uptake or are available inside scaffolds for cellular adhesion. These biochemical cues determine the

cell fate, especially for adherent cells. The integrin transmembrane proteins are composed of α and β subunits responsible for focal adhesion between cells and their ECM.[102] Focal adhesions, formed by clustered receptor-ligand interactions, can be temporary and permanent depending on their microenvironment. While in specific cells, focal adhesion occurs exclusively via one or many pathways, it is often regulated by the ligands that bind to the receptors in the cell membrane.[103]

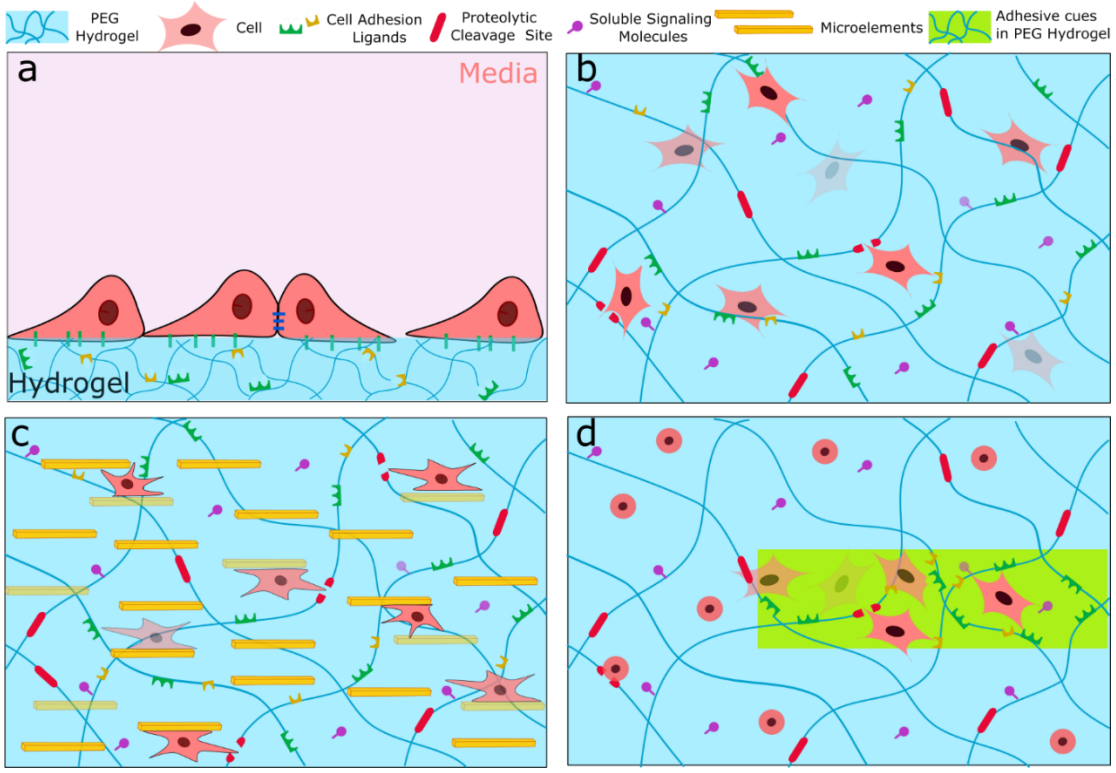

Figure 7. Schematic representation of cell adhesion a) on hydrogel with integrin-binding ligands, b) Cells encapsulated in 3D hydrogel matrix that is degradable on cell demand with proteolytic cleavage sites, soluble signaling molecules, and integrin-binding ligands integrated to the matrix. c) Additionally, integrin-binding ligands can be incorporated via short rod-shaped microgels that are mixed with injectable PEG hydrogels also bearing cell adhesion ligands. d) Integrin binding ligands can be incorporated spatially via photopatterning.

The smallest ligand binding to integrins is tri-aminoacid peptide Arg-Gly-Asparic acid (RGD), often flanked with other amino acids to improve the binding affinity.[104] Variants of linear RGD peptides were developed to improve affinity and selectivity towards integrin subunits, such as mono-cyclic RGD peptides and peptidomimetic ligands.[39] For example, a simple flanking of the linear RGD peptide with glycine (G)

at the N terminus and serine (S) at the C terminus results in a decrease in half-maximum inhibitory concentration (IC_{50}) values by 3 and 4 folds for $\alpha_v\beta_3$ and $\alpha_5\beta_1$ integrin subunits, respectively.[104] Lower IC_{50} values indicate a higher affinity to integrin subunits, and the lowest IC_{50} value was observed for heptapeptide GRGDSPK, which is 7 folds lower than for tripeptide RGD in the case of $\alpha_v\beta_3$. Similarly, the cyclization of linear RGD peptides (RGDfK) and incorporation of one D-amino acid residue between Asp (D) and Lys (K) improves affinity to integrin subunits and increases stability towards enzymatic degradation.[105]

The monocyclic RGD peptides show moderate to low IC_{50} values towards multiple integrin subunits, such as $\alpha_v\beta_3$, $\alpha_v\beta_5$, $\alpha_v\beta_6$, and $\alpha_5\beta_1$. For example, the lowest IC_{50} values are observed for $\alpha_v\beta_3$ subunits as cyclization improves integrin-binding affinity for $\alpha_v\beta_3$ in the range of 1.5–6.0 nM, in contrast to $\alpha_5\beta_1$ in the range of 141–236 nM.[104] Similar to flanking in linear RGD, flanking in cyclic RGD peptides with linear polyproline improves cell spreading and focal adhesions in rat embryo fibroblasts compared to other spacers like PEG.[106] Another class of high affinity and selective integrin-binding ligands is the peptidomimetics, which can distinguish between different integrin subtypes *in vitro* and *in vivo*.[107,108] It is important to understand the role of integrin-mediated adhesion to its corresponding ligands in the ECM for controlling cell fate in regenerative materials.

For nerve regeneration, scaffold development is desired specific to the requirements at the injury site. The De Laporte research group developed ANISOGELS with full-length fibronectin, fibronectin fragments, or linear RGD for oriented nerve growth. Although several hydrogel-based scaffolds have been developed for axonal regeneration, the optimal combination of biochemical, physical, and architectural cues in the microenvironment to induce unidirectional nerve growth in a fully synthetic scaffold is still not achieved.[54] In **Chapter 4,** I investigated the role of bicyclic RGD peptides in fully synthetic ANISOGELS. This novel class of adhesive bicyclic RGD peptides, consisting of two loops with tri-aminoacids, is easily synthesized and

offers a low immunogenic response. The first loop consisting of an RGD sequence imparts the cell adhesive cues, while the second loop has the potential to affect the RGD selectivity towards different integrin subunits (**Figure 8b**).[109,110] These peptides offer high selectivity towards $\alpha_v\beta_3$ and $\alpha_5\beta_1$ integrin subunits and demonstrate outstanding conformational rigidity and metabolic stability compared to commercially available ECM proteins or genetically engineered protein fragments.

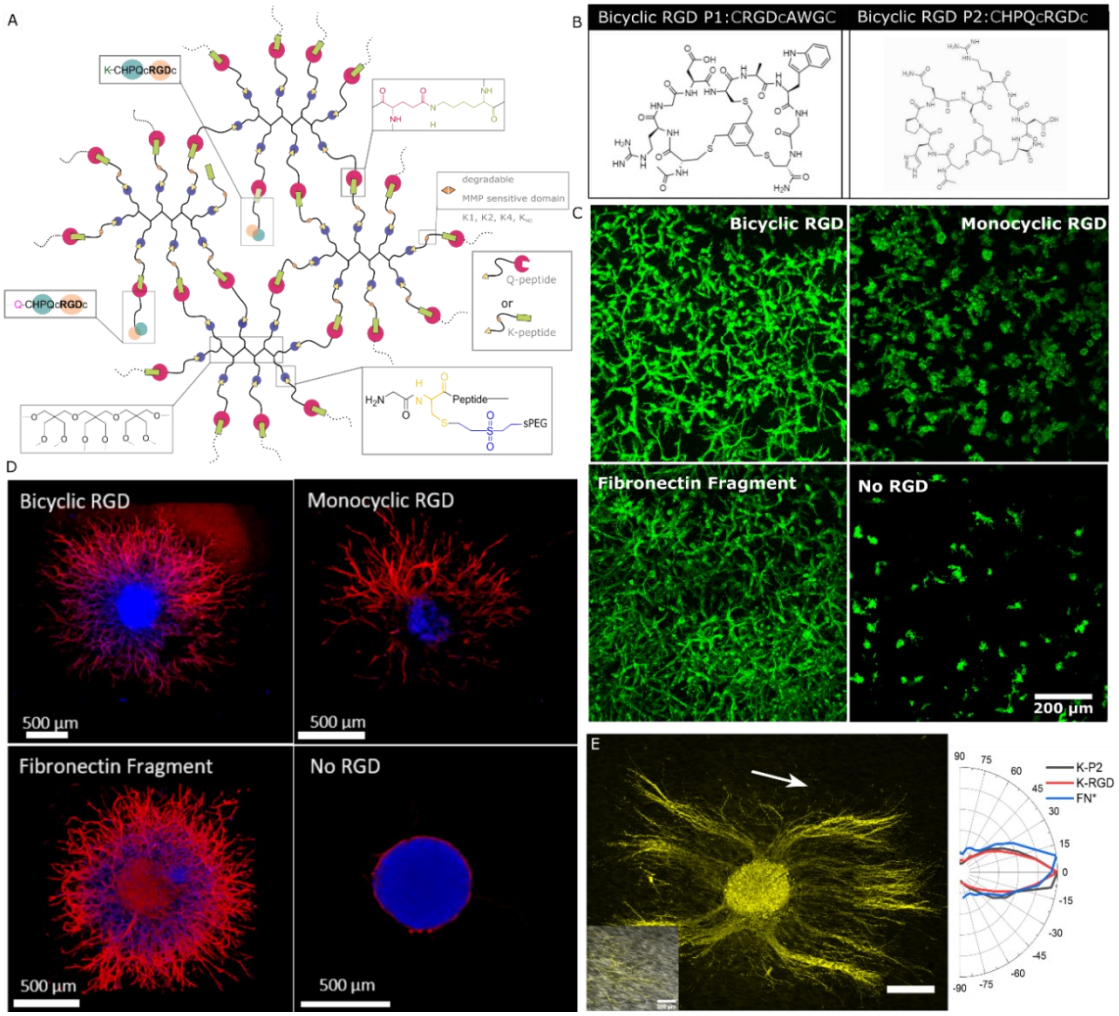

Figure 8. A) Schematic description of 8 arm PEG-Q and PEG-K crosslinked hydrogels bearing MMP sensitive domains and bicyclic RGD peptides. B) Chemical structure of bicyclic peptides selective for integrin $\alpha_v\beta_3$ and $\alpha_5\beta_1$, respectively. C) Influence of integrin peptide bearing PEG hydrogels on L929 mouse fibroblast growth showing superior cell growth in gels with bicyclic RGD peptides compared to monocyclic and no RGD. D) Similarly, the nerve from chick DRG growth is superior in gels with bicyclic RGD peptides compared to monocyclic and no RGD. Adding anisometric fibers to such hydrogels revealed superior nerve alignment.

Therefore, I investigated the role of the novel bicyclic RGD peptide, which was developed in collaboration with PEPSCAN, inside synthetic PEG hydrogels. The bicyclic RGD peptides are tethered into the backbone of the gels (**Figure 8a**) via transglutaminase-induced crosslinking, resulting in an improved microenvironment for 3D cell culture. Enhanced growth of mouse fibroblasts (**Figure 8c**) and nerve cells in gels tethered with bicyclic RGD peptides is observed (**Figure 8d**) in comparison to gels tethered with linear or monocyclic RGD peptides.[40] A slight increase in nerve length is shown with bicyclic peptides selective towards $\alpha_v\beta_3$ compared to $\alpha_5\beta_1$. This opens an opportunity for integrin-specific cell growth in artificial synthetic ECMs. The hydrogel microenvironment is further optimized by screening several MMP degradable crosslinkers in combination with bicyclic RGD peptides to obtain a fully synthetic ECM with optimized chemical and physical cues. To achieve directionality in the optimized hydrogels, anisometric orientable short fibers are incorporated in the PEG hydrogel to obtain a fully synthetic ANISOGEL, which imparts all the necessary growth cues for controlled and directional cell growth (**Figure 8e**). In addition, such hydrogels are injectable at the site of injury, which could improve the ability of the nerves to regenerate.

1.7 Transition from elastic to viscoelastic and strain-stiffening microenvironments

Unlike the native ECM, which is naturally fibrillar, viscoelastic, and strain-stiffening[111], covalently crosslinked synthetic hydrogels predominantly present an elastic, homogeneous microenvironment primarily addressing the role played by matrix stiffness and water content in the design of aECM.[112] Natural proteins, such as collagen and fibrin, offer a fibrous environment that is dynamically tunable. Their fibers provide a skeletal structure to the cells imparting tensile forces during ECM probing and docking, and subsequently, cell adhesion and migration. Such cellular mechanisms are vital to control cell proliferation and direct tissue repair and regeneration.[13] Although PEG behaves as a blank template that can be tuned for its

biological and architectural properties by incorporating different motifs, when crosslinked covalently, the hydrogel consists of innate homogeneous elastic properties that fail to mimic the biological properties, such as physical crosslinks, viscoelastic properties, and strain-stiffening behavior, which renders the gel dynamic with the ability to strain stiffen or stress relax at different time scales. Cellular mechanisms regulated by mechanosensitive proteins (YAP, MRTFA) and enzymes require an external mechanically responsive microenvironment inside synthetic artificial ECMs.[113,114] Introduction of degradable moieties, such as hydrolytically degradable esters[115,116] or proteolytically cleavable MMP ligands[26], alters the mechanical properties of the hydrogels moving away from the purely elastic environment.[117] However, hydrogels functionalized with reversible bonds present an alternative to elastic matrices by offering stress relaxing[20,113] or strain stiffening microenvironments[118]. Reports show that viscoelastic materials can dissipate cell-induced stress over time and mimic native ECM better than pure elastic gels.[113] For example, hydrazone bonds are reversible, imparting stress relaxation properties of biological tissues. PEG hydrogel with hydrazine functional groups allows crosslinks to rearrange in the time frame similar to cellular mechanisms, like extensions, for example, to enable cytoskeletal outgrowth in myoblasts to form myotubes.[20] However, hydrogels with self-healing ability are generally weak and do not hold their structure over the period required for regeneration.[119]

Recently developed synthetic matrices, such as poly-iso-cyanide (PIC) with oligo (ethylene glycol) side chains that self-assemble to form β-helical superstructures, employ non-linear mechanics in mimicking fibrillar proteins.[120] These filamentous polymers are tuned by altering their polymer contour length (Lc) to impart a wide range of fiber diameters that form bundles and their associated mechanical properties. The PIC bundles are strain stiffening, which means that after certain critical stress, the hydrogel responds rapidly by stiffening,[121,122] a phenomenon occurring in the native tissues at a short time scale. PIC hydrogels are formed above their tunable LCST (~15° C) when the ethylene glycol substitution in the polymer becomes hydrophobic,

resulting in a thermal switch. The helical structures of polymeric chains form bundles even at low concentrations (0.5 to 5 mg/mL) with a shear modulus ranging from 30 to 1000 Pa. Hydrogen bonds stabilize the side chains. A decrease in pore size is observed with increased polymer concentration and bundle diameter with a broad pore size distribution (nm to μm). The PIC polymer bundles with variable persistence length enable the formation of soft yet mechanically stable gels at low concentrations.[120] Cell responses to strain stiffening include differentiation of MSCs to adipose cells at lower critical stress with shorter PIC polymer and differentiation into osteogenic lineage in long PIC polymer at higher critical stress, revealing the role played by the rate sensitivity to strain stiffening during differentiation.[123] The PIC hydrogels are rendered bioactive by incorporating GRGDS peptides with controlled distances between adjacent RGD peptides.[118] While such gels provide an ideal environment for cell growth and aECM fabrication, they are susceptible to temperature fluctuations resulting in variable mechanical properties and sometimes fragile gels.

In **Chapter 5**, I investigated a combination of PEG and PIC gels to form interpenetrating polymer networks (IPNs) with properties from both hydrogels. Typically, an IPN consists of 2 or more polymer networks that are independently formed without covalent bonds between each other. One of the standard techniques to form IPN is a sequential formation where a formed hydrogel is swelled in another monomer and activator to form the interpenetrating networks. Another technique is the simultaneous formation of the two polymer networks by mixing different precursors to form independent networks.[124] Here, I employ the latter system with an interpenetrating network (IPN) with Q/K PEG (described in **Chapter 4**) and PIC hydrogels. The desired properties from the individual hydrogels are combined to create a synthetic hybrid artificial scaffold (**Figure 9a**). An increase in temperature (> 15°C) results in thermal gelation of PIC hydrogels with reversible physical crosslinks, while enzymatic crosslinking of 1 wt% PEG (with t > 20 mins) results in a chemically crosslinked soft PEG hydrogel system. While the IPN offers a strain stiffening matrix

at 37°C, the PEG hydrogels impart thermal and physical stability at all temperature ranges.

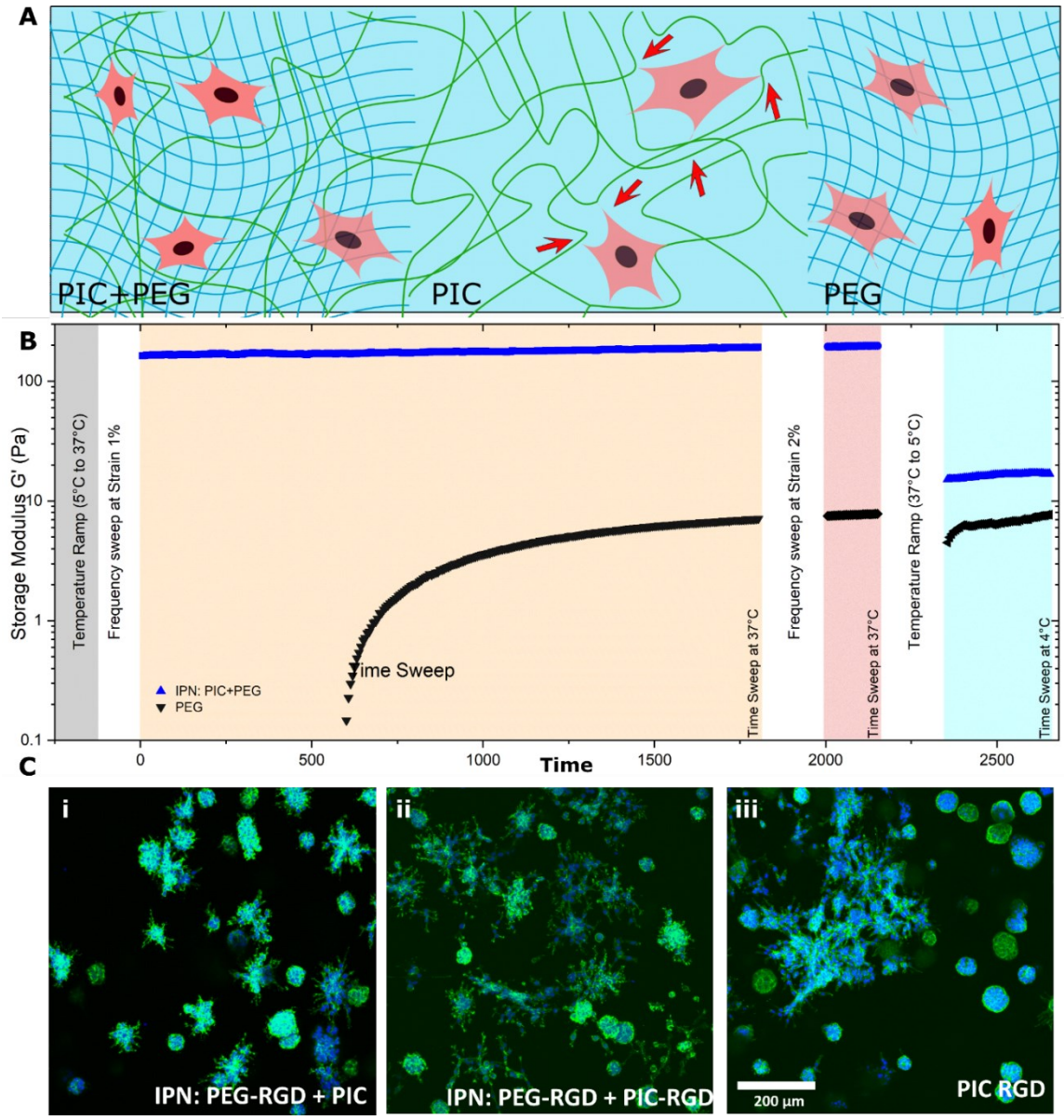

Figure 9 a) Schematic representation of hybrid hydrogel network with 8 arm PEG hydrogels and polyisocyanide gels forming interpenetrating networks (IPN) imparting properties of both elastic and viscoelastic matrix. b) Rheological properties are measured for IPN and PEG hydrogels by applying shear forces to measure the gelation kinetics at 37°C, and a temperature sweeps down to 4°C to decouple the properties imparted by PIC hydrogels c) 3D cell growth of mouse L929 cells inside PEG hydrogels in (i) IPN with PEG-RGD, (ii) IPN with PEG and PIC RGD, and (iii) only PIC RGD showing increased cell spreading in IPN compared to PIC alone.

At physiological temperature with fixed strain, the IPN has an increased stiffness by ~3 folds compared to the pure PIC gels and ~27 folds higher than the PEG hydrogels. The PIC hydrogel is dissolved on cooling, resulting in an exclusive PEG gel (**Figure 9b**). The cells encapsulated in the IPN show improved cell spreading compared to PIC hydrogels or PEG hydrogels alone (**Figure 9c**). Such hybrid hydrogel is investigated in **Chapter 6** and can be employed as an injectable scaffold possessing mechanical and biochemical properties of both elastic and strain stiffening hydrogels, moving a step closer to mimicking native ECM.

1.8 Hierarchical aECM constructs with spatiotemporal control via patterning

Traditional aECM matrices are predominantly static and isotropic and often fail to capture the biologically responsive feedback mechanism involving the dynamic, complex, and heterogeneous microenvironment, neglecting spatial and temporal triggers required to form specific tissue architectures.[125] Creating a user-defined biomolecular gradient[126], local spatial degradation[127], or temporal matrix stiffening[128] are essential, especially during tissue formation or disease development. This is achieved by patterning architectures essential for cell organization and mini-tissue formation in 3D.[125] Among the several non-invasive and non-toxic techniques available (**Chapter 2**), photopatterning offers the possibility to tune several parameters, such as local functionalization and crosslinking density, resulting in various aECM models.[129] Most 3D studies employ a single mode of homogenous crosslinking, whereas now it is possible to spatially alter the matrix stiffness to control the behavior of cells encapsulated. Opto-regulation can control both mechanical and biochemical properties inside the synthetic gels, altering one or many properties based on the desired tissue model.[129]

1.8.1 Regulating biomechanical properties

Opto-regulation allows for modifying mechanical properties by creating heterogeneities in an otherwise homogeneous hydrogel **(Figure 10a)** with high spatial and temporal control by either creating additional crosslinks to increase the matrix stiffness (**Figure 10b**) or cleaving crosslinks to make the gels softer (**Figure 10c**). At the same time, matrix stiffness can be introduced by crosslinking of un-crosslinked functional arms, such as acrylates[130] or reactive groups blocked by photoprotective groups (PPG). A report with acrylate-based hyaluronic acids gels with cell adhesive sites and MMP-cleavable crosslinkers showed that the local matrix stiffness could be tuned adjacent to the encapsulated cells. While the original network is "permissive" to remodeling and cellular spreading, only a portion of the total acrylate groups is consumed during initial crosslinking. Therefore, exposure to UV light post-crosslinking results in additional crosslinks with the remaining functional groups in the hydrogel, creating an " inhibitory " network to cell spreading.[131] An essential feature of PPG is their availability to be sensitive to a wide range of wavelengths (300 nm to 860 nm) that allows for incorporating multiple orthogonal PPGs in the same hydrogel.[132] Although most systems employ UV-based PPGs, such as nitro-benzyl groups, the far red photon (720 - 860 nm) based coumarin PPG is considered more cytocompatible and cell-friendly.[133,134] After light-induced deprotection, the unprotected reactive functional groups are available to either crosslink or link to bioactive domains. Alternatively, the deprotection leads to breakage of crosslinks to cleave the matrix, leading to an alteration of local stiffness that is essential to mimic tissue organization in the body with varying stiffness, ranging from soft neural tissues (100 - 1000 Pa), muscle tissue (8- 17 kPa), and stiff bone tissues (25- 40 kPa).[112] The importance of photo-stiffening was first demonstrated on 2D *in vitro* platforms where patterns using photomasks are created with light to form highly crosslinked hydrogels regions. Methacrylated hyaluronic acid hydrogels showed better MSC cell growth on UV exposed regions compared to non-exposed regions.[135] In the case of 3D PEG gels, on-demand photo-stiffening, presented a tuneable matrix with stiffness shuttling

from 10 to 50 kPa on exposure to UV at 365 nm. This system was employed as a tool to explore mechano-transduction pathways for cardiac fibroblasts, revealing the stiffness dependent NFAT nuclear localization is feasible by regulating substrate modulus over short time scales.[136] However, most photo-chemistry involved free-radical polymerization that uses radicals harmful to cells; hence a milder yet specific hydrogel system was developed using click chemistry between electron-withdrawing groups (EWG), like maleimide, vinyl sulphone, or acrylates, and electron-donating groups, like thiol or amine. Star-PEG bearing photo-protected thiols (SH) are mixed with their conjugate star-PEG-VS and on deprotecting the thiols with light, the two PEG precursors crosslink to form a gel with defined stiffness. The spatially and temporally controlled stiffness in such gels is regulated by altering light intensity.[137] Additional factors like pixel dwell time, magnification of the objective, and attenuation of the light path, control the degree of PPG deprotection. Although these techniques recapture part of the native ECM, they have to be constantly protected from exposure to light that triggers mechanical or biochemical alterations. While these techniques allow stiffness modulation by light, the same technique can be employed to incorporate bioadhesive ligands that enable cell adhesion.[130,138]

In contrast to additive crosslinking, light-induced photodegradation causes hydrogel crosslinks to cleave, resulting in subtractive modulation of the elastic modulus, thereby regulating or retracting cell migration in confined volumes. Degradation of local crosslinks using UV light allowed for the formation of hollow patterns inside non-degradable PEG hydrogel enabling controlled cell invasion.[139] Typically, cell migration is controlled by either restricting its available support by degrading the photopatterned region[140] or permitting migration in fabricated microchannels using photoablation[141]. In one study, the vascularized microchannels were fabricated by incorporating photo-degradable moieties in the gel backbone, resulting in the formation of hollow ducts in the light-exposed regions. The cross-sections of the ducts are fabricated between 10 to 200 μm^2, allowing endothelial cells to form hollow tubes in the proximity of stromal cells.[142] Evolving from such platforms, biofunctionalized

hydrogels were developed with PPG groups that spatially modulate the biomolecular ligand density of short peptides or proteins. Using a crosslinking mechanism via click-type photochemistry with oxime-based PEG hydrogels, stiffness modulation, and immobilization of multiple full-length proteins at micron-scale resolution was possible.[143] However, the duration of UV exposure dictates the mechanical properties along with the concentration of the biomolecule density. In many studies discussed above, opto-regulation of mechanical properties goes together with opto-regulation of biochemical properties inside the patterned regions.

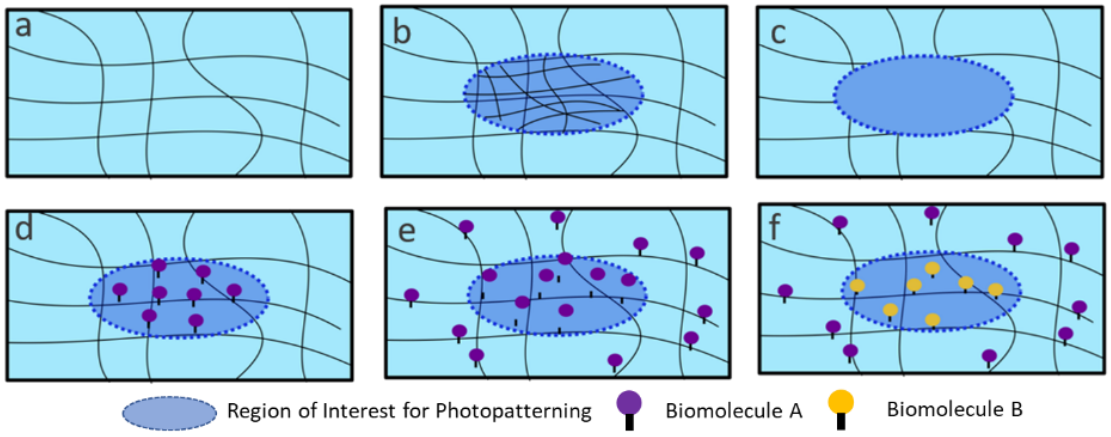

Figure 10. Schematic representation of biophysical or biochemical photopatterning in PEG hydrogels. a) Control hydrogel represents a homogeneous microenvironment. b) Increase in crosslinking density inside the region of interest, c) removal of crosslinks by ablation to tune the local biophysical properties in 3D PEG gels. d) Addition of biomolecules, e) removal of biomolecules or caging groups, and f) coupling of different biomolecules to the PEG hydrogel to tune local biochemical properties in a photopatterned hydrogel.

1.8.2 Regulating biochemical properties

Biochemical properties inside the hydrogels are altered by additive bio-functionalization (**Figure 10d**), subtractive bio-functionalization (**Figure 10e**), or by sequential cleaving of PPGs and locally tethering biomolecules (**Figure 10f**). Combing more than one biofunctionalization strategy is also feasible when orthogonal photo-chemistries are applied.[144] Here, the conjugating biomolecule is a mono-functionalized ligand with a reactive group that binds to the PEG arms like a hanging

pendant.[143] De Forest et al. developed a series of PEG hydrogel systems with bio-orthogonal photo-chemistries to achieve reversible immobilization of peptides and proteins of interest.[126] Caged functional groups with ortho-nitrobenzyl groups incorporated in the crosslinking arms are cleaved using light. After cleavage, the terminal site becomes an active site to bind peptides or proteins.[145] Such photo-triggerable systems enable caging of molecules, such as biotinylated antibodies, to enable region-specific immobilization of streptavidin, targeting selective cell attachment.[146]

A major challenge in tissue engineering lies in developing *in vitro* organoids, tumor models, or mini tissues with functional blood vessels that transport nutrients and oxygen into the tissues and remove waste to avoid the formation of a necrotic core. A non-invasive photo-chemical patterning offers a tangible solution by spatially directing cells inside biomolecular patterns in 3D scaffolds to address this issue. RGD peptides modified with PPGs allow for *in situ* regulation of cellular response on exposure to light.[147] HUVECs encapsulated inside PEG hydrogels with an MMP degradable matrix and caged RGD molecules as biochemical cues enable selective cell growth and migration confined in the photopatterned hydrogel regions. Furthermore, sequential photopatterning at several time points enables microvasculature formation in the newly activated region to achieve temporally controlled vasculogenesis.[148]

As discussed previously, the role of integrin-specific ligands is crucial in designing aECM scaffolds, and the development of a photo-triggerable variant of $\alpha_5\beta_1$ antagonist with a photo-caged group inhibited the biological activity of the ligand. Upon selective deprotection, HUVECs were attached exclusively to the photoactivated regions, highlighting integrin selectivity's relevance and importance.[149] Similarly, for other tissues, such as nerves, the short laminin-derived peptide IKVAV, known to induce neurite formation, was caged at its lysine (K) and conjugated to acrylamide-co-acrylic acid hydrogels. Site-selective biomolecule activation using visible light at 490 nm exposed free IKVAV available for neurites to follow the photopattern.[138,150]

In **Chapter 6**, I investigated the use of caged RGD and caged IKVAV as biomolecules inside 3D PEG hydrogels in collaboration with Prof. Del Campo (INM, Saarbrücken). I created biomolecular patterns in hydrogels resulting in a spatially controlled growth of DRGs (after 7 days) and fibroblast clusters (L929, after 5 days) inside the patterned regions (**Figure 12 c,d**). However, these results were not reproducible due to technical difficulties described in **Chapter 6**. Despite desired control in cell growth, the gels have to be protected from visible light throughout the culture period to prevent unspecific decapping of RGD, even though the PPG are mainly sensitive to UV light. Hence, I employed a two-step process for photo-patterning, where the caged group is an intermediate between the basal network and biomolecule. This method enables binding of more than one biomolecule sequentially. In another similar study, modified agarose hydrogels with capped nitro benzyl cysteine are deprotected on exposure to UV resulting in free thiols to further react with maleimide containing RGD at physiological conditions enabling the growth of primary neurons from DRG.[151] Thus, confined patterning of biochemical cues in 3D gels is feasible without having to protect the scaffold from light throughout the study.

Hyaluronic acid (HA) based gels are often employed as a scaffold for neural tissue engineering. Modifying HA with lysine and glutamine residues enable tuneable gelation kinetics in a highly specific manner in the presence of transglutaminase, similar to the PEG-KQ system described above and in **Chapter 4**. Neural cells from embryonic cortices extracted from rats encapsulated in these gels showed long-term stable and coordinating spiking activity.[152] This principle was applied with PEG gels where the caged intermediate is a caged lysine-containing peptide tethered to the star-PEG-VS backbone by Michael addition reaction via a cysteine. The system employs a caging nitrobenzyl group that protects lysine and activates the amine upon light exposure (**Figure 11a**), reacting further to the glutamine-bearing biomolecule of interest (BOI) via a highly specific transglutaminase reaction in the presence of activated factor XIII.[153,154] This system employs the crosslinking and biofunctionalization mechanism discussed in **Chapter 4** but here, the mechanism is

applied only for biofunctionalization instead of crosslinking. The photopatterning experiments were performed in MMP degradable sPEG hydrogels crosslinked via Michael-type addition using star-PEG-VS and linear di-cysteine MMP sensitive peptides.

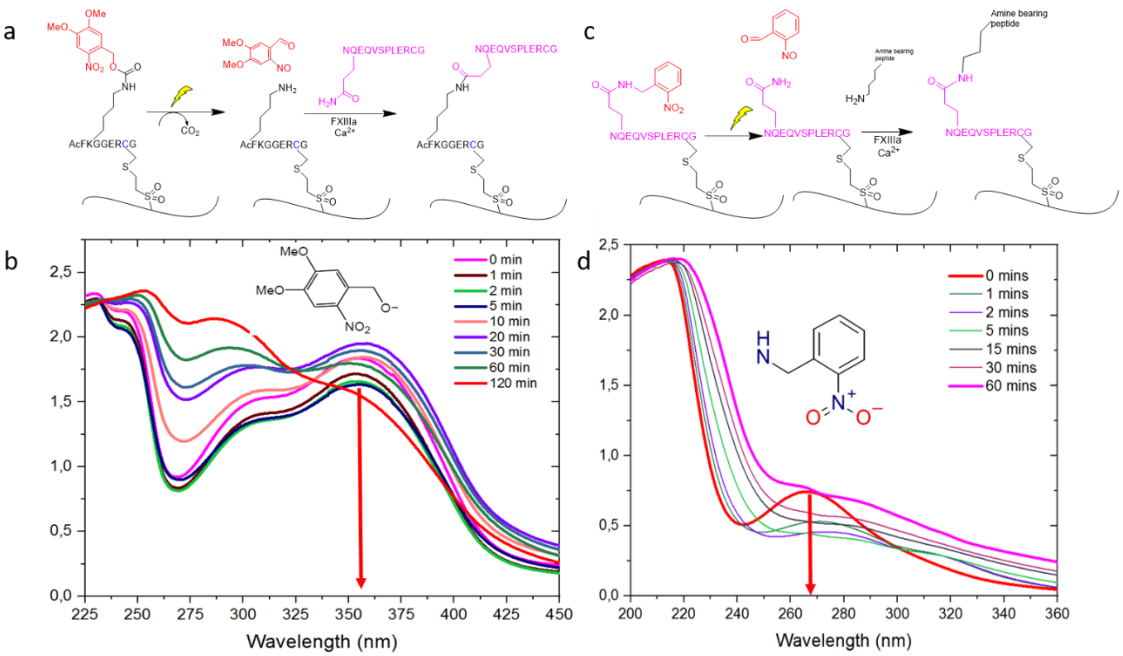

Figure 11. a) The reaction scheme of Caged Nvoc protecting amine of lysine peptide is cleaved using light which can be coupled to a glutamine bearing peptide (NQEQVSPLERCG) which can be modified to bear a biomolecule of interest. b) The decapping is performed using a lamp at 365 nm, and its spectrum is measured over 120 minutes. c) Similarly, the o-nitrobenzyl group protecting an amide group is cleaved using a 365 nm lamp exposing the free glutamine group. d) The decapping spectra are measured over 60 minutes.

The deprotected K peptides bind to biomolecules bearing the specific transglutaminase sequence (NQEQVSPL).[155,156] During these studies, I observed that the presence of such flanking peptide sequences (NQEQVSPL) reduces nerve cell growth in comparison to RGD ligands without these flanking amino acids. This screening was performed on a thin film made from sPEG-NCO[157], which binds to the free amine of biomolecules, creating a thin layer of biomolecules available for cells. Thus, I adapted the patterning system to remove the NQEQVSPL peptide sequence to improve nerve cell growth. Therefore, I switched the caging amino acid from lysine to the glutamine inside an NQEQVSPL peptide sequence attached to the PEG

backbone. The caged glutamine-containing peptide was engineered and produced with Prof. Peter Timmerman, PEPSCAN B.V, NL. Using this method, the BOI can be any ligand bearing a lysine or a free amine to conjugate with the de-protected glutamine, which renders this system more versatile and practical. Such a spacer-free BOI opens the possibility of applying a wide range of biomolecules into the photo-patterned region (**Figure 11c**). The decapping kinetics of both the caged lysine and caged glutamine showed that the duration and choice of laser wavelength are crucial for photopatterning as this may be the limiting/slowest step in bio-patterning (**Figure 11b, d**). Therefore, I investigated the influence of these patterning parameters by quantifying the density of free amines immediately after decapping capped lysines. This revealed that with tuning the laser exposure time or pixel dwell time, the density of the decapped free amines can be easily controlled (**Figure 12b**). Over 1h duration of photopatterning with 405 nm laser was required to achieve strong contrast between patterned regions and non-patterned regions. Further investigation revealed that a higher intensity laser is required to obtain the required contrast between patterned and non-patterned regions.

A limitation in the reported system is that when the laser light passes through the hydrogel, the entire light path is decapped, with the strongest decapping efficiency at the plane of focus. Hence, I employed a two-photon laser (TPL) assisted patterning at a wavelength of 700 nm to achieve a high spatial control inside the hydrogels in the z-axis. The two high-frequency photons enable controlled and high-resolution spatial patterning. Application of TPL in other reports shows that PEG hydrogels with BCN groups are formulated with a PPG bearing an azide and an MMP-based crosslinker. On exposure to the 2 photon laser, the nitro benzyl group is cleaved off, creating hollow spaces in the pattern region to fabricate channels for endothelial cells in the presence of stromal cells.[142] This system allowed the formation of vascularized channels with diameters ranging from 10 to 200 μm. The potential to use near infra-red light in TPL opens avenues to tightly focus spatial biomolecular patterns down to 0.5 microliter volumes in deep tissue up to 10 cm.[158] TPL is also applied on photoresist

resins as described in **Chapter 3** to create 3D scaffolds by covalent crosslinks to fabricate structures with distinct biomolecular coatings.[159]

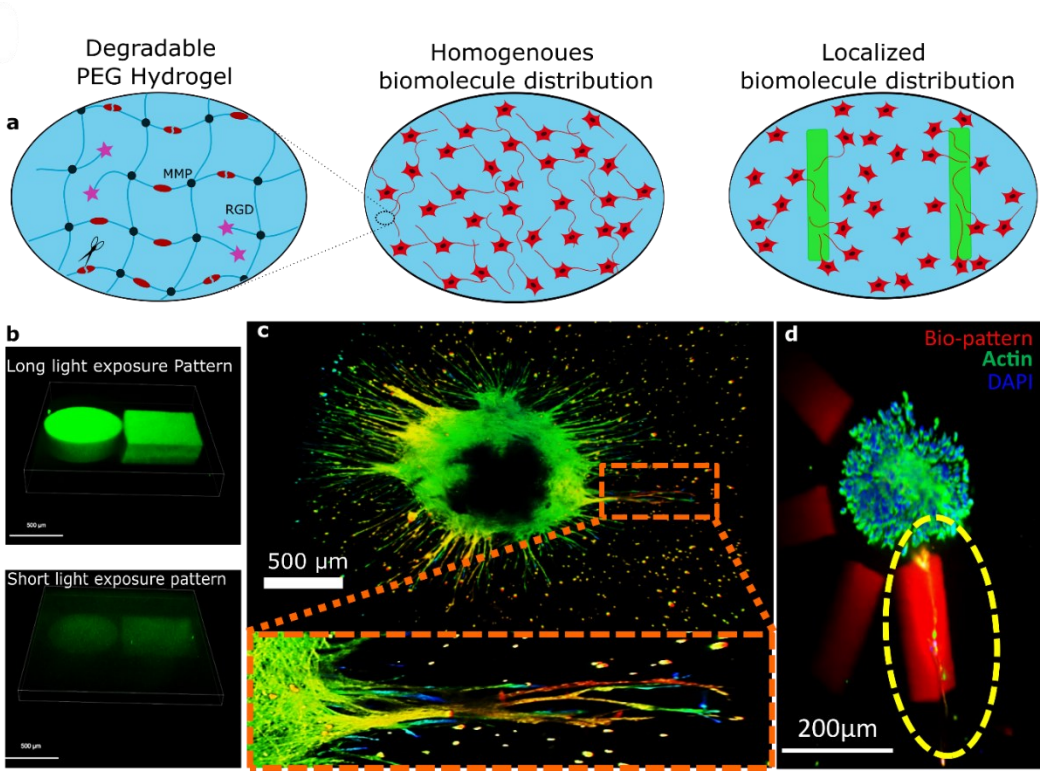

Figure 12. a) The Schematic representation of degradable hydrogels with MMP sensitive crosslinkers and biomolecules are now translated to spatiotemporally defined regions using photopatterning. b) Quantifying density of decapped lysine peptide using CBQCA assay that detects free amine concentration at both short (1 min) and long (60 mins) exposure times. c) 3D Neurite outgrowth in photo-patterned regions after 7 days. d) Similarly, invasion of L929 fibroblast cluster inside photopatterned regions after 5 days.

1.9 Summary

This doctoral thesis reports multiple strategies to develop 3D aECM for directed *in vitro* cell growth. The influence of different biomaterial parameters, such as chemical, physical, and architectural cues, on cell growth is characterized. **Chapter 1** discusses the research motivation highlighting the most relevant literature in the field of aECM development towards hierarchical scaffolds, its limitations, and my approaches to specifically address these limitations. It provides the red line through my thesis. **Chapter 2** highlights state-of-the-art in more detail: i) ECM development, ii) Engineering integrin-binding domains, iii) Fabrication techniques for surface

topographies and iv) Synthetically derived 3D scaffolds. **Chapter 3** describes the role of architectural cues in orienting nerve cells on 2D platforms developed using a high-throughput TPL system. The ability of nerves to follow discreet anisometric microelements is systematically investigated. Subsequently, the role of supporting cells in creating aECM platforms is realized. **Chapter 4** describes the transition from 2D to 3D scaffolds, which is essential for mimicking relevant tissue models *in vivo.* Synthetic PEG hydrogels tethered with novel integrin-specific bicyclic RGD peptides are investigated, reporting superior nerve growth compared to linear or monocyclic RGD peptides. ANISOGELS made with magnetically orientable fibers provided oriented nerve growth in these hydrogel systems. **Chapter 5** illustrates the importance of the viscoelastic and strain-stiffening microenvironment in aECM design and the role of interpenetrating networks of PIC and PEG showing superior mechanical properties compared to the individual gels for cell growth. **Chapter 6** discusses in detail the techniques to spatially photo-pattern biomolecules relevant for cell adhesion. Here, two different photo-patterning systems are explored that do not alter the biomechanical properties. The caged RGD system and the caged Q/K systems both show possibilities for directed and spatial control of cells. The variety of PPG available in different wavelengths paves the way from *in vitro* photopatterning towards *in vivo* photopatterning to create biochemical gradients in injectable aECM scaffold. To summarize, the PEG hydrogel reported in this thesis is a versatile system that can be employed as a promising injectable scaffold with integrin selective adhesion cues, imparting viscoelastic properties in combination with PIC-PEG IPNs, and finally enabling oriented cell growth using ANISOGELS or through bio-patterning.

Chapter 2. State of the art

2.1 Extracellular Matrices (ECMs)

ECM provides the fundamental structural and biochemical support required for cell growth development.[160] The characteristic functions of ECM include cellular response to biochemical and mechanical signals, permeation and perfusion of nutrients gradients, transport of cell-cell signals, and aid in cell differentiation, proliferation, and apoptosis.[161],[162] The cues imparted by the ECM to the cells and vice-versa guide dynamic remodeling of the ECM to obtain specific microenvironments or niches[163] for cellular reorganization and tissue formation.[16] Interactions between cell membrane receptors and chemical ligands in the ECM that are essential for cellular metabolisms involving cascade signaling, especially in the adherent cell.[164] Such ligands in the ECM act as anchor sites promoting cell adhesion, while gradients promote cellular migration.[165,166] Integrins are heterodimeric cell membrane proteins with α- and β-subunits acting as bidirectional transmembrane receptors.[167] ECM matrices composed of native proteins such as fibronectin[168], and laminin,[169] primarily consist of ligands that are used by the integrin subunits for anchorage. The specific sites in the protein responsible for integrin binding are reverse-engineered to find the smallest integrin recognizable ligand bearing 3 amino acids: Arg-Gly-Asp (RGD).[170] Other peptide ligands include Ile-Lys-Val-Ala-Val (IKVAV), and YIGSR[33] present in laminin proteins and are relevant for neuronal tissues.[171,172, 173] To recapitulate the ECM, it is essential to comprehend the essential features of the ECM to generate artificial functional tissue scaffolds.

2.2 Naturally derived biopolymers as scaffolds

Natural ECM consists of a network of hydrated proteoglycans coiled around fibrous proteins. Scaffolds developed from natural ECM are often processed from whole ECMs

or are isolated and purified from individual ECM components such as collagen[174], fibrinogen[175], elastin, fibronectin, and laminin.[176] These components are viscoelastic, cyto-compatible, and support cell growth without modification.[13] Hydrogels are the sought after material due to their water retention ability and biopolymer-based hydrogels are often coupled with artificial materials to form stable and reproducible scaffolds.[177]

Collagen is the most predominant fibrillar protein present in the ECM of connective tissues that provide structural support. Thermally initiated collagen fibril assembly during hydrogel formation provides tensile strength and enables the formation of controlled architecture.[178] Some of its limitations include the production of collagen gels with stiffness >1kPa without chemical crosslinking and long-term culture that causes the gels to contract and shrink.[179] Fibrinogen is an endogenous protein that is enzymatically crosslinked using FXIII activated by thrombin to produce fibrin during wound healing.[180] They are often employed in cultures involving wound healing and angiogenesis.[181] The fibrils are highly extensible with longitudinally aligned fibers used as a scaffold for traumatic peripheral nerve injuries.[182] Most commonly, fibrin is used as a sealant to stop bleeding.[183] However, its protease-induced degradation limits long-term culture. Similarly, elastin is an important ECM fibrous protein that contributes toward structural integrity, and flexibility enduring repeated cycles of stretch and relaxation in tissues. They are largely present in skin, ligaments, cartilages, arteries, and lungs.[184]

In most tissues of the human body, fibronectin (FN) and laminin are primary protein components of ECM that support tissue regeneration in dermal, connective, and neuronal tissues.[185] FN can bind to a variety of molecules like growth factors and involve in cell signalling via integrin receptors.[30] They are essential during developmental stages and especially during wound healing.[168] While these proteins are produced by cells endogenously, large production of these proteins results in high variability with batches. Additionally, requiring cost-intensive purification and

temperature-specific storage to prevent denaturation. Often modifications like crosslinking, or mixing with stabilizers are required for direct usage of such proteinaceous hydrogels due to their thermal and osmatic sensitivity. Hence full-length FN or fragments of FN (9*-10/12-14) is applied in synthetic ECM as biochemical cues.[25]

Matrigel is one of the widely studied hydrogels composed of laminin, type IV collagen, proteoglycan, and growth factors.[186] Unlike collagen, they self-assemble into a hydrogel at physiological temperature. Although Matrigel is a golden standard for 3D in vitro culture, its tumorigenic origin, diverse composition, and variability in the mechanical and chemical properties pose a reproducibility issue.[187]

Some polysaccharides like alginate are derived from brown algae which consist of β-D-mannuronic acid M units and α-L-guluronic acid G units assembled as block copolymers.[188] They form ionic crosslinking using divalent cations (Ca2+ or mg2+) to form ionic bridges between G units. Alginate cannot support cells without modification, hence integrin-binding ligands such as RGD are often employed to make alginate hydrogel cytocompatible.

Another popular non-sulfated glycosaminoglycan is hyaluronic acid (HA) which is composed of disaccharide units of glucuronate and *N*-acetylglucosamine. [189] HA is predominantly found in skin and cartilage and is produced in microbial fermentation in E.coli. HA is tunable for its physical and biochemical properties by modifying HA with functional groups to enable crosslinking and bioconjugation.[190]

2.3 Engineered integrin-binding domains

Though proteins offer ideal matrix environments, parts of these proteins responsible for adhesion, growth factor binding, and integrin-binding sites are reverse engineered to obtain local ligands that carry out similar functions. For example, RGD a tri-amino acid peptide derived from fibronectin and laminin is the smallest integrin

recognizable ligand which is vastly explored in TE to render a material bio-adhesive. Similarly, short laminin peptides such as IKVAV and YIGSR derived from α-and β-chain respectively, demonstrate a strong influence on cellular adhesion and tubule formation in endothelial.[191,192] The covalently immobilized RGD, IKVAV, and YIGSR in PEG hydrogels have different effects on tubule formation while a combination of RGD and YIGSR together shows improved tubule length and diameter invitro.[37] While proteins are naturally bulky and need to be extracted from endogenous sources, engineered protein fragments are short domains of native protein that contain the desired amino acids responsible for key functions of the native protein itself. Active domains responsible for cell adhesion, linkers to couple to hydrogels, and growth factor binding are engineered to obtain less bulky fragment domains replicating native protein conformation. For example, fibronectin fragment FNIII 9*-10/12-14 (51 kDa) bearing cell-adhesive RGD and PHSRN domains in FNII9-10, is combined with growth factor binding domains FNIII 12-14[30]. Enhanced conformational stability is achieved on mutation (represented by *) from leucine 1408 to proline in FN 9-10 enhancing regeneration in the skin and bone tissue due to synergistic signaling between adjacently placed integrin and growth factor domains.[31,193]

2.4 Two-Dimensional artificial microenvironments

2.4.1 Microfabrication strategies

Controlled architecture in microenvironments is fabricated using microfabrication techniques that deposit or remove materials from substrates to create spatially defined patterns. Techniques such as etching[194], electro or solvent-assisted spinning[195], soft lithography[196], contact printing[197] and photolithography[198] are employed to make scaffolds. Several limitations are posed for dry etching, which often expels toxic gases and the desired dimensions depend on the laser intensity, angle of laser incidence, and etching rates.[73] Though electro and solvent-assisted spinning have good control over fibers diameter and surface topography, it has limited control over the

mechanical properties.[195,199] Soft lithography allows the fabrication of microscale topographies using a mask or template.[200] Contact printing allows biochemical surface modification essential for cell growth on substrates. Photolithography is popularly used to create patterns using light allowing spatial control over surfaces. Acrylamide-based hydrogels were photo-patterned to create functionalized surfaces that covalently bind proteins exclusively promoted nerve cell growth and the neurons showed active synapse.[197] Some of its limitations include fabricating curved structures, which is now possible using direct writing techniques involving two-photon lithography[128] or volumetric printing[201]. However, the fabrication requires multiple steps and a cleanroom facility is essential for such expensive equipment. Combination of master (negative) created from photolithographic techniques and scaffold itself from replica molding by soft-lithography is a simple and widely used procedure. Reproducible stamps are created from single master with high topographical feature resolution.[73,202]

2.4.2 Role of substrate topographies as biophysical cues

A brief synopsis of the state of the art is presented reporting topographies influencing cellular morphology or alignment developed using one of the above-mentioned fabrication tools. Patterned glass surfaces with aligned Schwann cells were used as a mold to prepare a PDMS substrate with inverse topography (soft lithography). These PDMS films which now consist of Schwann cell morphologies were then rolled into conduits. An increase in neurite guidance of postnatal rat pup dorsal root ganglia (DRGs) was observed when the conduit was made with topographies oriented parallel to the axis of the conduit compared to perpendicular.[203] This knowledge was then transferred to substrates with elliptical micropillars as somas, continuous lines as axons, and a combination of both revealing that the lines have a stronger influence on the axonal alignment, compared to elliptical pillars or a combination of lines and pillars.[204] This report opened a wide range of avenues to study in-vitro platforms using topographies that provide continuous guidance cues for neurites. The dimensions of

the topographies, their inter-element distances, and aspect ratio play a critical role in altering cellular mechanisms to cause morphological, directional, or physiological modifications. A study on continuous microchannels (height: 0.6 μm; width groove = ridge = 25 μm) induced exclusive guidance for the growth of spiral ganglion neurons parallel to the microchannels in contrast to fibroblasts.[205] Similar study on photopolymerized microgroove patterns revealed that the alignment of DRG neurons increased with an increase in channel depth (1 to 8 μm) while the alignment decreased with an increase in distance between the channels (10 to 50 μm). [206] For PDMS grooves and ridges with equal widths, Schwann cell alignment was higher for lateral groove dimensions of 20 μm with a depth of 2.5 μm compared to flat or lower lateral groove dimensions (4 or 1 μm with a depth of 850 or 350 nm, respectively). [207] Two distinct guidance phenomenon is reported here where topography with channel sizes smaller than the cell bodies prevents the cell to reach the bottom of the substrate, therefore, the neurite growth is only along on top of the channels while the second phenomenon describes boundary guidance, where the cells have enough space to go between the topography reaching the bottom. Tonazzini reports that the boundary guidance is stronger than the contact guidance denoting that sensing walls have a higher impact than the depth cavities.[207] A study with nanoimprinted grooves made of poly (ethylene-co-vinyl acetate) (EVA) report the regenerative capability in DRG neurons from rats after an on-site injury. The topography induces linear growth along the grooves with the highest alignment with pitch length (distance between adjacent grooves) of ~900 nm and depth of ~165 nm.[208] A similar study using PMMA confirms the influence of equally spaces nano ridges and grooves (200 nm each) with a depth of 300 nm in aligning DRG neurons. The larger groove width is reported to decrease axonal guidance.[209] The neurites are observed to grow on ridges than grooves, which may be due to the smaller groove width and deeper groove depth, unlike the previous study. Polycaprolactam fibers fabricated by solvent-assisted spinning were fabricated with controlled inter-fiber distances that induce linear nerve growth in chick DRG neurons. The fiber topography with grooved features in combination with an inter-

fiber distance (IFD) of 30 μm showed the maximum aligned neurons in comparison to IFD such as 10, 50, and 100 μm.[199] Photopolymerized micropatterns (10 μm wide alternating ridge and valley with 1.5 μm high) were able to direct spiral ganglion neurons overcoming conflicting directional chemo-repulsive cues.[210] This reveals the dominance of physical cues over repulsive chemical cues when directing neurite growth or orientation. A large-scale screening involving isometric, radial, linear, and anisometric PDMS-based microelements fabricated from Si molds was used to study the topographical effect on hippocampal nerve length. The continuous and anisotropic discreet topographies promoted axonal growth compared to the isotropic discreet and flat topographies.[211]

2.4.3 Discontinuous physical guidance

While continuous geometries showed aligned nerves at lower periodicities and heights, the discontinuous array with isometric geometries, mostly made of silica or PDMS, showed neurite growth on or in between the microelements, without a primary growth direction.[77] The shape of the micropillars has been shown to influence the growth direction, for example, hexagonal micropillars fabricated using soft lithography showed 6 predominant growth directions in hippocampal nerve cells.[212] Similarly, the distances between the isometric micropillars also affect the growth direction. Park et al reported that cylindrical micropillar (5 μm height) array with different inter-pillar distances (Along the x- and y- direction) between them direct nerve cells with one primary growth direction.[213] Here the interelement distance of 3 μm along the proximal axis and 12 μm along the distal axis enables nerve growth along the proximal axis in comparison to equally spaced micropillars (3 μm) along the proximal and distal axis.[213] Another study with anisometric micro-cones fabricated using laser etching allowed the formation of elliptical cones that are pseudo discreet. These substrates linearly promoted nerve growth with one primary direction.[75]

In **Chapter 3**, I report the use of high throughput microarray platform designed and fabricated using two-photon lithographic techniques which allow spatial control at

high resolution. Previous reports explore guidance by a continuous feature that influences axon orientation and alters their length, number of dendrites, the orientation of growth cone, and movement of cells in confined spaces. Here I explore the role played by interelement spaces influencing nerve alignment which employs fewer materials to achieve similar alignment cues.

2.5 Synthetically derived 3D scaffolds

Though 2D platforms offer high reproducibility and control of cell fate, they fail to recapitulate the 3D microenvironment. Synthetic hydrogels as aECM scaffolds pose a favorable alternative to naturally derived ECM scaffolds due to their reproducibility and modular control. Synthetic ECMs are predominantly three-dimensional networks of polymer chains crosslinked by either covalent bonds or physical interactions.[214] The ability of hydrogels to form a highly porous network at low polymer concentration and retain aqueous biological fluids provides an ambient environment to the encapsulated cells. Hydrogels are engineered to offer a tuneable microstructure by firstly controlling the physical characteristics by altering stiffness, degradation rates, elasticity, viscoelasticity[122], and secondly the chemical composition by incorporation of bioadhesive ligands and growth factors.[215,216] Further, these are tuned to create controlled spatial heterogeneities inside the hydrogel for temporal control. The hydrogel precursors are synthesized with a high degree of control preventing batch-to-batch variability and overcoming the limitations of natural biopolymers. Thus an ideal aECM material is desired to possess the precision control offered by manufactured synthetic materials in combination with the benefits of bioactive properties of an ECM-based material.[217]

Peptide-based hydrogels. Peptides are a class of molecules synthesized to form chains of amino acid monomers linked by peptide (amide) bonds (N=CO). The shortest peptides are dipeptides which consist of 2 amino acids joined by a single peptide bond, followed by tripeptides, tetrapeptides, etc. Hydrogels derived from polypeptide sources are completely synthetic and enable assembly into hierarchical structures to

mimic native proteins.[218] Peptide amphiphile nanostructures are designed to mimic the activity of vascular endothelial growth factor (VEGF) that enable proangiogenic behavior in endothelial cells.[219] Self-assembling peptides that form nanofibers of ~10 nm diameter forming a 3D hydrogel are known to enhance cell survival rate after grafting into the injured spinal cord. Combining the designer peptide with IKVAV and RGD motifs showed predominant nerve growth but only along the wall of the injury cavity.[220]

Elastin-based hydrogels: Elastin-like polypeptides, composed of pentapeptide sequence with VPGXG, where X can be substituted to any desired amino acid except proline.[221] Thermally responsive ELPs are soluble below the transition temperature and undergo a phase transition and aggregate above the transition temperature. These chains are produced using recombinant technology in E. coli in a controlled dispersity with mechanical properties of native elastin.[222] ELPs are easily modified with bioadhesive cues such as RGD[223] or functional groups such as azide and cyclooctyne to enable catalyst-free click crosslinking, resulting in a wide range of mechanical properties.[224] These gels at physiological temperature are not transparent and require combining with a polymer such as PEG to form hybrid hydrogels with good optical transparency.[225]

Polyethylene Glycol: Polyethylene glycol (also called poly (ethylene oxide)) is an inert synthetic, hydrophilicity, non-biodegradable, non-immunogenic polymer widely used as hydrogel in tissue engineering.[226] They are often used as a 'blank slate' to tether biochemical cues, as they are usually resistant to protein adsorption. Manipulation of chain length and functional modification of linear or multi-arm (star) PEG at its hydroxyl end groups offers a platform to perform different chemistries.[227] The star-shaped core in a multi-armed PEG network enables both crosslinking as well as biofunctionalization in the same PEG molecule.[228] Moreover, sPEG polymers crosslinked below overlap concentration (c*) show uncontrolled heterogeneous pores compared to hydrogels formed above c* due to free dangling and un-crosslinked arms

in the sPEG molecule.[229] Incorporating terminal or side-chain functional groups in PEG polymers allows fabrication of hydrogel with versatile microstructures, as well as bio-functionalization. This is achieved by covalently linking different biomolecules such as adhesion peptides like RGD[32] or growth factors such as vascular endothelial growth factor VEGF[27] at low PEG concentrations.[216]

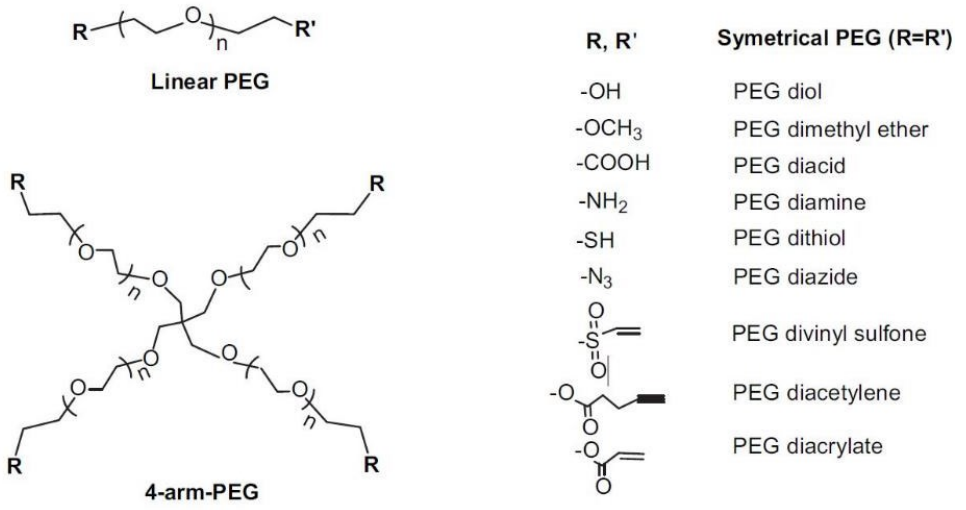

Figure 1. Structures of linear PEG and 4-arm PEG with various functional end groups. Adapted from reference [164] with kind permission from Elsevier.

Due to their transparent optical properties, these hydrogels are suitable for photochemical triggering to spatially and temporally create heterogeneities. This is achieved by either incorporating or removing ligands that impart biochemical or biomechanical properties to the hydrogel. PEG itself is not degradable, however, incorporating hydrolyzable motifs in its crosslinks or incorporating protease cleavable crosslinks renders the synthetic matrix degradable.[26] PEG hydrogel is elastic in nature and thus does not impart the native viscoelastic ECM properties. However, its advantages lie in its versatility to functionalize different terminal groups with simple chemistry as well as form multi-arm PEG conjugates (**Figure 1**).

Several crosslinking strategies have been explored with PEG hydrogels for in vitro cell applications due to their stability and hydrophilicity. The crosslinking strategies can be classified into chemical methods and physical methods.[230] While physical

crosslinks include hydrogen bonding, electrostatic bonding, and ultrasonication[231], chemical crosslinks are covalent in nature that are permanent (**Figure 2**). Most common crosslinking methods reported include 'click reaction' such as Michaels Additions[232], oxime formation[233], enzyme-induced crosslinking[154,234], or Diels-Alder reactions[235,236]. Most of these reactions are cell-friendly and enable crosslinking at physiological pH and temperature in an aqueous (isotonic) medium.[237] Some applications require rapid crosslinking via photopolymerization that is often initiated with UV light involving radicals, which on long exposure to cells are harmful.[238,239]

While Michael addition is the most sought-after mechanism for crosslinking and biofunctionalization due to its mild and specific conditions that are suitable for in vitro cell encapsulation, their addition requires a reaction between a nucleophile to an electron-withdrawing group (EWG) bearing the double bonds. Maleimides, Vinyl sulphones, and acrylates are employed as the EWGs while thiol (-SH) and amines (-NH2) are employed as nucleophiles.[240,241] Early reports with multi-arm functionalized PEG or star PEG (sPEG) polymers involved acrylates and thiols to form soft hydrogels for protein delivery.[242] Eventually, this model was translated and applied for cell encapsulation with controlled biomolecular and degradation cues.[243] Replacing the core PEG, alternates such as hyaluronic acid and heparin-based compounds were used with PEG-diacrylate to fabricate hydrogels crosslinked with thiol-modified heparin for the local delivery of growth factors.[244] Speidel *et al.* reported the use of 4 arm PEG acrylates crosslinked with heparin-binding peptides sequence with thiol via Michael addition as a scaffold for cardiac progenitor cells that can be injected for in vivo cell engraftment.[245] Similarly, rapid crosslinking 4 arm PEG-maleimide coupled with protease cleavable peptide crosslinker, biofunctionalized with VEGF growth factors and cell adhesive ligands like RGD peptides demonstrated an engineered matrix for pancreatic islet cells by controlling the growth factor release profile kinetics and degradation profile.[246] While the gelation kinetics for Michael type addition are mildly controlled by altering the pH and the temperature, predominant control is achieved by employing a strong EWG.

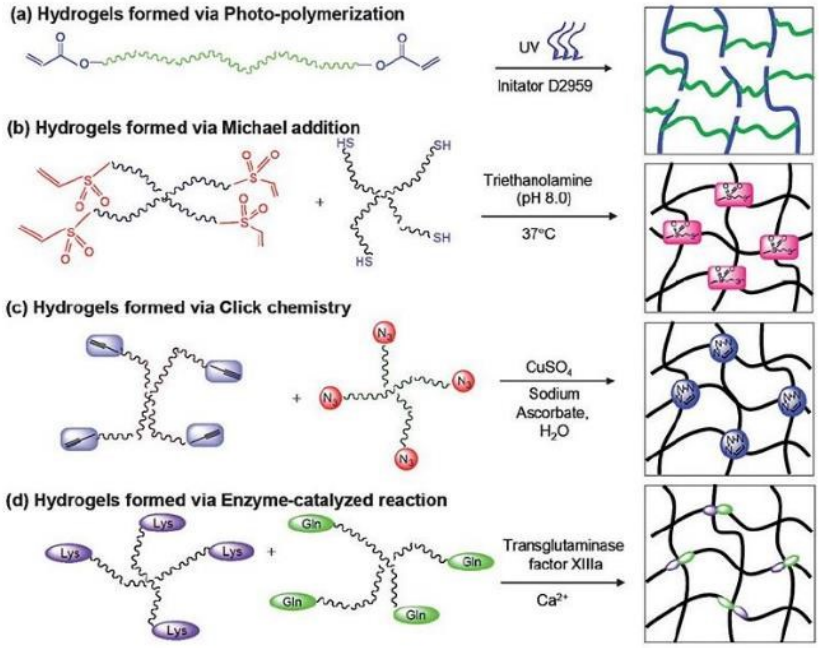

Figure 2. Crosslinking reactions to form PEG-based hydrogels (a) via photo-polymerization (b) by Michaels Addition (c) via click chemistry (d) enzyme-mediated crosslinking. Adapted from reference[226] with kind permission from the Royal Society Of Chemistry

Maleimides have the highest tendency for electro withdrawal followed by PEG-vinyl sulfone (PEG-VS), and PEG-acrylate.[247] While the role of cell adhesive domains played a prominent role in determining cell fate, researchers began to investigate several adhesive domain peptides like RGD, YIGSR, IKVAV and its combinations inside 3D hydrogels with cells. As peptide modification is simple and results in high yield at high purity, it is easy to couple simple thiols like cysteines to the to these biomolecules.[248] To incorporate highly specific crosslinking and bioconjugation, enzymatic crosslinking was developed mimicking fibrin clots using FXIII as an enzyme.[156] This was developed as two unique PEG conjugates each bearing complementary functional groups that form an iso-peptide bond in the presence of activated FXIIIa.[249] The two PEG conjugates each bear glutamine (Q) and lysine (K) peptide residue [155] and the mechanism involves the reaction between the γ-carboxamide group on the glutamine and the ε-amino group on the lysine residue to form isopeptide side-chain. [250] sPEG conjugates developed with complementary residues as described earlier with FXIIIa allowed the formation of soft scaffolds for 3D

in vitro nerve growth when supporting adhesion cues like fibronectin fragments were incorporated. Superior nerve growth was reported in this synthetic scaffold when the linear RGD peptides was replaced with fibronectin fragment.[25] Similarly, cyclic RGD peptides, especially bicyclic RGD peptides selective to integrin binding domains when incorporated enzymatically in PEG Q/K gels showed superior nerve growth compared to linear RGD and comparable nerve growth to fibronectin fragment.[40] (**Chapter 4**)

Similar to transglutaminase reactions, PEG-Peptide conjugates were developed to induce tuneable crosslinking in the presence of Sortase A and tuned to degrade with the same enzymatic reaction prompting the growth of human mesenchymal stem cells (hMSCs) in 3D.[251] Several advantages support bacterial ligase Sortase A (SA) over FXIIIa. Firstly, they can be produced in large amounts in the laboratory unlike FXIIIa which is produced from purified donor blood, and secondly, they are stable in solution compared to FXIIIa.[252]

Polyisocyanide (PIC) hydrogels: Unlike purely elastic PEG hydrogels, ethylene glycol substituted PIC polymers are viscoelastic in nature and mimic strain stiffening behavior. These biomaterials impart nonlinear stress responses observed in tissues like skin, cartilage, and muscles. PIC polymer forms beta helical structures with substituents like ethylene glycol in every carbon in its backbone. The stability of the PIC is enhanced when the substituent is further conjugated with D-L-di-alanine which stabilizes the helical structure with hydrogen bonds. A key advantage of this material is its ability to form gels at low concentrations (0.5 – 2 mg/mL) resulting in soft hydrogels with storage modulus between 40 and 1000 Pa (**Chapter 5**). A wide range of mechanical characteristics can be tuned by altering the length of the polymer. Additionally, the PIC can be rendered bio-adhesive by coupling RGD peptides to the terminal functional groups. While the length of the ethylene glycol determines the solubility of the PEG polymer, they also shift the lower critical solution temperature (LCST) forming PIC polymer fibers above the LCST. However, the PIC hydrogels are

not thermally stable and reversible in nature, as a decrease in temperature below LCST makes the fibers soluble once again.

2.6 Techniques for Patterning in soft hydrogels

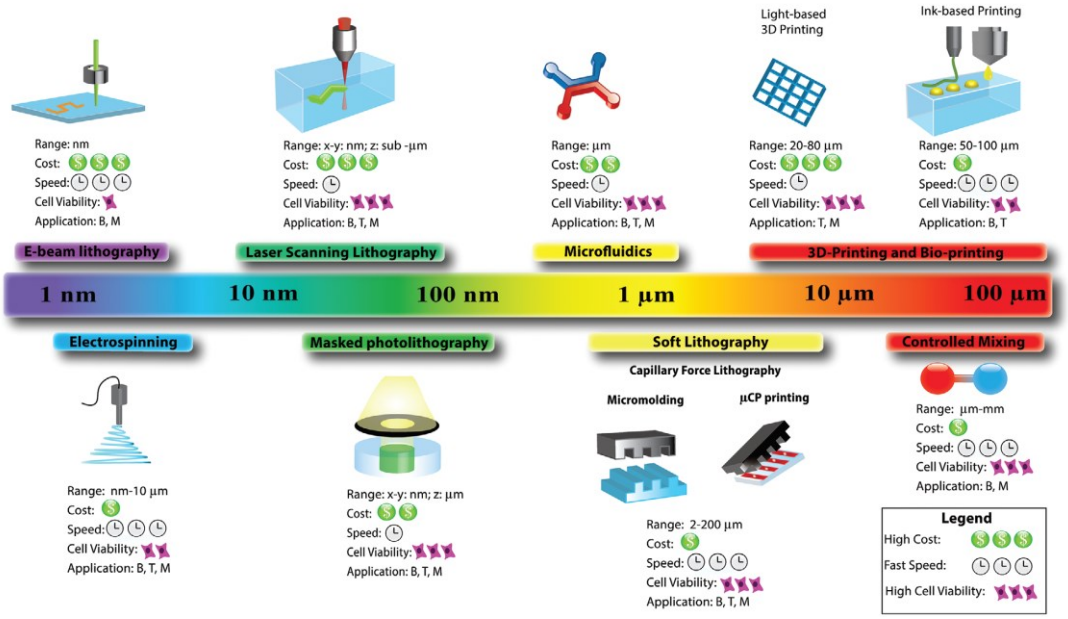

Figure 3. Micropatterning techniques are used to create biochemical, mechanical, and architectural patterns on and in hydrogels over a wide range of dimensions, depicting unique resolution, cost, speed, and cytocompatibility. Adapted from reference[253] with kind permission from John Wiley and Sons.

Several microfabrication techniques are employed to mimic the biophysical, biochemical, and architectural characteristics of the native ECM. These are obtained by incorporating biologically relevant cues in 3D space. Properties such as porosity, local stiffness, and biochemical gradient can be altered inside the hydrogel by achieving spatial and temporal control. Some of the techniques to pattern in 3D include Soft lithography, Gel in gel assembly, inkjet printing, Microfluidic patterning, and photopatterning which are discussed in the next section. [253]

2.6.1 Soft lithography

Soft lithography utilizes the techniques of transferring patterns from pre-designed molds/masks to the desired scaffold. Encompassing a wide range of dimensions, the

resolution of this technique lies with the size of the patterns in the mold, that is fabricated by etching silicon wafer.[254] The wettability of the liquid elastomer also contributes to the resolution. Its main advantage is rapid prototyping at low working costs. Flexible PDMS is employed as the elastomer to obtain replica molds, allowing easy transfer of gradients or biophysical cues to the hydrogel scaffolds. Among the several techniques to transfer cues from PDMS mold to hydrogels, micro-molding, and microcontact printing (μCP) are the most popular. Micro-molding involves a simple transfer of information such as grooves, ridges, or pits into the hydrogel scaffold[255], however, μCP involves the transfer of biochemical cues in the form of ink deposition on or in the gel.[256] Gobaa et al developed a high throughput platform with soft hydrogel as microwells. These microwell arrays were developed using μCP techniques where each well has a custom biomolecule of interest (BOI). Such platforms enabled monitoring cell-cell interactions on adipogenic and osteogenic differentiation of adherent MSCs based on their local micro well stiffnesses.[257] In this study, a combination of micro molding and μCP were both applied where the biomolecule spotted silicon stamps were used to create wells as well as transfer biomolecules.

2.6.2 Inkjet and Extrusion Printing

Inkjet printing involves either dispensing biomolecules onto a hydrogel substrate that can adsorb or chemically crosslink the BOI of interest whereas extrusion printing (bioprinting) involves dispensing biomaterials that are ready to crosslink after ejecting from the nozzle.[258] In the former, the printing substrate is often a hydrogel and the biomolecule printing volumes are limited from pico to microlitres to achieve spatial resolution.[259] Depending on the spot size requirement, more than one drop can be dispensed on the substrate per spot or multiple per spot. Inkjet printing is contactless and can generate high throughput micro spots with desired biomolecular combination suitable for cells.[260] Whereas for the latter involving extrusion-based bioprinting, the viscosity of the biomaterial or bioink is often the bottleneck resulting in clogging.

Additionally, the pressure imparted on the liquid ink to eject imparts stresses to the cells resulting in loss of function. However, the bioprinting technique enables the fabrication of complex shapes incorporating spatial heterogeneities relevant to cell growth and proliferation. Decellularized ECM is used as bioinks to closely mimic the native tissues, in combination with FDA-approved PCL fibers to reinforce the structure and the stability of the printed scaffold.[261] Skeletal muscle cells were encapsulated in Biopolymer-derived hydrogel bioinks commercially available. Mature myotubes were formed in nano fibrillated cellulose(NFC)/alginate-fibrinogen crosslinked with calcium chloride and thrombin.[262]

2.6.3 Gel in gel

The gel in gel hydrogels is fabricated by combining multiple layers of hydrogels into a single scaffold. They bear different compositions in each layer and assemble them to mimic native tissue architecture.[263] Spatially distinct trilayer scaffolds were developed to mimic articular cartilage by using a variety of material compositions of PEG-DA. Three distinct zones were fabricated with PEG-DA in combination with both methacrylated chondroitin sulfate, and Hyaluronic acid to mimic the superficial, transitional and middle zone.[264] However, the combination of gels to form sandwich systems is now simplified by altering the building blocks from bulk gels to spherical microgels which are easily assembled layer by layer.[47,265] Anisometric microgels are favored for their large surface area available for either crosslinking or biofunctionalization. Rommel et al reported that two PEG-based microgels with specific functional groups crosslink with one another resulting in the formation of a stable scaffold supporting fibroblast and endothelial cell invasion.[266] sPEG-heparin microgels were fabricated via microfluidics and encapsulated inside a soft bulk gel. Prostate cancer cells were incorporated inside the stiff microgels while the surrounding soft gel was nourished with heparin-bound growth factors and adhesion ligands. HUVECs were incorporated inside the surrounding soft gel to promote the

formation of a capillary network. The multiphasic microtissue model overcame the limitation of monophasic hydrogel materials in mimicking native heterogeneities.[267]

2.6.4 Photo-Patterning/lithography

Hierarchically engineered ECM matrices enable us to understand the role of the local 3D microenvironment and its influence on tissue formation.[268] Photopatterning with a mask on 2D substrates has now been replaced with confined light exposure in bulk materials to understand cell-material interaction in 3D space.[269,270] The laser patterning approach is applied either using a focused laser beam or a multi-photon laser to achieve spatial control.[271] The patterning resolution is often limited by the wavelength of the light exposed and scattering inside the hydrogel, however, sub-micrometer level control is achieved inside a transparent hydrogel.[128] The key advantage of this technique includes contactless in situ modulation of the local aECM microenvironment, which is often non-destructive and cytocompatible. Macromolecular hydrogel platforms are designed and developed with properties that can be modulated by light at specific time points.[272]. The degree of spatial patterning relies on the crosslinking chemistries which are orthogonal and offer the possibility to incorporate biologically relevant cues like growth factors.[273] Photoactive species are developed for all relevant wavelengths starting from 350 nm to 800 nm and distinguished into different classes.[274] While nitrobenzyls and coumarins are active species at lower wavelength spectrum, PhoCl and ruthenium complexes are active at middle order visible wavelengths. The higher-order wavelengths are is sensitive to Azobenzene–cyclodextrin based supramolecular complexes.[274]

2.7 Development of hierarchical scaffolds using light

The simplest form of spatial control achieved using light is either by photolytic addition[275] and/ or subtraction[276],[142] of scaffold materials. While in the former, uncrosslinked free functional groups are allowed to be crosslinked, in the latter, the crosslinked groups are photo degraded. This is achieved by incorporating

photosensitive motifs which undergo rapid changes in their structure. For example, modified agarose-based gels protected with -SH groups on irradiation with UV light exposes free SH groups available. Thus, allowing biomolecules like RGD peptides (modified with maleimide) which are easily diffusible to bind to the free -SH in confined volumes. Such scaffolds demonstrated selective neuronal growth in the patterned regions bringing one step closer to fabricating hierarchical aECMs.[151] Similarly, photodegradation is a technique commonly adapted to soften the gel network or create 3D localized channels for controlled cell invasion and migration. PEG hydrogels are fabricated using cytocompatible strain-promoted azide-alkyne cycloaddition (SPAAC) between sPEG- tetrabicyclononyne (sPEG-BCN) and a linear diazide bearing crosslinker. The popular mechanism for channel fabrication by degradation is to incorporate oNB groups which are present in the backbone of an MMP degradable crosslinker (**Figure 4a**). Two-photon irradiation cleaves the crosslinker bearing the o-NB group, resulting in the fabrication of channels controlled in 3D in the presence of encapsulated stromal cells. Endothelial cells are then seeded inside the hollow channels to fabricate vascular networks. (**Figure 4 b,c,d**). After photo decaging, the ends of the crosslinker bearing the RGD become available for cell adhesion and thus promote the endothelialization of in situ fabricated channels.[141]

Biochemical modification of substrates is equally relevant to biophysical modulation. One of the simplest methods to generate biopatterns in 3D hydrogels is by exploiting acrylate chemistry and free radical polymerization. Bioinert PEG-acrylate hydrogels are photopatterned by swelling them in solutions containing biomolecules with acrylates and treating them with light for biofunctionalization to generate local 3D patterns (**Figure 6a**).[130,277] the evolution of photopatterning has allowed us to now pattern more complex and dynamic full-length proteins to regulate cell fate.[278] For example, endothelialization of aECMs is essential to promote healthy viable 3D tissue models in vitro, hence spatial photoactivatable growth factors are essential that allows controlled angiogenic signal presentation. Nair et al developed a peptidomimetic of the vascular endothelial growth factor (VEGF) that can be activated using light.[279] This

photoresponsive analog is rendered inactive in the presence of the caged group 3-(4,5-dimethoxy-2-nitrophenyl)-2-butyl (DMNPB) on the scaffold. Light trigger offers an irreversible de caging to expose the angiogenic cues to encapsulated endothelial cells and promote angiogenesis.[279] Reversible bio-patterning strategies have been investigated using a combination of two orthogonal photo chemistries in sPEG hydrogels. The first reaction involves radical-induced thiol-ene click chemistry to bind biomolecules bearing a thiol motif using visible light (490nm – 650 nm), while the second reaction involves the removal of these ligands by decaging the o-NB ether mediated by UV (365 nm).[126] Biomolecular gradients were achieved by binding Fluro-labelled RGD peptides to the hydrogel using vibible light (**Figure 5 a,d**). In addition, complex gradients were fabricated by photodegradation of these bioadhesive ligands using the orthogonal UV light chemistry with the help of a slitted photomask(**Figure 5 b,c,e**).

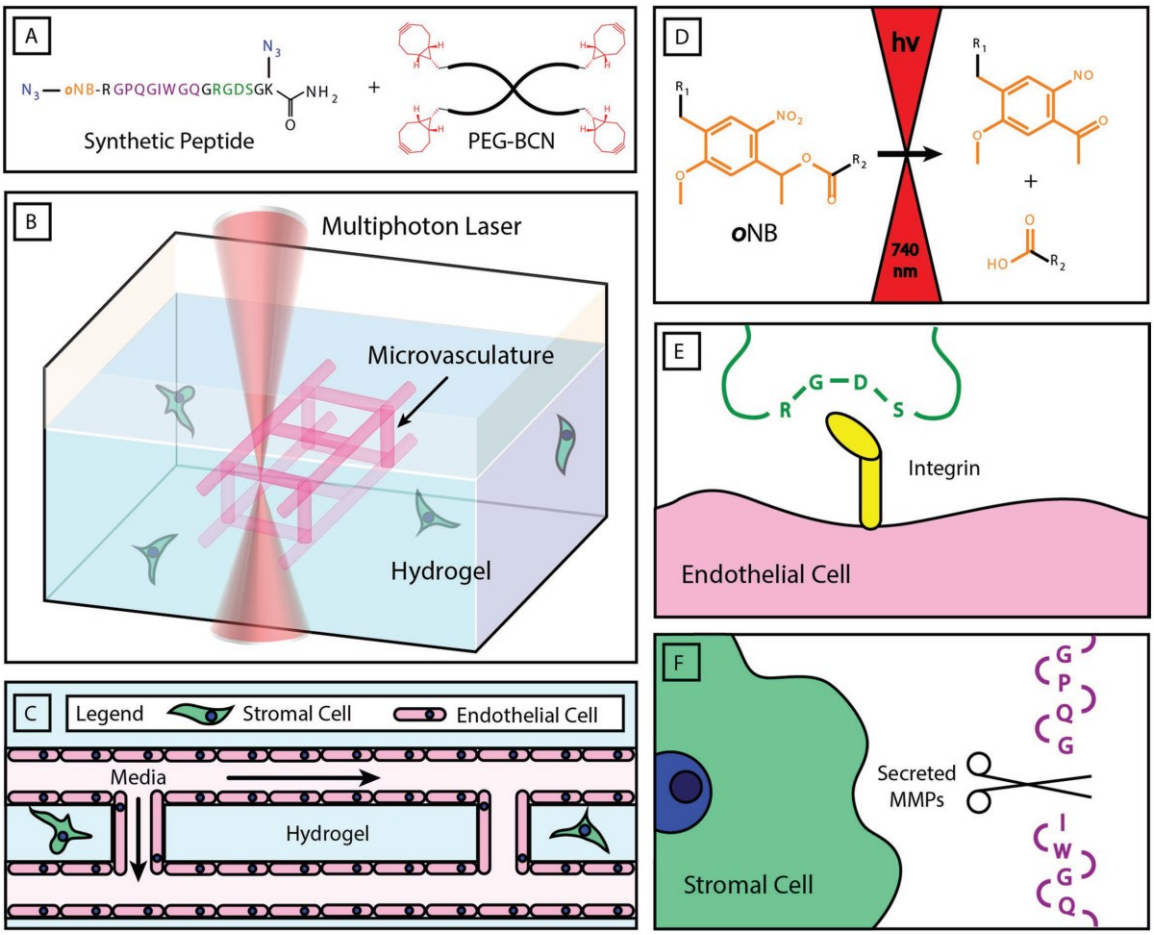

Figure 4. 3D in vitro two-photon patterning. A) Formulation of photosensitive hydrogel using BCN functionalized sPEG and photo-cleavable azide-based crosslinker. B) Spatial photopatterning using 2 photon lithography with 3D control including the Z-axis. C) the photo patterned regions are cleaved to form hollow micro-vasculatures after seeding with endothelial cells. D) The degradation products of oNB photocleavage yield nitroso- and acid-terminated by-products. E) RGD moieties incorporated in the crosslinker promote cell adhesion and F) MMP sensitive peptide sequence enables enzymatic cleavage to enable on-demand aECM. Adapted from reference[141] with kind permission from John Wiley and Sons.

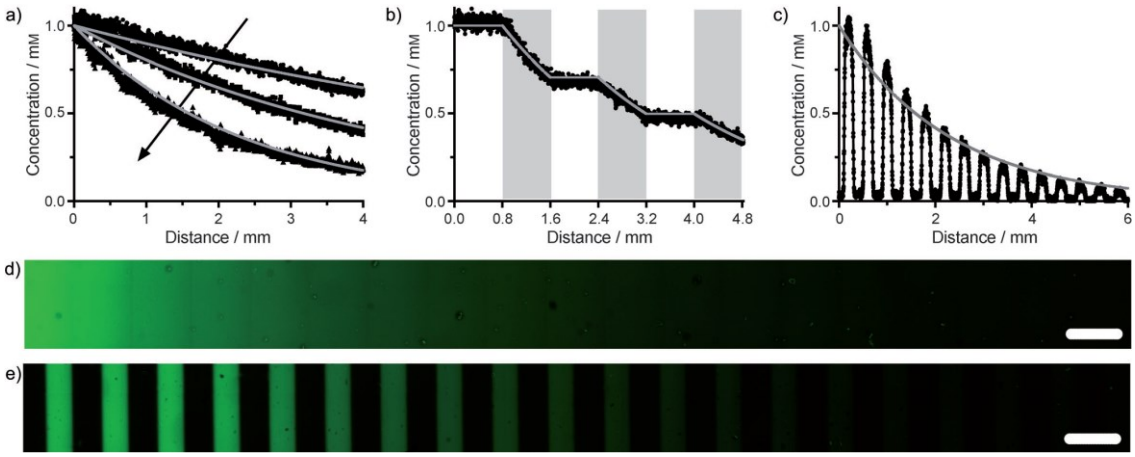

Figure 5. RGD peptide bearing a fluorophore was patterned inside sPEG hydrogels by using unmasked light (a, b, d) or with a mask that contains 200 μm slits spaced 200 μm apart (c, e). The pre-patterned samples were subsequently exposed to gradients of UV light that were generated by a moving opaque photomask. By shuttering the light (b) or releasing pre-patterned lines (c, e), unique gradients in the peptide concentration were generated across the network. Scale bars=400 μm. Adapted from reference[126] with kind permission from John Wiley and Sons.

While radical-based chemistries are often cyto-incompatible, alternative strategies are explored to achieve spatial biopattern with mild yet specific reactions.[273,280,281] Enzymes like Factor XIII and Sortase A are employed to tether specific motifs to the hydrogel backbone using photochemistry principles. These photo-sensitive hydrogel substrates on exposure to light undergo a photoinitiated decapping or deprotection of the caged group revealing the functional group of interest, thus being available for the further enzymatic reaction. The bioactive motifs are immobilized only in the light-activated regions while the surround remains inert (**Figure 6b**).[88,282] More recently photoactivatable adhesive peptides were developed with laminin peptides and peptidomimetics for spatiotemporal control of neuronal growth.[150] However, constant

protection from light is essential throughout the culture periods. The new class of reversible bio patterning, combing the benefits of both photomasks and laser scanning lithography was employed to control protein immobilization. The SPAAC reaction was employed for network formation, in combination with a photo-deprotection with oxime-ligation sequence for incorporating proteins and an oNB photocleavable group for protein removal. (**Figure 6d**) The photocleaved regions were now available to bind multiple proteins. These reversible chemistries offer a high-resolution heterogeneity fabrication with orthogonal chemistries to promote specific tissue formations and recreation of dynamic cellular microenvironments.

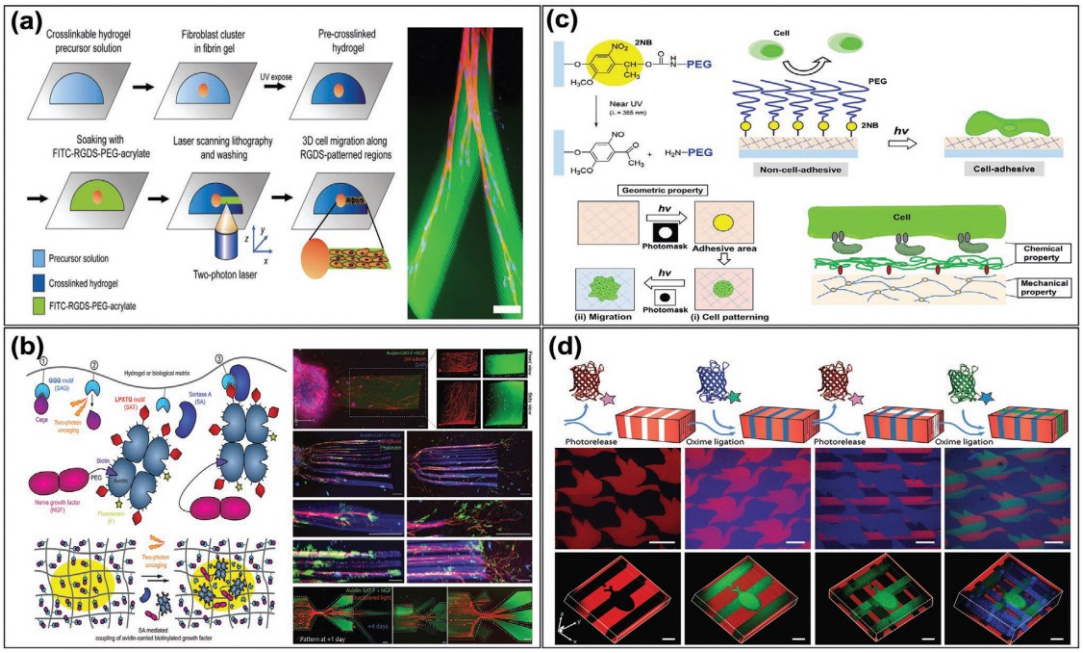

Figure 6. Photopatterning of biochemical cues a) 3D patterning of RGD peptides using a multiphoton laser to enable selective migration of fibroblasts in the bio patterned regions[277] (Scale bar:100 μm) b) Multiphoton patterning involving photo-uncaging to ligate growth factors via enzymatic pathways (Left). Invasion of axons into confined NGF photo-patterned regions. c) Photo decapping on exposure to UV releases caged groups exposing free polyacrylamide (PAAm) hydrogels available for cell adhesion. d) sequential photo release and oxime ligation of aldehyde-tagged proteins (top). Masked-based lithographic techniques at 365 nm to sequentially pattern defined shapes throughout the gels in addition to multiphoton lithography in PEG hydrogels. Scale bar = 100 μm. Adapted from reference[253] with kind permission from John Wiley and Sons.

Chapter 3. Anisometric Microstructures to Determine Minimal Critical Physical Cues Required for Neurite Alignment

Sitara Vedaraman, Amaury Perez Tirado, Tamas Haraszti, Jose Gerardo-Nava, Akihiro Nishiguchi and Laura De Laporte

In nerve regeneration, scaffolds play an important role in providing an artificial extracellular matrix with architectural, mechanical, and biochemical cues to bridge the site of injury. Directed nerve growth is a crucial aspect of nerve repair, often introduced by engineered scaffolds imparting linear tracks. The influence of physical cues, determined by well-defined architectures, has been mainly studied for implantable scaffolds and is usually limited to continuous guiding features. In this report, we investigate the potential of short anisometric microelements in inducing aligned neurite extension, their dimensions, and the role of vertical and horizontal distances between them. This provides crucial information to create efficient injectable 3D materials with discontinuous, *in-situ* magnetically oriented microstructures, like the Anisogel. By designing and fabricating periodic, anisometric, discreet guidance cues in a high-throughput 2D *in vitro* platform using two-photon lithography techniques, we were able to decipher the minimal guidance cues required for directed nerve growth along the major axis of the microelements. These features determine whether axons grow unidirectionally or cross paths via the open spaces between the elements, which is vital for the design of injectable ANISOGELS for enhanced nerve repair.

3.1 Introduction

Implantable and injectable artificial scaffolds, such as conduits[98,283–285], fibers [97,286], and

hydrogels[287] have been developed to promote directed nerve growth after injury. The internal structure of implantable scaffolds generally contains an aligned architecture in the form of long fibers, elongated pores, or channels that provide physical and mechanical guiding stimuli to enable oriented nerve growth.[288] The presence of directional cues inside the biomaterial scaffolds is crucial to facilitate re-connection of the nerves with their appropriate targets[99] to regain partial or complete function. More recently, research has focused on creating injectable materials with the ability to form anisotropic structures.[50] This is important to create low-invasive therapies for soft, oriented neuronal tissues, such as the spinal cord. For example, the Anisogel consists of magneto-responsive rod-shaped microgels or short fibers that orient *in situ* in the presence of a low magnetic field, while a surrounding hydrogel precursor solution crosslinks to immobilize the 3D anisotropic structure after removal of the magnetic field.[82] Compared to implants, the Anisogel system consist of small injectable alignable elements that lead to discontinuous, individually aligned guiding structures that span the entire length of the material. Therefore, understanding the effect of the structure dimensions and aspect ratios, and the vertical and horizontal distances between the elements is an important step towards successfully steering neurite growth in a linear manner. However, we believe that the currently reported material systems have not yet studied the effect of discrete anisometric topographic elements in a controlled manner.

So far, continuous topographies, such as long patterned lines (ridges and grooves)[66,69,207,208], nanowires[289], and fibers[199,290], or discontinuous topographies, such as nano-[291] and micropillars[194,292,293] have been produced to study directed growth of neural or neurogenic cells. Microfabrication technologies, such as etching[194], electro/dry spinning[195], soft-lithography[196], photo-lithography[198], and wrinkle formation[294] have been employed to fabricate these nano- and micro-interfaces with a wide range of materials and architectures to gain further information on cell-material interactions.[73,200] For example, topographies that mimic native ECM were developed by inverse molding of aligned Schwann cells on patterned glass surface.

The obtained polydimethylsiloxane (PDMS) films were rolled into conduits with Schwann-cell like topographies oriented parallel to the axis of the conduit, resulting in increased neurite guidance compared to topographies oriented perpendicular to the conduit's axis.[203] A study with continuous grooves and ridges with equal widths (periodicity 20 μm) on a PDMS film reported higher Schwann cell alignment with groove depths of 2.5 μm compared to flat or lower lateral groove dimensions (periodicity: 4 or 1 μm) and depths (850 or 350 nm).[207] In another study with continuous microgrooves and ridges (depth 1 μm) developed with photo-lithography of methacrylate polymers, reduced nerve alignment was observed when the lateral distance increased from 10 to 50 μm, while neurite orientation improved for deeper pattern depth up to 8 μm.[295] On a smaller scale, nano ridges with widths ranging between 100 and 800 nm demonstrated preferential nerve growth on the ridges, while the highest alignment was observed on equally spaced ridges and grooves of 200 nm each.[209] Compared to sharp edge patterns, gradually sloping grooves and ridges were produced, demonstrating that the optimal lateral groove spacing for oriented nerve growth was dependent on the groove depth. Maximum alignment of spiral ganglion neurons was achieved on both lateral spacings at 50 or 10 μm at a groove depth of 8 or 1 μm, respectively.[198] Wrinkles with even more natural features created via uniaxial mechanical stretching/plasma treatment of PDMS reported that the inter-wrinkle distances (width) dominate the effect on cell alignment in comparison to the amplitude (depth) of the wrinkles. [296] A wrinkle width of 26 μm and amplitude of 2.9 μm allowed for differentiation of human bone marrow-derived MSCs to neurons, thus exploring topography-mediated neuronal differentiation.[297]

In contrast to continuous patterns, the role of substrates with discontinuous guiding elements has not been widely explored. Isometric micropillars with dimensions of 1-2 μm and interpillar distances of 1-2 μm were fabricated with ion etching techniques and guided nerve cells in a straight path.[293] Here, the shape of the isometric pillars determines the direction of neurite growth, for example, hexagonal micropillars (width 1.6 μm and height 3 μm), with inter-pillar distances of 1.4 μm reported linear

neurite extension in six preferred growth directions following the edges of the hexagonal shape.[79] Therefore, the physical guidance afforded by the micropillar array failed to provide one primary growth direction, while continuous guiding cues induced unidirectional growth.[211] In the case of discreet topographies, the ability to retain the growth direction is influenced by the dimensions, aspect ratio, and inter-elemental spacing of the elements. For example, discontinuous elliptical microcones (spikes) with subcellular dimensions, fabricated by laser irradiation on Si wafer and oriented parallel to one another show improved neurite alignment.[75] Despite their ability to direct neurite growth, a lack of control in the spatial positioning and architecture of microcones using this technique limits its applicability as a screening technology for our purpose. In another study, discreet anisometric rectangular (length: 45 μm, width: 3 μm) nano-high ridges were fabricated via photolithography at fixed inter-element distances (vertical spacing: 6 μm, horizontal spacing: 30 μm), demonstrating that for low topographies between 10 and 50 nm, the alignment of the neurites with the nanoridges depends on the angle of incidence, while for higher nanoridges above 50 nm, growth cones reaching the elements in a perpendicular manner will still move parallel to the ridges.[298,299]

Despite much progress in the field, a good understanding of the effect of dimensions and aspect ratio of discrete elements, and the vertical and horizontal distances between them, on unidirectional nerve growth is still unknown but an important step to develop injectable materials that form anisotropic structures *in situ*, such as the Anisogel.[50] These materials are extremely important for creating low-invasive therapies to repair and regenerate soft, oriented tissues, such as the spinal cord. To study this without the inherent variability of the distances between anisometric microstructures inside the 3D constructs after injection, we present a simplified platform using two-photon lithography (TPL) technique to produce controlled anisotropy with discrete, anisometric elements in a 2D model. This technique offers a high-throughput system to study the effects of different physical parameters with defined dimensions and interelement distances on axonal growth and alignment, and

thus to obtain a deeper understanding of axon navigation in contact with biomaterials.[100] The substrate is coated with gelatin and primary sensory nerve cells harvested from chick dorsal root ganglia (DRGs) are cultured. The ability of neurons and other cells to continue growing in a pre-defined direction after they lose their guidance cue is ventured. Although *in vitro* surfaces have previously been employed to understand the influence of substrate geometry and topographies on axonal growth and neural tissue guidance,[57,209,292,300,301] the role of discreet anisometric cues with discreet multi-axial, interelement spacing, acting as geometrical constraints to induce axonal guidance, has not been studied before. Such a system can provide information on the minimal physical guidance cues that are required for directed nerve growth, replacing the conventional continuous implantable scaffolds with new injectable regenerative therapies. [52,82]

3.2 Results and Discussion

3.2.1. Substrate preparation

Custom-designed anisometric microelement arrays are 3D printed by TPL using the Nanoscribe system. These substrates are developed to understand cell-substrate interactions while allowing for long-term cell culture. An acrylate-based resin is printed onto acryl-silanized glass coverslips to produce polymeric anisometric microelements with various inter-elemental spacing **(Figure 1a)**. The computer-aided design enables rapid fabrication of multiple array micropatterns on a single glass substrate, which allows for testing one cell population on multiple differently spaced microelement patterns. The fabricated substrate is robust and transparent allowing bright field imaging for time-lapse microscopy, and the microelements show auto-fluorescent that can be detected at excitation: 480 - 550 nm **(Figure 1c-ii).** To improve cell-substrate interactions, the resulting high precision microstructures **(Figure 1c-i,ii,iii)** are coated with cell adhesive proteins and poly-L-lysine. Anisometric microelements with dimensions 20 x 1 x 10 μm (length x width x height, aspect ratio

of 20) are used in this study. In order to provide a pseudo-3D environment[292], the height of the microelements was set to 10 μm in an attempt to prevent neurites from crossing over them **(Figure 1a)**. Micropatterns are fabricated with horizontal spacings (HS) ranging from 5 to 200 μm (distance between elements at their longest side), and vertical spacings (VS) between 0 and 200 μm (distance between elements at their shortest sides). Substrates without vertical spacing are continuous and act as a positive control while flat substrates without any micropatterns are used as a negative control. The space between the microelements creates a paradigm for the cells and axons to decide their growth direction. By varying the inter-element distance, it is possible to systematically study and understand its role in neurite alignment and the ability of the elements to promote unidirectional growth.

3.2.2 Cell – Substrate Interactions

Since the cells and neurites normally do not attach to unmodified glass or the acrylate-based microelements, various cell-adhesive molecules were tested to be used as a coating to improve cell attachment. Poly-L-lysine has shown to support nerve growth through interactions of its positive electrostatic charge interaction with the negatively charged ions in the cell membrane and was compared to ECM proteins, such as fibronectin and laminin, and gelatin (derived from collagen) **(Figure 1b)**.[302,303] Fibronectin, followed by gelatin and laminin show high neurite growth per covered area but 10 mg/mL gelatin was selected for coating the substrates due to its lower costs. The resulting SEM images of highly ordered microelements (double-headed arrow) **(Figure 1c-i)** with cultured cells demonstrate cell-substrate interactions (arrowheads), where cells align in between and across multiple microelements **(Figure 1c-iv)** and stretch to connect the microelements **(Figure 1c-v)**. This suggests that the gelatin coating is present on both the glass and polymerized microelements. At higher magnification, the cell structures resemble both cell lamellipodia and filopodia (white single-headed arrowheads) probing and adhering to the walls of the microelements **(Figure 1c-vi, vii)**. Few cells are also observed on the top of the microelements and

stretch to reach the bottom of the substrate **(Figure 1c-viii)**. Their ability to sense the biochemical cues for anchorage allows the cells to gather information about the substrate and to find suitable paths to follow. The integrin-binding sites, present in the ECM molecules, provide a chemical stimulus to create contact attachment points, that alter the motility of the growth cone (GC) by activating specific integrin receptors in the cells, leading to subsequent secretion of ECM proteins resulting in modification of their environment.[68]

3.2.3 Influence of inter-elemental spacing on neurite orientation

The micropattern arrays with patterns presenting 36 different combinations of inter-elemental distances (HS and VS) were studied and networks of polarized nerve cells, extending their axons were observed on the bio-functionalized substrates with anisometric microelements **(Figure 2, 3)**. The anisotropy created by the microelements influences the growth direction of the neurites **(Figure 4a)**. Overall, we observe that the increase in inter-elemental distance (either VS or HS) above a certain threshold decreases neurite alignment along the microelements. Fluorescence micrographs show a combination of microelements (green) and β-tubulin stain (red) **(Figure 4a)**. An elliptical orientation kernel is used to determine the direction of the neurites and is represented by a color-coded image **(Figure 4b).** By filtering out the bodies of the nerve cells, interference with the alignment analysis is prevented. The shape of the orientation distribution of the microelements distinguish between neurites grown on a flat substrate without a micropattern array, and the neurites in the presence on a micropattern array (VS: 20 μm, HS: 50 μm) (**Figure 4c)**. The presence of the aligned microelements influences neurite outgrowth along the major axis of the microelements as indicated by the narrow distribution (green line) close to that of the highly aligned microelements (blue line). In contrast, orientation of neurite growth in the samples without any micropattern have a broad distribution with multiple peaks (red line). Introduction of the anisotropic microelement array facilitates neurite guidance and results in oriented extension along the microelements, resulting in a

narrow distribution with a peak around a preferred direction (indicated as 0°), depending on the inter-element spacing. These results are in accordance with the study performed on discreet microcones showing that neurite alignment is higher for anisometric microcones in comparison to isometric microcones.[75]

To study the degree of neurite orientation in between microarray patterns with different vertical and horizontal spacing, the discreet orientation distribution of neurites is normalized to the maximum count in the histograms. As previously reported, neurite orientation parallel to the channel wall in continuous microchannels was higher for channel widths of 20 - 30 μm, compared to wider channels (up to 60 μm) and to that of flat substrates.[304] In this report, this width is associated with the HS parameter. Therefore, to investigate the effect of discontinuous tracks, arrays of microelements (20 x 1 x 10 μm, L x W x H) presenting VS between 0 and 200 μm under a constant HS of 20 μm were used. As VS increases, the shape of the distribution changes from a sharp single peak distribution around 0° to a broadened and flattened distribution, an indication of loss of neurite alignment along the major axis of the microelements **(Figure 5a, 5b)**.

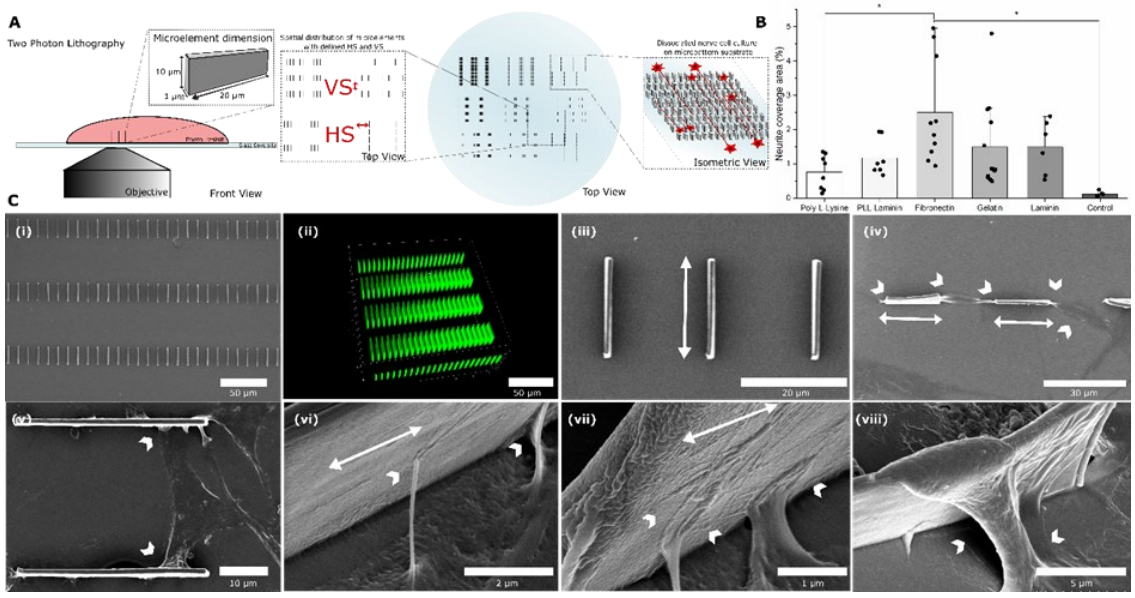

Figure 1. Development and fabrication of micropattern substrates. **(A)** Schematic of two-photon lithography to develop microelements from computer-aided design. The micropattern

is designed with custom inter-element spacing by varying the horizontal spacing (HS) and vertical spacing (VS) on a single substrate in high-throughput. **(B)** Comparison of neurite coverage among different cell-adhesive coatings showing higher neurite outgrowth on gelatin and fibronectin coatings. **(C)** SEM images of micropatterns show **(i-iii)** highly ordered two-photon polymerized microelements that autofluorescence in the green channel. **(iv)** Cells align along the microelements. The ability of cells to sense the microelements and stretch in between them is observed **(v)**. Cell-material interaction (arrowheads) is achieved by the exploration of the finger-like projection of filopodia **(vi)** and web-like structures of lamellipodia **(vii).** Some cells are observed interacting with the microelement from the top reaching the bottom of the substrate **(viii)**. Arrowhead: lamellipodia, filopodia and cell-material interaction, double-headed arrow: microelement. Data presented as mean ± SD, $n \geq 3$, P-values are calculated using one-way ANOVA with Bonferroni correction, $^{*}P<0.05$, $^{**}P<0.01$.

For a micropattern with a VS of 5 μm, the neurites are primarily guided along the major axis of the microelements. While a peak at 90° can be observed in the case of a VS of 200 μm, suggesting that at long interruptions of the linear tracks, the short axis of the elements (1 μm wide) also provides physical guidance **(Figure 6)**. More important, even at this high VS up to 200 μm, the ability of the cells to recognize the anisometry of the microelements is evident as the shape of the distribution is still retained around 0° despite the peak observed at 90°. This demonstrates that the nerve cells respond stronger to the long axis of the guiding elements, even if vertically spaced at a distance 10 fold higher than their length and HS. These observations illustrate the power aligned discrete microelements retain, compared to continuous guiding paths.

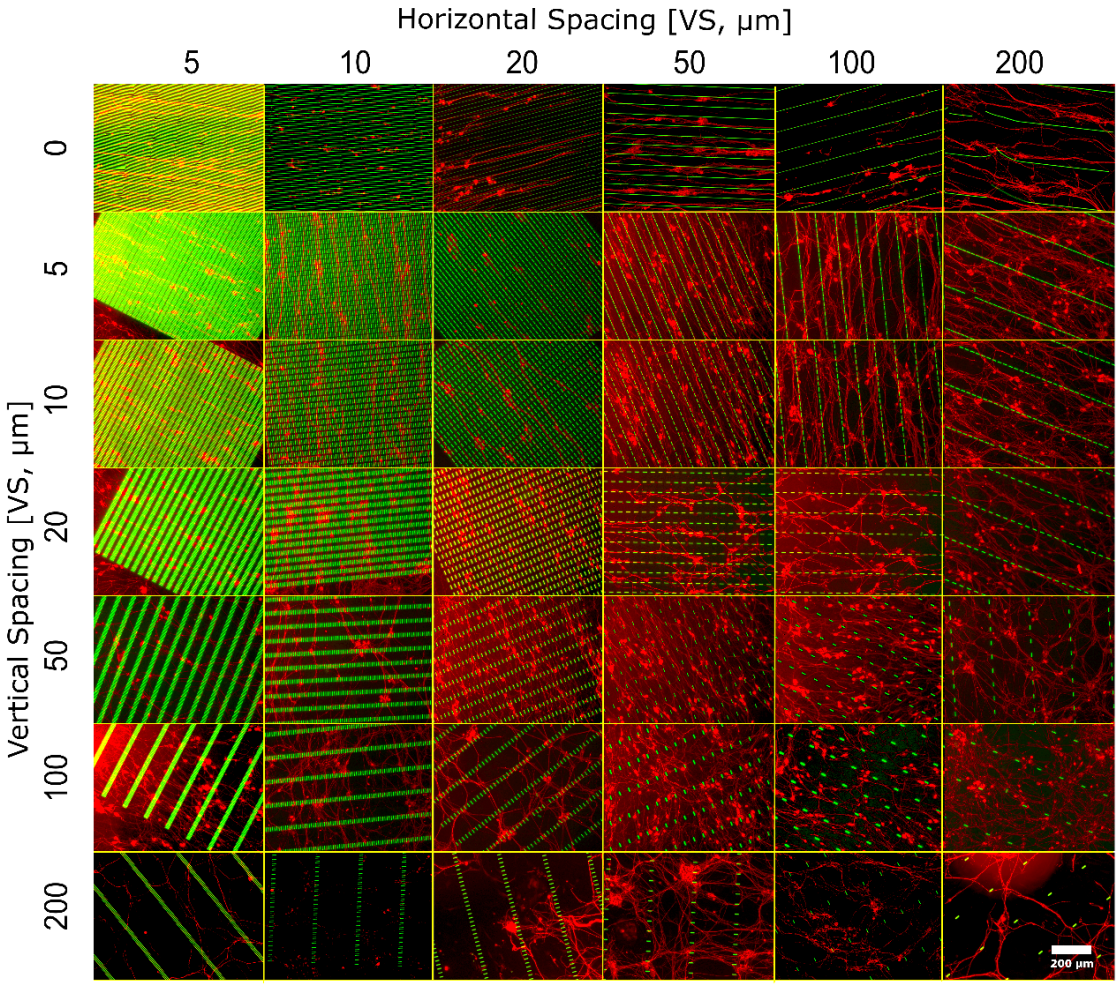

Figure 2. DRG cultured for 3 days and immunostained (TUJI) on micropatterns with different interelement spacing. An array of varying interelement spacing ranges from 0 - 200 µm in vertical spacing (VS) and 5 - 200 µm in horizontal spacing (HS). The microelements are observed in the green channel and the nerve cells are observed in the red channel.

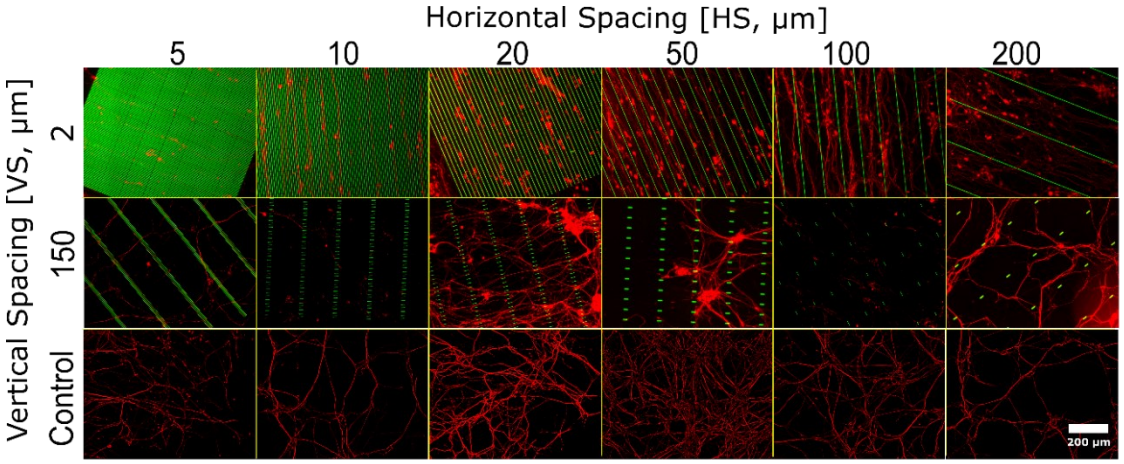

Figure 3. DRG cultured for 3 days and immunostained (TUJI) on micropatterns with different interelement spacing VS = 5 µm, 10 µm, 20 µm, 50 µm, 100 µm and 200 µm with HS = 2 µm,

150 µm and controls without microelements. The microelements are observed in the green channel and the nerve cells are observed in the red channel.

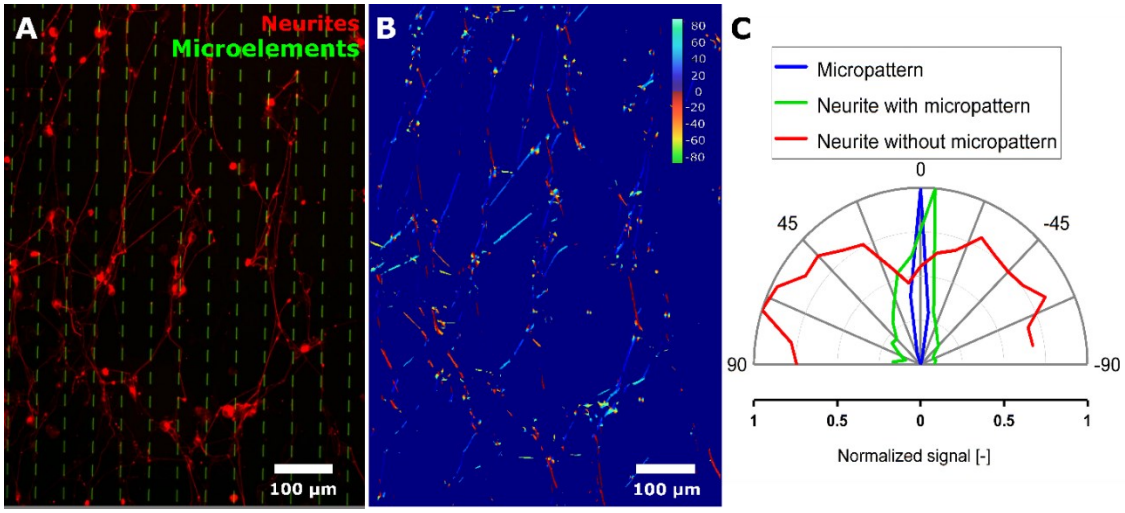

Figure 4. The images are processed to obtain the orientation distribution of the extending neurites on the micropatterned substrate. The multichannel image **(A)** is split into its corresponding channels revealing the primary orientation of the microelements. On applying the anisometric Gaussian orientation kernel, an alpha image **(B)** is generated to depict the direction of the neurites. The orientation distribution around the direction of the anisometric microelements (0˚) obtained is further plotted, here for VS: 20 µm and HS: 50 µm **(C)**, to compare with the distribution of the microelements and the distribution of neurites without microelements (control). The shape of the distribution indicates the influence of the microelements on neurite alignment.

In contrast, when the VS is fixed at 20 µm and HS is varied **(Figure 5b)**, the increase in HS influences the shape of the orientation distribution to a larger extent. At higher HS (200 µm), the orientation distribution gets shifted towards ±90° and the cells move along the guiding elements, as well as in between the guiding elements, resulting in the major fraction of neurites oriented in the direction perpendicular to the long axis of the microelements. Understanding the role of physical guidance along the major or minor axis of anisometric microelements is crucial in systems where the changing the VS or HS or both, alters neurite growth direction. When primary neurons are cultured on a flat gelatin-coated substrate without microelements, their axonal extension is random without any directionality and thus no principal peaks in the orientation distribution are observed **(Figure 5d)**.

The neurite orientation distribution is measured ranging from -90° to 90° with the major axis of the microelements orienting at 0° (**Figure 5c**). This distribution is analyzed by determining the interquartile range (IQR) **(Figure 5e, 5f)**. The IQR is calculated as the difference between the angle (°) at the 75th percentile of neurite orientation and the 25th percentile of neurite orientation depicting the 'middle 50%' of the neurite orientation distribution. This allows for the quantification of neurite orientation along a certain direction. Lower IQR values (< 90°) indicate over 50% of the neurite orientation along a certain direction, whereas higher IQR (> 90°) suggest random neurite outgrowth. While the IQR reveals oriented growth in a specific direction, it does not convey whether this direction is along the microelements. Hence, an additional parameter is needed to measure the neurite orientation along the major (parallel) and the minor axis of the microelements (perpendicular) **(Figure 5g)**. The combined information provided by the IQR and the percentage of neurites parallel or perpendicular to the microelements reveals the neurite growth direction. It is intuitive to assume that at a lower inter-element spacing, neurite alignment increases, in contrast to higher inter-element spacing with less physical guidance cues. This is confirmed by the higher IQR values that are obtained when the VS increases for a fixed HS **(Figure 5e, 5f)**. On the other hand, the orientation distribution histograms **(Figure 5a, 5b)** demonstrate that discreet microelements can provide physical guidance for the neurites to grow along the major axis of the microelement even at large VS up to 50-100 μm, depending on HS.

Despite the continuous alternating probing of the growth cone, neurites tend to retain quasi linear paths due to their inherent rigidity and resistance towards bending.[305] This supports our observation that interrupted guidance cues are able to provide sufficient support to sustain unidirectional growth even with larges spacing between them. In contrast, a different trend is observed for the IQR when HS increases at a constant VS. In this case, an initial decrease in IQR is observed when HS increases from 5 to 10 or 20 μm, which could be due to the lack of space for the neuronal cell bodies (~ 10 μm) to reach and adhere to the bottom of the substrate when HS is too

small.

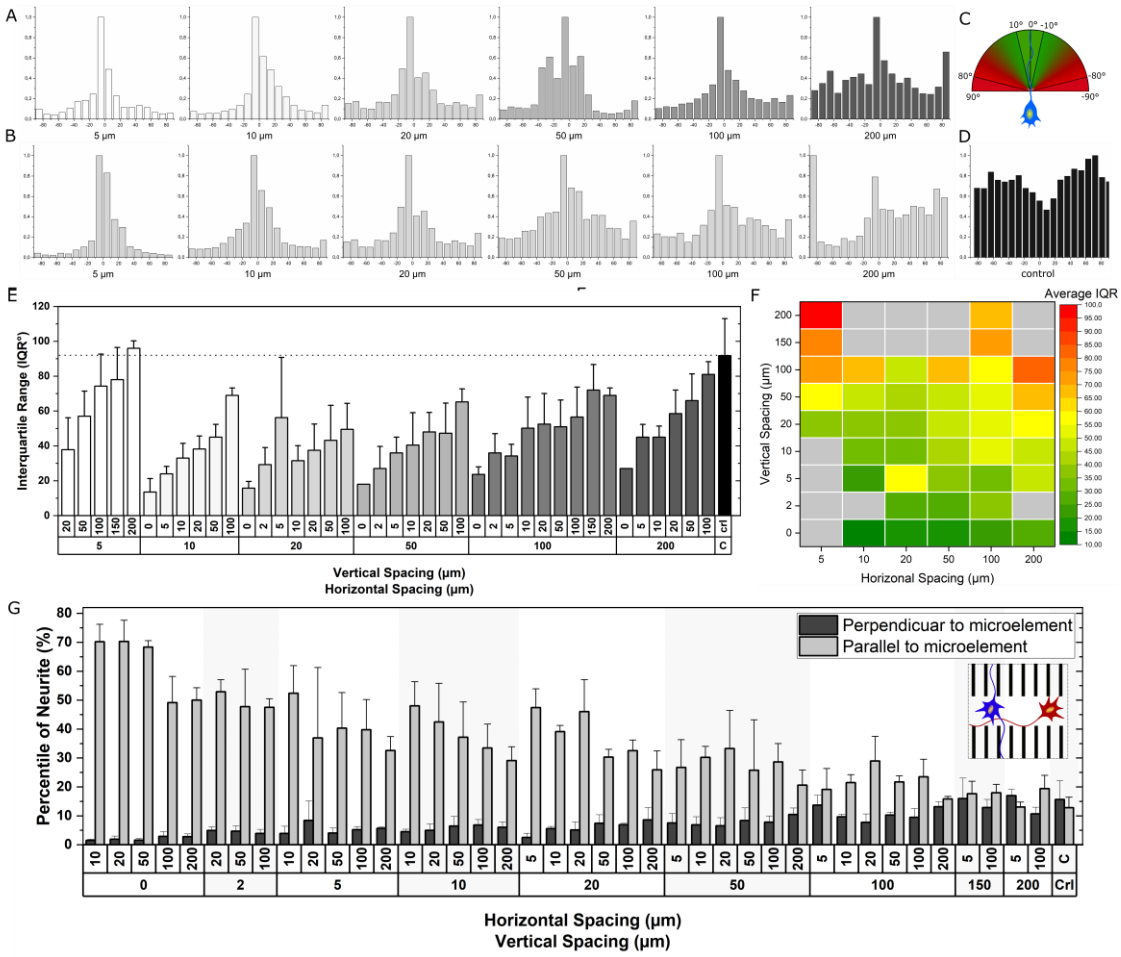

Figure 5. Orientation analysis of immunostained DRG neurons cultured on micropatterns with different inter-elemental spacing VS and HS. **(A)** Orientation distribution of neurites with a fixed HS (20 µm) and variable VS (5-200 µm). **(B)** Orientation distribution of neurites with a fixed VS (20 µm) and variable HS (5-200 µm). **(C)** A pictorial description of neurite orientation in a polar coordinate system. **(D)** negative control substrate without any microelements. **(E)** The IQR of all the micropattern conditions with altering VS and HS. **(F)** Map showing average IQR for different combinations of HS and VS. **(G)** Percentile of neurites growing along the direction of the microelements, as well as perpendicular to the direction of the microelements. (**G-inset**) Schematic representation of neurite growth along the major axis of the microelement (blue) and minor axis of the microelement (red). Data presented as mean ± SD, n ≥ 3.

Even though the cells can deform to adjust to this topographical constrain, most of the cells were observed on top of the microelements with only some axon protruding to reach the bottom of the substrate for a micropattern array with HS equal to 5 µm. These observations are in line with previously reported continuous microchannels

(channel width of 5 μm, height of 25 μm), where reduced neurite outgrowth was observed.[306] As aligned neurites have a positive feedback effect on the directionality of neighboring neurons, fewer axons can negatively influence overall alignment and thus result in higher IQRs. Therefore, there is a critical lower limit for HS ~ 10 μm to provide sufficient space for the neuronal bodies to settle in between the microelements leading to neurite polarization (**Figure 7**). The IQR trend for HS > 10 μm shows an increase with increasing HS at constant VS. In comparison, the previously reported study on neurite alignment in the presence of discreet periodic, isometric, micropillars (1 μm diameter, 5 μm height) showed an increase in neurite alignment when HS increased from 3 μm to 12 μm for a constant VS of 3 μm.[307] Here, neurons were also mainly growing on top of the topography in the case of HS and VS equal to 3 μm. Interestingly, for the several micropattern arrays tested here, neurite orientation remains oriented along the major axis of the microelement. Highly aligned neurite networks are observed at lower VS (5 - 50 μm), in combination with a range of HS (10 - 200 μm) showing little dependency of the IQR-VS trends to HS during physical guidance. For micropattern arrays with VS ≥ 150 μm at HS of 5, 100, or 200 μm, IQR values above 90° were observed.

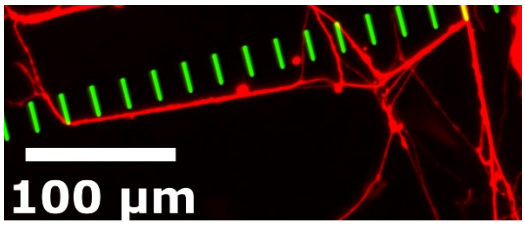

Figure 6. Neurite growing perpendicular to the major axis of the microelements at VS = 200 μm and HS= 20 μm.

The ability of the neurites to retain their growth direction in between the microelements depends on the proximity of the guidance cues available. The neurites have two possible directional cues available after they lose their contact to the physical guidance **(Figure 5g, inset)**, either perpendicular (red) or parallel (blue) to the microelement. An elliptical, 'Mexican hat' orientation kernel is employed to measure

the orientation of neurites and the percentages of neurite segments (N_s) growing along the major axis of the microelements (parallel, (0° ± 9°)) or the minor axis of the microelements (perpendicular, (-81° > N_s > 81°)) are studied for different inter-elemental spacing HS and VS **(Figure 5g, Methods)**. The percentages of neurites growing in parallel and perpendicular to the microelements are consistent with the IQR data **(Figure 5e, 5f)**, with the percentile of neurites growing in parallel to the major axis being the highest at low VS (2-20 μm) for all tested HS, while it reduces gradually with increasing VS. In contrast, the fraction of neurites growing perpendicular to the microelements is increasing with increasing VS. At higher HS (100, 200 μm), HS equal to 5 μm, and VS (100 , 150 , 200 μm), neurite growth shows limited directionality with similar low fractions of neurites (~15% to 20%) growing perpendicular or parallel to the microelements, demonstrating a behavior that mirrors that of flat control substrates. The maximum difference in parallel versus perpendicular neurite growth is observed at a VS of 5 μm and HS of 10 μm, where > 52% of the neurites align along the microelements and only < 4% orient perpendicular to the microelements. As nerve cells follows the major axis of the micropatterns, changing the micropattern orientation changes the primary growth direction (**Figure 8**).

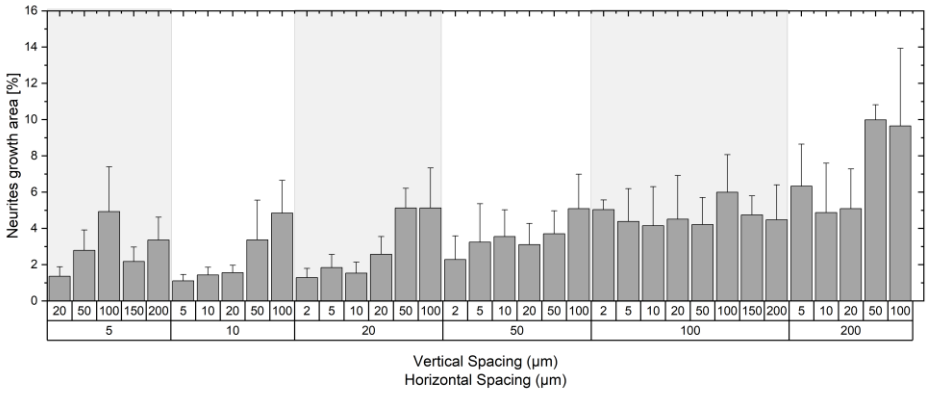

Figure 7. Neurite growth area [%] is plotted for difference VS and HS per field of view.

In view of developing scaffolds with minimal guiding cues, and therefore less material, estimating the space occupied by the guiding elements is of great importance. Our

research shows that in comparison to the volumes occupied by a continuous guidance cue, the space occupancy of discrete guidance cues under similar conditions can be reduced by 20 vol% **(Figure 9)**. Arrays of microelement with different VS and HS but similar percentages of neurites growing parallel to the microelements also have comparable IQR values. As an example, a neurite orientation distribution of IQR ~35°, $N_{s||}$ ~ 45%, $N_{s\perp}$ ~ 4% is observed in micropatterns with both large HS and small VS (HS: 100 μm, VS: 2 μm), as well as for equally spaced HS and VS (20 μm). In the first case, the pattern takes up 91% of the total guidance area that would be occupied by single continuous guides of the same width, while the equally spaced micropattern reduces the guidance area further to only 50%. However, when looking at the total volume occupied by the microelements in the array, the HS=100, VS= 2 array takes only 0. 90% of the total volume, compared to 2.38% occupied by the elements that are equally spaced (**Figure 10**). In contrast, at high VS and low HS, (HS: 5 μm, VS: 200 μm), we observe that the percentile of neurites growing perpendicular to the microelements ($N_{K\perp}$16.99%) is higher than those growing in parallel ($N_{K||}$ 13.03%) (**Figure 5g**). This shows that the directional guidance cue imparted by the long axis of the anisometric microelements can be overruled by spatial arrangements of the guidance cues with low HS and high VS. In the case of an injectable Anisogel, in which anisometric, magneto-responsive guiding elements align *in situ*, it is challenging to obtain anisometry in interelemental spacing.

Hence, a more isometric HS and VS has been achieved in our previous reports, showing that a distance of ~ 22.5 μm) is the most efficient inter-microgel spacing for nerve guidance in 3D fibrin-based ANISOGELS using rectangular microgels (width 2.5 μm, length 50 μm) with aspect ratio of 20. Here we demonstrated that thinner elements (2.5 μm versus 5 μm width) enhance the rate of nerve growth due to a reduced cross section, which can impair neurite extension in the direction parallel to the long axis of the elements. [53] As an axon has a diameter of 1 μm, we chose this as width for our elements and an aspect ratio of 20.

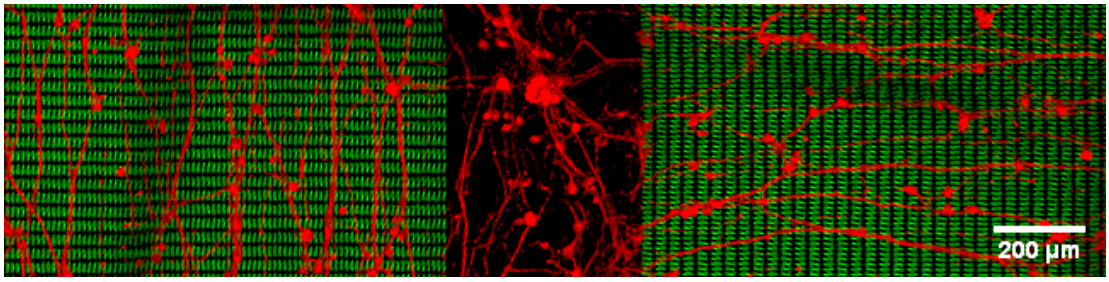

Figure 8. Nerve growth direction is promoted along the major axis of the microelements (VS = 10 µm HS= 10 µm) with their major axis in the vertical (left) or horizontal (right) direction, compared to random growth when no microelements are present (middle).

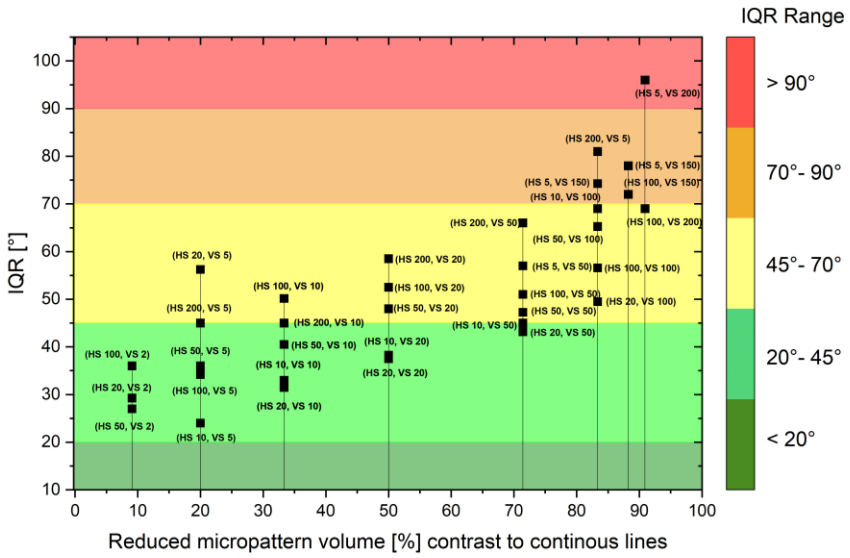

Figure 9. IQR vs reduction in the volume of guiding microelements in comparison to continuous microelements with the same HS. Data presented as mean.

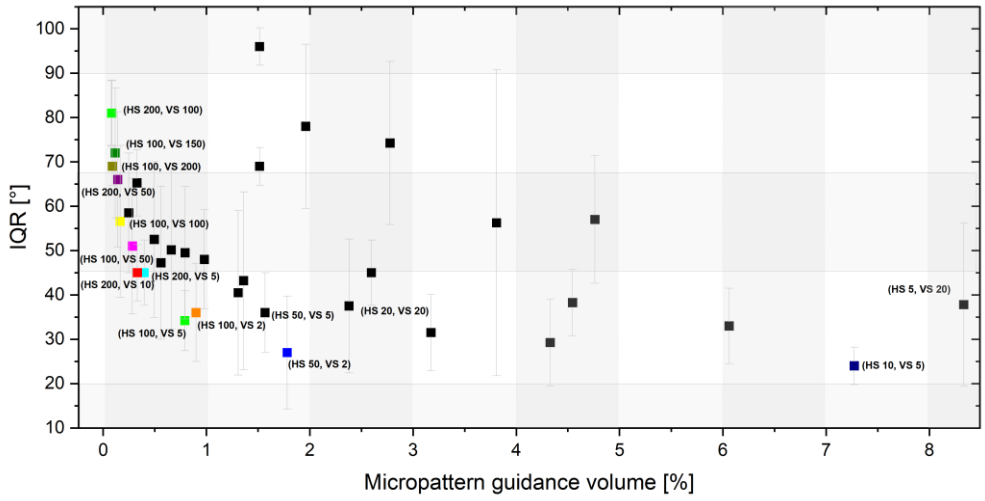

Figure 10. IQR vs vol% of guiding microelements in comparison to flat substrates. Data presented as mean ± SD, n ≥ 3.

3.2.4 Supporting cells influence axonal directionality

The orientation of the neurites is influenced by the microelements but can also be affected by the other supporting cells and their alignment. This can be observed by performing live imaging of the cultures on the micropattern platforms **(Figure 11a, 11b)**. Bright field time-lapse analysis shows the growth cones (GC) of the nerve cells exploring their surroundings. The GC acts as a motile growth sensor and is affected by physical[74] and chemical[308] factors, which result in signaling cascades causing morphological and directional changes.[70,309] During the advancement of the GC, an alternate exchange between stochastic and deterministic behavior occurs, with a transition step in between, where the cues of the environment influence the steering of the neurite axon.[67] Unlike previously reported observations [306], where cells are spatially restricted along continuous ridges of the groove, the GC in our setup senses its local environment in all directions, detecting the periodic guidance from the microelements and steering in between the microelements **(Figure 11a).** It was observed that GC exploration and directionality are influenced by the neighboring cells, as the GC can form temporary or permanent connections with these cells. In some cases, the GC chooses the shortest path to connect to its neighboring cells ignoring the influence of the microelements when it has the choice to follow a microelement or to connect with another neuron or supporting cell in its direct vicinity. This is likely due to chemoattractants produced by the cells. As the influence of the supporting cells is sometimes stronger than the influence of the micropattern, axons can grow perpendicular to the major axis of the microelements to form a neural network **(Figure 11b)**. Neurons have the innate ability to make connections to other neurons and in some cases to other types of cells, such as epithelial tissues, for cell-cell communication. They undergo morphogenesis to grow and extend as neurites until the neurons form a circuit connecting the brain and body.[59,62]

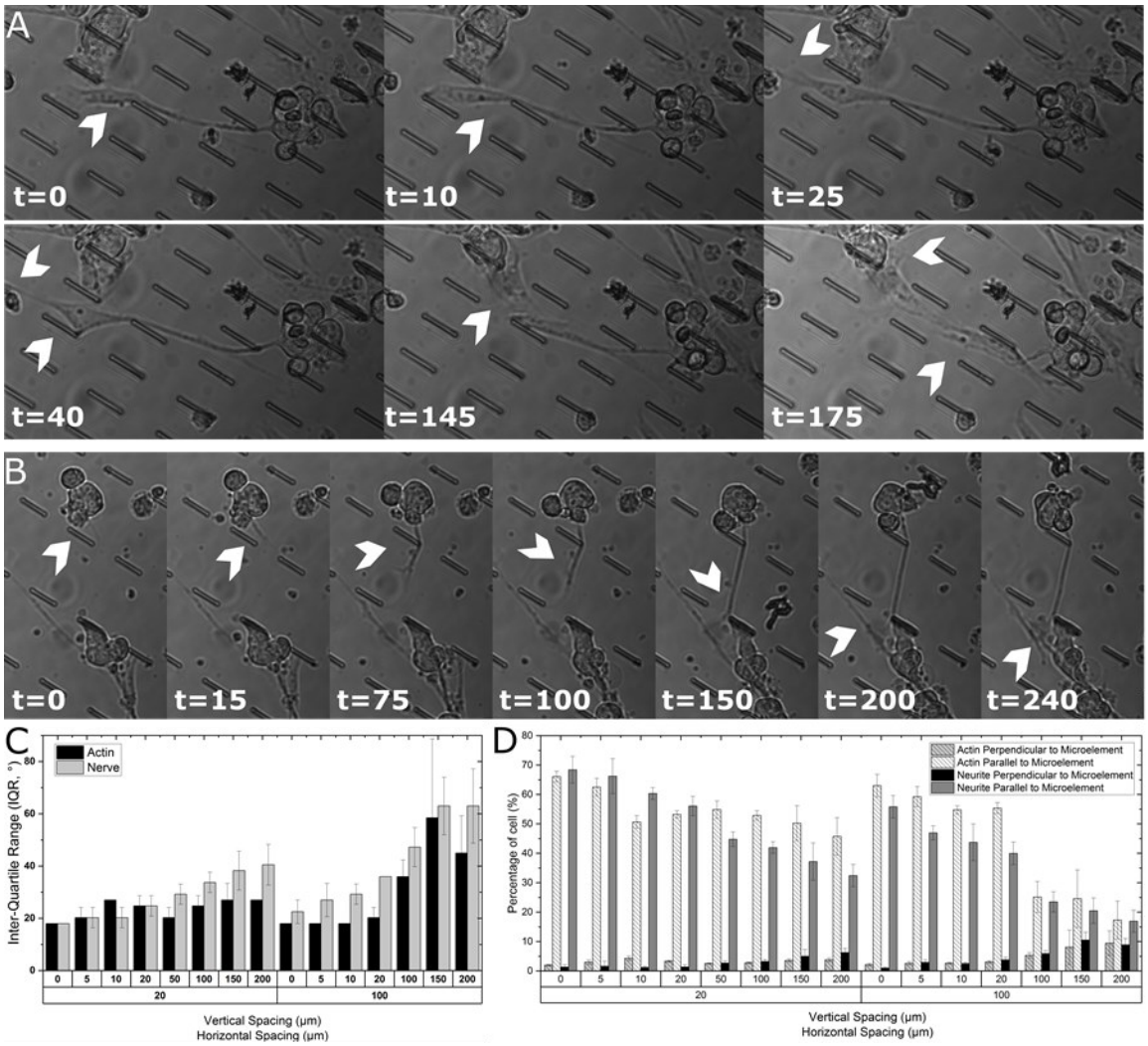

Figure 11. Influence of microelements and supporting cells on the neurite steering direction. (i) Live imaging of axonal steering on anisometric micropattern substrates. Different time points (minutes) reveal that the axons steer in between the microelements, sensing different physical cues and other cell bodies. Micropatterns with interelemental spacings of VS = HS = 20 µm and (ii) VS=20 and HS= 50. (Scale: Length of microelement = 20 µm) (iii) IQR corresponding to the orientation of neurites and actin positive cells. (iv) Percentile of cell growth along the major and minor axis of the microelements for neurites and actin positive cells. Data presented as mean ± SD, n ≥ 3.

In the case of a microelement array with VS = 20 µm and HS = 50 µm **(Figure 11c)**, an IQR of ~50° is observed, where ~30% of neurites grow along the major axis of the microelements, and ~7.5% growing along the minor axis of the microelements. In this case, although a major component of neurite growth is along the microelements, the proximity of the other cells has a strong influence on the direction of the neurite alignment. Unfortunately, it is very difficult to decouple the influence of proximal

cells and microelements on neurite alignment as the supporting/other cells are an integral part of any neural network and their morphology is also affected by the microelement patterns. Comparing the GC motility between a micropattern array and flat control substrates reveals that the guiding microelements play a major role in the realization of directed neural networks. The supporting cells stained for actin filaments are oriented along the direction of microelements for inter-elemental spacing smaller than the cellular dimensions **(Figure 12).** This is consistent with previously reported work, demonstrating actin and nuclear reorganization of cells in confined spaces.[310] The orientation distributions (IQR) of the actin positive cells and neurites are compared with each other for VS 0-200 µm at a HS of 20 or 100 µm **(Figure 11c, 12)**. For each stain individual, an increase in IQR is observed for increasing VS, with a steeper increase in the case of 100 µm. This denotes a stronger influence of VS along the major axis of the microelements for a large horizontal spacing. Comparing the percentiles of cells oriented perpendicular and parallel to the microelements, a similar trend is observed (**Figure 11d**). With decreasing VS for a given HS, the fraction of neurites and supporting cells, oriented parallel to the microelements, increases. Therefore, the results demonstrate that the orientation of supporting cells is also influenced by the inter-elemental spaces between the microelements and may thus indirectly affect neurite directionality.

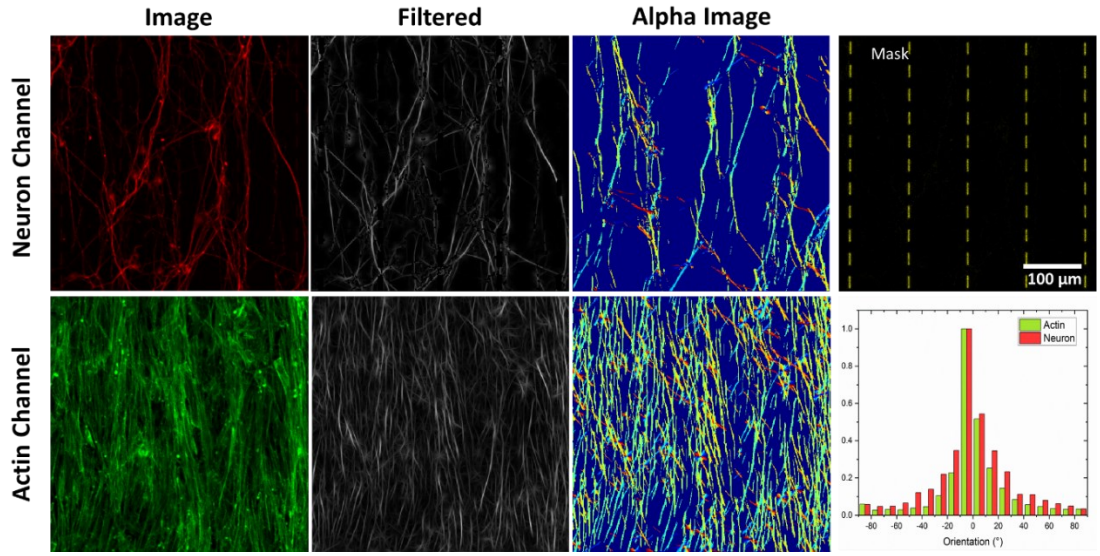

Figure 12. Image processing of neuron and actin channels to obtain orientation distributions.

3.3 Conclusion

A microelement array with custom-designed, anisotropic, and discreet guiding cues was developed to study the ability of discontinuous elements to influence the orientation of neurite outgrowth in a systematic, high-throughput manner. A methodic alteration in both the vertical and horizontal inter-element spacing between the microelements reveals their interplay in inducing neurite alignment for the first time. As expected, an increase in neurite alignment occurs along the major axis of the microelements at lower horizontal and vertical distances. A microelement array with a VS of 5 μm and a HS of 10 μm showed the highest neurite alignment (> 52%) parallel to the major axis of the microelement, with only < 4% neurite extension perpendicular to this direction and an IQR of ~24°. This array is associated with a reduction in the total volume of guidance cues by 20% in comparison to continuous patterns. Interestingly, micropatterns resulting in similar neurite alignment (IQR~ 36°) are observed with different HS and VS combinations, leading to different total volumes needed as guiding elements. This shows that the amount of material required as guiding cues can be reduced without compromising cell guidance, proving that it is possible to develop highly efficient orientation systems. In addition, moderate alignment (IQR < 50°) is observed at smaller VS (5 μm) with larger HS (200 μm) and for larger VS (100 μm) and with smaller HS (20 μm). Overall, this report shows the power of discrete anisotropic guiding elements to orient neurite outgrowth, while the minimal amount of physical guidance can be determined by altering the inter-element spaces. While we demonstrate that several micropattern arrays with anisometric inter-elemental distances showed directed neurite growth in a 2.5D system, achieving a similar approach in a full 3D system presents a challenge due to limitations in generating arrangements with defined asymmetric HS and VS. Furthermore, live time-lapse imaging of these *in vitro* platforms revealed that neighboring cells (neurons or actin positive supportive cells) in combination with anisometric microelements play a role in creating a directed neural network. The

results of this work brings us one-step closer to understanding the complexity of the formation of neural tissue by physical microfeatures. This information can be used for the development of engineered tissue regeneration strategies such as 3D injectable scaffolds that aim to provide minimal guiding cues for directed nerve growth and repair.

3.4 Experimental section

Microfabrication of microelements: The design of the base microelement with dimensions of length 20 μm, width 1 μm and height 10 μm and the patterns with different interelement spacing ranging from 5-200 μm in horizontal spacing and 2-200 μm in vertical spacing were designed in G-code using software DeScribe 2.5.3 (Nanoscribe GmbH). All the micropatterns in this study were fabricated using TPL (780 nm, ~100 fs, 80 MHz), using a 63x NA, 1.4 immersion-based objective with a voxel size of xy= 0.25 μm and z= 0.4 μm enabled the fabrication of structures at a resolution < 1 μm. The patterns were printed on acryl silanized glass coverslips to improve attachment of the elements to the substrate.

Surface functionalization: Ø30 mm glass coverslip (Menzel Glaser # 1.5, Thermo Scientific, USA) is cleaned with isopropanol/acetone (Sigma-Aldrich, ≥99.8%) in an ultra-sonication bath for 5 minutes. The cleaned glass coverslips are incubated in a 0.8% v/v solution of 3-(trimethoxysilyl) propyl acrylate (Sigma-Aldrich, 92 % with 100 ppm butylated hydroxytoluene BHT) in acetone overnight at room temperature. This allows the crosslinking between the photoresist and glass substrate at its interface improving microelement anchorage on the substrate. The silanized glass substrates are rinsed with deionized water and dried in a flow of nitrogen.

TPL: 100 μL of photoresist (IP-L 780) is drop cast on the silanized substrate. Laser power 60%, scan speed 20000 μm s^{-1}, galvo mirror speed 300μm s^{-1} is optimized. The smallest photo polymerization volume (1 voxel) has an elliptical shape with a width of 0.33 μm and a height of 0.80 μm. These are printed layer-by-layer with a slicing

distance of 0.5 μm. The uncrosslinked polymer resin is dissolved using propylene glycol monomethyl ether acetate (PGMEA), (Sigma-Aldrich, ≥99.5%) for 30 minutes at room temperature and washed with isopropanol. The substrate is dried in a flow of nitrogen.

Bio-functionalization: Substrates were individually coated using different biomolecules such as poly-L-lysine (0.1 mg mL^{-1}, PLL, Sigma-Aldrich); mouse laminin (10 μg mL^{-1}, Invitrogen), PLL (0.1 mg mL^{-1}) and laminin (10 μg mL^{-1}, PLL-Laminin) in combination; human fibronectin (10 μg mL^{-1}, Sigma-Aldrich); gelatin (10 mg mL^{-1}, Sigma-Aldrich, from bovine skin) at 37°C for 30 minutes and dried at room temperature.

Cell Culture: Dissociated dorsal root ganglions (DRG) extracted from 10-day old chicken embryos were dissected and cleared from other supporting tissues and temporarily collected in Hank's balanced salt solution (HBSS) supplemented with 6 g/L glucose. Pooled DRGs were then dissociated into single primary nerve cells (PNCs) by incubating them in Trypsin (1X, Sigma Aldrich) for 30 mins at 37°C, followed by trituration through a fire-polished glass pipet several times until a single cell suspension was obtained. The cells are panned for 2 h at 37°C to obtain pure neuronal cells by separating adherent cells such as fibroblasts and Schwann cells. The cells were suspended in Dulbecco's modified Eagle medium (DMEM), supplemented with 10 % fetal bovine serum (FBS), 1% antibiotics/antimycotics (AMB) and 20 ng/mL of β-nerve growth factor (NGF, Peprotech). The seeding density of the cells is controlled by using PDMS rings to confine the area of cell growth on the micropattern. A seeding density of 150 cells/mm^2 was chosen to study the growth of neurites and cultured at 37 °C, 5 % CO_2 and 95 % humidity for 3 days. DRG tissue was extracted in accordance with the local animal ethics regulations and the European Directive 2010/63/EU.

Immunostaining: After 72 h in culture PNCs were fixed in prewarmed (37 °C) 4% paraformaldehyde (PFA, AppliChem) in phosphate buffer saline (PBS, 1X, pH 7.4) for 20 minutes. The substrate is washed twice with PBS and permeabilized using 0.1 %

Triton X-100 (Sigma-Aldrich) in PBS for 3 minutes. After a short PBS wash (2x) substrates were incubated with primary anti-tubulin (1: 250, TUJ1 monoclonal antibody mouse-derived, Biolegend) in 5 % bovine serum albumin (BSA, Sigma-Aldrich) in PBS solution for 4h at RT, and washed twice for 30 min with PBS. The secondary antibody Alexa Fluor 633 goat anti-mouse was added and incubated for 2 followed by a final PBS wash. To stain actin, phalloidin-iFluor 594 (1: 1000, Abcam) is added, incubated for 2 hours. Samples were counterstained using 4′,6-diamidino-2-phenylindole (DAPI) (1: 100, Thermo Fischer Scientific) by incubating the substrate for 10 minutes followed by PBS wash (x2) for 30 minutes.

Imaging: Samples were visualized with a Zeiss Axio Observer Z1 microscope equipped with an Axiocam MR Camera or with a laser scanning confocal microscope (SP8 Tandem Confocal, Leica Microsystems Inc.). In the case of SP8, the light sources are a diode 405 (for DAPI fluorescence), argon-ion laser adjusted to 488 nm emission (fluorescence from microelements), diode-pumped solid-state laser 561 nm (iFluor 594), and helium-neon laser 633 nm (Alexa Fluor 633). The images are acquired in sequential channels or with suitable detector settings to avoid cross-talk between signals. The substrates are imaged with 20 µm Z stack height with a slicing distance of 1 µm. Image processing is performed using LasX, AxioVision, Image J and Python.

Neurite Orientation Analysis: Neurite alignment induced by the microelements is quantified by analyzing the beta-tubulin signal (red channel) and the microelements signal (green channel). A slight overlap of the microelement signal is still observed in the neurite images, which is then eliminated by subtracting the microelements from the neurite resulting in a signal corresponding only to tubulin. The orientation of the tubulin positive structures is analyzed using an elliptic differential kernel. The kernel is calculated as a rotated 'Mexican hat' (the second derivative of a two-dimensional Gaussian) function with a broad and a narrow width in X and Y direction respectively. The procedure has the following main steps. (i) Background correction and highlighting features. (ii) Constructing binary masks. (iii) Convolution with the

rotated kernel. (iv) Identifying orientation based on the highest intensity in the convolved images along the angle axis (Z-axis), then removing unwanted data points applying the binary masks defined above in (ii).

Background correction: Images are blurred using a Gaussian kernel with a radius of 60 pixels (matrix size: 121 x 121 pixels) and standard deviation (\sigma) of 20 pixels. This background is subtracted from the image, and negative values are set to zero. The image is then smoothed using another Gaussian kernel, with a window radius of 5 pixels (matrix size 11x11 pixels), and width (σ) of 1 pixel. The dynamic range of the image was then compressed around its mean value applying a square root function. In detail, first the image was divided by its mean value, then the square-root was applied, and the result was multiplied back with the mean.

Binary Masks: Two types of binary masks were created. One was using the image of the microelements. This image was converted to a binary image keeping all pixels below 50% of its maximal intensity. The pattern was further eroded using a simple erosion operator two times. This removes every pixel which has at least one zero neighbor. Data are kept where this filter was nonzero. The second filter uses a structure tensor to characterize the local neighborhood of each point. Blobs are assumed for relative intensities above 1% of the amplitude maximum, where the coherence around each point is less than 0.5. [311,312] The local neighborhood is 5 times the size of the smoothing filter. Data are removed where this filter was nonzero.

Convolution with kernel and maximum image: Convolution with the rotating kernel results a set of 2 dimensional images, forming a Z-stack, where the Z-axis is the orientation angle of the kernel. The maximum is collected along this Z-axis for each pixel into a 'maximum image', and the angle where this maximum occurred is recorded into an 'alpha' image. A threshold is applied to this maximum image using Otsu's method, and all points are erased below this threshold. Then those points are also removed which were defined by the binary masks above. The remaining points are used to collect the corresponding angular values (discreet intervals of 9° between

-90° and +90°). A histogram is determined from the angles. The whole process is implemented in Python, and the core functions are available online as part of the ImageP package on Launchpad [https://launchpad.net/imagep]. Alternatively, the angular values are post-processed in R and the angles are reoriented to the angle defined by the microelements in order to compare the relative orientation properties.

Statistical Analysis: Data points are shown as mean average with error bars indicating standard deviation with sample size ≥ 3. One-way ANOVA and pair comparisons using Bonferroni and Tukey's methods are performed to determine statistical significance, and the p values for statistical significance are represented with stars: * $p < 0.05$, ** $p < 0.01$. Statistical analysis is done using OriginPro 2020.

3.5 Future scope

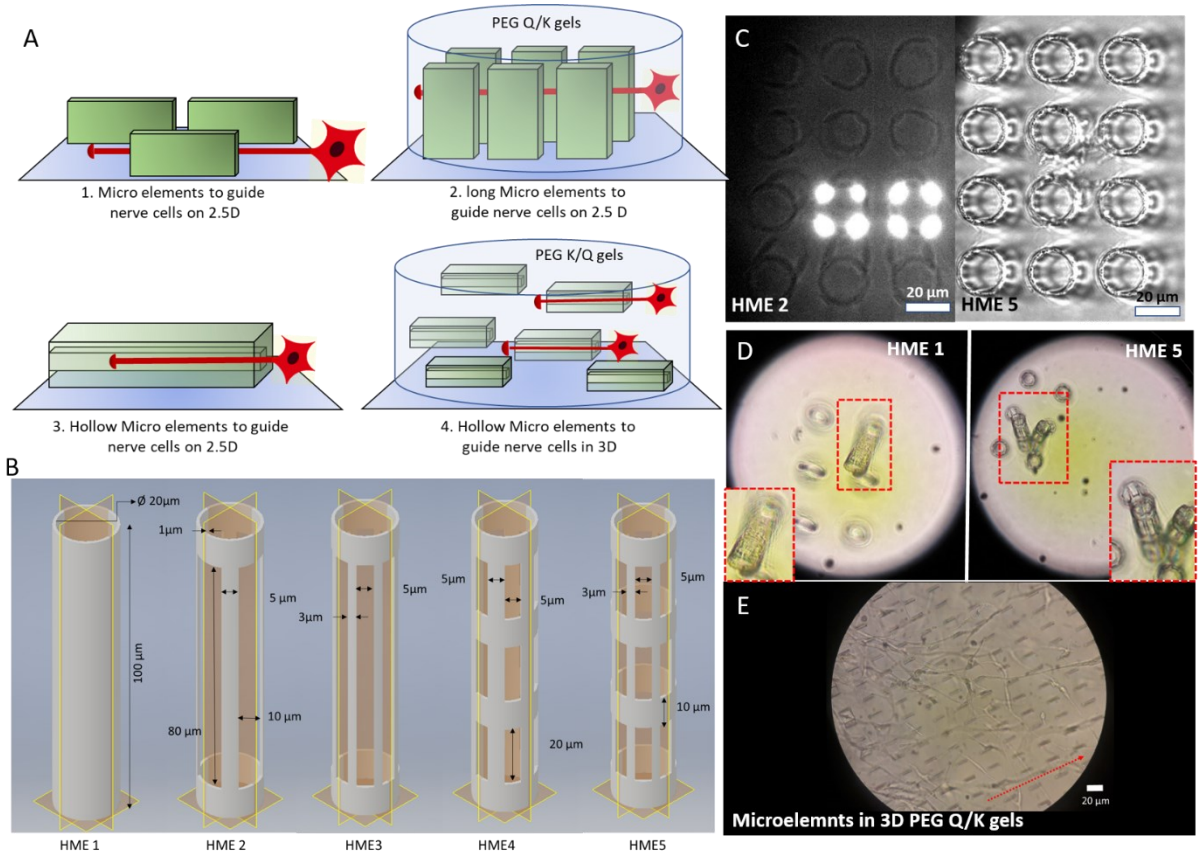

Figure 13. a) Schematic evolution of microelement array from 2.5D to 3D (top) followed by fabrication of hollow microelements and encapsulating them in 3D synthetic PEG hydrogels. b) Evolution of CAD design of hollow micro channels/elements from simple tube-like

structures to complex shapes that support cell orientation. c) Fabricating HME2 and HME 5 using TPL (top view). d) HME 1 and HME 5 under a bright field microscope. e) Bright-field images of in vitro nerve cell growth showing cell guidance in a 3D micro array platform surrounded with PEG hydrogel.

Translating the 2.5D platform described earlier to the 3D platform involves applying the obtained information on minimal guidance cues and translating it into a 3D microelement array. For example, tall elements were fabricated using TPL of dimensions 20 μm x 1μm with a height of up to 200 μm (**Figure 13a, top**). These tall micro-walls lose their stability and collapse due to their high aspect ratio on the z-axis. Hence, I used PEG Q/K gels (**Chapter 4**) to support the stability of the free-standing tall microelements and provide a hydrogel casing encapsulated with cells. I was able to culture primary nerve cells dissociated from DRGs in this platform to orient nerve cells in 3D space (**Figure 13e**). A gradual evolution from tall micro-walls to hollow microelements is desired (**Figure 13 a, bottom**) to address the stability issue and reduce material usage. Fabrication of hollow channels was realised by designing features in a CAD model (**Figure 13b**). Smooth hollow channels were then altered to bear additional cavities for nutrient exchange and fabricated using TPL (**Figure 13c**). Harvesting hollow micro channels/elements are possible by placing the fabricated substrate in an ultrasound bath. However, the yield is low. An additional optimization is desired to translate simple microelements in ANISOGELS to complex shape bearing microelements.

Chapter 4. Bicyclic RGD peptides enhance nerve growth in synthetic PEG-based ANISOGELS

Sitara Vedaraman, Dominik Bernhagen, Tamas Haraszti, Christopher Licht, Arturo Castro Nava, Abdolrahman Omidinia Anarkoli, Peter Timmerman, and Laura De Laporte

Nerve regeneration scaffolds often consist of soft hydrogels modified with extracellular matrix (ECM) proteins or fragments, as well as linear and cyclic peptides. One of the commonly used integrin-mediated cell adhesive peptide sequences is Arg-Gly-Asp (RGD). Despite its straightforward coupling mechanisms to artificial extracellular matrix (aECM) constructs, linear RGD peptides suffer from low stability towards degradation and lack integrin selectivity. Cyclization of RGD improves the affinity towards integrin subtypes but lacks selectivity. In this study, a new class of short bicyclic peptides with RGD in a cyclic loop and 'random screened' tri-aminoacid peptide sequences in the second loop is investigated as a biochemical cue for cell growth inside three-dimensional (3D) synthetic poly(ethylene glycol) (PEG)-based ANISOGELS. These peptides impart high integrin affinity and selectivity towards either $\alpha_v\beta_3$ or $\alpha_5\beta_1$ integrin subunits. Enzymatic conjugation of such bicyclic peptides to the PEG backbone enables the formulation of an aECM hydrogel that supports nerve growth. Furthermore, different proteolytic cleavable moieties are incorporated and compared to promote cell migration and proliferation, resulting in enhanced cell growth with different degradable peptide crosslinkers. Mouse fibroblasts and primary nerve cells from embryonic chick dorsal root ganglions (DRGs) show superior growth in bicyclic RGD peptide conjugated gels selective towards $\alpha_v\beta_3$ or $\alpha_5\beta_1$, compared to monocyclic or linear RGD peptides, with a slight preference to αvβ3 selective bicyclic peptides in the case of nerve growth. Synthetic ANISOGELS, modified with bicyclic

RGD peptides and containing short aligned, magneto-responsive fibers, show oriented DRG outgrowth parallel to the fibers. This report shows the potential of PEG hydrogels coupled with bicyclic RGD peptides as an aECM model and paves the way for a new class of integrin selective biomolecules for cell growth and nerve regeneration.

4.1 Introduction

The native neuronal tissue is soft (0.1-1 kPa) and consists of a highly ordered microarchitecture to enable connections between neurons and their supporting cells to form a functional neural network.[313] Efficient nerve regeneration in an artificial extracellular matrix (aECM) is achieved by mimicking the extracellular matrices (ECM) with three-dimensional (3D) scaffolds where the cells inside the scaffold experience a combination of chemical, physical, and architectural cues.[18,314] *Ex vivo* mimicry of biological systems is established to create relevant models and micro-environments that enable cells to adhere, proliferate and migrate either by squeezing through the aECM (amoeboid) or by degrading their local environment by secreting proteases (mesenchymal).[315] Most of the studied ECM mimicking neural niches and 3D scaffolds are based on endogenous protein sources, such as collagen[316], fibrin[286,317], hyaluronic acid[152,318], or a combination of these.[319,320] Although proteinaceous gels or scaffolds offer a natural environment for cell growth, their batch to batch variability and lack of controlled properties are limiting factors. On the other hand, scaffolds made from synthetic polymers or other macromolecules are reproducible, more resistant to immunogenic reactions, and easy to vary in properties, such as stiffness, degradability, architecture, biomolecule modification, etc.[321] To combine the advantages of both natural and synthetic building blocks, hybrid materials are often employed. Arginylglycylaspartic acid (Arg-Gly-Asp or RGD) is the smallest integrin recognizable ligand present *in vivo*, which is widely used to induce cell adhesion in synthetic scaffolds[322]. For example, elastin-like proteins (ELP) with controlled RGD ligand density and optimized scaffold stiffness enabled neurite outgrowth of chick

dorsal root ganglions (DRGs).[323] Semi-synthetic scaffolds, prepared from PEGylated albumin or PEGylated fibrinogen enabled nerve growth at low concentrations of PEG (1.6 w/v% and 2.3 w/v%, respectively) with 0.8 w/v% of the respective proteins.[177] Besides RGD, the laminin-derived adhesion peptide IKVAV is often employed to induce vascularization and innervation, for example in composite hydrogels consisting of elastin-like polypeptides and PEG, creating a microporous environment with controlled mechanical properties.[324] In the case of non-endogenous sources, proteinaceous gels, such as silk[325] and alginate[326]-based hydrogels provide a promising environment as a 3D neuronal scaffold.

In the case of polymeric hydrogel scaffolds, the mechanical properties can be varied by the composition, structure, molecular weight, reaction mechanism, and concentration of the pre-polymer, and optimized to support nerve growth and axon protrusion.[25,327] Inside these constructs, spatial distribution[323,328] of integrin-binding ligands and the internal structure are crucial factors in bio-mimicking the native cell microenvironment. Designing hydrogels with large pores that facilitate perfusion of growth factors and nutrients[329], while at the same time permitting temporally controlled degradation is primordial to promote cell proliferation and enable cell motility and scaffold invasion.[330] Among the several reported polymeric hydrogel systems, PEG-based networks offer a biocompatible microenvironment for cells with a low risk of immune reaction. By using degradable crosslinks, the degradation products can be eliminated from the body via natural biochemical mechanisms.[22,331,332] The PEG system used in this report employs an enzymatic crosslinking and bio-conjugation method, inspired by fibrin clotting,[24] while degradation moieties are included in the backbone to enable proteolytic degradation by matrix metalloproteases (MMPs).[22,26] These MMP sensitive domains in the crosslinker degrade when cells produce MMPs, resulting in gel degradation on cell-demand and providing space for growing cell populations. Such a system has been reported by our group to promote 3D nerve growth when a specially designed fibronectin fragment FNIII9*-10/12-14 was coupled inside the gel.[25] Compared to linear RGD, much lower

concentrations of the fragment were sufficient to support cell growth. FNIII9*-10/12-14 has previously demonstrated to enhance wound and bone regeneration when bound to a fibrin gel, likely due to the synergistic effect of providing integrin binding domains adjacent to growth factor binding domains.[31] In the case of RGD coupling to a synthetic fibrin-mimicking PEG gel, Ehrbar et al. determined the binding efficiency via the transglutaminase reaction using release studies by reverse phase chromatography and mass spectroscopy, resulting in ~ 72% RGD binding efficiency for 5 wt/v % gels in the case of 4.3% RGD peptides of total PEG-K arms.[234] We previously translated these gels with FNIII9*-10/12-14 to ANISOGELS to create anisotropy imparting gels by incorporating magneto-responsive rod-shaped microgels or short fibers and aligning them along external magnetic field lines to promote unidirectional neurite extension.[25]

Integrin binding domains, incorporated inside aECMs are involved in bidirectional transmembrane signalling between cells and their environment and play an important role in cell growth.[102] Integrins are involved in the regulation of physiological processes such as migration, proliferation, survival, and apoptosis. The focal adhesion mechanisms between the ECM ligand and the integrin receptor heterodimers, consisting of α and β integrin subunits, have been extensively studied.[103,333] Linear RGD peptides, cyclic RGD peptides, and peptidomimetic ligands have evolved progressively for binding integrin subunits.[334] Flanking linear RGD peptides with amino acids, such as glycine (G) at the N terminus and serine (S) at the C terminus, results in a decrease in half-maximum inhibitory concentration (IC_{50}) values by 3 and 4 folds for $\alpha_v\beta_3$ and $\alpha_5\beta_1$ integrin subunits, respectively.[41] Lower IC_{50} values indicate a higher affinity to integrin subunits and the lowest IC_{50} value is observed for heptapeptide G**RGD**SPK, which is 7 folds lower than for tripeptide RGD in the case of $\alpha_v\beta_3$.[41] Similarly, the cyclization of linear RGD peptides (RGDfK) and incorporation of one D-amino acid residue between Asp (D) and Lys (K) improves affinity to integrin subunits and increases stability towards enzymatic degradation.[41,105] Monocyclic RGD peptides show moderate to low IC_{50} values towards multiple integrin subunits, such

as $\alpha_v\beta_3$, $\alpha_v\beta_5$, $\alpha_v\beta_6$, and $\alpha_5\beta_1$. The lowest IC_{50} values are observed for $\alpha_v\beta_3$ subunits and cyclization improves integrin $\alpha_v\beta_3$ binding affinity in the range of 1.5-6.0 nM and integrin $\alpha_5\beta_1$ binding affinity in the range of 141-236 nM.[41] Similar to flanking in linear RGD, flanking in cyclic RGD peptides with linear polyproline improves cell spreading and focal adhesions in rat embryo fibroblasts in comparison to other spacers like PEG.[106] Another class of high affinity and selective integrin-binding ligands are the peptidomimetics, which can distinguish between different integrin subtypes *in vitro* and *in vivo*.[107,108]

It is important to understand the role of integrin-mediated adhesion to its corresponding ligands in the ECM for achieving directed cell fate in tissue engineering applications. For example, the ability of cells to sense the mechanical properties of its fibronectin based ECM is mediated by the synergy between the α_5 β_1 and α_v-class integrin subunits.[335] Similarly, the inter-dependence of integrins ($\alpha_5\beta_1$,$\alpha_v\beta_3$) employed during focal adhesions is explored on 2D platforms with integrin specific RGD-coupled gold nanoparticles on PEG gels. The study revealed that during focal adhesion, the recruitment of $\alpha_v\beta_3$ integrins occurs on patterned substrates that are exclusive for $\alpha_5\beta_1$, but the vice versa is not true.[336] In addition, 3D hyaluronic acid hydrogels with specific integrin activation ($\alpha_3/\alpha_5\beta_1$) induced sprouting in an endothelial cell angiogenic model *in vitro* and enabled the formation of non-leaky blood vessels in stroke models.[318] Such examples show the importance of integrin-mediated cell adhesion and migration, which in turn determines cell fate.

In this report, a new class of integrin selective engineered bicyclic peptides with one loop containing the integrin-binding RGD peptide is employed to study neuronal growth in 3D PEG-based hydrogels and ANISOGELS. These peptides have demonstrated greater conformational rigidity, metabolic stability, and most importantly, high integrin selectivity. The primary loop consists of an RGD peptide flanked with cysteine residues that bind to a tri-covalent scaffold (1,3,5-tris(bromomethyl)benzene). The secondary loop consists of a tri amino-acid sequence,

which is screened using a 'random approach' and imparts the potential to affect the RGD selectivity towards different integrin subunits ($\alpha_v\beta_3$ or $\alpha_5\beta_1$).[109,110] Elastin-like recombinamers (ELR), produced with recombinant proteins and coupled with bicyclic RGD peptides selective for $\alpha_5\beta_1$ show an increase in HUVEC proliferation at early periods of culture.[337] Here, we describe for the first time the effect of bicyclic RGD peptides for nerve growth in synthetic 3D PEG hydrogels to study the affinity towards selective integrin sites. Soft, synthetic, degradable multi-arm PEG hydrogels are enzymatically crosslinked using transglutaminase and conjugated with different bicyclic RGD peptides. Domains cleavable by MMP 1, MMP2, and plasmin are incorporated in the PEG precursors to enable on cell-demand degradation at the crosslinking arms. The MMP 1 and MMP 2 sensitive domains enable extensive cell growth inside the hydrogel. Expansion of both mouse fibroblasts and primary nerve cells from chick DRGs is investigated and compared with linear and monocyclic RGD and a specific fibronectin fragment FNIII9*-10/12-14[31] (FN*). Bicyclic RGD conjugated gels show superior nerve and fibroblast growth. Also, cell growth and innervation in PEG gels are dependent on the type of proteolytic cleavable MMP-sensitive peptide present in the crosslinker. Finally, fully synthetic ANISOGELS are prepared by mixing and orienting short, magneto-responsive polycaprolactone (PCL) fibers (diameter ~ 5 μm, length ~ 50 μm, 1 vol %) before crosslinking of the surrounding PEG hydrogels, modified with the bicyclic peptides and optimal degradation domain VPMS↓MRGG (K_2). Embedded DRGs inside ANISOGELS, tethered with bicyclic RGD peptides (K-P2 RGD), linear RGD (K-RGD) and fibronectin fragment (FN*) demonstrate unidirectional nerve growth.

4.2 Results and discussion

4.2.1 Designing RGD conjugated PEG hydrogels

Nerve and fibroblast cell growth in synthetic PEG hydrogels is compared among bicyclic peptides and standard RGD peptides, commonly used for biomaterial development. The RGD peptides are tethered to the PEG hydrogels **(Figure 1a)** either

by its amine in the lysine (K), its amide in glutamine (Q), or via the amine from the N terminus of any unmodified RGD peptide. The RGD peptides with K or Q residues bind to the arms PEG-Q or PEG-K, respectively. Transglutaminase reaction between the Q and the K residues is initiated in the presence of an enzyme (activated FXIII), resulting in the formation of an iso-peptide bond.[338] The multiple arms in PEG facilitate crosslinking and bio-conjugation simultaneously. PEG polymer is used at 1 wt/v% to fabricate hydrogels with a storage modulus of ~ 10 Pa[25], to which a fixed concentration (100 μM) of RGD peptide is conjugated. In a previous report, we demonstrate superior cell growth using this RGD concentration.[25] The proteolytic cleavable sites are incorporated in the arms of PEG-K; PEG-K_1: FKGG-**GPQG↓IWGQ**-PEG (K_1), PEG-K_2: FKGG-**VPMS↓MRGG**-PEG (K_2), PEG-K_3: FKGG-**K↓K↓GHK↓LHL**-PEG (K_3). These MMP sensitive domains are cleaved by proteases. However, PEG-K_{ND}: FKGG-**GDQGIAGF**-PEG (K_{ND}) **(Figure 1d)**, where the 8 amino acid sequence not degraded by MMPs.[22,339]

Mixing the precursor solution with the cells and controlling the crosslinking rate by the concentration of activated Factor XIII (FXIIIa) enables 3D encapsulation of cells. Bicyclic RGD peptides, engineered by Bernhagen et al., contain two loops, consisting of an RGD sequence and integrin selectivity imparting sequence, where Ala-Trp-Gly (AWG) results in selectivity towards $\alpha_5\beta_1$ and loop His-Pro-Gln (HPQ) leads to selectivity towards $\alpha_v\beta_3$ **(Figure 1b)**. Bicyclic RGD peptides **(Figure 1c)** (K-linker-C_{T3}**RGD**c_{T3}AWGC_{T3}[109], NQEQVSPL-C_{T3}RGDc_{T3}AYJC_{T3}G, GC_{T3}**RGD**c_{T3}AYJC_{T3}, K-linker-C_{T3}HPQc_{T3}**RGD**c_{T3}[110], NQEQVSPLC_{T3}HPQc_{T3}**RGD**c_{T3}G, GC_{T3}HPQc_{T3}**RGD**c_{T3}), cyclic RGD peptides (cyclo-**RGD**fK[41], cyclo-**D**fK[K-linker]**RG**), and linear RGD peptides (K-linker-G**RGD**S, NQEQVSPL**RGDS**PG, G**RGD**S[41]) are used as cell adhesive domains in this study with controls, such as scrambled second loops (K-linker-C_{T3}**RGD**c_{T3}WGAC_{T3}, K-linker-C_{T3}PQHc_{T3}**RGD**c_{T3}) and scrambled RGD peptides (K-linker-C_{T3}GDRc_{T3}AWGC_{T3}, K-linker-C_{T3}HPQc_{T3}GRDc_{T3}). Fibronectin fragment FNIII 9*-10/12-14 is used as positive control and PEG gels without RGD as another negative control.

4.2.2 Influence of RGD peptides on fibroblast growth

Hydrogels conjugated with RGD peptides enable the spatial distribution of integrin-binding ligands for cell adhesion, spreading, and proliferation. These peptides are classified based on their structure as linear, cyclic, and bicyclic, reporting an increase in integrin affinity and selectivity based on IC_{50} from former to the latter.[41,109,340] L929 mouse fibroblasts are encapsulated within the hydrogel at a fixed cell concentration. 3D cell growth in multiple planes is quantified after staining for actin filaments and imaging as z-stacks. A 200 µm z-stack image (**Figure 3**) of cells in a K-P2 conjugated hydrogel is represented by a color-coded depth profile, showing homogeneous cell distribution. Cells show different morphologies depending on the type of RGD peptide tethered to the hydrogels (**Figure 2a**).

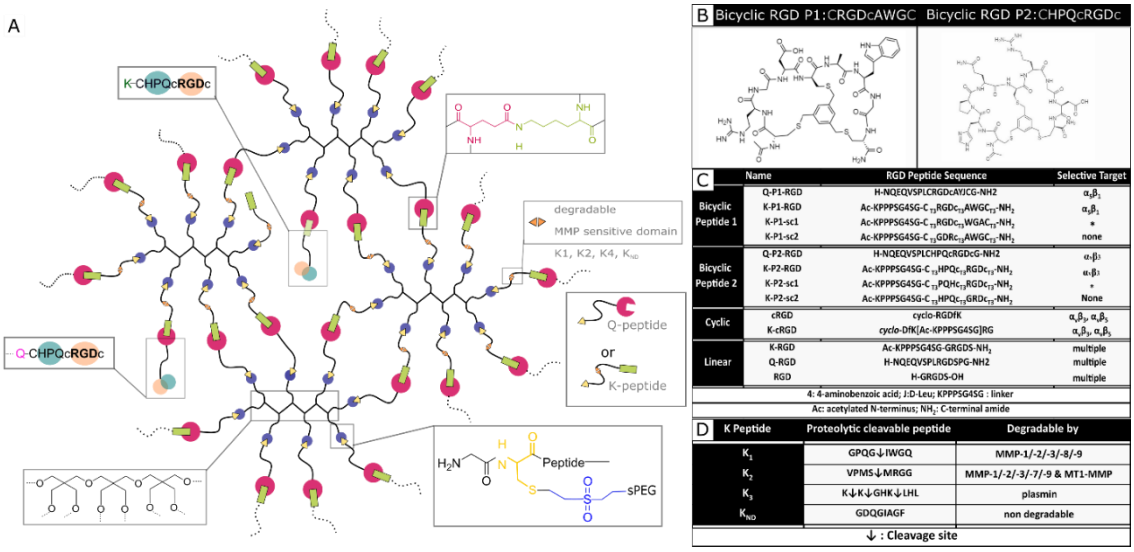

Figure 1. PEG hydrogel system. A) Schematic of PEG hydrogel system with MMP cleavable arms in PEG-K precursor and RGD peptide conjugation via its K and Q residues. B) Representative bicyclic RGD peptides P1 and Bicyclic RGD peptide P2, selective for integrin α5β1 and αvβ3 respectively. C) Summarized peptide sequences for bicyclic, mono-cyclic, linear RGD peptides indicating selective integrin target. D) Proteolytic cleavable amino acid sequences incorporated in the 8-arm PEG-K precursor.

The cells inside the hydrogels with bicyclic (K-P1, K-P2) and monocyclic (K-cRGD) RGD peptides spread and stretch to form network-like structures, in contrast to cells

in gels with linear RGD (K-RGD) or no RGD. For hydrogels, modified with linear RGD, only some cells stretch, while others are more rounded with small protrusions (white arrows) resembling filipodia. In the control condition without RGD, most cells appear rounded, even though some cells are able to spread, likely due to their natural production of ECM proteins and proteases. The superimposed z stacks of the actin-stained images are compared for their cell invasion area (%) per field of view (**Figure 2b**). K-P2 is the only peptide that statistically leads to similar cell invasion, compared to FN*, suggesting that the fibroblasts used in this culture may be more sensitive to $\alpha_v\beta_3$ binding domains. This is in agreement with the fact that the mono-cyclic peptide (more selective to $\alpha_v\beta_3$[41]) leads to better cell invasion compared to the linear RGD peptide, which has 5x lower affinity to $\alpha_v\beta_3$ and binds to both $\alpha_v\beta_3$ and $\alpha_5\beta_1$[41]. In addition, none of the RGD peptides have the synergistic domain PHSRN, which is required for efficient $\alpha_5\beta_1$ binding.[341] This could explain the fact that the bicyclic peptide P2 shows a higher binding affinity towards $\alpha_v\beta_3$ (IC_{50}: 30 nM[340]) compared to peptide P1 towards $\alpha_5\beta_1$ (IC_{50}: 173 nM[109]).

Among the bicyclic RGD peptides tethered via K, the peptide K-P2 show significantly higher cell invasion compared to K-P1, however, no such difference is observed in the case of bicyclic RGD tethered via Q. In addition, the K-P2 peptide leads to higher cell invasion compared to Q-P2, with the K-peptide having the shorter linker. Factors affecting the performance of a bicyclic peptide leading to the differences in cell behaviour can thus be attributed towards their Q or K residue peptide linkers, spatial availability of RGD peptide, and binding efficiency. When comparing the RGD peptides with fibronectin fragment FNIII9*-10/12-14 (5 μM, FN*)[25], the fragment results in a more dense cell network. We reason that FN* provides a more natural ECM mimicking environment, compared to the RGD peptides, as the RGD sequence in FNIII10 can work together with its synergistic PHSRN sequence in FNIII9*,[341] which is not present in any of the peptides used. In this experiment, linear K-RGD is employed to compare with the K-cRGD as both Q-RGD (100 μM) and K-RGD (100 μM) have a similar RGD potency when a proliferation assay is performed with L929

fibroblasts grown on thin PEG substrates **(Figure 4)**. Further, a comparison of cell invasion in 3D gels, modified with Q-RGD (100 μM) or FN* (5 μM), leads to a similar Q-RGD vs FN* ratio (ratio: 0.59) **(Figure 5)** as when comparing K-RGD (100 μM) with 5 μM FN* (ratio: 0.57) **(Figure 2b)**.

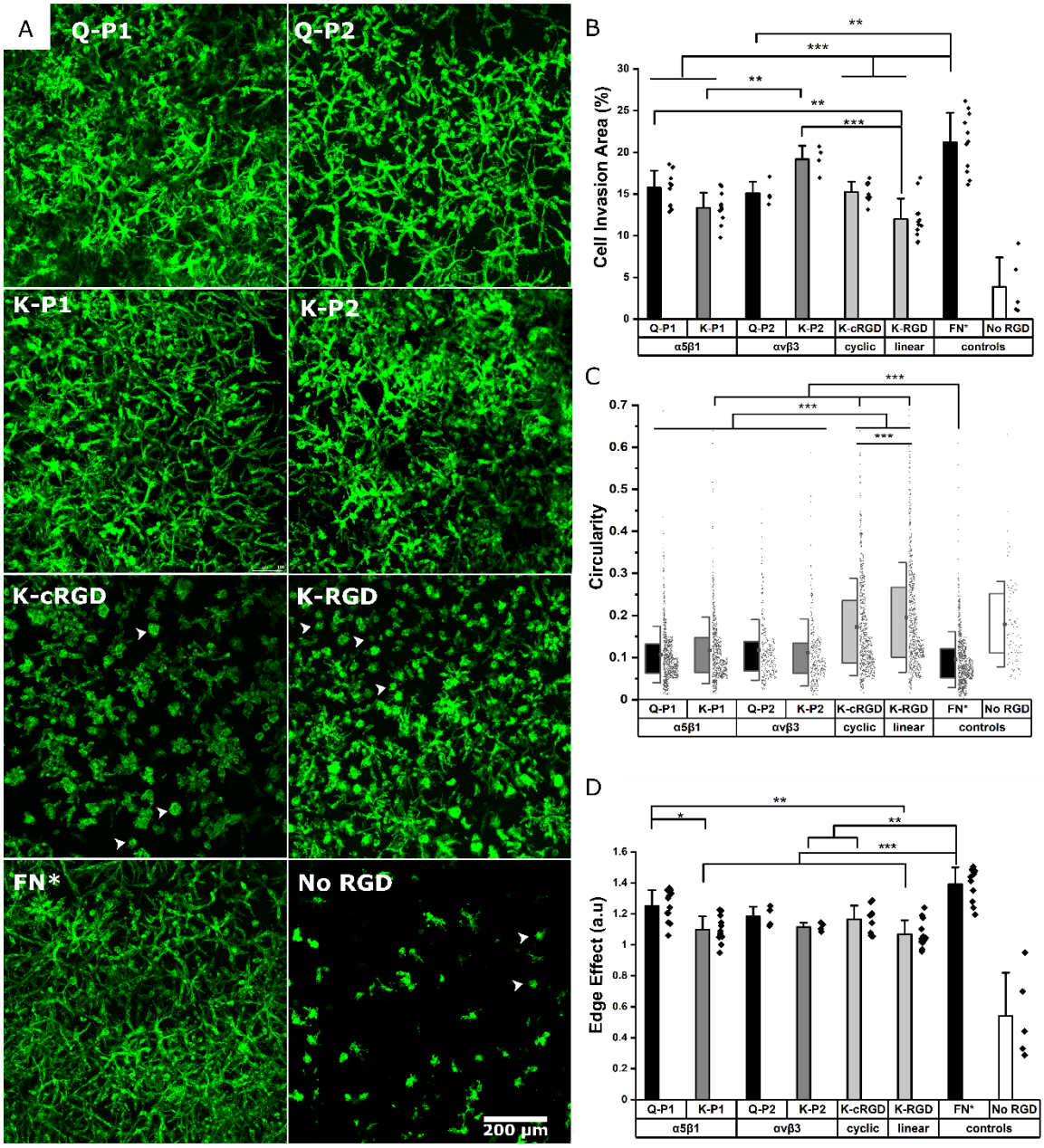

Figure 2. Different RGD peptides and fibronectin fragment influencing fibroblast spreading and growth in PEG gels. A) Mouse fibroblast cells immunostained for actin filaments in PEG hydrogels with bicyclic RGD peptides tethered via Q (Q-P1, Q-P2) or K (K-P1, K-P2) residues, monocyclic RGD (K-cRGD), linear RGD (K-RGD), fibronectin fragment FNIII9*-10/12-14 (FN*) and no RGD as control. White arrows

indicate circular non-spread cells B) z-stack of PEG hydrogels tethered with K-P2 represented color-coded depth profile of actin stained fibroblasts in 3D. B) Cell invasion area (%) of superimposed z-stack fluorescent micrographs. Quantification of shape factors using C) circularity, and D) edge effect of cells inside PEG gels modified with different RGD peptides. Data presented as mean + s.d. and statistical significance performed using one-way ANOVA with Bonferroni comparison (* $p < 0.05$; ** $p < 0.01$; *** $p < 0.001$).

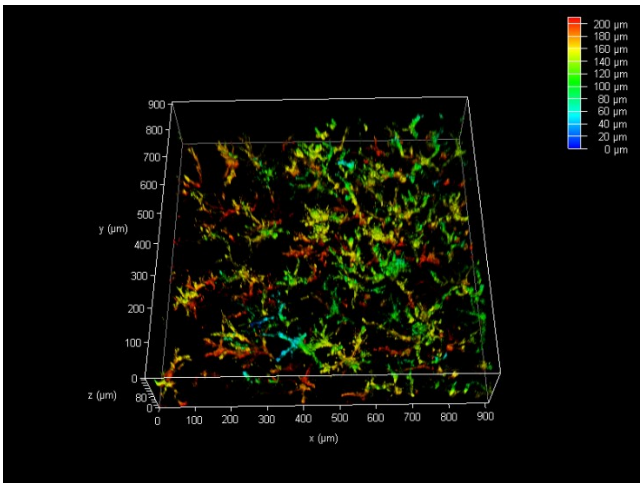

Figure 3. L929 fibroblasts were cultured in PEG hydrogels tethered with K-P2 RGD bicyclic peptide, fixed and immunostained for actin fluorescent markers, and imaged with a minimum z-stack size of 200 µm (color-coded), showing homogeneous cell distribution.

In parallel to the cell invasion area (%), which is a function of cell proliferation inside the hydrogels, the shape factors of the invading cells is investigated by quantifying the *circularity* and *edge effect* of the cells or cell clusters, which account for the shape, as well as the size of the cells. Since most of the hydrogel conditions support cell spreading, it is difficult to image single cells inside the network of fibroblasts. Hence, a c*ircularity* analysis tool **(Figure 6)** is employed to compute the perimeter of single cells or cell clusters. *Circularity* measures the irregular shape of spread cells and cell clusters, with a *circularity* of 1.0 indicating a rounded cell and a well-spread cell being represented by a circularity closer to 0. All bicyclic RGD peptides Q-P1, Q-P2, K-P1, and K-P2 show significantly lower *circularity* (0.10 to 0.12) compared to cyclic RGD (K-cRGD, 0.16)) and linear (K-RGD, 0.19; Q-RGD, 0.15) **(Figure 2c, Figure 5)**. FN* still has the lowest *circularity* (0.09), validating the high network-like cell spreading

observed in the fluorescent micrographs. No statistical difference in *circularity* is observed between the bicyclic peptides, inferring to the possible recruitment of multiple integrins during fibroblast cell adhesion and migration.

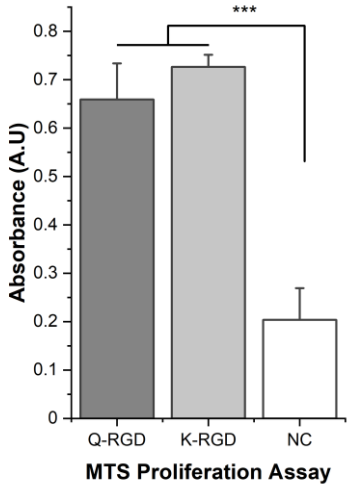

Figure 4. A similar RGD potency is observed between Q-RGD and K-RGD when a proliferation assay is performed with L929 fibroblasts cultured on thin PEG substrates coupled with Q-RGD (100 μM) or K-RGD (100 μM).

Multiple integrin receptors contribute during focal adhesion kinase mediated fibroblast migration, such as $\alpha_5\beta_1$ and $\alpha_4\beta_1$ playing a major role and $\alpha_v\beta_3$, $\alpha_v\beta_6$, and $\alpha_v\beta_8$ a minor role on fibronectin.[342] Similarly, the edge detection tool - *edge effect* - computes the 'perimeter' to 'square root of surface area' ratio, which is directly proportional to cell spreading **(Figure 2d, Figure 5 c)**. A higher ratio reflects more spread cells. However, if multiple cells are clustered together or cells in multiple planes are overlapping with one another in the superimposed images, an increase in cell area is associated with a reduction in the *edge effect* and an increase in *circularity* due to hidden perimeters inside the clusters. While circularity considers the shape factor, the edge effect in addition considers how much the cells are expressing local protrusions (**Figure 6a**). FN* showed the largest *edge effect* followed by bicyclic RGD peptides, Q-P1, Q-P2, and monocyclic K-cRGD peptides. A significant increase in *edge effect* is observed for bicyclic Q-P1 compared to the linear K-RGD. Similarly, a significant increase in *edge effect* is observed for FN* compared to the bicyclic K-P1,

K-P2, monocyclic K-cRGD, and linear K-RGD. Therefore, the combined reduction in *circularity* and increase in *edge effect* **(Figure 6 b)** demonstrate the higher cell spreading for bicyclic RGD peptides compared to linear and monocyclic RGD peptides.

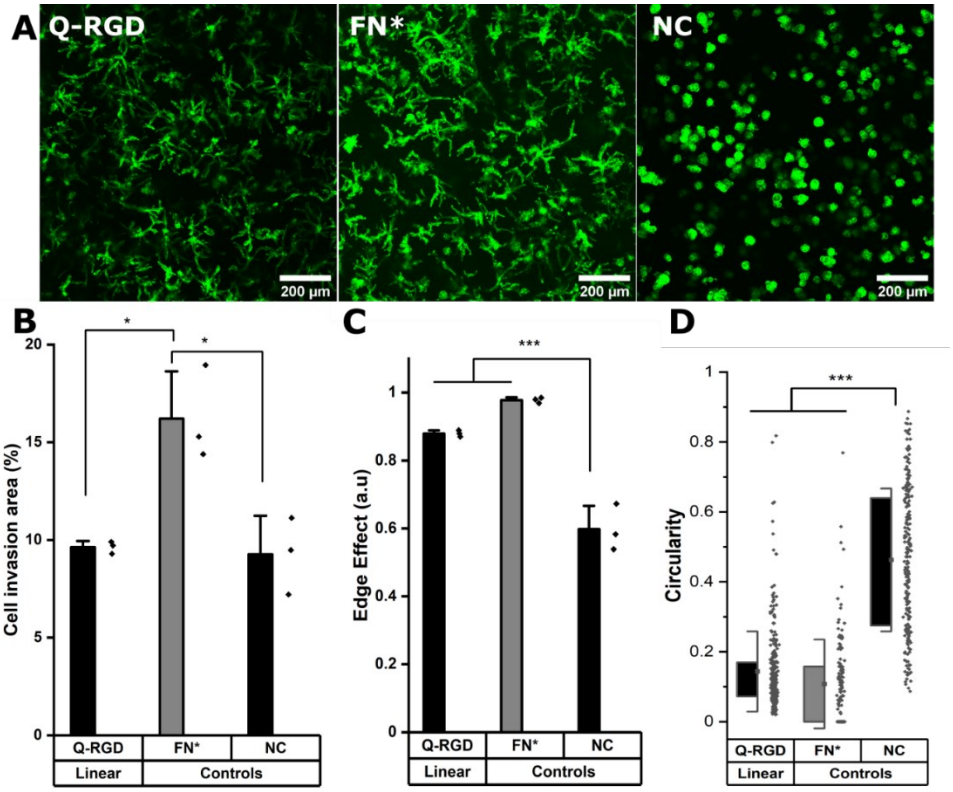

Figure 5. A) L929 cells encapsulated in PEG hydrogels tethered with Q-RGD and FN* showing actin filament (green) spreading across multiple planes in comparison to the negative control (NC) where the cells are predominantly rounded. B) Superior cell invasion is observed in FN* compared to Q-RGD and NC, however, the C) Edge effect and D) Circularity show that the cells are spreading well in Q-RGD and FN*.

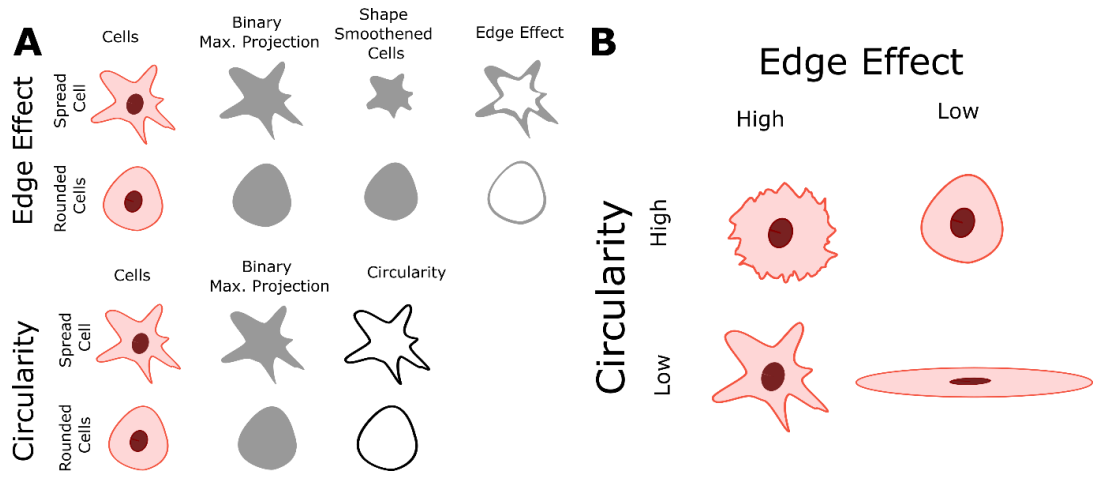

Figure 6. A) Schematic representation of stages in quantifying edge effect which is a combination of shape factor as well as the local protrusions, and circularity which measures the roundness of the cells. B) Interdependence of circularity and edge effect resulting in different cell morphologies relevant in 3D cell growth.

4.2.3 Influence of different degradable MMP sensitive domains on fibroblast growth.

To render the hydrogel degradable, MMP sensitive domains are incorporated in the arms of the PEG-K precursors. This enables on cell-demand hydrogel degradation as the cells secrete the enzymes needed to cleave the crosslinks. This creates physical space for the cells to migrate and proliferate.[331] PEG gels fabricated with di-cysteine K_1 or K_2 peptides as linear degradable crosslinkers previously reported an increase in cell invasion for K_2 in comparison to K_1 in the case of mouse myofibroblasts, owing to its high catalytic constant k_{cat} for MMP1 and MMP2.[22] Similarly, K_3 derived from Secreted Protein Acidic and Rich in Cysteine (SPARC) has been demonstrated to be degraded by plasmin, while its high k_{cat} enhanced cell invasion in PEG gels.[339] Here, the growth of mouse fibroblasts is investigated in bicyclic K-P2 RGD-modified PEG hydrogels depending on these three proteolytic sensitive domains (K_1, K_2, K_3), and compared to a non-degradable domain (K_{ND}) and no RGD. The fluorescent micrographs stained for actin (**Figure 7a**) and their corresponding cell invasion areas (%) (**Figure 7b**) indicate a significantly higher level of cell growth in PEG gels crosslinked with K_1 or K_2 (> 17.5 %) degradable domains and tethered with bicyclic K-P2 RGD peptide, when compared to their controls without RGD (< 13 %).

The lower levels of cell growth in K_1 and K_2 gels in the absence of RGD indicate that the cells partly try to rescue themselves by secreting both ECM proteins and proteases. These observations are in agreement with a previous report from our research group where an increase in native fibronectin production by fibroblast cells was observed in the presence of bioinert microgels inside 3D Anisogel, compared to RGD-functionalized microgels.[54] A low cell invasion area is observed for K_3 gels with (~ 13.5 %) and without (~ 2 %) K-P2 RGD peptide, with the K_3, no RGD showing exclusively rounded single cells in 3D. Although Patterson et al. reported improved cell invasion

in gels made with K_3 peptide, the results obtained here are not demonstrating enhanced cell growth.

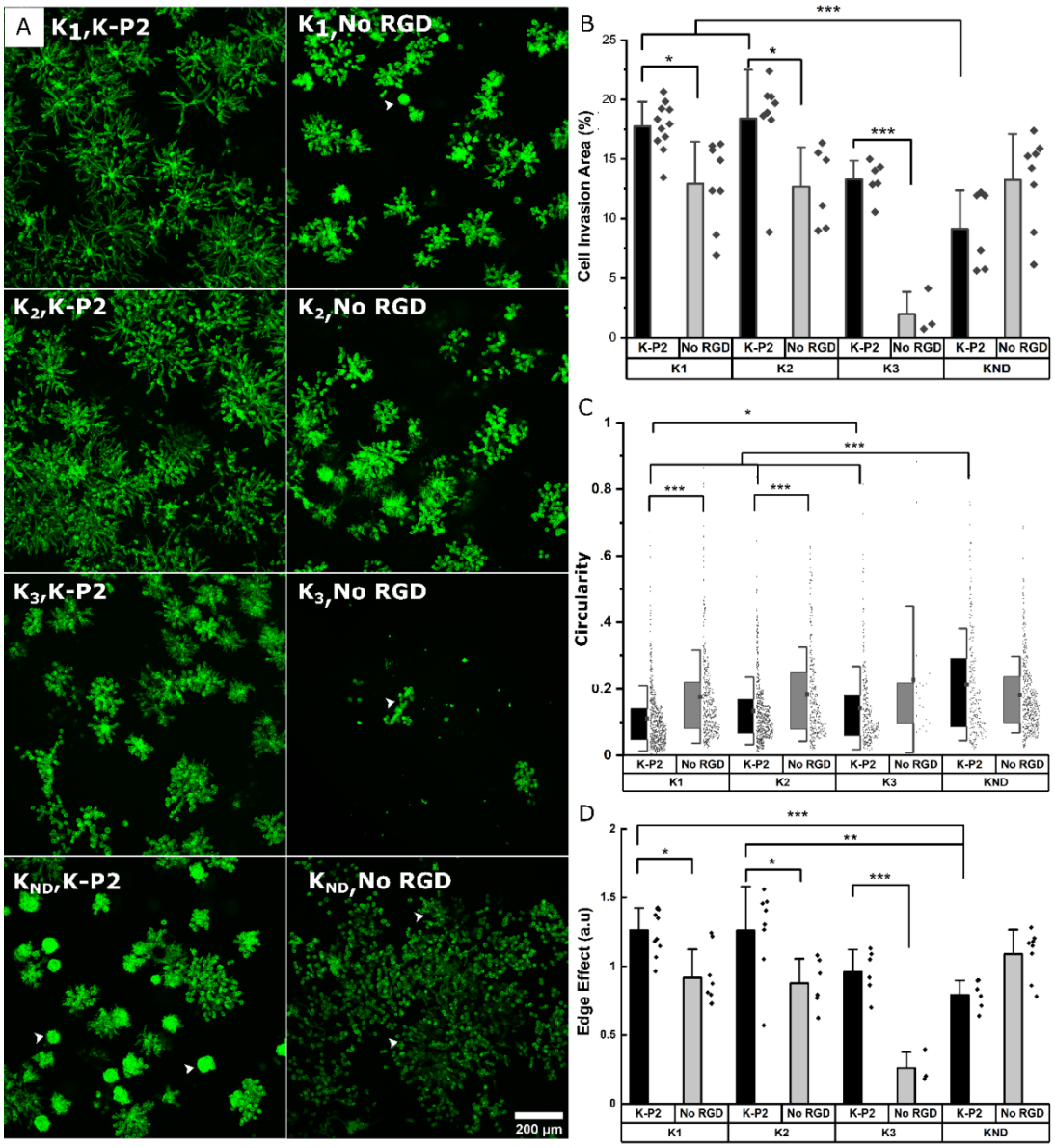

Figure 7. MMP sensitive domains influencing fibroblast growth in PEG gels. A) Mouse fibroblast cells immunostained for actin filaments in PEG hydrogels with different MMP sensitive domains (K1, K2, K3, and KND) and bio-functionalized with 100 µM bicyclic K-P2 RGD peptides or no RGD as control. B) Cell invasion area (%) of superimposed z-stack of fluorescent micrographs. Quantifying cell shape using C) circularity and D) edge effect tools. Data presented as mean + s.d. and statistical significance performed using one-way ANOVA with Bonferroni comparison (* $p < 0.05$; ** $p < 0.01$; *** $p < 0.001$).

The PEG gels prepared with K_{ND} show a low cell invasion area (%) and a high *circularity* (**Figure 7c**), indicating low cell spreading and moderate cell proliferation. However, in the presence of K-P2 RGD, the cells appear more clustered, which suggests that the presence of RGD does promote cell proliferation but due to lack of open space, spreading is limited. In the case of the edge effect **(Figure 7d)**, the hydrogels with degradable environment show higher edge effects for cells in gels modified with K-P2 compared to no RGD. Hydrogels with crosslinkers K1 and K2 have the highest edge effect offering a favourable environment for cell growth and spreading. Overall, the multi-parameter analysis reveals high fibroblast growth in hydrogels crosslinked with K_1 or K_2 degradable domains in the presence of bicyclic K-P2 RGD peptides, in comparison to K_3 and $K_{ND,}$ highlighting the importance of degradable domains in par with the cell adhesive ligands when developing artificial ECM scaffolds for functional cell growth.

4.2.4 Influence of RGD peptides on nerve growth

To study the effect of RGD peptides on nerve growth, DRGs are encapsulated in PEG precursors with a fixed RGD concentration of 100 μM. The explants are cultured in PEG-based hydrogels, modified with bicyclic RGD (K-P1, K-P2, Q-P1, Q-P2), linear RGD (K-RGD, Q-RGD, RGD), or monocyclic RGD (K-cRGD, c-RGD), and controls (no RGD, FN*) hydrogels. DRGs are cultured for 7 days, fixed, immunostained for β-tubulin fluorescent markers, and imaged with a minimum z-stack size of 200 μm (Figure 9). Neurite outgrowth (Figure 8a) is analyzed using an image processing platform developed in-house to compute the nerve length at half-maximum density and the longest distance travelled by nerve from the edge of the explant. The fluorescent micrographs of bicyclic RGD peptide (K-P1, K-P2) show superior nerve growth in length (at half-maximum density) (~ 600 μm) compared to monocyclic (K-cRGD, 420 μm) and linear (K-RGD, 270 μm), while comparable extension is observed among the bicyclic RGD peptides and FN* (520 μm).

Consistent with the bright field images, the negative controls without RGD show minimal innervation of the PEG gels. This can be rationalized by the production of ECM proteins and proteases as discussed in the previous section. To quantify nerve growth, the distance of neurite extensions from the edge of the DRG is measured radially, until the distance where the neurite density drops to half of the maximum density (Figure 8b). This reveals superior neurite growth in bicyclic RGD gels (K-P1, Q-P2, and K-P2) compared to the hydrogels, modified with linear RGD (K-RGD). Interestingly, neurite growth in gels, tethered with bicyclic RGD via K residues shows longer neurite extensions at half-maximum density compared to their corresponding bicyclic RGD peptides conjugated via Q residues.

Interestingly, this difference is only observed for bicyclic peptide selective towards $\alpha_5\beta_1$ whereas, no such major difference nerve growth is observed between bicyclic peptide selective for $\alpha_v\beta_3$. In addition, bicyclic RGD peptides with integrin selectivity towards $\alpha_5\beta_1$ or $\alpha_v\beta_3$ show significantly better nerve growth compared to bicyclic peptides with a scrambled secondary loop, which imparts integrin selectivity, highlighting the influence of integrin selectivity in nerve growth. Scrambled RGD peptides (RDG) in the first loop also lead to worsened neurite outgrowth. The neurite growth at half maxima for Q-RGD (~ 450 μm) is comparable to that of the monocyclic RGDs but is not significantly different than the two other linear RGD peptides. Enhanced neurite length at half-maximum density is observed for bicyclic RGD peptides (K-P1, Q-P2, K-P2) in comparison to our previously optimal condition FN* (5 μM)[25], however, no statistical significance is observed. Such enhanced nerve growth is likely attributed towards the spatial cyclic conformation of the RGD loop in combination with the integrin selective secondary loop.

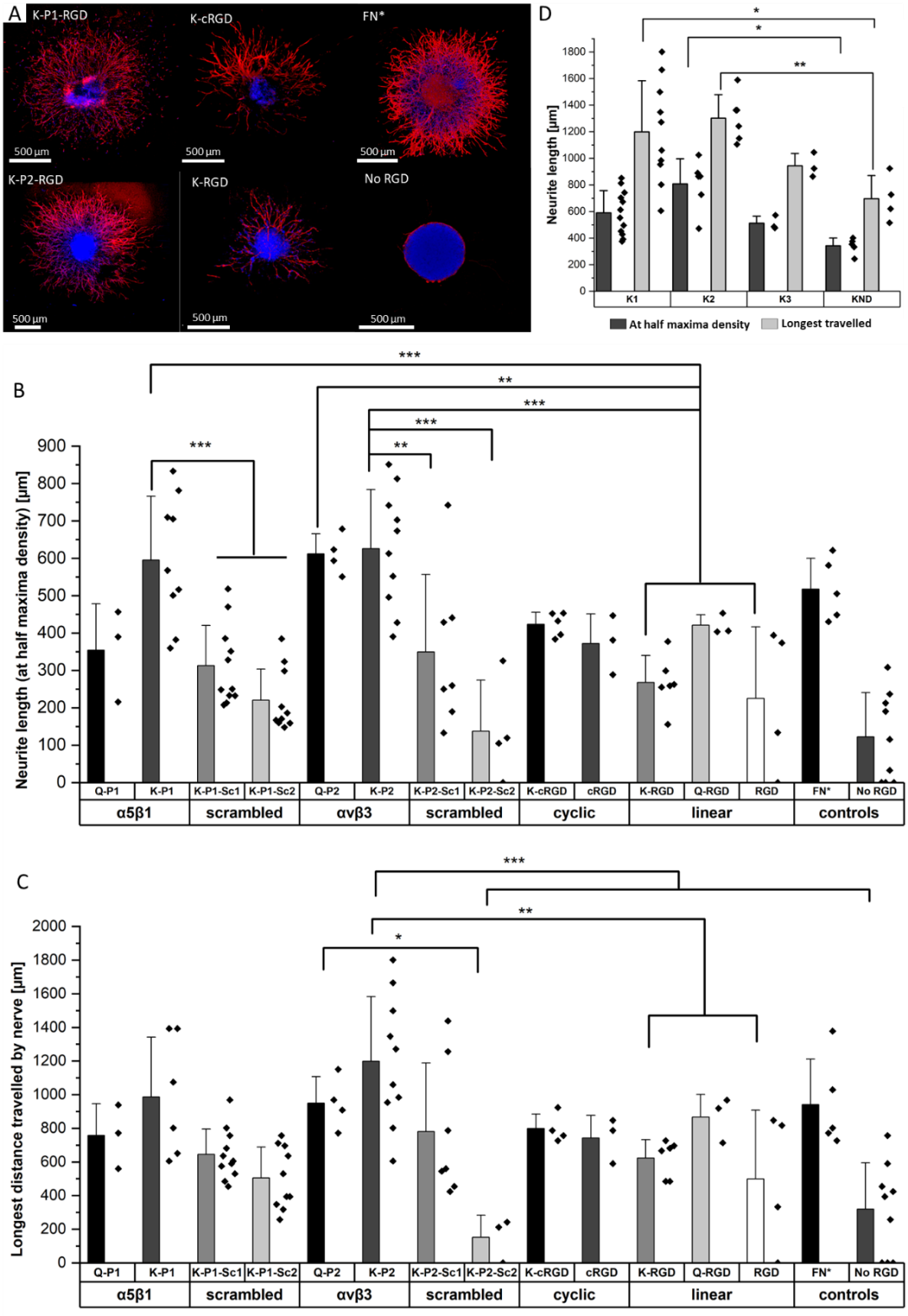

Figure 8. Innervation of PEG gels modified with different RGD peptides and MMP sensitive domains. A) Neurite outgrowth from DRGs in PEG hydrogels tethered with various RGD peptides, fibronectin fragment FN*, and full-length fibronectin. B) Neurite length at half-maximum density for different RGD peptides and its scrambled sequences, compared to FN*. C) Longest distance travelled by nerve for RGD peptides, compared to FN*. D) Neurite length

at half-maximum density and the longest distance travelled in PEG gels with different MMP sensitive domains (K1, K2, K3, and KND), and bio-functionalized with bicyclic K-P2 RGD peptides. Data presented as mean + s.d. and statistical significance performed using one-way ANOVA with Bonferroni comparison (* $p < 0.05$; ** $p < 0.01$; *** $p < 0.001$).

Next to the neurite length at half-maximum density, the longest distance travelled by nerve inside the gels is compared among the different RGD-tethered hydrogels **(Figure 8c)** with both parameters demonstrating similar trends. The longest neurite outgrowth distance (longest distance travelled by nerve) of ~ 1200 μm is observed for bicyclic RGD peptide (K-P2), selective for $\alpha_v\beta_3$ integrin subunits, which is significantly longer than for linear RGD peptides K-RGD (~ 600 μm) and RGD (~ 500 μm). These results are in compliance with our previous observations of dissociated DRGs cultured on 2D sPEG hydrogels, where a larger decrease in nerve growth is observed when α_v integrins are blocked relative to α_5 integrins, revealing the importance of α_v integrins in nerve growth. Similarly, integrin $\alpha_v\beta_3$ is reported to bind an RGD sequence in immunoglobulin Ig6 to promote neurite outgrowth in DRGs and retinal cells.[343] Also, cellular migration of avian neural crest cells involves interaction between integrin $\alpha_v\beta_3$ and vitronectin,[344] while an upregulation in $\alpha_v\beta_3$ is reported on astrocytes post-ischemia.[345]

4.2.5 Influence of degradable MMP sensitive domains on nerve growth

The different scaffold degradation domains are also investigated for neurite growth. Similar to the fibroblast culture, three proteolytic sensitive domains (K_1, K_2, K_3) and one non-degradable domain (K_{ND}) are investigated in hydrogels modified with bicyclic RGD peptides (K-P2) **(Figure 8d)**. The neurite length at half-maximum density in K-P2 tethered gels with K_1 and K_2 crosslinkers is significantly longer in comparison to K_{ND} gels with K-P2. Among K_1 and K_2 with K-P2, longer neurite growth is observed for K_2, however, no statistical significance between them is computed. Although K_3 is degradable by plasmin, it shows comparable nerve length to the non-degradable K_{ND}. In addition to neurite length at half-maximum density, the longest distance travelled by nerve is quantified for these gels, revealing a similar trend with

K_2 gels conjugated with K-P2 RGD with a distance travelled by ~ 1300 µm, followed by K_1 gels with K-P2 RGD with ~ 1200 µm **(Figure 8d)**. Both K_3 and K_{ND} hydrogels, conjugated with K-P2 RGD, enable their longest travelled nerve up to ~900 µm and ~700 µm, respectively.

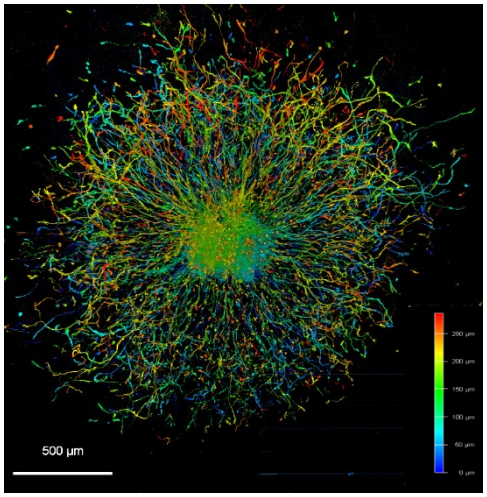

Figure 9. DRGs are cultured for 7 days in PEG hydrogels tethered with K-P2 RGD bicyclic peptide, fixed and immunostained for β-tubulin fluorescent markers, and imaged with a minimum z-stack size of 200 µm (color-coded).

4.2.6 Oriented nerve growth using anisometric magneto-responsive short PCL fibers

Among the investigated RGD bicyclic peptides and different proteolytically degradable domains, K-P2 RGD modified MMP-based K_2 PEG gels lead to the best nerve growth. Therefore, this combination is employed to prepare synthetic ANISOGELS with short magneto-responsive polycaprolactone (PCL) fibers (diameter of ~ 5 µm and length of ~ 50 µm), which are incorporated at a concentration of 1 v/v% and aligned in the presence of a low external magnetic field (50 mT) before crosslinking of the surrounding PEG gel.[25] The short anisometric fibers act as directional guidance cues, function as physical barriers, and induce mechanical anisotropy in the hydrogel to trigger nerves to grow parallel to their orientation, resulting in neurite alignment. K-P2-modified ANISOGELS are compared with linear (K-RGD) and fibronectin fragments (2µM, FN*) and their respective controls without short fibers. Magnetically oriented fibers resulted in highly aligned neurites **(Figure**

10a). The dimensions of the fibers and their innate surface properties are known to affect the cell adhesion and alignment of cells and nerves.[52,195] Neurite orientation is analyzed with defined anisometric orientation kernels resulting in a range of orientation distributions between -90° to +90°. K-P2, K-RGD, and FN* all have a narrow distribution of aligned nerve growth with maxima around 0° **(Figure 10b)**. Bright-field images superimposed with tubulin-stained (yellow) ANISOGELS show nerve growth along the direction of the fibers **(Figure 10c)**.

All of the ANISOGELS studied showed superior nerve alignment compared to their respective controls without oriented short fibers **(Figure 10d)**. ANISOGELS tethered with Bicyclic RGD (K-P2), linear RGD (K-RGD) and fibronectin fragment (2 μM, FN*) have comparable FWHM of ~ 80° with no statistical significance between them. We define that nerves are highly aligned when the FWHM < 90°.[53] These observations are consistent with our previous report on fully PEG-based ANISOGELS tethered with fibronectin fragments.[25]

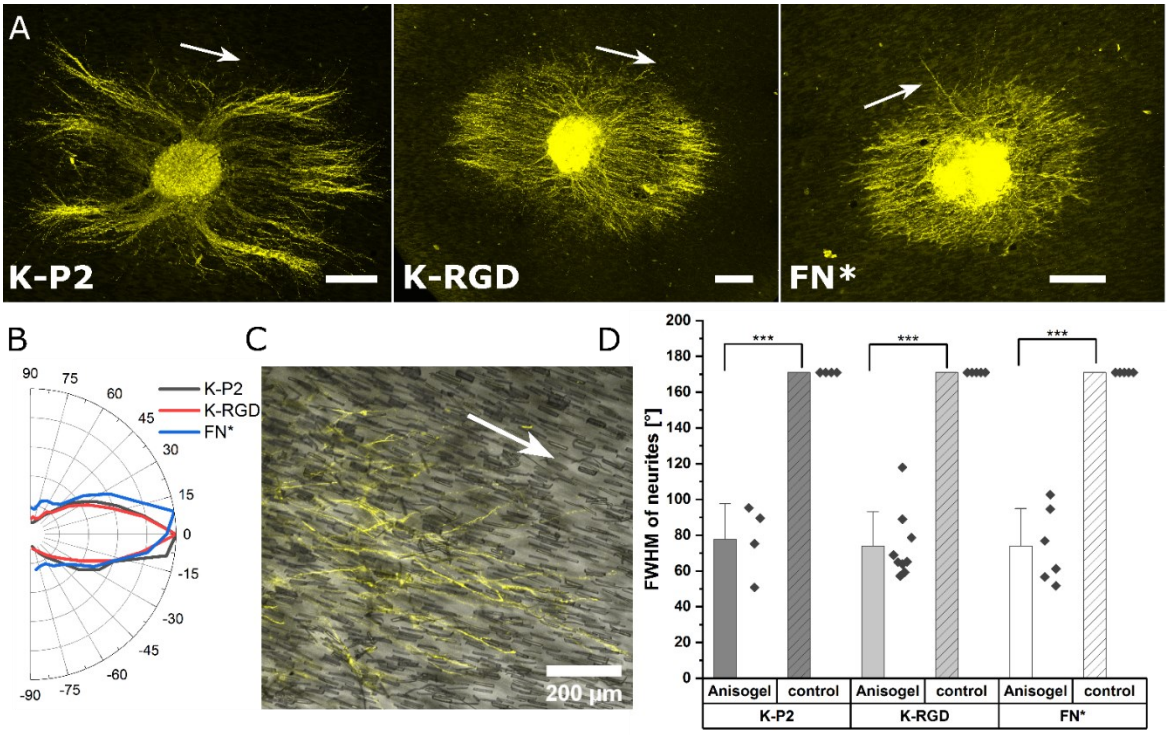

Figure 10. ANISOGELS to induce nerve alignment in bicyclic RGD peptide tethered PEG gels. A) DRG encapsulated in short fiber-based Anisogel, stained for β-tubulin

(yellow) in PEG hydrogels with K2 MMP degradable crosslinker in combination with bicyclic RGD peptides (K-P2), linear RGD peptides (K-RGD), and 2 μM fibronectin fragments (FN*), Scale bar 200 μm. White arrows indicate the direction of magnetically oriented fibers. B) Neurite distribution is plotted radially from 90 to -90° revealing narrow distribution for bicyclic, linear, and fibronectin fragments around 0°. C) Superimposed bright field and tubulin stained Anisogel with K-P2 revealing neurite alignment along the direction of the short anisometric PCL fibers. D) Full width at half-maxima (FWHM, °) is quantified for neurite orientation distribution in DRGs with (short fiber-Anisogel) and without (control) and plotted among different biomolecules.

4.3 Conclusions

PEG hydrogels crosslinked with proteolytically degradable domains and RGD bicyclic peptides selective towards integrin subunits are investigated to improve fibroblast growth and nerve extension inside synthetic PEG-based hydrogels. The short bicyclic RGD peptides are easily tethered to the PEG hydrogels via their amine or glutamine linkers. Fibroblast cells in 3D PEG gels show high network like formation compared to cells in gels tethered with linear and cyclic RGD peptides. The bicyclic peptides significantly enhance nerve growth (at half-maximum density) length (~ 600 μm) and the longest distance travelled (~ 1,200 μm) when compared to linear and mono-cyclic RGD peptides. In the case of nerve growth, the $\alpha_v\beta_3$ selective P2 bicyclic peptides slightly outperformed the engineered fibronectin fragment FNIII9*-10/12-14, however not significantly. Degradable MMP cleavable crosslinkers incorporated in the gels with bicyclic RGD peptides improve cell invasion for K_1 (GPQG↓IWGQ) and K_2 (VPMS↓MRGG) MMP degradable crosslinkers and a marginal increase in cell growth for both fibroblasts and nerves in the case of K_2. This report demonstrates for the first time the large potential of bicyclic RGD peptides inside PEG-based hydrogels, showing superior fibroblast and nerve growth compared to linear and monocyclic RGD peptides. Including oriented magneto-responsive short fibers inside bicyclic RGD-modified ANISOGELS demonstrates highly aligned nerve growth in the direction along the oriented fibers comparable to ANISOGELS modified with the fibronectin fragment.

4.4 Experimental Section

Fabrication of PEG gels. 8-arm 20 kDa PEG (Jenkem Technology, USA) is conjugated separately with two types of peptides, H-N**Q**E**Q**VSPLERCG-NH_2 (PEG-Q) and Ac-F**K**GG-GPQG↓IWGQ-ERCGNH_2 (PEG-K_1) or alternative MMP-sensitive domains (Pepscan, Netherlands) bearing conjugated Q and K amino acids, respectively. A stoichiometric ratio of 0.477 w/v % PEG-Q and 0.522 w/v % PEG-K is crosslinked in the presence of activated Factor XIII (20 U/mL, CSL Behring GmbH, 1250 U FXIII). Factor XIII is activated with thrombin (200 U/mL) buffered with 10 mM TRIS, 25 mM $CaCl_2$, and 150 mM NaCl for 30 min at 37 °C (briefly vortexing every 5 min). A buffer solution (10X, 0.1 M $CaCl_2$, 0.5 M Tris, 1.1 M NaCl) is used to regulate the osmotic pressure of the gel precursor. All RGD-based bio-functional cell adhesive peptides are coupled to the gel at 100 μM concentration of the final gel volume, resulting in a ratio of 1:24 between RGD peptides and total arms of star PEG molecules. In the case of complete peptide coupling, either 7.75% of the PEG-K arms would be tethered with RGD peptides or 8.46% of the PEG-Q arms, depending on the peptide domain used. The gels are incubated at 37 °C for 30 minutes for crosslinking and cultured in media.

Peptide synthesis. First, the linear RGD-sequences and other integrin-selectivity-promoting peptides are synthesized via Fmoc-based solid-phase peptide synthesis using a fully automated peptide synthesizer as described by Bernhagen et al. [109] Subsequently, these peptides are dissolved to 0.5 μM concentration in a 1:3 mixture of Acetonitrile (ACN) /MilliQ-water and mixed with ~1.1 equivalent of tris(bromomethyl) benzene (T3; dissolved in pure ACN at 10 mM concentration) until homogeneity, and left at room temperature for 1 h. Then, the reaction is quenched with 10% TFA/H2O to pH < 4 and the reaction mixture is purified via preparative HPLC, followed by lyophilization. All peptides were produced in PEPSCAN. B.V, the Netherlands.

Encapsulation of cells in 3D hydrogel scaffolds and cell culture. L929 mouse-derived fibroblasts cells (ATCC, Germany) and DRGs from 10 days old embryonic chicks are

harvested in RPMI and Hanks Balanced Salt Solution (HBSS, Gibco), respectively. In the case of single fibroblasts, the gel precursors are mixed with a pre-counted cell suspension in a defined volume, resulting in a cell concentration of 500/μL. Individual DRGs are embedded manually into the hydrogel precursors using tweezers. The cell encapsulated hydrogels or ANISOGELS are flipped every 10 minutes to ensure a homogeneous cell distribution and after 30 min, the gels are incubated with media at 37 °C to ensure complete precursor crosslinking before adding the media. The crosslinked gels are cultured for 7 days in RPMI basal medium, enriched with 10% Fetal Bovine Serum (FBS, Biowest) and 1% Antibiotic-Antimycotic (Gibco) for L929 cells and DMEM, enriched with 20 ng/mL nerve growth factor, 10% fetal bovine serum (FBS, Biowest) and 1% Antibiotic-Antimycotic (Gibco) in the case of DRGs. The media is exchanged every two days, and the cell-loaded gels are cultured at 37 °C, 5 % CO2, and at 95 % humidity.

Anisogel Fabrication. Short magneto-responsive rod-shaped fibers are produced via solvent-assisted spinning (SAS) based on previous reports.[52] A polymer solution with 17 w/v% polycaprolactone (PCL) is prepared by dissolving PCL in 50:50 v/v chloroform: acetic acid, while superparamagnetic iron oxide nanoparticles (SPIONS) are dispersed into the solution before SAS.[52] The fibers are collected on a cylindrical rotating drum and harvested for cryo-cutting at desirable lengths. The fiber concentration in the PEG hydrogel precursor solution is approximately 1 v/v%. The Anisogel precursor mixture is cast on a DRG between two magnets generating a field of ~ 50 mT. This enables the fibers to align parallel to the magnetic field lines during crosslinking of the surrounding PEG-based hydrogel. The bulk matrix around the aligned fibers is allowed to crosslink for 30 minutes at 37°C before adding more media.

3D immunofluorescent staining. All the incubation steps in this staining protocol are performed on a plate shaker (at 30 rpm) unless stated otherwise. Encapsulated cells in 3D gels are washed twice with PBS for 30 minutes and are fixed with 4% paraformaldehyde (PFA) in PBS for 1 h on a plate shaker. After fixing, the gels are

washed twice with PBS for 1 h and treated with 0.1% TritonX-100 for 40 minutes, and further washed twice with PBS for 1 h. For L929 fibroblasts, the gels are treated with iFluor- phalloidin 488 or 594 (Abcam, Germany) (1:1000) in PBS in combination with DAPI (1:100) and incubated for 4 h. The gels are washed twice with PBS for 1 h each and stored until imaging. The encapsulated DRGs in the gel are blocked with 5% bovine serum albumin (BSA) (Sigma, Germany) in PBS for 4 h, followed by the addition of primary Beta-tubulin antibody TUJ1 (BioLegend, USA) (1:250) in 5% BSA solution for 18 h. The gels are washed twice with PBS for 1 h before adding the secondary antibody Alexa Fluor 633 goat anti-mouse (Invitrogen, Germany) (1:1000) in PBS and DAPI (1:100). The secondary antibody solution is incubated for 4 h and washed twice for 1 h each and stored in PBS until imaging with confocal microscopy.

Imaging. Laser scanning confocal microscopy (SP8 Tandem Confocal, Leica Microsystems Inc.) is used to image the Z stacks of the cells encapsulated in the hydrogel. Air objective of 10X /0.3 N.A magnification is used to obtain fluorescent micrographs by exciting the fluorophores at different wavelengths and obtaining the emission signals at multiple channels.

Analysis of Fibroblast growth. The Z stack images are converted into a maximum projection image using FIJI image J after the background calculated with a rolling ball filter (size =20) has been subtracted. The image is then converted into an 8-bit image with an auto-Otsu threshold to convert the images to binary. These images are referred to as threshold images and the percentage of cell invasion areas is computed. Cell invasion here is quantified based on % of actin pixels per field of view or per image. This data can be a combination of cells that are spread, as well as rounded cells, taking cell proliferation into account. To obtain a smoothened image, the threshold images are further treated with a shape smoothening plugin (relative proportion fds=5, absolute number fds=5). The edge effect is analyzed using the formula:

$$Edge\ effect\ (\%) = \frac{Area\ (\%)\ of\ threshold\ cells - Area\ (\%)\ of\ smoothened\ cells}{\sqrt{Area\ (\%) of\ threshold\ cells}}$$

In addition, each cell or cell cluster is analyzed for its circularity, after applying the 'Otsu' threshold, the images are processed using a particle analyzer tool (FIJI, Image J) for particle sizes > 500 pixels. Hence, cells that are spreading well does not guarantee that they undergo similar proliferation and invasion rates. On the other hand, a large cell invasion does not always mean the cells are healthy and spreading. Cell invasion and the edge effect are both computed per field of view, while the circularity is measured for each cell or cell cluster. The data obtained from different gel conditions are compared and plotted in Origin.

Analysis of Neurite outgrowth. The Z stack images are converted into a maximum projection image using FIJI image J. The explant/core of the DRG is manually fitted into a mask and the position of the centroid of the mask is used as the center for radial analysis. The tubulin-stained images are Gauss smoothened with a window radius of 5.0 pixels and a width of 1.0 pixel. Power law dynamic compression/expansion is applied with power 0.5. The binary images subtracted with the explant mask are used for radial analysis. The number of non-zero pixels at subsequent radial distances from the center of the mask is computed. The number of non-zero pixels as a function of distance (radius) is obtained, which is further computed to get pixel density = pixels/unit area. Neurite growth at half-maximum density is computed by measuring the distance between the edge of the DRG explant and the distance at which the neurite density reaches half-maximum. The longest distance travelled by nerve is defined as the distance from the edge of the DRG explant until the pixel density < 0.001 pixels/μm^2 **(Figure 6)**.

The orientation of neurites inside a PEG-based Anisogel. Neurites stained for β-tubulin are imaged as z-stack. Neurite alignment is quantified inside the 3D hydrogel starting 10 μm above the first neurite in focus, starting from the bottom. A stack size

of 100 μm is imaged and the maximum z-projection is used for orientation analysis. The DRG core is converted into a mask to remove from the image during orientation analysis. Neurite orientation is quantified using an elliptical Mexican hat filter (a Laplace operator applied on an elliptic two-dimensional Gaussian function) as previously reported.[25] The orientation kernels are designed to account for only the neurite data, excluding non-specific stains. The angles of the orientation kernels are plotted as a histogram and the maxima are set to zero to compare the relative distributions among other neurite orientations and thus using the full width at half-maximum (FWHM) as a measure of the degree of alignment of neurites in the ANISOGELS. Based on our previous reports, lower FWHM [FWHM< 90°] indicates higher neurite alignment.[53]

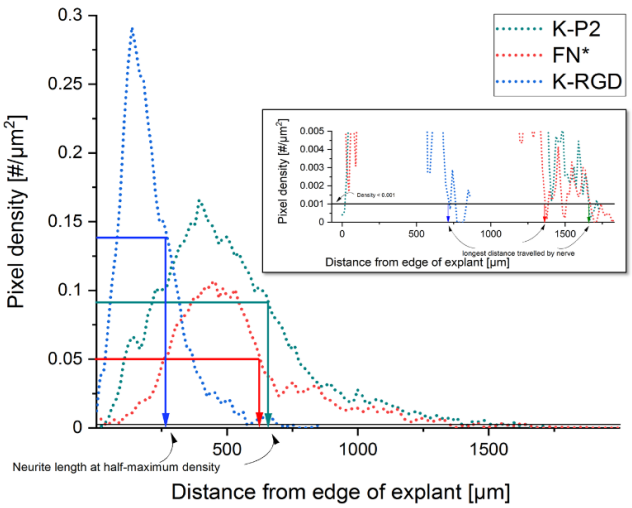

Figure 11. Analysis of neurite outgrowth using pixel density to compute the neurite length at half-maximum density and the longest distance travelled by nerve.

Statistics. Statistical analysis is performed in Origin 2016 for Windows. A one-way ANOVA is applied with p-values below 0.05 being considered significant in combination with Bonferroni correction.

4.5 Future Scope

In tissue engineering, creating macro-pores inside synthetic PEG hydrogels is desired to provide ample space for cell invasion in 3D.[346] Here, I attempted a preliminary study

to encapsulate degradable microgels (μgels) to mimic hollow cheese hole-like structures (**Figure 12a**). The μgels were produced using microfluidic techniques with a final gel concentration of 5 wt/vol% (**Figure 12b**) with a diameter of 75 μm. A simple click reaction between 6 arms 12K Vinyl-sulphonate functionalized PEG polymers and 6 arms sPEG 12k thiol functionalized polymers occurs in the microfluidic channels to produce spherical microgels. The μgels are produced with either 1mM GRGDSPC or kept inert without RGD. The novelty behind using Vinyl-sulphonate (VSate) μgels lies in their ability to degrade rapidly, resulting in bulky pores inside the surrounding gel. The composition of the surrounding gel employed here is 1 wt% PEG Q/K gels tethered with 100 μM K-P2 bicyclic RGD peptides. L929 mouse fibroblasts were encapsulated in the PEG Q/K gels at a cell concentration of 100,000 cells/ mL. While conditions with RGD tethered μgels showed no cell proliferation in the inert PEG Q/K gels (**Figure 12b**), the gels with inert μgels in PEG Q/K tethered with 100μM bicyclic RGD peptides showed drastic cell growth and proliferation (**Figure 12c**). Cells are stained for actin filaments and they appear to engulf the microgels, spread on the cell-microgel interface, and invade the hybrid hydrogel (**Figure 12 d,e**). While several internal reports revealed the toxicity of the degradation products from PEG-VSate, no such observations were made in this study. Further investigation is required to study the degradation kinetics of the PEG-VSate microgels. Such hybrid μgel in gel models enable the fabrication of hierarchical scaffolds with spherical and rod-shaped microgels induced pores available for tissue formation.

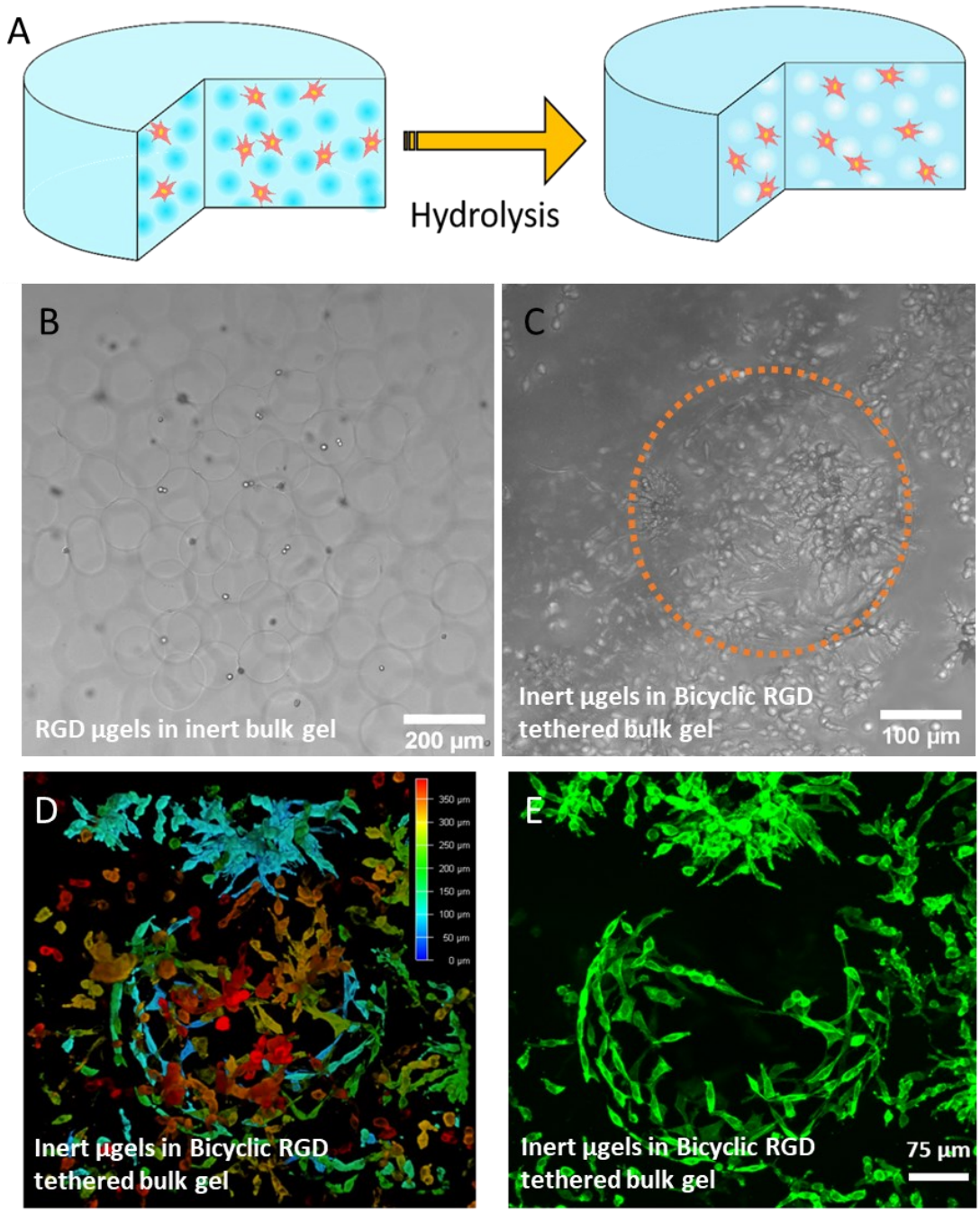

Figure 12. a) Degradable microgel embedded hydrogel platform to create macro-pores in scaffold on hydrolysis. b) Cells encapsulated in RGD tethered µgel inside inert PEG hydrogel. c) proliferating cells in inert µgels with bicyclic RGD functionalized surrounding PEG Q/K gels. d) Color-coded Z stack rendering e) actin stained images of cells engulfing microgels in 3D space.

Chapter 5. Interpenetrating Poly-Iso cyanide and PEG networks enable cell invasion

Sitara Vedaraman, Aron Kirschner, Max Schüler, Susan Babu, Kaizheng Liu, Paul Kouwer, Laura De Laporte

5.1 Introduction

While the native tissues in the body are complex, often dynamic, and possess non-linear mechanical properties which are difficult to mimic using elastic hydrogels[347], cells predominantly thrive in environments where they can actively manipulate and remodel their ECM by either digesting their local environment by producing proteases or deposition of endogenous proteins.[348] As previously discussed in **chapter 4**, PEG acts as a blank template that can be tuned for its wide biological and architectural properties. However, its innate homogeneous elastic properties fail to mimic the dynamic and reversible crosslinks that impart compartmentalized or gradient ECM properties to the cells.[113,349] Although stiffness is often used as a characteristic and representative property to understand mechanical properties, these static elastic or storage modulus values play little role in understanding dynamic cell-ECM interactions.[350]

Natural proteins such as collagen, and fibrin, offer a fibrous environment that is dynamically tunable and provide a cytoskeletal structure that imparts tensile forces during ECM probing, docking, and subsequently, cell adhesion and migration.[179,351] Such cellular mechanisms play a vital role in controlling cell proliferation and directing tissue repair, regeneration, or development.[13,352] The stress induced by cells alters fibrous ECM initiating the filaments to contract, resulting in stress propagation through the filaments to generate contraction-induced stiffness gradients.[353] Similarly, interaction with ECM triggers reaction pathways inside the cells. For example, by

mechano-sensing the stiffness of the ECM, cellular metabolism, and gene expression are regulated by shuttling proteins (YAP/TAZ, MRTFA) between the cytoplasm and nucleus.[354,355] In fibrous proteins, the non-linear elasticity allows transmission of forces over longer ranges, enabling long-distance cell-cell communications.[353] In the case of collagen matrices, a repetitive cycle of force generation by cells followed by collagen strain stiffening enables mechanical feedback between cells and ECM interactions, especially in tumor microenvironments.[351]

Investigating such responsive microenvironments led to the development of synthetic gels that possess biologically relevant features such as strain stiffening[356], stress relaxing[113], shear-thinning[357,358], or dynamic bonds[359]. Several materials are developed to recapitulate such dynamic environments using reversible bonds imparting self-healing properties. HA-based synthetic hydrogels enable non-covalent host-guest interactions and allow for shear thinning. Such unique properties enable injectability and further allow printing through extrusion.[357] Similarly, supramolecular hydrogels developed with non-covalent interactions are often reversible and adaptable to matrix remodeling. In one example, RGD functionalized ureido-pyrimidinone (UPy) groups as supramolecular building blocks assemble into fibrous hydrogels allowing cell invasion in 3D.[359] Such features support cell growth inside the hydrogel independent of pore size and its ability to degrade.[360,361] Unlike fibrous scaffolds, polysaccharide-based hydrogels impart stress relaxation properties that are biologically relevant. Chaudhuri et al. demonstrated that increasing the stress relaxation rate in alginate gels enabled MSCs to thrive and differentiate into specific lineages inside artificial ECMs.[113,114] While stress relaxation is known to dominate at shorter time scales involving integrin clustering and cell adhesion, strain stiffening is a time-independent characteristic that depends on forces applied by the cells after adhesion.[350]

Strain stiffening is a prominent feature observed in nature in semiflexible, filamentous proteins, where a linear relationship between stress and stiffness is observed below the critical stress. However, above this threshold, the matrices show a non-linear

stiffening response, often multiple times stiffer than their initial stiffness.[179] Similar to fibrin, soft tissues like cornea, lung parenchyma, and blood vessels become stiffer when increased strain is applied, preventing tissue damage.[362] While some systems are fully reversible when the strain is removed, predominantly, most systems are only partially reversible. The flexibility, persistence length, and nature of crosslinks in the filaments, play a significant role in altering the critical stress and the final matrix stiffness.[362] On the contrary, stiffening in matrices by applying external strain allows rearrangement of fibers parallel to the strain direction creating matrices for aligned tissue growth.[363] In this study, fibrin gels cultured with myoblasts and HUVECs showed oriented proliferation and lumen formation when uniaxial strains were applied.[364] Thus, the desire to replicate viscoelastic and biologically relevant properties brings us closer to developing synthetic alternatives bearing native properties.

This chapter investigates synthetic alternatives imparting mecahno-responsive properties using recently developed poly-iso-cyanide (PIC) based gels. These synthetic matrices are composed of PIC with oligo (ethylene glycol) side chains that self-assemble to form β-helical superstructures, which employ non-linear mechanics in mimicking fibrillar proteins.[120] The PIC fibers are composed of favorable 4_1 helical structures[365] of polymeric chains (**Figure 1a,b**) to form bundles. These filamentous polymers are tuned for their polymer contour length (L_c) and diameter to impart a wide range of tunable mechanical properties. The PIC bundles are strain stiffening which means that after certain critical stress, the hydrogel responds immediately by stiffening.[121,122] This phenomenon often occurs in the native ECM like actin and myosin filaments.[122]

When dissolved in solution, the PIC polymers form into the desired gels only above their transition temperature (T_{gel}) when the ethylene glycol substitution in the polymer becomes hydrophobic. The side chains of the PIC are modified with D-L-di-alanine with oligo (ethylene glycol), which are further stabilized by hydrogen bonds.[366] The length of PEG side chains influences the solubility and the lower critical

solution temperature (LCST).[367] Additionally, the length of the ethylene glycol side determines the gelation temperature of the polymer solution from 5 °C to 60 °C.[368] The PIC polymer bundles with tuned persistence length enable the formation of soft yet mechanically stable gels even at concentrations as low as 1 mg/mL or 0.1 wt/vol % with storage modulus starting from ~20 Pa onwards.[120] With an increase in the polymer concentration, a decrease in pore size is observed due to an increase in the number of polymer bundles rather than an increase in bundle diameter.[120]

Additionally, the PIC polymers are functionalized with biomolecules like RGD peptides[121] and are used in wound healing and 3D printing applications.[369,370] Analyzing the structural properties using 3D fluorescence imaging revealed heterogeneous pores with an average pore diameter between 1.8 μm to 3.7 μm and reported that the length of PIC polymer strongly affects the stiffness of the gels and has minimal influence on fiber architecture.[371] The PIC hydrogels are rendered bioactive for cell encapsulation and culture by incorporating RGD peptide motifs with controlled distances between adjacent RGD peptides.[118]

A study reported that MSCs differentiated into adipose cells with shorter PIC polymer at lower strain stiffening, whereas they differentiated into an osteogenic lineage with longer PIC polymer at higher strain stiffening microenvironment.[123] These hydrogels were exploited for their thermo-reversibility to harvest cells in vitro by cooling the material below its LCST.[123] Similarly, the cell functions such as spreading can be improved by lowering the critical stress of the PIC hydrogels resulting in a gel with a stronger stiffening.[118] While the PIC hydrogels have several advantages, their thermal reversibility to liquefy at a temperature below their LCST is a prominent disadvantage with *in vitro* models and demands constant storage above their LCST.

Bioinspired hybrid networks constituting PIC and biopolymers are developed to mimic biological networks. The combination of semiflexible and flexible polymers is reported to improve the mechanical properties of scaffolds. Jaspers *et al.* reported that the combination of PIC with synthetic materials bearing different persistence lengths

like stiff, semiflexible, or flexible materials to form independent double network composites imparted non-linear mechanical properties to the resulting hydrogels. While the PIC/ carbon nanotubes (CNT) showed the most strain response, the PIC/fibrin reduced stiffening due to fibrin's semiflexible polymers. For flexible acrylamide (AAm) networks, the resulting hydrogel with PIC/AAm shows the lowest stiffening response.[372] In another example, an extremely responsive hybrid network with pNIPAM and PIC was developed, which could increase its stiffness by 50-fold only by increasing the temperature by a few degrees. Such dynamically switchability in hybrid interpenetrating networks mimics myosin motor stress fibers.[122] In this Chapter, we combined the merits of PIC with the previously discussed PEG hydrogels (**Chapter 4**) as an interpenetrating network and observed a 2-fold increase in stiffness of the resulting gel compared to PIC and a 10-fold increase in comparison to PEG. With 2% strain and at 10 Hz frequency, the gel's stiffness was increased by 38%.

Combining polymers bearing different mechanical properties will bring us closer to developing biohybrid materials with linear and non-linear mechanical properties. Interpenetrating polymer networks (IPNs) are composed of 2 or more polymers independently forming a network within one another. As they do not form a covalent bond with one another and hence in most cases, retain their individual properties. Among the different types of IPNs, the sequential IPNs are formed when a hydrogel is swelled in another prepolymer or monomer with an activator solution, triggering the formation of two interpenetrating networks within one another. In such cases, the first polymer network is not hindered by the presence of the second network. However, the vice-versa is not valid. In the case of simultaneous IPN, two polymer networks are mixed to form independent networks within one another simultaneously.[124] In this chapter, I will apply a combination of the two systems to form an interpenetrating network (IPN) with PEG Q/K hydrogels (**Chapter 4**) and the optimized PIC hydrogels. The desired mechanical properties from the individual hydrogels are combined to create a synthetic hybrid artificial scaffold.

5.2 Results and Discussion

5.2.1 Characterization of PIC hydrogels for in vitro applications

The PIC prepolymers substituted with 1k and 2k Da ethylene glycol side chains were employed (Kouwer Lab, Radboud University, the Netherlands). The stable PIC hydrogels were fabricated between concentrations ranging from 1 mg/mL to 2 mg/mL with gelation triggered at around ~15° C (**Figure 1c**). The stiffness of the hydrogels was measured using a rheometer where the storage modulus G' ranged from ~20 Pa to ~150 Pa with an increase in PIC polymer concentration at 37°C. To incorporate biofunctional domains, RGD peptides were pre-functionalized to the PIC polymers at controlled distanced (d) (**Figure 1 a,b**).

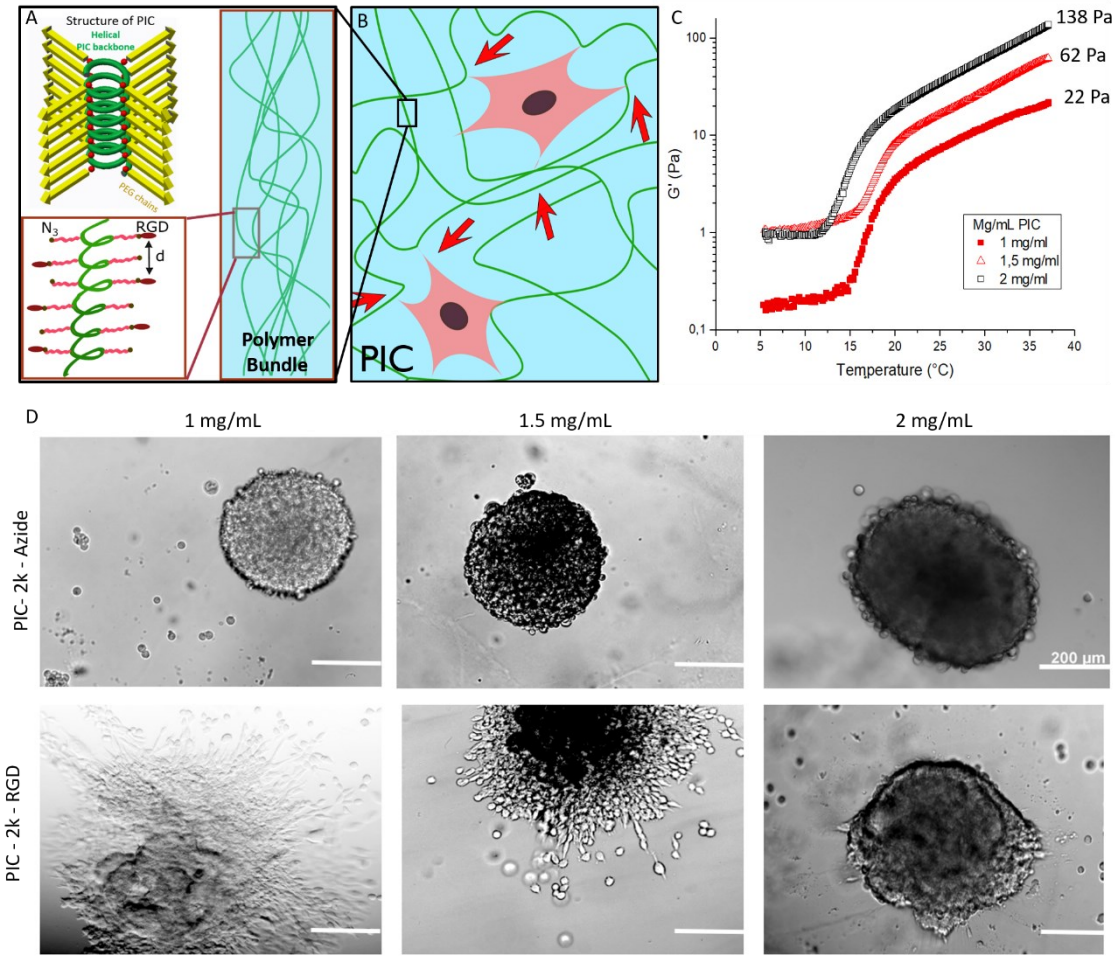

Figure 1. a) Schematic representation of 4_1 Helical PIC polymer bundles (green) with PEG side chains (yellow) inside a b) PIC hydrogels with cells. c) Rheology data showing storage modulus over temperature for PIC polymers with concentrations of 1, 1.5, and 2 mg/mL. d) Cell invasion by L929 cell spheroids (1500 cells/ spheroid) when encapsulated in PIC-azide (no biomolecule) and PIC-RGD hydrogels at different concentrations. No cell invasion into the gels was observed in all concentrations of PIC-azide, while an increase in the concentration of PIC RGD resulted in reduced cell invasion. 1mg/mL PIC-RGD was most suitable for cell invasion, migration, and proliferation.

Cell experiments were performed using L929 mouse fibroblast cell spheroids obtained using the hanging drop technique. The spheroids are encapsulated in a cold polymer precursor and then allowed to gel at 37°C for 30 minutes. This ensures uniform gel distribution around the spheroids. The fibroblast spheroids were cultured in 1 mg/mL, 1.5 mg/mL and 2 mg/mL PIC concentrations with and without RGD peptides. While cell invasion into the PIC gels was observed in bright field imaging for 1 and 1.5 mg/mL PIC hydrogels, a decrease in cell invasion was observed with increased PIC concentration. The negative controls with PIC- azide showed no cell invasion after 7 days of culture (**Figure 1d**). Hence the RGD bearing PIC polymer at 1 mg/mL was chosen as a basis for further experiments.

PIC hydrogels bearing different PEG polymer chain length (1k and 2k Da) at 1mg/mL was then used to encapsulate L929 cells. These cells were cultured for 7 days and stained for actin filaments. The fluorescent micrographs revealed improved cell invasion and proliferation in PIC-RGD hydrogels with 2k PEG side chains compared to 1k Da (**Figure 2 d,e**). The controls without RGD showed no cell growth and proliferation in 2k-Azide (N_3) except for mild filapodial protrusions (**Figure 2 b,c**). However, in PIC-1k- N3, minimal cell sprouting was observed despite the absence of RGD peptides (**Figure 2a**). A color-coded Z stack image reveals the uniform distribution of proliferating cells in 3D (**Figure 2f**).

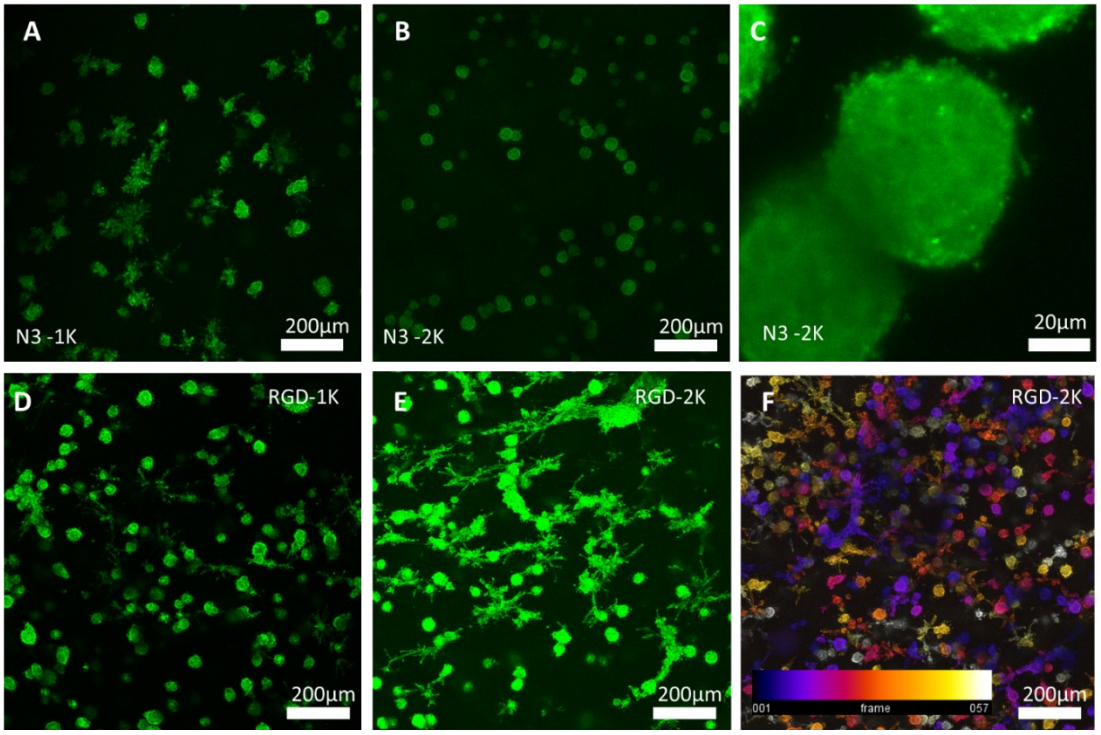

Figure 2. a) Immunostained maximum z-projections micrographs of L929 cells (500 cells/µL) suspended in PIC gels with linear oligo (ethylene oxide) chains of length 1k and 2k. a,b,c) The Actin stained micrographs show poor to no cell invasion by L929 cells when encapsulated in PIC-azide (N3, no biomolecule) 1k and 2k hydrogels. d,e) PIC-RGD hydrogels with different chain lengths, an increase in cell invasion is observed for PIC with 2k PEG side chains. f) A color-coded Z-stack represents cell invasion in all planes.

Although the gel fabrication and cell encapsulation with thermo-reversible PIC hydrogels were easy, the temperature sensitivity during fixing and staining resulted in the loss of several replicas posing difficulty in reproducibility. Hence an attempt to crosslink the PIC polymer bundles and stabilize the hydrogels was made by incorporating linear crosslinkers. PIC-2k polymer with acrylate functionalized terminal groups was employed to crosslink with linear di-thiol 2k-PEG crosslinkers. Rheology experiments were performed with temperature sweep on different molar combinations between thiol from crosslinker and acrylates from PIC. The temperature ramp triggered gelation at 15°C, which is consistent with experiments by Liu et al. The precursor mix was heated to 37°C for stable gel formation and cooled below gelation temperature (Tgel). With an increase in thiol concentration, we observed an increase in storage modulus at 5°C, below Tgel, indicating the Michael

Type addition between acrylates and PEG dithiol. At equimolar acrylate to thiol concentration, the PIC gels, upon cooling, retained a part of their initial stiffness (35 Pa) at 4°C. However, when decreasing the molar ratios of acrylate to thiol, the stiffness at 4°C gradually reduced to 1 Pa (**Figure 3**). Here we report in vitro crosslinking in PIC gels to alter the mechanical stability of the PIC hydrogels.

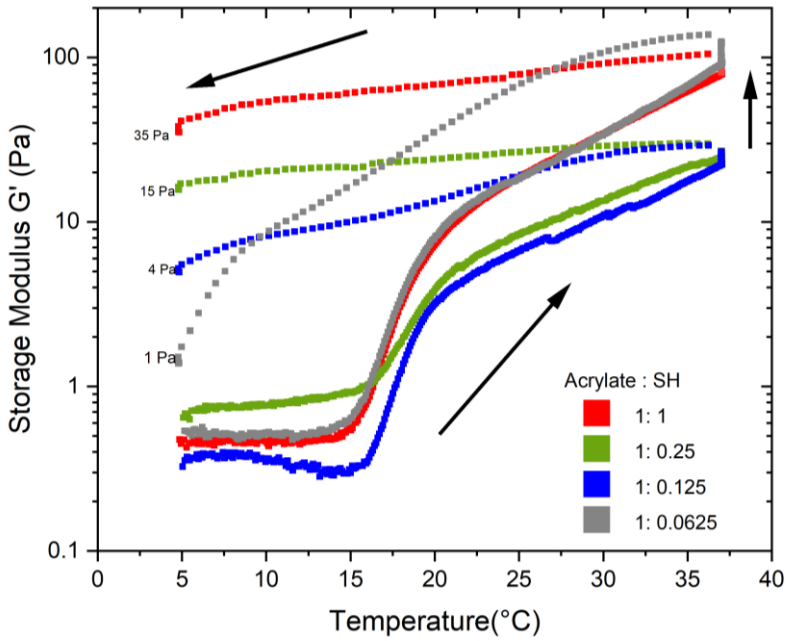

Figure 3. 1mg/mL of 2k-PIC Acrylate prepolymers are reacted with different stoichiometric ratios of linear PEG di-thiol. We observed an increase in storage modulus during the temperature ramp from 5°C to 37°C. The crosslinkers are allowed to react at pH 7.4 for 30 minutes and then a decreasing temperature ramp from 37°C to 5°C resulting in the retention of a part of the initial stiffness at 5 °C for a 1:1 ratio of thiol to acrylate.

Though this technique to crosslink the hydrogels improved its stability and shelf life, the production of PIC acrylate at RU Netherlands was not reproducible. Hence, we opted for an alternative technique to stabilize the gels using hybrid networks. Here we employed a combination of PIC and PEG hydrogels.

5.2.2 Characterization of interpenetrating networks (IPN) of PIC and PEG

Oscillatory rheology measurements were performed to evaluate the mechanical characteristics of 1 mg/mL of PIC, 10 mg/mL of PEG, and both in the IPN. For the IPN, an increase in storage modulus is observed when the temperature is raised from

5 °C to 37 °C with a gradient of 2 °C/min, and the gel is formed at T > ~15°C (**Figure 5a**), similar to the PIC control. Meanwhile, At 37°C, the PEG precursor initiates to crosslink enzymatically after 15 minutes. Though the gel precursor is mixed simultaneously, PIC hydrogels are formed first, followed by PEG gels inside the PIC scaffold. Though the PEG is not crosslinked, it is likely to pose a steric hindrance to the PIC prepolymers during bundle formation. Similarly, since the PIC bundles are already formed when the PEG is crosslinked, the PEG network is likely to be sterically hindered by the PIC bundles. The stiffness of the PIC, PEG, and IPN after 60 mins are 15 Pa, 70 Pa, and 190 Pa, respectively. A two-fold increase in the Hybrid-IPN compared to the PIC hydrogel and a 10-fold increase compared to the PEG hydrogel at 37°C (**Figure 5b**). The IPN-based hydrogels have a higher storage modulus than the cumulative stiffness of their components. It is important to note that though the weight fraction of PIC (1 mg/mL) is 1/10th of the PEG (10 mg/mL), it offers 5 folds higher storage modulus than PEG owing to their building blocks and ability to form bundles, unlike the PEG. Similarly, we observe the PIC hydrogels lose their integrity with a reverse temperature ramp while the PEG retains its stiffness at 10 Pa at 5°C (**Figure 5 c,d**). The differences between the heating and cooling curve for IPN networks demonstrate this characteristic (**Figure 6 a,b**). Like the PIC hydrogels, the IPNs are also strain stiffening in nature. The storage modulus of IPN at 1 and 2% strain is 275 Pa which is 27 times the PEG control and 2.5 folds PIC control at a similar strain (**Figure 6c**).

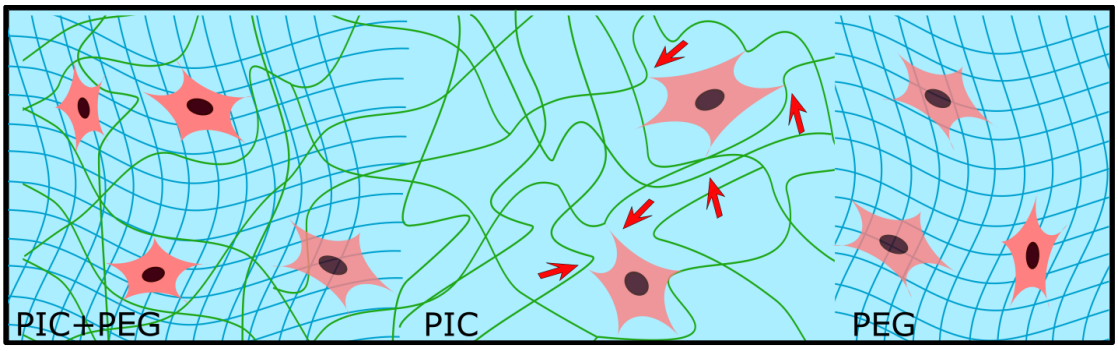

Figure 4. Schematic representation of two low polymer-containing gels combined to form interpenetrating networks to impart stability and improve mechanical properties.

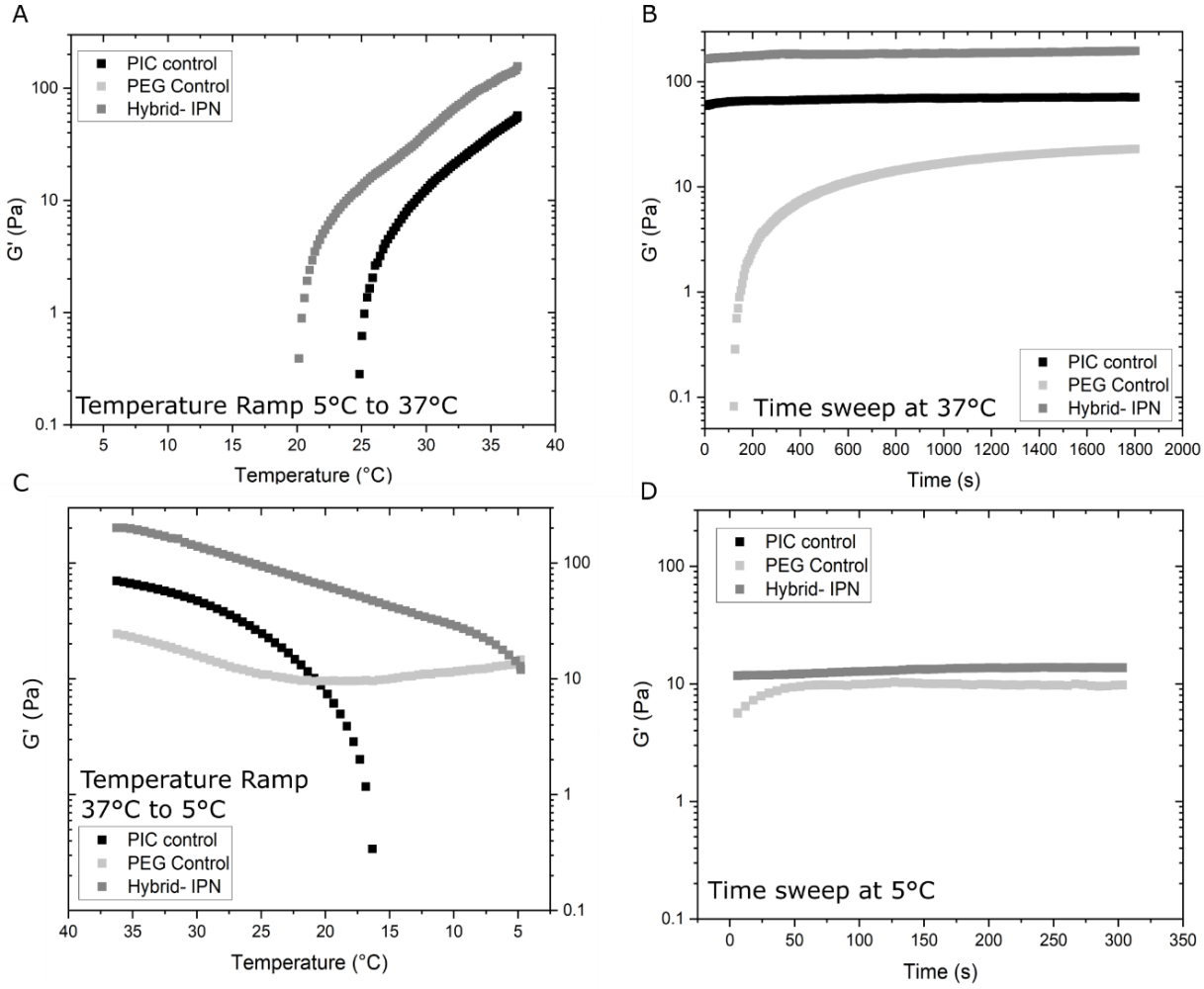

Figure 5. Mechanical Characterization of Hybrid-IPN. The results of oscillatory rheology on hybrid IPN hydrogels compared to 1 mg/mL PIC and 10 mg/mL PEG. There are four steps during this protocol, a) temperature ramp from 5°C to 37 °C, b) time sweep at 37 °C for 1h, c) reverse temperature ramp from 37°C to 5 °C, and d) a time sweep at 5°C for 5 minutes.

5.2.3 Influence of Interpenetrating networks on cell fate

L929 cells are encapsulated inside the PIC-PEG IPN to investigate the cell-material interaction. RGD peptides are used as biomolecules, and they are either tethered to the PEG Q/K gels or the backbone of the PIC polymers. In the case of negative controls without biomolecules, PEG without RGD and PIC with azide functionalized polymers were employed. The concentration of the biomolecules is kept constant at 100 μM. Several combinations of PIC-PEG IPN were formulated, encapsulating L929 fibroblasts. The cells were cultured in the IPN for 5 days, fixed, and stained for actin and DAPI (**Figure 7**). Most cell invasions were observed in IPN with RGD tethered to

both PIC and PEG, followed by IPN with RGD in PEG and then IPN with RGD in PIC. The images are analyzed for circularity of the cells, indicating if the cells are more spread (Circ~0) or more rounded (Circ ~ 1). When the cells thrive in a microenvironment, adherent cells are spread, forming tissues. The image analysis is consistent with visual interpretation with the lowest circularity for the IPN with RGD functionalized for both PIC and PEG. The least cell invasion is observed in PIC Azide, with no RGD having the highest circularity value (**Figure 7**).

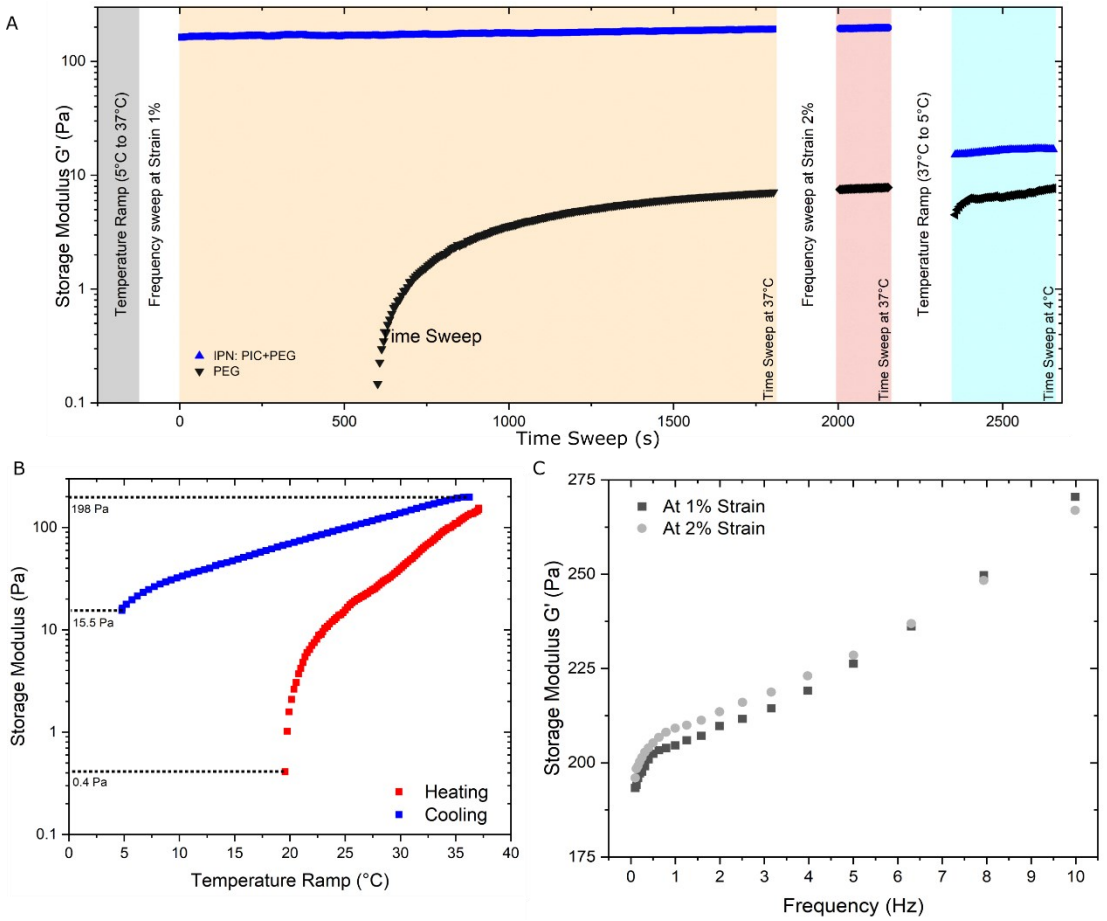

Figure 6. Mechanical Characterization of Hybrid-IPN. The results of oscillatory rheology on hybrid IPN hydrogels. The d There are 4 steps during this protocol, a) time sweep, b) Heating and cooling ramp at 4°C and 37°C, and c) frequency sweep at 1 and 2% Strain.

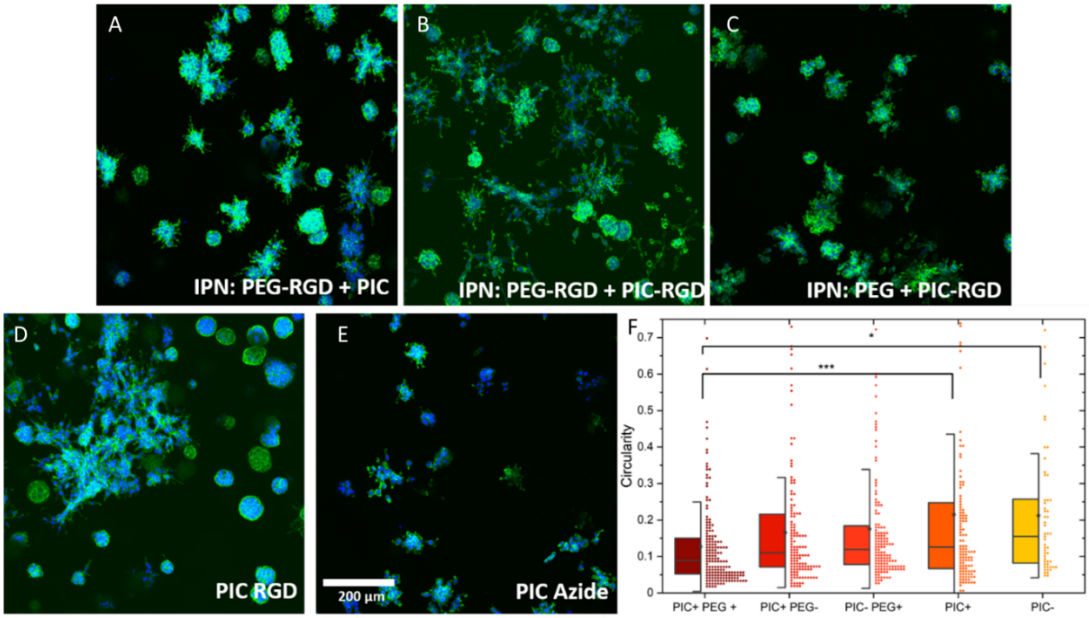

Figure 7. Actin stained micrographs of cells encapsulated in a-c) IPN consisting of PIC and PEG with RGD and controls such as d) PIC-RGD and e) PIC-N_3 (PIC-Azide). f) Circularity is analyzed for the cells revealing increased cell invasion in IPN with RGD tethered to PIC and PEG.

5.2.4 Innervation of PIC hydrogels

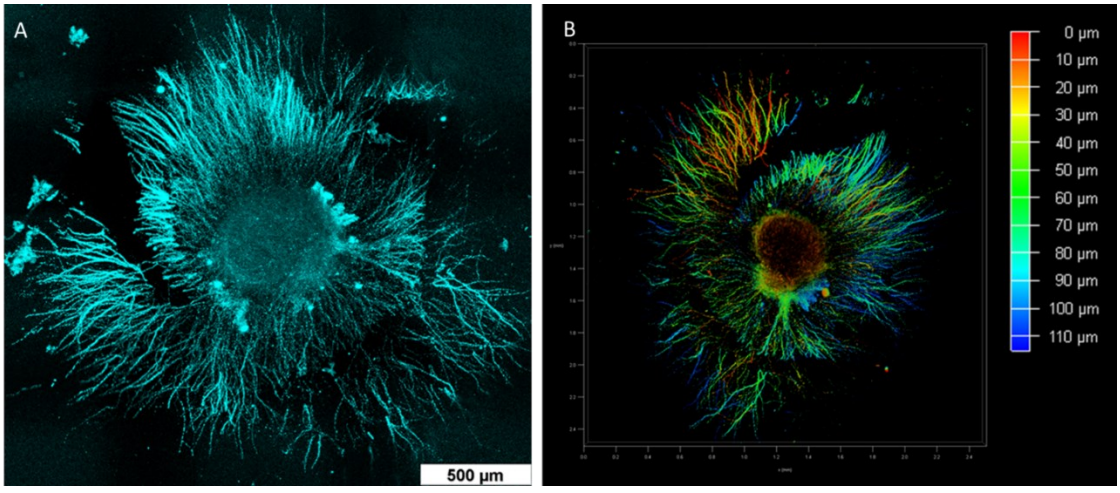

Figure 8. Tubulin-stained micrographs of DRGs encapsulated in 0.75 mg/mL PIC acrylate after 7 days of culture. Fibronectin was mixed inside the precursor gel to render the matrix biofunctional. In both images, the gels are observed to be broken due to the mechanical instability of the PIC hydrogels. b) Color-coded Z stack image revealing innervation in all planes up to a height of 120 µm.

DRGs from embryonic chick were encapsulated in PIC acrylates with 1μM Fibronectin as biochemical cues. Different PIC concentrations were tested starting from 0.75 mg/mL to 2mg/mL. Among them, neurite growth from DRGs was observed only in PIC acrylate with a concentration of 0.75 mg/mL. The tubulin-stained micrographs show long neurite extension of lengths >500 μm (**Figure 8a**), and the color-coded z stack show innervation along the z planes up to a height of 120 μm (**Figure 8b**). However, we observed the gels to be disintegrated in several regions due to their weak structural integrity. Since high PIC concentrations do not support nerve growth, IPN is a choice of material to support both cell growth and retain material integrity.

5.2.5 Development of PIC ANISOGELS

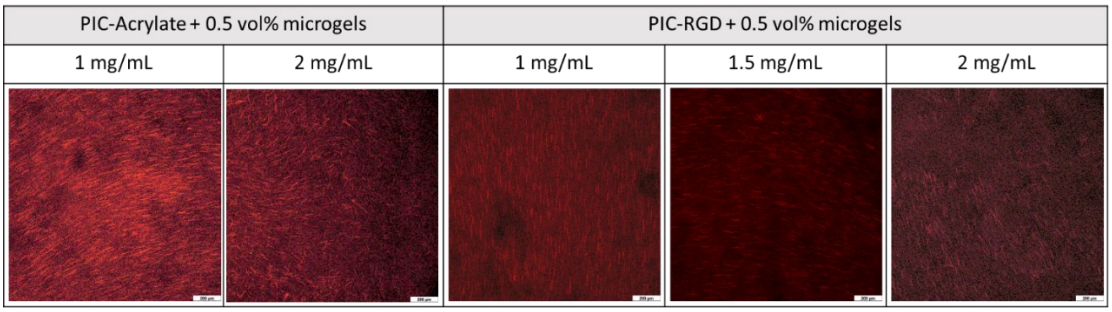

Figure 9. 2.5x2.5x25 μm microgels at 0.5 vol% concentration are encapsulated inside PIC acrylate and PIC RGD gels at concentrations ranging from 1mg/mL to 2 mg/mL unidirectional alignment along the direction of the magnetic field.

ANISOGELS were fabricated using microgels fabricated from PRINT techniques bearing the size 2.5x2.5x25 μm and encapsulated in PIC acrylate and PIC RGD-based hydrogels in the presence of a magnetic field. The rhodamine-labeled microgels imaged are oriented for all PIC concentrations (**Figure 9**); however, the degree of orientation is lower at higher PIC concentrations due to high precursor viscosity and rapid thermally induced gelation kinetics. This investigation allows us to formulate IPNs after optimizing the gelation kinetics to enable microgel orientation.

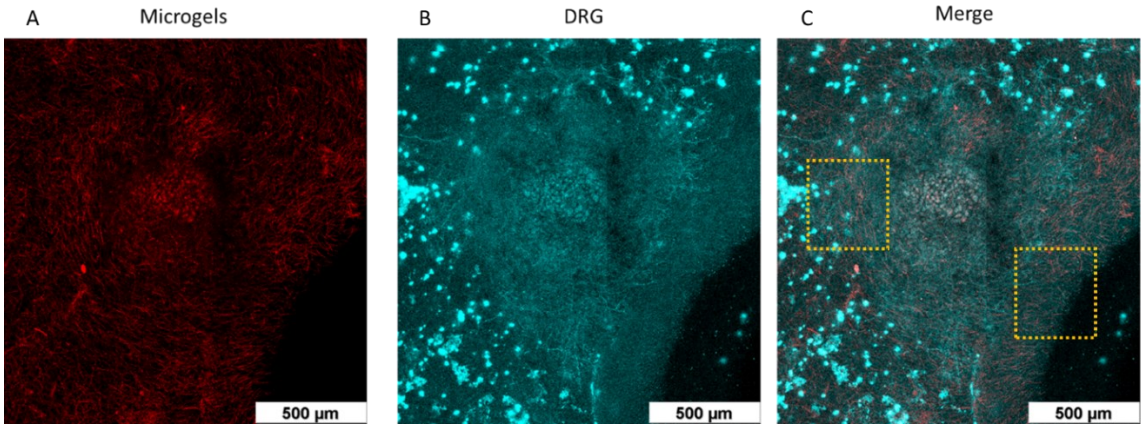

Figure 10. IPN formulated with PIC acrylates 1mg/mL and 1 wt/vol% PEG Q/K gels as ANISOGELS and cultured for 7 days. a) The microgels are stained for rhodamine b) the DRGs are stained for beta-tubulin showing nerve growth with low contrast to the background. c) The merged images of microgels and cells reveal that the cells are guided by the microgels locally, but no global direction is observed.

IPNs were formed using 1mg/mL PIC acrylates and 1 wt/vol% of PEG Q/K gels as ANISOGELS with 2.5x2.5x25 µm microgels in the presence of an external magnetic field of 100 mT (**Figure 10**). The immunostained micrographs reveal that the rhodamine-labeled microgels failed to orient along one primary direction (**Figure 10a**). However, the neurites in some regions were able to align locally along the direction of the microgels (**Figure 10 b,c**). Although the IPN-based ANISOGELS were able to stabilize the structure of the gel from disintegrating, the high viscosity and the gelation kinetics of the IPN could not orient microgels in one primary direction. Further investigation with a freshly prepared PIC batch is necessary to confirm the existing issues as often batch-to-batch variability of PIC is observed.

5.3 Conclusions

The native ECM is composed of properties like stress relaxation and strain stiffening, which synthetic PEG gels cannot reproduce. Hence, we employed PIC hydrogels which are thermo-reversible, strain stiffening, and cell compatible. To render the matrix viscoelastic and yet stable, IPN was developed by combing the merits of both PEG and PIC hydrogels. The hybrid hydrogel offers thermal stability from PEG while

offering strain stiffening properties of the PIC hydrogels. In vitro results with L929 fibroblast cells and nerve cells from DRGs revealed that cell invasion and neurite extension are both feasible in an optimized hydrogel composition. IPN bearing RGD peptides in both precursors showed increased fibroblast invasion in 3D than the PIC RGD alone. The IPN was translated into ANISOGELS by adding short anisometric microgels, which are magnetically orientable to create a viscoelastic synthetic oriented scaffold. Further investigation is required to comprehend the cell-material interactions of the IPN-based ANISOGELS.

5.4 Experimental Section

PIC polymers. Polyisocyanides were synthesized as previously reported.[118] Triethylene glycol functionalized isocyano-(D)-alanyl-(L)-alanine monomer (M1) and the corresponding azide-terminal monomer (M2) were copolymerized to form PIC polymers. The polymerization was done through nickel catalysis by changing the catalyst to monomer ratio, and the polymer's length was adjusted between 1k Da and 2k Da. After polymerization, the polymer was precipitated in a di-isopropyl ether, collected through centrifugation, dissolved in dichloromethane, and precipitated two more times before being air-dried.

RGD functionalization. GRGDS (H-Gly-Arg-Gly-Asp-Ser) was used to bio-functionalize the PIC polymers described in previous reports.[123] In short, GRGDS peptide is dissolved in a borate buffer (pH 8.4) at 6 mg ml^{-1} and mixed with a BCN-NHS in DMSO in a 1:1 ratio by continuous mixing for 24 hours at RT. Next, the azide functionalized polymer was separately dissolved in acetonitrile to achieve a concentration of 2.5 mg ml^{-1}. Next, the coupled BCN-GRGDS solution is mixed (at 95% molar equivalency of azide polymer) with the azide polymer and allowed to react for 24 h at RT. Finally, polymer-peptide conjugation was precipitated in di-isopropyl ether and air-dried for 24 h.

Rheology Measurements. The mechanical properties of the interpenetrating hydrogels were measured using a 20 mm stainless steel conical plate geometry (Discovery HR-3, TA instruments) with a fixed gap of 51 μm height or 74 μL volume gel was used to measure the storage and loss modulus of the hydrogels while crosslinking in situ. First, the polymer precursor is loaded on the cold Peltier plate at T= 5 °C, with a temperature ramp of 1°C/min until 37°C. The moduli were measured in the linear viscoelastic regime at strain at 1% and frequency = 1 Hz for 30 minutes to ensure complete crosslinking. Next, the hydrogel is subjected to oscillatory stress frequencies ω = 0.1 to 10 Hz at strains 1 % and 2 %. A second temperature ramp from 37 °C to 5 °C at 5 °/C is performed on the gels at strain 1 % and frequency 1 Hz. Finally, the moduli are measured again at 5 °C with a strain of 1 % and frequency of 1 Hz.

In vitro PIC hydrogel formulation. PIC polymers are weighed and dissolved overnight in water at the desired concentration at 4°C. The PIC polymers are always freshly prepared. L929 Mouse fibroblast (ATCC, Germany) cells suspended in RPMI media supplemented with 10% fetal calf serum (FCS, Biowest) and 1% Antibiotic-Antimycotic (AMB, Gibco) is encapsulated in a precursor mix of 10 mg/mL of PIC-RGD and 10 mg/mL of PEG-RGD. The gel precursors are mixed with a pre-counted cell suspension in a defined volume, resulting in a cell concentration of 500/μL. The controls are performed with and without RGD for both PIC and PEG. First, the precursor solution (at 5°C) is cast on a well plate (glass bottom IBIDI) at 37°C and allowed to crosslink further in the incubator for 30 minutes. The hydrogel is flipped every 5 minutes to ensure homogeneous suspension of cells inside. Next, the crosslinked hydrogel is supplemented with media (RPMI 1640, 10% FCS, 1% AMB) and cultured for 5 days at 37°C in a humidified atmosphere with 5% CO_2 with media is exchanged every two days.

3D Immunostaining. The encapsulated cells inside the hydrogel are washed with PBS for 30 minutes (twice, at 37° C) and subsequently fixed with 4% paraformaldehyde (PFA, 37°C) in PBS on a plate shaker for 1 h. After fixing, the gels are washed twice

with PBS for 30 minutes and treated with iFluor- phalloidin 488 or 594 (Abcam, Germany) (1:1000) in PBS in combination with DAPI (1:100) and incubated for 4 h. The gels are washed twice with PBS for 1 h each and stored until imaging with confocal microscopy. All the steps were performed at 37 °C under static conditions.

Imaging. Laser scanning confocal microscopy (SP8 Tandem Confocal, Leica Microsystems Inc.) is used to image the Z stacks of the cells encapsulated in the hydrogel. Air objective of 10X /0.3 NA magnification is used to obtain fluorescent micrographs by exciting the fluorophores at different wavelengths and obtaining the emission signals at multiple channels.

Cell morphology analysis. The Z stack confocal images are converted into a maximum projection using FIJI image J. The background calculated with a rolling ball filter (size =20) is subtracted, and the image is converted into an 8-bit image with an auto-Otsu threshold. Cell invasion is quantified based on % of actin pixels per field of view or image. Each cell or cell cluster is analyzed for its circularity using a particle analyzer tool (FIJI, Image J) for particle sizes > 500 pixels. Cell invasion is computed per field of view, while circularity is measured for each cell or cluster. The data obtained from different gel conditions are compared and plotted in Origin.

Statistical Analysis. Data points are shown as mean average with error bars indicating standard deviation with sample size ≥ 3. One-way ANOVA and pair comparisons using Bonferroni and Tukey's methods are performed to determine statistical significance, and the p values for statistical significance are represented with stars: * $p < 0.05$, ** $p < 0.01$. Statistical analysis is done using OriginPro 2020

Chapter 6. 3D photo-patterning hydrogels to incorporate biochemical ligands for directed cell growth

Sitara Vedaraman, Shreyas Ramakrishna, Aleeza Farrukh, Julian Hüffel, Delphine Blondel, María Aránzazu del Campo Bécares, Matthias Lutolf, Laura De Laporte

Spatio-temporal control over the aECM composition is essential to model hierarchical tissues, create injuries, pathological models and evaluate potential therapies. This is often achieved by in situ incorporating chemical gradients in the 3D aECM. Photo-patterning chemical ligands that impart biological cues to cells such as adhesion peptides, ECM proteins, or its protein fragments enable spatially control over cellular interaction with aECM promoting cell invasion and facilitating cell-cell interaction to achieve hierarchical tissue scaffolds artificially. To establish precise control over cell invasion in 3D, a mild enzymatic patterning technique is employed to locally tether cell adhesive biomolecules inside 3D PEG hydrogels. The mechanical properties of the hydrogel are optimized, and the biochemical gradient is created using light employing cues such as RGD, IKVAV, YIGSR, and fibronectin fragments to allow controlled cell invasion in 3D. This technique enables oriented cell growth, mimicking native tissue such as spinal niche, allowing to study its injury model and possible repair strategies or as ex vivo models, such as skin models.

6.1 Introduction

The development of hierarchical aECM often involves the incorporation of controlled heterogeneities that recapitulate features of the native tissue microenvironment with appropriate structural, biochemical, and architectural cues.[83] Popularly, the

patterning on substrates allowed the creation of chemical gradients of varied shapes that are often used as cell culture platforms created using soft lithography, photolithography[373], or electrochemical deposition[374]. However, such techniques do not mimic the native ECM as the patterns are created on planar or pseudo-3D substrates, as discussed in **chapter 1**. The ability to spatiotemporally control cell migration and growth is a crucial research area in developing biomimetic scaffolds. This level of control can be achieved by introducing spatial biochemical stimuli in combination with supportive mechanical stimuli.

Recently, photopatterning has become a popular technique to induce non-invasive, cell-friendly stimuli inside aECM[88,130,276]. This approach utilizes the principle of incorporating cell adhesive biochemical ligands in localized regions inside a hydrogel using light/laser.[128] Photo patterning of biochemical peptides and proteins inside three-dimensional hydrogels has been developed to control the interaction with specific cell types spatially.[158] This level of control enables the formation of artificial extracellular matrices (aECM) to create a biomimetic environment for the cells to form tissues[18]. Especially in synthetic hydrogels with homogenous microenvironments, chemical patterns permit the immobilization of proteins and peptides, creating local heterogeneity.[151] While a degradable micro-environment offers cells to create the physical space required for migration and proliferation,[22,375] photoablation degrades parts of the scaffold exposed to light allowing spatial control in cell invasion and migration inside 3D patterned regions.[376–378] Alternatively, photo-encapsulating cells, [379] or photopatterning of chemical cues[277,380] in a degradable environment enabled controlled cell invasion inside 3D PEG gels. Photo-patterning facilitated the formation of endothelialized channels in the presence of stromal cells enabling cells of multiple lineages to organize and co-culture in a controlled manner.[141] Biochemical patterning with light allows immobilizing biomolecules in defined volumes without altering the physical structure. A common issue is the formation of a necrotic core in aECM tissues due to a lack of blood vessels transporting oxygen and nutrients. Non-invasive chemical patterning offers a tangible solution

enabling spatial cell growth in 3D aECMs. For example, photo-protected RGD in PEG hydrogels allowed the formation of blood vessels during in vivo transdermal patterning using UV (350 nm- 365 nm).[147] To provide a platform to examine the disease, damage, and repair models, I further adapted a mild enzymatic patterning technique developed in the group of Prof. Matthias Lutof, to locally tether neuro-adhesive biomolecules inside poly (ethylene glycol) (PEG) hydrogels.[88] This platform involves photo-caged linkers binding to hydrogel backbone, allowing enzymatic crosslinking of biomolecules at the patterned region.[153,273]

Designing cell-specific biochemical ligands for creating spatial gradients is crucial for 3D photopatterned hydrogels. Peptides derived from ECM proteins like laminin and fibronectin are screened for cell growth.[381,382] While the relevance of RGD peptides is thoroughly investigated in **Chapter 4,** short laminin peptides (SLP) are explored and optimized for photo-patterning. It is essential to screen the SLP combinations and concentrations[377] for creating spatiotemporal adhesive biopatterns. IKVAV and YIGSR are used together with RGD peptides. The IKVAV peptide derived from the α chain has shown promising results for neural regeneration after spinal cord injury, with and without the combination with RGD, when incorporated in self-assembling peptides. Especially in its amphiphilic forms to induce alignment in nerve growth[383,384] and promote neurogenesis in adult neural stem cell cultures.[385] While the IKVAV pentapeptide is hydrophobic and unstable in aqueous environments resulting in aggregation, a 12-mer-I[K]VAV peptide with a caged motif tethered at the lysine is developed by Prof. Del Campo (INM Saarbrucken) to promote hydrolytic stability and enable photopatterning. The Caged I[K]VAV expresses cell adhesive ligands only on light irradiation at the desired wavelength promoting the growth of neural stem cells.[386]

Similarly, the pentapeptide YIGSR from the laminin β chain has been shown to inhibit metastases and promote cell attachment of human umbilical vein endothelial cells (HUVECs), human foreskin fibroblast (HFF), and human vascular smooth muscle cells

(HVSMC).[192] In the case of neuronal cells encapsulated in fibrin matrices, tethering a combination of YIGSR, IKVAV, RGD, and RNIAEIIKDI peptides stimulated increased neurite outgrowths from DRGs.[38] Protein fragments like FN-9*-10/12-14 are another class of biomolecules known to support cell adhesion and binding nerve growth factors such as brain-derived neurotrophic factor (BDNF) and neurotrophin-3 (NT-3).[387] 3D patterning such neuro-adhesive peptides opens avenues to guide neuronal and supporting cells, which require different engagement domains and growth factors inside an aECM. In this study, I engineered RGD, IKVAV, YIGSR, and fibronectin fragments-based biomolecules, which can enzymatically bind to the photoresponsive hydrogels imparting controlled spatial biochemical cues.

In this study, sPEG-VS and sPEG-MAL-based hydrogels were crosslinked with degradable linear peptides at physiological conditions via Michael-type addition. The 3D synthetic scaffold is rendered photosensitive by incorporating caged linker peptides, which are susceptible to light. The biomolecules are bound to the gels via a transglutaminase reaction between lysine and glutamine residues (**Chapter 4**). The hydrogel is optimized for its mechanical and biochemical properties to enable cell growth and proliferation for L929 fibroblasts. Two specific photo-patterning strategies involving the transglutaminase (TG) reaction mechanisms are investigated; caged lysine ([K]) peptides[88] and a novel reverse-engineered system with caged glutamine ([Q]) peptides. While a certain TG peptide sequence is essential for the biomolecules of interest (BOI) in the former, the latter can be applied with any BOI bearing a free primary amine. Similarly, optimal light irradiation conditions were tested to obtain biopatterns with high contrast with their surroundings. In vitro experiments with DRGs and fibroblasts revealed preferential migration of cells into the pattern region; however, cell migration in the surrounding matrices is also observed, inferring a lack in contrast between biopattern and its surrounding. Two-photon light patterning strategies are explored, and further investigation is necessary to conclude the results.

6.2 Results and Discussion

6.2.1 Optimization of neuro-adhesive peptides for photopatterning

A thin sPEG-NCO film coated on an amine-functionalized substrate enables amine-bearing biomolecules such as peptides or proteins to adhere as a monolayer. This platform enables rapid cell growth screening and enables viability assays (**Figure 1b**) on a 2D substrate. I employed this platform to determine the optimal concentration and combination of neuro-adhesive peptides such as RGD and YIGSR to grow dissociated primary embryonic chick DRG cells. The sPEG NCO stored in DMF is treated with water, and the terminal ends of the multi-arm PEG are converted to amine groups, which further reacts with the unreacted isocyanide terminal groups and forming a urea bond.[388] While some of the arms of the sPEG-NCO covalently bind to the amino groups on the well plates, the others are available to crosslink with one another and bind amine-bearing biomolecules. Hence a covalent immobilization of peptides is feasible on such thin sPEG-NCO films, and the initial challenge is finding the optimal concentrations for cell growth.

Several concentrations of RGD and YIGSR peptides were screened both in combination and individually. At 100 μm RGD concentration, prominent neurite growth was observed after three days of culture on the PEG films, and on staining for beta-tubulin, long thin neurites from the cell body were observed (**Figure 1a**). A combination of the equimolar ratio of the two peptides resulted in superior nerve growth. By systematically reducing the concentration of the peptides while maintaining the stoichiometric ratio, the lowest concentration that still supports nerve growth is 15 μM of YIGSR and 15 μM of RGD. Hence this combination was employed in the following study.

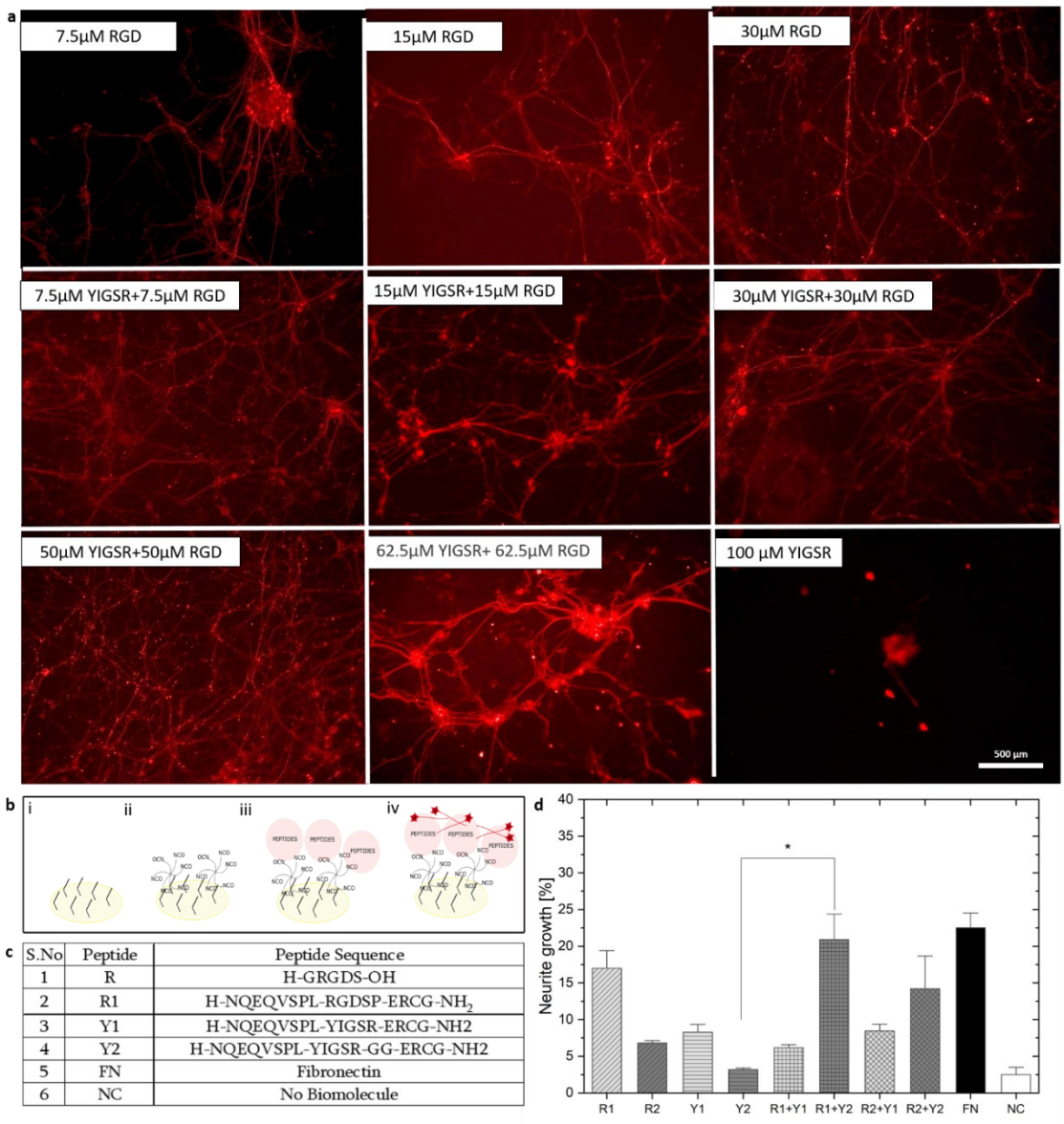

S.No	Peptide	Peptide Sequence
1	R	H-GRGDS-OH
2	R1	H-NQEQVSPL-RGDSP-ERCG-NH_2
3	Y1	H-NQEQVSPL-YIGSR-ERCG-NH2
4	Y2	H-NQEQVSPL-YIGSR-GG-ERCG-NH2
5	FN	Fibronectin
6	NC	No Biomolecule

Figure 1. Neurite extension on PEG film, coated with a) combinations of RGD and YIGSR and its control, b) Schematic representation of the substrate coating with biomolecules, c) tabulated peptide code and its corresponding sequence, and d) Percentage of the area of neural growth in films immobilized with different adhesion peptides.

To enable enzymatic photo-patterning, Mosiewicz et al., described the cell adhesive peptides require a specific transglutaminase sequence NQEQVSPL and a cysteine (C) to tether fluorophore to visualize the biomolecules. Thus, the peptides are designed with amino acid sequences NQEQVSPL-RGDSP-ERCG (NQRGD-2), NQEQVSPL-YIGSR-ERCG (NQYIGSR-1), and NQEQVSPL-YIGSR-GG-ERCG (NQYIGSR-2), where NQYIGSR bears a spacer between the NQEQVSPL and ERCG (**Figure 1c**).

These peptides are similarly immobilized on sPEG-NCO gels, and primary nerve cells were cultured for five days. The outgrowth was measured using ImageJ by estimating the area of nerve cell growth. The positive control (fibronectin 1μM) and GRGDS (15μM) show > 15% neurite outgrowth, whereas the NQYIGSR (15μM) and NQRGD (15μM) show less than 10% neurite outgrowth per field of view (**Figure 1 a, d**). NQ-RGD and NQ-YIGSR-2, however, show> 20% neurite outgrowth, and the combination of NQ-RGD and NQ-YIGSR-1 shows greater than 12.5% neurite outgrowth. Thus, proving immense scope for combining cell adhesive peptides for enhanced neural growth. These results are consistent with the reports from Schense et al., where they describe a synergistic effect when combining four different types of cell-adhesive peptides at equimolar concentrations .[38]

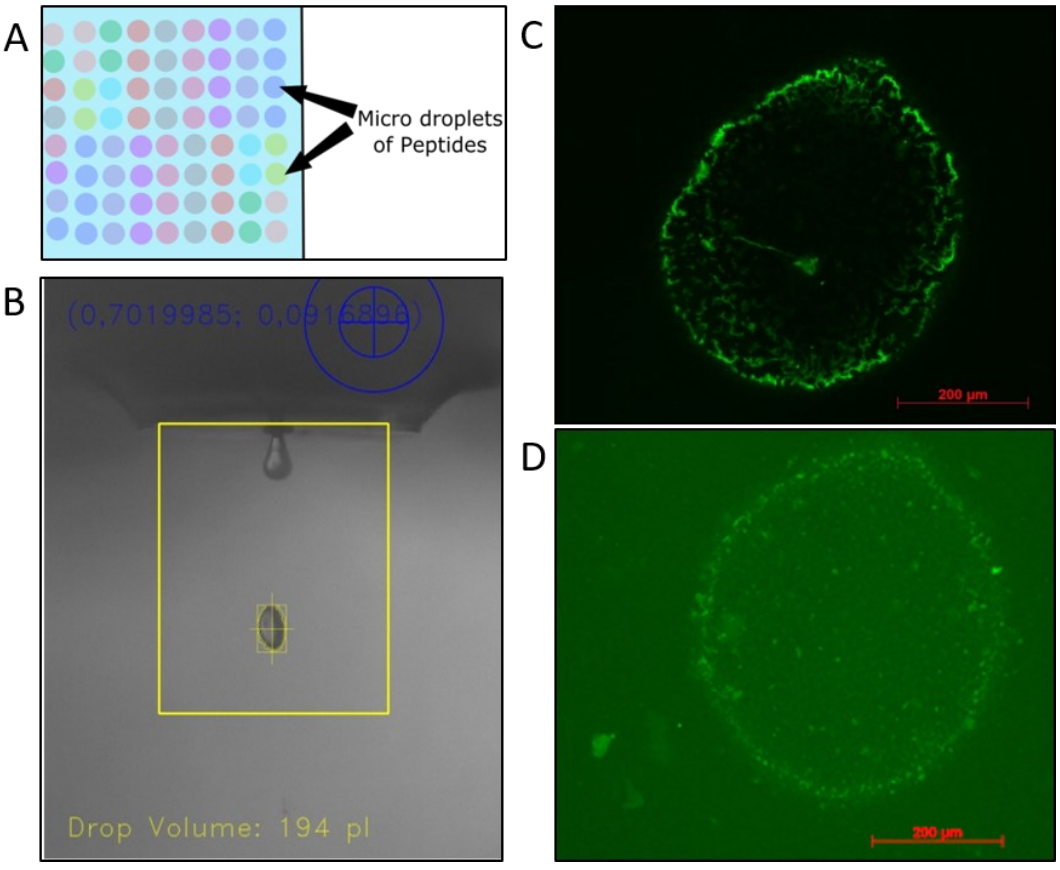

Figure 2. High throughput biomolecules screening platform using an automatic droplet dispenser. B) The droplets are optimized using a piezo dispenser to eject picolitre volumes. C) The biomolecules are labeled with a fluorescent dye are cast on a PEG-NCO thin film to obtain microspots. C) dried Peptide spot and D) hydrated peptide spot on PEG NCO films using optimized conditions.

The sPEG-NCO thin-film high-throughput screening platform allows rapid and customized biomolecule screening for cell adhesion and ECM production. These thin films can be obtained by spin coating or drop-casting between spacers on substrates functionalized with silane. The thickness was measured using ellipsometry, revealing the PEG film thickness between 5-8 μm. Combined with an automatic dispenser (Micro drop Technologies), an array of peptides coated surfaces in high throughput is obtained to screen biomolecules for a single population of cells (**Figure 2a**). I optimized parameters such as frequency of droplet release, number of drops per spot, and the volume of droplets (**Figure 2b**). As a proof of principle, Alexa Fluor Maleimide was used to label GRGDSPC using its cysteine terminals by Michael Type addition to visualize the peptide binding spot (**Figure 2 c,d**). The desired spot size of ~480 ± 10 μm was achieved at 150 Hz frequency, with 50 droplets of 194 pL per spot resulting in 9.7 nL of RGD binding to the PEG NCO substrate per spot (**Figure 2 c,d**). Further experiments to investigate cell response in sterile and aseptic conditions are desired.

A similar system was explored by Gobaa et al. to produce high throughput microarray by stamping biomolecules on partially crosslinked PEG hydrogels. In addition, they tested the influence of cell-cell interaction on the differentiation of MSCs into adipogenic.[257] PEG-NCO films offer a great potential to replace such expensive PEG hydrogels for 2D high-throughput cell screening. However, 2D platforms do not fairly recapitulate the native tissue niche; hence such platforms can be only applied for rapid screening purposes.

6.2.2 3D PEG hydrogel development for in vitro cell growth

20k Da, 4 arm star PEG polymers are crosslinked with MMP sensitive peptides at pH 7.4 and 37°C temperatures. The MMP peptide sequence is designed with di-thiol end groups to facilitate Michel-type addition on both the terminal ends. The middle part of the peptide sequence is similar to the collagen MMP site (**Table 1**), which is readily cleavable in cellular protease (**Figure 3a**).[339] The photolabile groups employed here are

caged lysine and caged glutamine peptides, which bear a cysteine to bind to the hydrogel. The PEG hydrogel allows tuning of mechanical properties by altering the PEG concentration, crosslinking density, degradable domains in the crosslinker, and concentration of adhesive peptides. To mimic the ECM of nerve tissues, soft gels are formulated with concentrations of 2.5 % to 4% wt/vol% of PEG to identify the desired range of stiffnesses. In the rheometer, the precursors are crosslinked in situ at 37°C for 2h. The stiffness was measured using a shear-inducing geometry to measure the storage modulus (G'). The G' varied from 30 Pa to 2000 Pa for the PEG concentration ranges mentioned above (**Figure 3b**). Hence the desired stiffness for 3D cell invasion for fibroblasts and later in nerve cells was chosen to be below 1 kPa. However, the super-soft gels like 2% PEG pose difficulty during photopatterning, and the addition of bioadhesive ligands like RGD peptides will also consume the PEG-VS arms, which will further cause a reduction in stiffness. Hence, the desirable stiffness range was between 3- 3.4% of PEG, consistent with previous reports that reported optimal cell invasion for MSCs at 3.4 wt/vol%.[153] Hence I applied this concentration to study different rheological parameters.

Table 1. List of MMP sequences applied in the study to optimize cell invasion in 3D

CROSSLINKER	PEPTIDE SEQUENCE	DEGRADABLE BY
16W1	Ac-GCRE**GPQG**↓**IWGQ**ERCG-NH_2	MMP-1/-2/-3/-8/-9
16W2	Ac-GCRE**VPMS**↓**MRGG**ERCG-NH_2	MMP-1/-2/-3/-7/-9 & MT1-MMP
16W3	Ac-GCRE**FPLR**↓**MRWD**ERCG-NH_2	MMP-1/-2, plasmin
16W4	Ac-GCRE**KKGH**↓**KLHL**ERCG-NH_2	MMP-2, plasmin
16WSc	Ac-GCRE**GDQGIAG**FERCG-NH_2	n.d.
HS-PEG-SH	HS-CH_2-(CH_2-CH_2-O)$_n$-CH_2-SH	n.d.

Different shear frequencies were applied to the hydrogel to measure the stability of the gel. The stiffness for a frequency sweep ranging from 0.1 Hz to 100 Hz (**Figure 3c**) revealed that the gels disintegrate only after 20 Hz, inferring a stable yet soft gel for cell applications. The gelation kinetics was measured by plotting the storage modus over time. The gels were formed within 30 minutes when no RGD was incorporated in the precursor solution. However, the crosslinking initiation for 3.4% PEG

hydrogels with 0.6 mM RGD at pH of 7.4 at 37°C was at 30 minutes, followed by a plateau in stiffness after completion of crosslinking around ~ 50 minutes (**Figure 3c**). Such slow crosslinking often results in sedimentation of the encapsulated cell during in vitro experiments. Hence it was essential to understand the role played by the addition of cysteine pendants (like RGD or caged peptides or linkers) in this PEG system (**Figure 3d**). As expected. An increase in caged K peptide drastically reduced the stiffness of the hydrogel with a maximum cysteine pendant concentration of 2mM (**Figure 3e**).

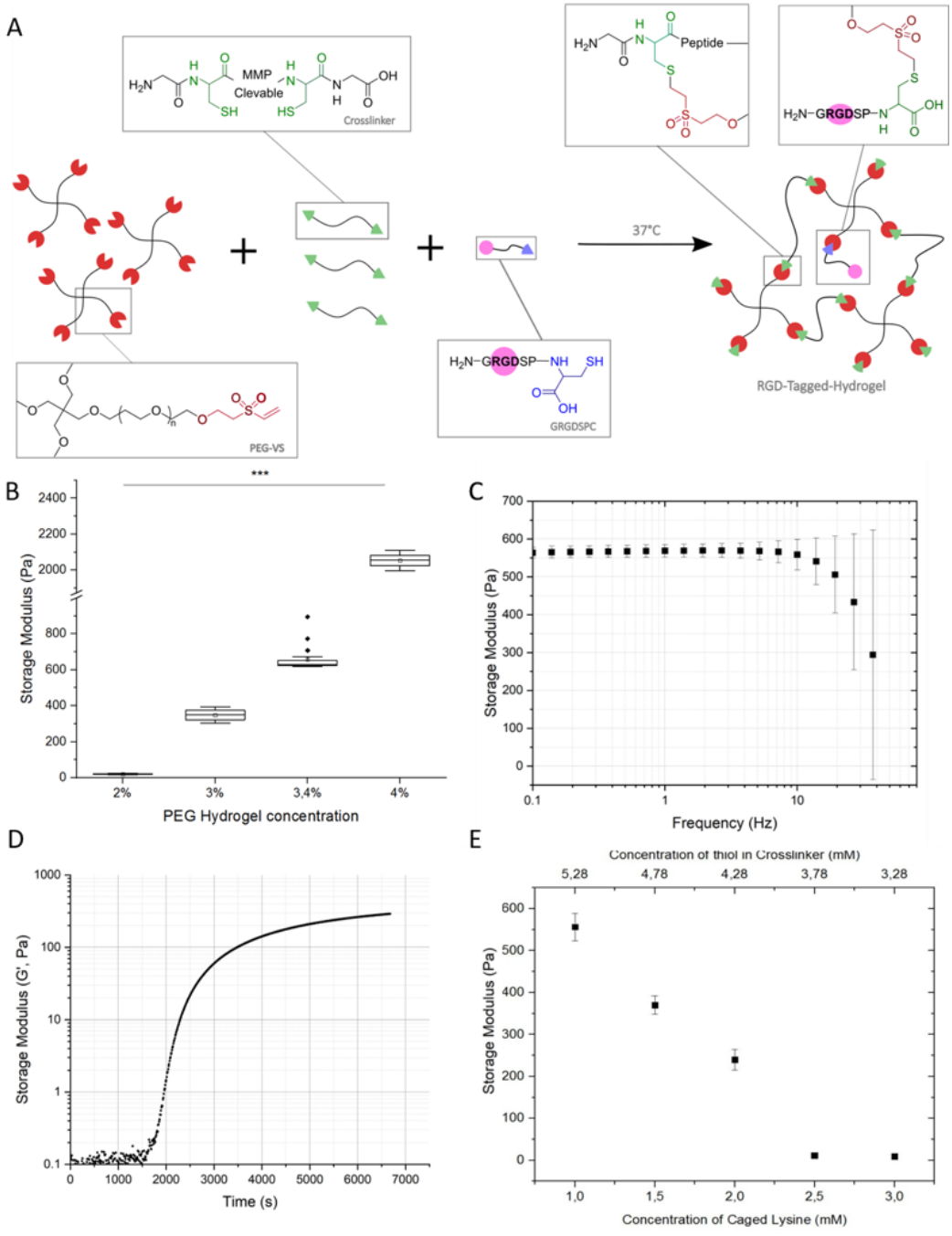

Figure 3. a) Schematic description of PEG VS with Linear di cysteine crosslinkers with RGD peptides binging via Michael type addition. b) Rheology measurement of Storage Modulus for PEG hydrogels from 2 wt% to 4%. C) The stability of gels at 3.4 wt/vol % is realized by measuring the storage modulus over different frequencies. D) The gelation kinetics of the hydrogel is obtained from Storage modulus vs. time at 37°C, where the crosslinking is initiated at 20 minutes and completed when reaching a plateau at 50 mins for 3.4% PEG with 0.6 mM RGD. E) A decrease in storage modulus of the hydrogels was observed with increase in the cysteine pendant concentration. Data presented as average ± s.d.

In vitro experiments were performed to test the cell response in the optimized hydrogel composition. The screening was performed with L929 mouse fibroblast cells, by altering the concentration of the PEG network (2% to 7%), tuning the degradable domain in the crosslinker (**Table 1**), and finally regulating the bulk degradation kinetics by altering the ratio of degradable to non-degradable domains. Preliminary screening for the biomolecule concentration revealed that the proliferation of cells detected via MTS assay in 3D hydrogels with 30 μM RGD peptides is statistically similar to 100μM RGD peptides. Hence, lower concentration was explored to screen other above parameters due to high RGD costs.

While screening for different PEG network concentrations between 2.5% and 7%, 3.4 wt/vol% hydrogels showed the most invasive microenvironment with 30 μM GRGDSPC as a biomolecule. The stained micrographs for actin filaments were imaged as Z-projections and superimposed (**Figure 4a**). This observation was quantified using an image analysis algorithm (**chapter 4**), where the edge effect of the cells revealed the percentage of micro protrusions inside the 3D scaffold, which in turn reveals information on cell invasion (**Figure 4b**). On the one hand, the rounded cells were observed in 5% and 7 % PEG network concentrations with and without biomolecules owing to the highly-dense polymer network and the inability of cells to degrade the crosslinker rapidly. On the other hand, the results show that with reduced gel stiffness, cells do not have enough spatial proximity to the integrin-binding site to provide enhanced cell spreading. Hence, 3.4 wt/vol% was chosen for the next systematic screening.

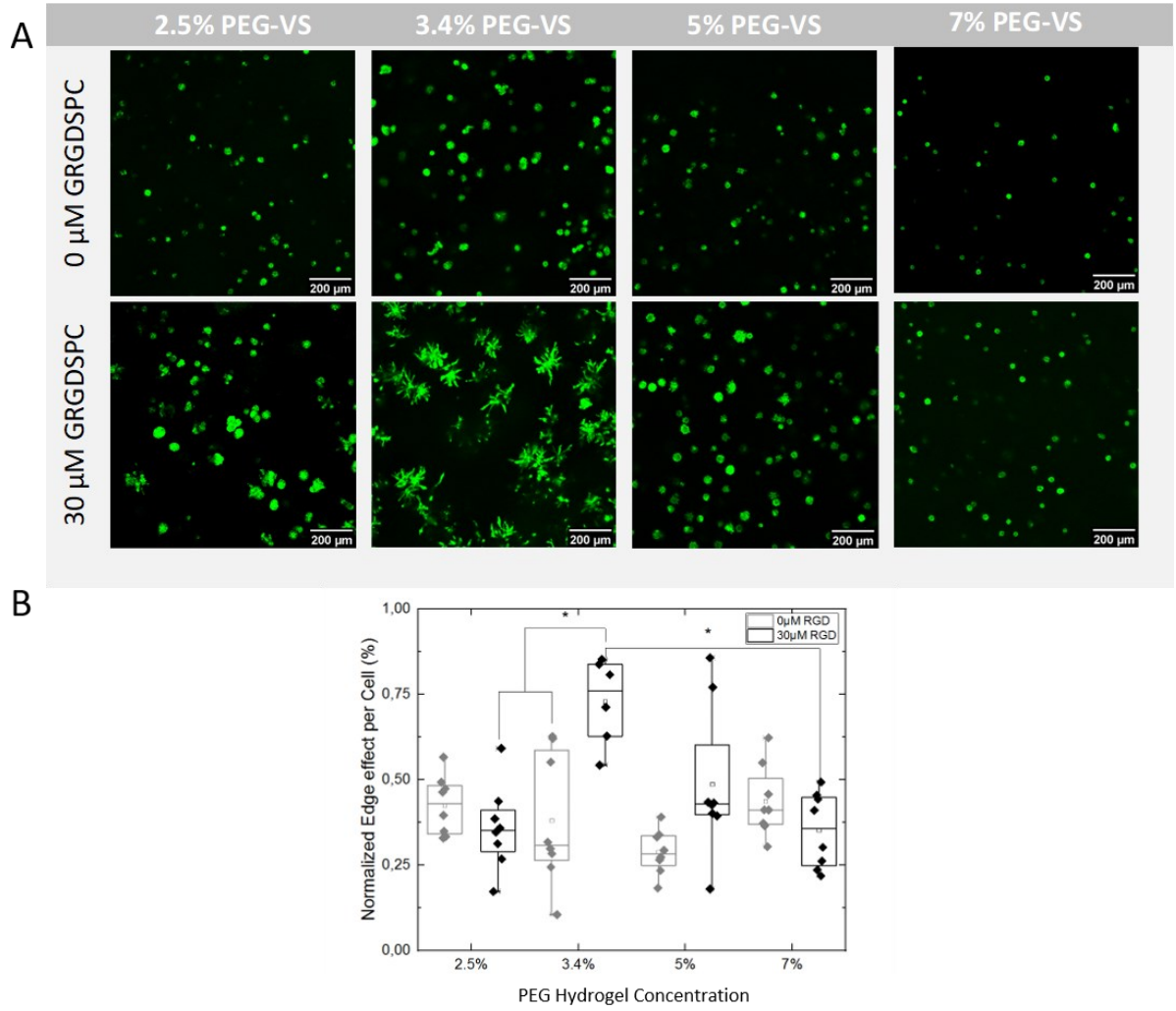

Figure 4. A) L929 cells are encapsulated in 3D PEG hydrogels with different PEG concentrations ranging from 2.5% to 7%. The optimal cell growth was observed in 3.4 % PEG with 30 µM GRGDSPC peptides for cell adhesion. B) The cell invasion is quantified as the protrusions obtained during cell invasion called normalized edge effect per cell (%). Data presented as average ± s.d. and statistical significance was performed using two-way ANOVA with Bonferroni and Tukey comparison (*$p < 0.05$, **$p < 0.01$).

The cells encapsulated are degrading on demand by secreting proteases. By altering the domains in the crosslinker responsible for degrading, we can tune the degradation kinetics in vitro. Four different linear di-cysteine crosslinkers (16W1-16W4) were explored, each with a unique degradable domain. As a control, non-degradable peptide and PEG-based crosslinkers were tested (16Wsc and HS-PEG-SH). 16W2 and 16W1 show the most invasive microenvironment for L929 cells with the biomolecules as adhesion sites (**Figure 5a**). While in control gels, the cells were primarily dead with

and without biomolecules due to the lack of space available for the cells to proliferate and migrate. Similar image analysis on fluorescent micrographs revealed a higher cell invasion for gels with crosslinker 16W2 followed by 16W1 and 16W4 (**Figure 5c**).

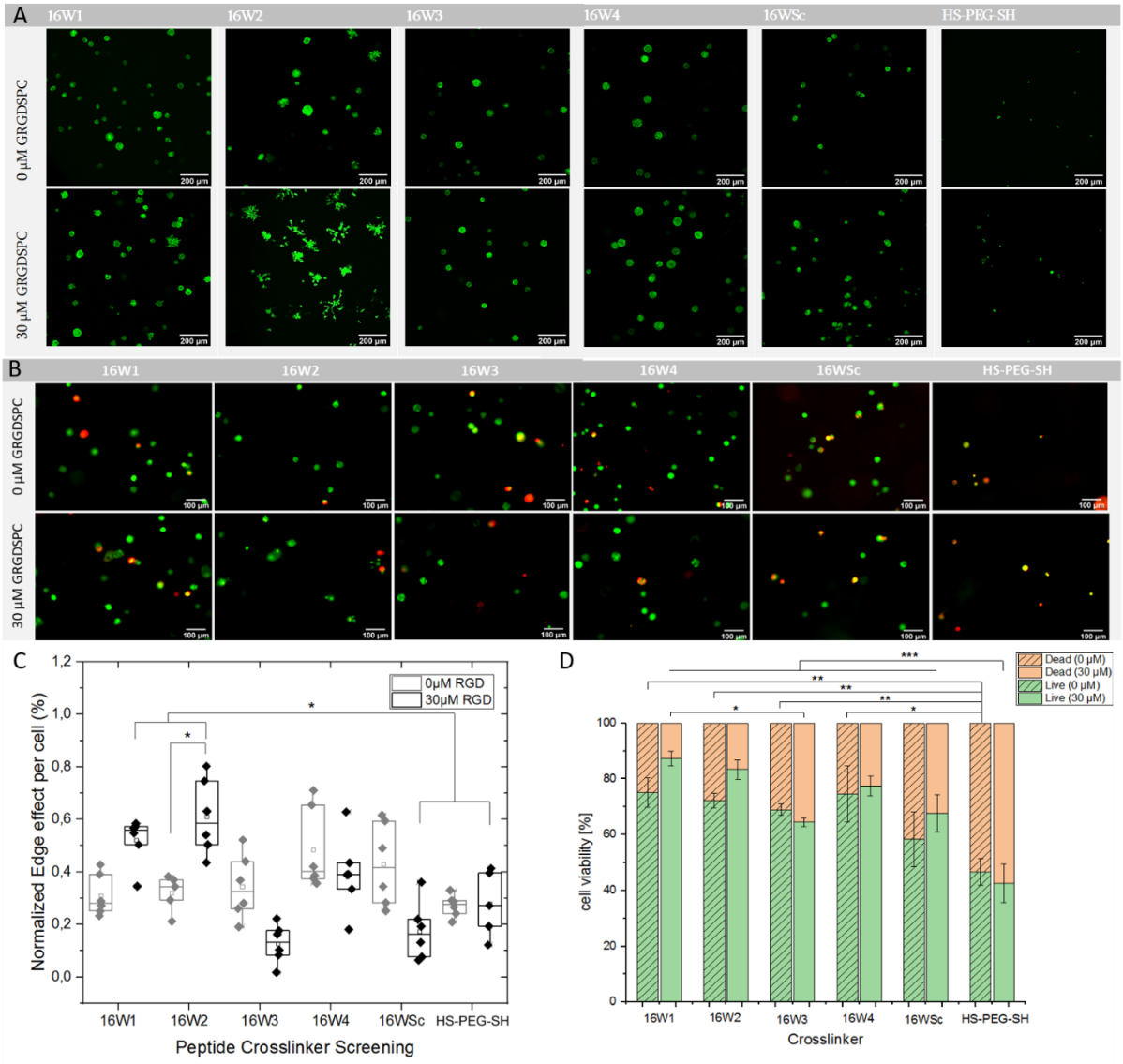

Figure 5. a) The 3.4 wt% PEG hydrogels are now crosslinked with different MMP cleavable groups (16W1- 16W4), Scrambled non-cleavable groups, and non-degradable PEG are tested to screen the optimal cleavage site for L929 cells for cell invasion with and without GRGDSPC. The cells are stained for actin filaments and c) quantified. b) Live dead assay is performed on the gels in culture and d) analyzed. Data presented as average ± s.d. and statistical significance was performed using two-way ANOVA with Bonferroni and Tukey comparison (*$p < 0.05$, **$p < 0.01$).

The increased cell invasion in hydrogels with 16W2 degradable domains may be due to the additional protease sensitivity from MMP 7 and MT 1 (**Table 1**). The Live-Dead

assay images revealed that the cells in the degradable microenvironment could survive even without RGD peptides (**Figure 5b**). On quantifying the images from live dead assay, higher cell viability (> 80%) was observed for 16W2 and 16W1 and reduced viability for other degradable hydrogels. The lowest cell viability(< 40%) was observed for the non-degradable PEG crosslinker (**Figure 5d**).

To understand the interdependency between the adhesive and degradable domains, hydrogels with a combination of MMP-degradable and non-degradable crosslinkers were formulated with L929 cells. 16W2 crosslinker was employed as the degradable crosslinker as it showed the most invasion and the PEG di-thiol crosslinker was the most non-invasive crosslinker. As expected, a gradual decrease in cell invasion is observed with an increase in the concentration of the non-degradable crosslinker (**Figure 6a**). Hydrogels with up to 50% HS-PEG-SH provided moderate cell invasion conditions, whereas the cells in hydrogels with a higher ratio of non-degradable crosslinker showed a little interaction with their surrounding gel. On quantifying the actin stained images, the edge effect quantification shows higher cell invasion in the fully degradable hydrogel with 100% 16W2 crosslinker with biomolecules (**Figure 6b**). Despite the presence of biomolecules, the non-degradable hydrogels promoted no cell invasion.

Prolonged storage of the PEG-VS and the crosslinker peptides at -20°C resulted in a gradual loss in functionality due to repeated freeze and thaw cycles which affect the mechanical properties. Hence, PEG-VS is stored as powder aliquotes, whereas crosslinkers with thiols that are more prone to disulfide bond formations must be characterized every three months for their thiol concentration using an Ellman's assay. We explored options to increase the gelation kinetics from a crosslinking duration of 50 minutes to 20 minutes. To achieve faster crosslinking, the gelation kinetics can be tuned by altering the temperature, pH, the electron-withdrawing group (EWG), and concentration of the reacting molecules of the hydrogel precursor. With the desire to produce soft 3D invitro hydrogels and based on the previous

reports[153], the concentration of the reacting molecules was not altered. However, it was essential to reduce the gelation time to prevent cell sedimentation. Hence 4 arm maleimide functionalized PEG was employed to crosslink with the linear crosslinker and tether with the biomolecules. However, replacing VS with maleimide resulted in instantaneous crosslinking under 1s, causing the pipet tips to clog. Hence, to facilitate a workable precursor with uniform mixing, different ratios of PEG-VS and PEG-MAL were screened for their gelation kinetics. Among the different screening conditions, 60: 40, where 40 % of the functional VS was replaced with maleimide (MAL) at pH 7.4, had the most suitable gelation kinetics of 40 minutes (**Figure 7a**).

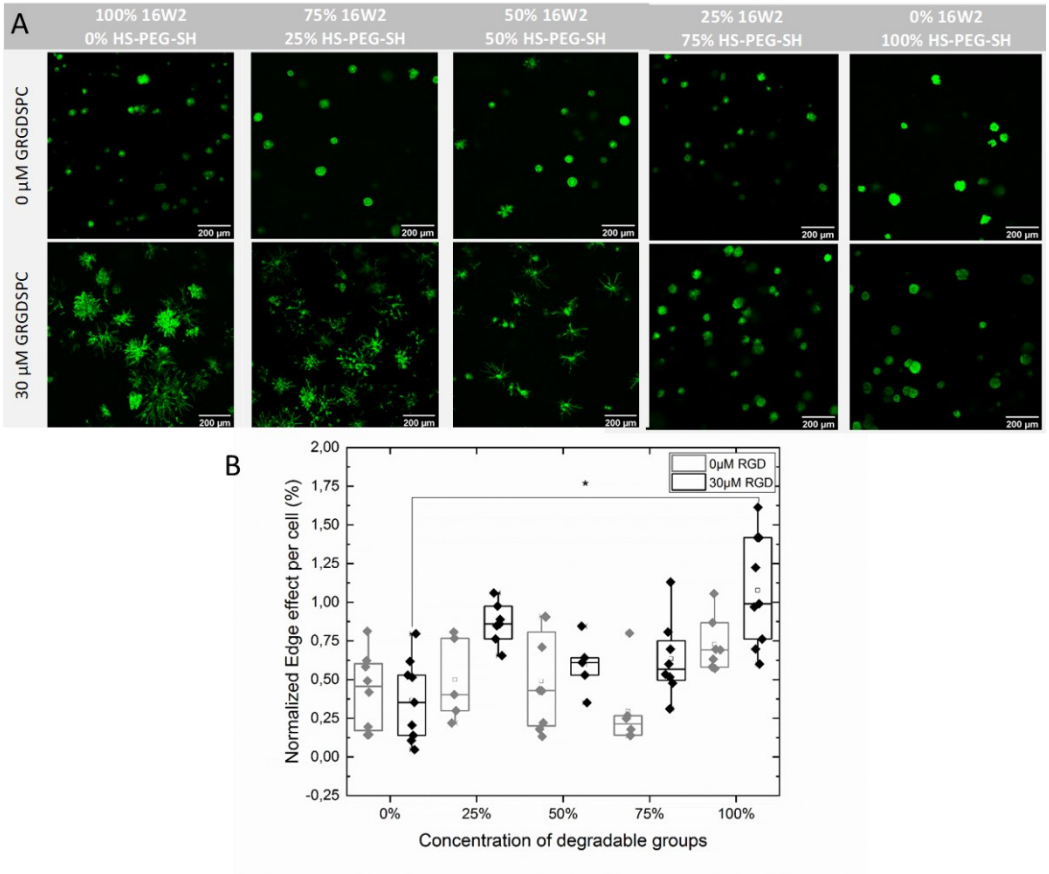

Figure 6. A) Combination of degradable and non-degradable crosslinkers is employed, revealing a decrease in cell invasion with the increase in the fraction of non-degradable crosslinkers. B) Edge effect analysis revealed similar trends. Data presented as average ± s.d. and statistical significance was performed using two-way ANOVA with Bonferroni and Tukey comparison (*$p < 0.05$, **$p < 0.01$).

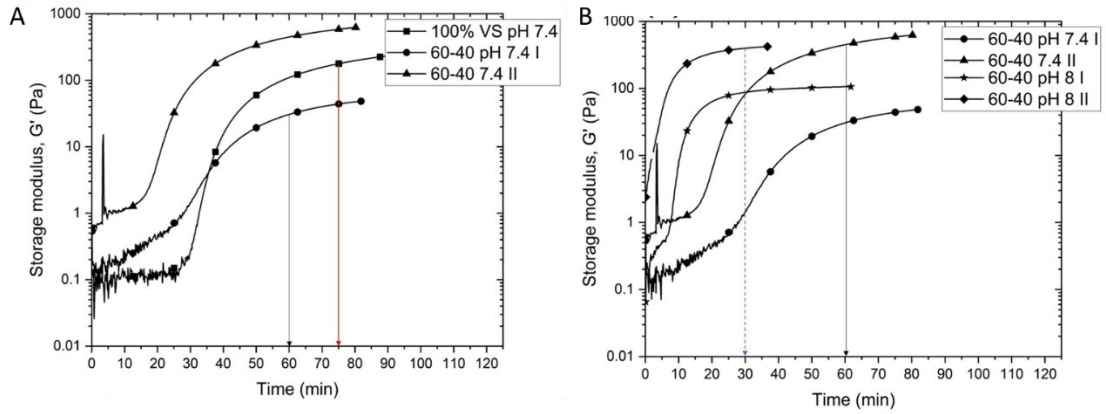

Figure 7. (a) Stiffness (G') vs. time curves for PEG hydrogels of different compositions at pH 7.4. The black arrow indicated the gelation time for PEG VS-MAL hydrogels. The red arrow indicated gelation time for PEG VS hydrogel. (b) Effect of pH on crosslinking kinetics and role on storage modulus for 3.4wt% PEG VS-MAL hydrogels. The solid line indicated gelation time for hydrogels at pH 7.4. The dotted line indicates the gelation time for hydrogels at pH 8. Multiple rheology measurements are plotted to show the variability in storage modulus.

However, an increase in gelation kinetics was not evident until the pH of the precursor solution was altered from 7.4 to pH 8, and the crosslinking time was reduced to 20 minutes (**Figure 7b**). We also observed that the gel's stiffness with 60:40 VS to MAL had inconsistent storage modulus resulting from batch to batch variability. The lack of reproducibility with maleimide-based gels owes to the heterogeneous pores formed when the maleimides crosslink rapidly with the crosslinker. These observations were consistent with previous reports.[389,390] The gelation kinetics were quantified using rheology measurements using 20 mm conical plate geometry.

A simple method to couple linear peptides like RGD is by adding spacer amino acids bearing thiol residues like cysteine to enable thiol-Michael addition with PEG precursor. However, a sharp contrast between the pattern region and the background is essential for in vitro cell guidance and growth for photopatterning. Hence the biomolecules incorporated need to be both high in potency and concentration. Thus GRGDSPC is mixed in the precursor solution in several concentrations (0 mM to 1 mM) to decipher the maximum optimal RGD concentration for cell growth in the sPEG 60:40 VS:MAL hydrogel combination. As the cysteines in the RGD compete

with the cysteines in the crosslinker to bind to the VS, a thorough optimization is essential. We attempted to decipher the maximal concentration of RGD molecules that can be tethered without compromising the structure of the hydrogel yet supporting cell growth.

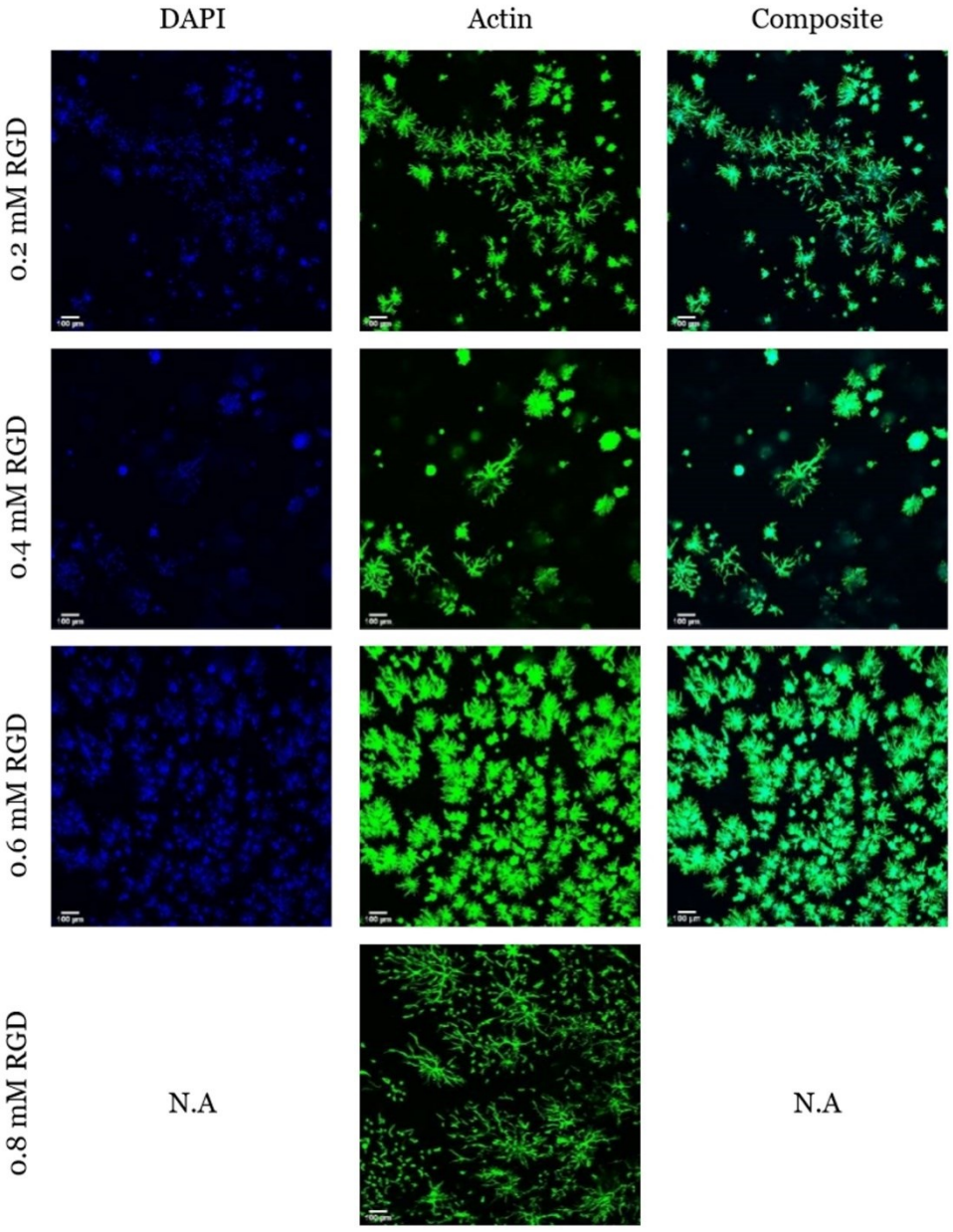

Figure 8. Maximum intensity Z-projections of fluorescently-labeled RGD tagged PEG hydrogels at different concentrations of GRGDSPC (DAPI: 405 nm, Actin: 594 nm, stack size:150μm). NA indicates that gels could not be imaged as gels were not formed or were extremely weak and did not encapsulate cells. (Scale bar 100 μm)

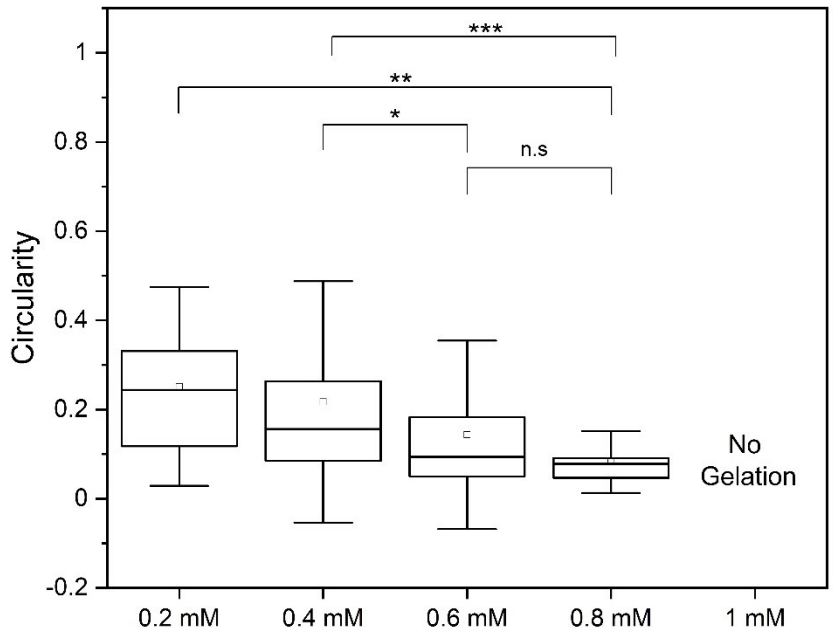

Figure 9. The circularity of 3D distributed L929 cells in 3.4% PEG-VS PEG-Mal hydrogels with different concentrations of adhesion peptide GRGDSPC. Data are presented as mean ± SD.

We know from previous sections that 30 μM is already sufficient for cell invasion; however, the attempt now is made to incorporate the highest concentration of biomolecules for photopatterning application; hence all tested concentrations (0.2 mM to 0.8 mM) GRGDSPC peptides show improved cell invasion in 3D. The fluorescent micrographs stained for actin revealed that the cell spreading is visually higher at 0.6 mM and 0.8 mM with dense cell sprouting than in 0.2 mM and 0.4 mM RGD tethered hydrogels. Several rounded cells were observed in 0.2 mM and 0.4 mM RGD tethered hydrogel, indicating that the density of RGD is less or the density of the matrix is high to promote uniform cell invasion (**Figure 8**). Empirical validation for these observations was performed using the superimposed z stack of the fluorescent micrographs stained for actin filaments. A computational algorithm was employed to analyze the circularity of the cells. Higher the circularity (closer to 1) means that the shape of cells to closer to a sphere, whereas low circularity (closer to 0) interprets higher sprouting and cell invasion (**Chapter 4**, **Methods**). While the hydrogels with 0.8 mM GRGDSPC show the highest proliferation with the lowest cell

sphericity indicating extensive protrusions, it lacks reproducibility due to heterogeneous network formation and failure to encapsulate cells. Hence, 0.6 mM RGD tethered peptide, which showed equally extensive cell spreading and low circularity with reproducible gels, is applied for further experiments (**Figure 9**). It is essential to note that the gels bio-functionalized with 1 mM RGDC did not crosslink due to lower VS arms available for crosslinking. It is relevant to note that no statistical circularity differences were observed between gels functionalized with 0.6 mM and 0.8 mM RGD.

6.2.3 Rendering 3D PEG hydrogel bioactive with K and Q peptides as Linkers

In enzymatic photopatterning, the biomolecules are spatiotemporally tethered to a PEG hydrogel through the transglutaminase reaction with uncaged lysine peptides.[153] This requires the BOI to bear a peptides sequence 'NQEQVSPL'. The combination of BOI and NQEQVSPL is known to support cell growth much more diminutive than peptides without NQEQVSPL (**Figure 1d**). Hence, I attempted to translate the existing system from protected lysine to protected glutamine. By translating from caged K to caged Q system, an attempt to eliminate the inhibitory growth effect of NQEQVSPL is made. The N[Q]EQVSPLERCG is bound via the cysteine to the PEG backbone in the protected glutamine system. In control experiments, peptides without caging motifs are tested for in vitro experiments with L929 cells (**Figure 9, 10**). Here we explored the sequential biofunctionalization where the gels with K-peptide linker were treated with NQEQVSPL-RGD-ERCG (Q-RGD), and the gels tethered with Q-peptide linker hydrogels were treated with RGD bearing an amine (K-RGD) solutions. Since the incubation is performed after the hydrogel is crosslinked, the diffusion of the BOI depends on parameters such as concentration, temperature, time, and enzyme concentration. After 90 minutes, the unbound biomolecules are washed. The equimolar concentration of the incubation solution with solution volumes five times greater than the gel volume was used.

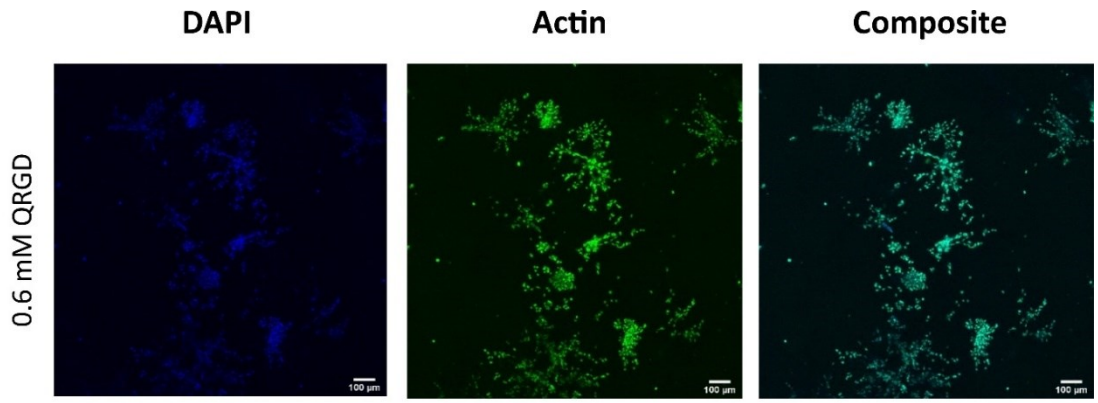

Figure 10. Maximum intensity Z-projections of fluorescently labelled DAPI, Actin, and merged channels in 3D PEG hydrogels functionalized with RGD via K-peptide (stack: 200 µm).

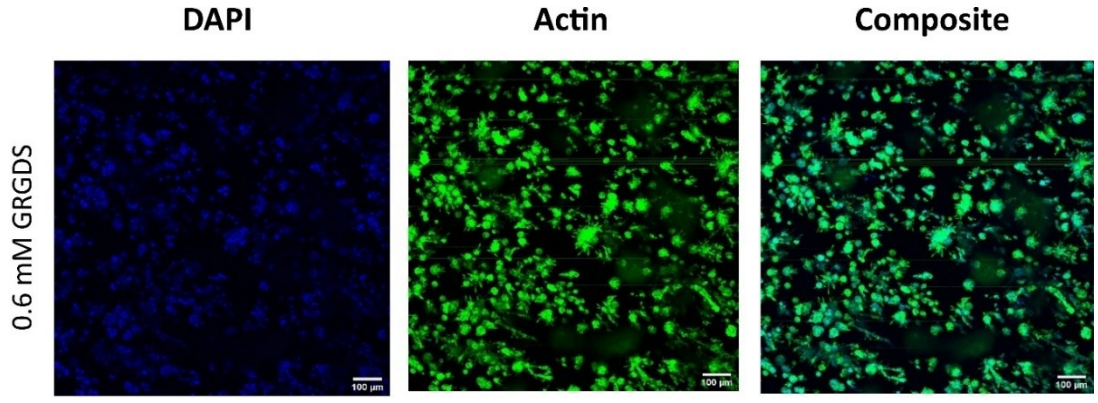

Figure 11. Maximum intensity Z projects of fluorescently labelled DAPI, Actin, and merged channels in 3D PEG hydrogels functionalized with RGD via uncaged Q-peptide (stack: 200 µm).

The fluorescent micrographs stained for DAPI and actin revealed that the gels functionalized with 0.6 mM Q-RGD bound to K peptide showed moderate 3D cell invasion and growth (**Figure 10**). In contrast, cell invasion with 0.6 mM GRGDS bound to Q-peptide showed superior cell invasion (**Figure 11**). Though the gels were formed at pH 8 rapidly and employed a sequential biofunctionalization method, this procedure had its demerits. The elevated pH resulted in precipitation of the Ca^{2+} ions, which are essential for activation of FXIII during the incubation. This may be due to the buffering solution at pH 8, FXIIIa, and the $CaCl_2$ when in contact with the formulated gel. Skin-like precipitation on the hydrogel surface was observed,

preventing imaging. Additionally, preparation of the RGD incubation solution with FXIIIa in large amounts was required. Therefore, a new enzyme-linked biofunctionalization method needed to be developed to combat these issues.

Meanwhile, Broguiere et al. developed a novel, single-step functionalization protocol to bind nerve growth factor (NGF) to hydrogels using Sortase A.[154] This protocol was adapted to our hydrogel system by combining the formulation and biofunctionalization steps. The new protocols now require 10x lower volumes of FXIIIa enzyme and RGD peptides. Secondly, the incubation and washing duration in the hydrogel is drastically reduced. However, the unbound RGD peptides require additional washing. Here we promote the unbound RGD and FXIIIa to diffuse out of the gel rather than in the sequential biofunctionalization protocol where the molecules are promoted to diffuse into the gel. Similar control experiments with uncaged K and Q peptides were developed. The immunostained images of cells encapsulated in PEG gels bearing K-peptide with Q RGD and Q-peptide with GRGDS tethered hydrogels are investigated (**Figure 12, 13**).

The fluorescent micrographs of gels with Q-RGD bound to K-peptide at 0.6 mM and 1.2 mM showed increased cell proliferation than gels with no biomolecules (**Figure 12a**). On analyzing the images for edge effect and circularity (**Figure 12 b, c**), no significant differences were observed between the circularity of 0.6mM QRGD and gels without RGD (0.0 mM). Despite visual observations, the data obtained could not confirm the statistical difference. Thus, Q-RGD at 1.2 mM showed the most cell invasion with both the quantification techniques and hence applied for the single-step photopatterning experiments. It is important to emphasize that although the concentration of RGD peptides tethered is limited to the concentration of K peptides during gel formation, the diffusion kinetics play a crucial role in tethering Q-RGD peptides, confirming that a higher concentration of RGD peptides promotes diffusion for biomolecule binding. Analyzing the actin filament invasion per image, gels with

Q-RGD at 1.2 mM concentration had a cell invasion area of 21.99 %, while gels with 0.6 mM Q-RGD had only 8.50% of cell invasion.

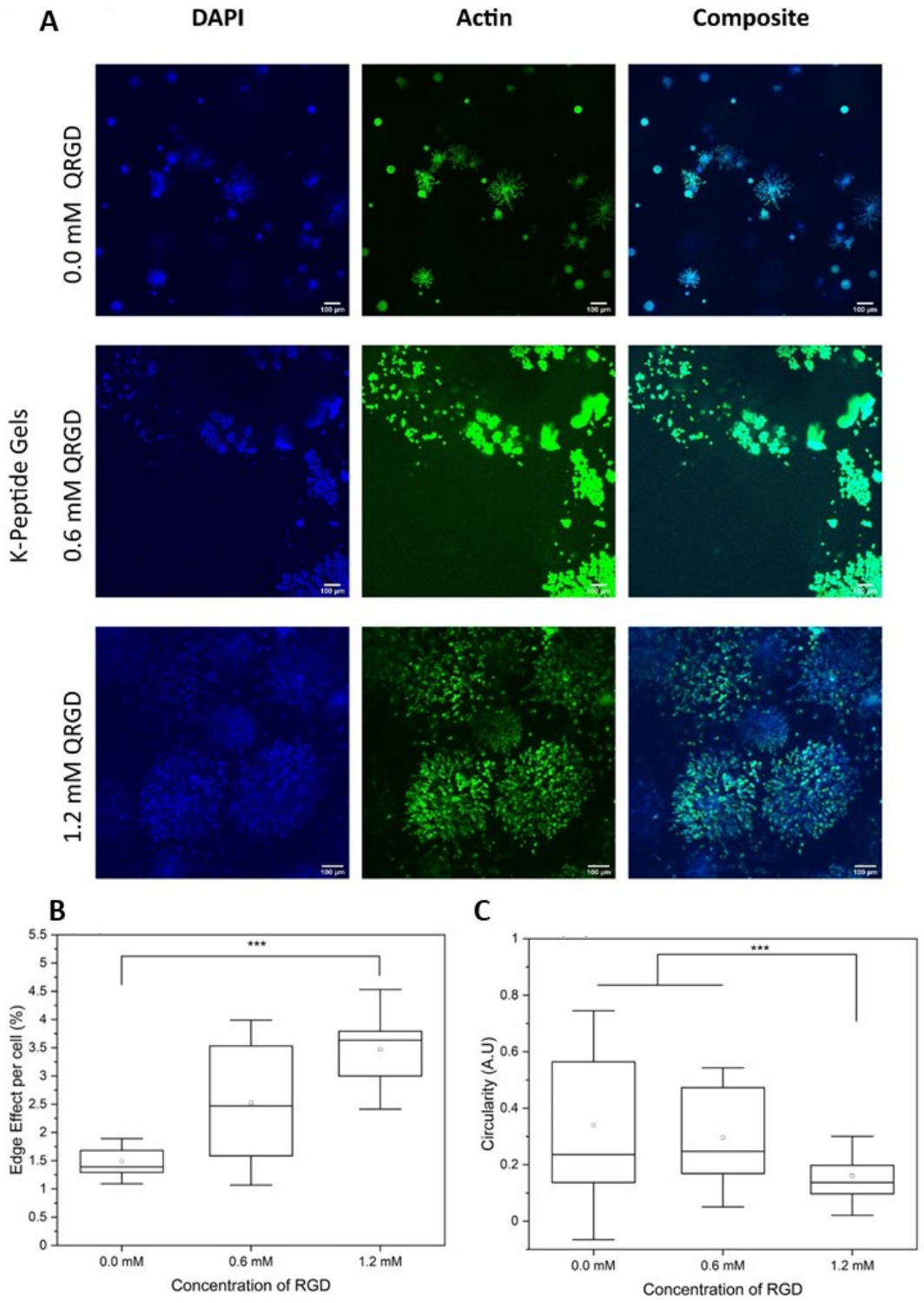

Figure 12. (a) Maximum intensity Z-projections of 3D distributed fibroblasts in PEG-VS, PEG-MAL hydrogels functionalized with different concentrations of RGD via K-peptide (DAPI:

405 nm, Actin: 594 nm, stack size:200 µm). (b) Edge effect of cell in hydrogels (c) circularity of cells in hydrogels.

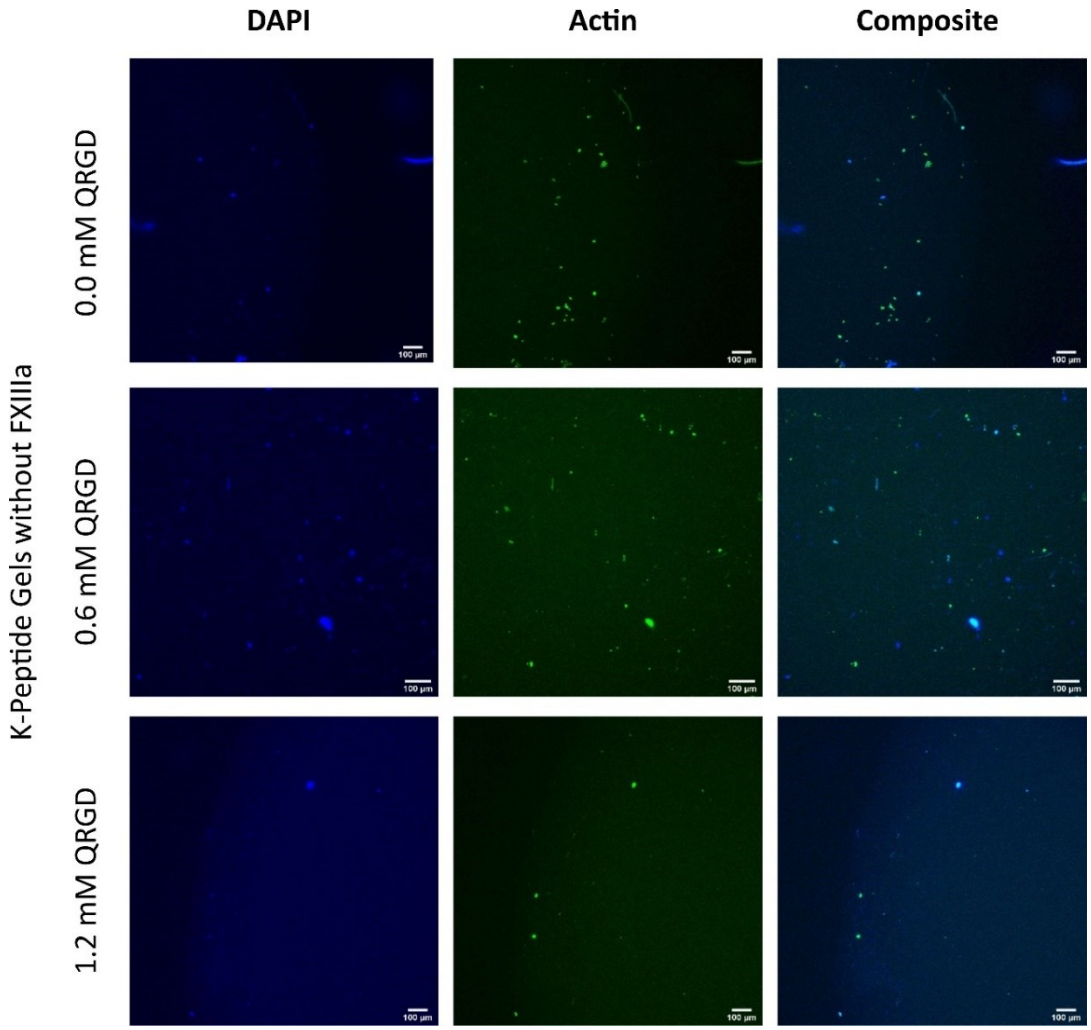

Figure 13. Fluorescent Z-stack images of fibroblasts in PEG VS-MAL hydrogels with K-peptide linker without FXIIIa in the gel mix

Control experiments were performed to ensure that the Q-RGD peptides in the hydrogel are covalently binding only in the presence of FXIIIa and not in its absence. Hence Q-RGD peptide hydrogels were formulated without FXIIIa (**Figure 13**) with L929 fibroblasts and cultured for 7 days. Cell appeared rounded, and no cell invasion or proliferation was observed at different Q-RGD concentrations revealing that only bound RGD peptides contributed to cell adhesion and unbound RGD peptides are easily washed out.

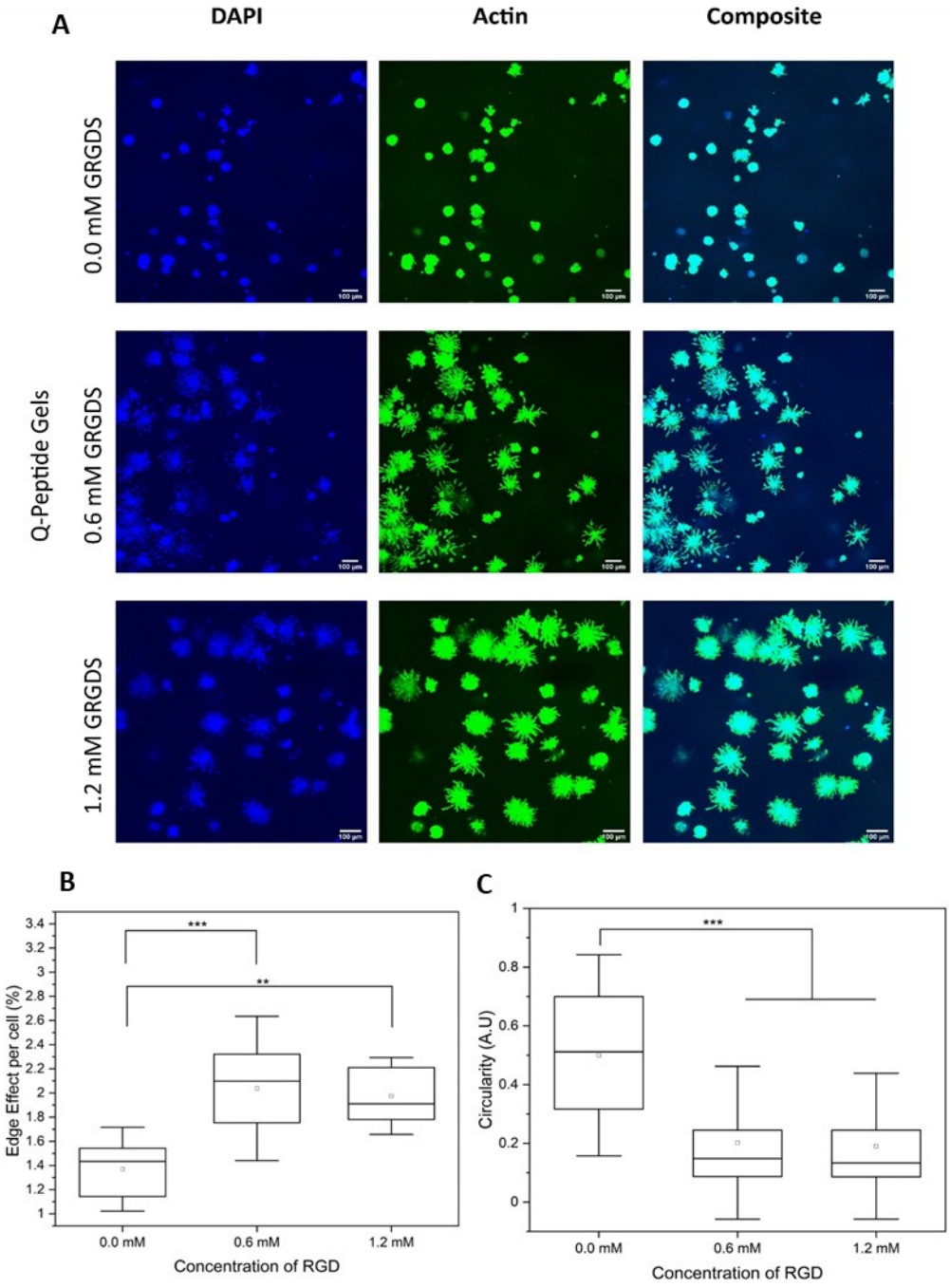

Figure 14. (a) Maximum intensity Z-projections of 3D distributed fibroblasts in PEG-VS, PEG-MAL hydrogels functionalized with different concentrations of RGD via Q-peptide (DAPI: 405 nm, Actin: 594 nm, stack size:200). (b) Edge length effect of cell in hydrogels (c) circularity of cells in hydrogels.

Similar experiments were performed with GRGDS peptide, which bears a free amine in the N terminal resembling RGD tethered with lysine (K-RGD). The encapsulated cells were stained for actin filaments and DAPI after 7 days of culture (**Figure 14a**).

The visual observation reports that the cell invasion in gels with Q-peptide tethered with GRGDS are more prominent than in those without RGD peptides. Both the concentration of GRGDS showed similar cell invasion for L929 fibroblast. Quantifying the images for edge effect and circularity revealed that the cell invasion is significantly higher for both concentrations of GRGDS compared to the control (**Figure 14 b,c**). Lower circularity is observed for both 0.6 mM and 1.2 mM GRGDS revealing that no significant differences occur. An increase in RGD concentration for the Q-peptide linker is not essential for enhanced cell invasion.

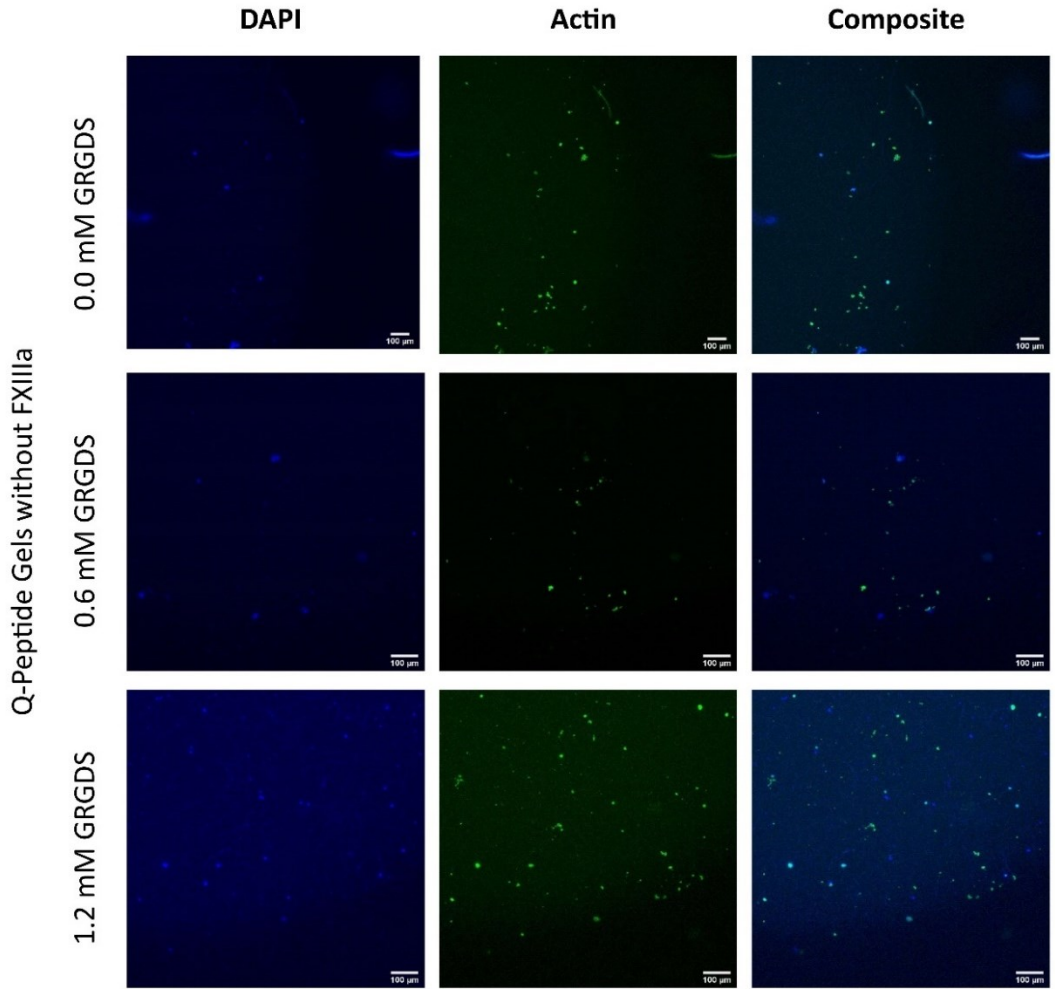

Figure 15. Fluorescent Z-stack images of fibroblasts in PEG VS-MAL hydrogels with Q-peptide linker without FXIIIa in the gel mix

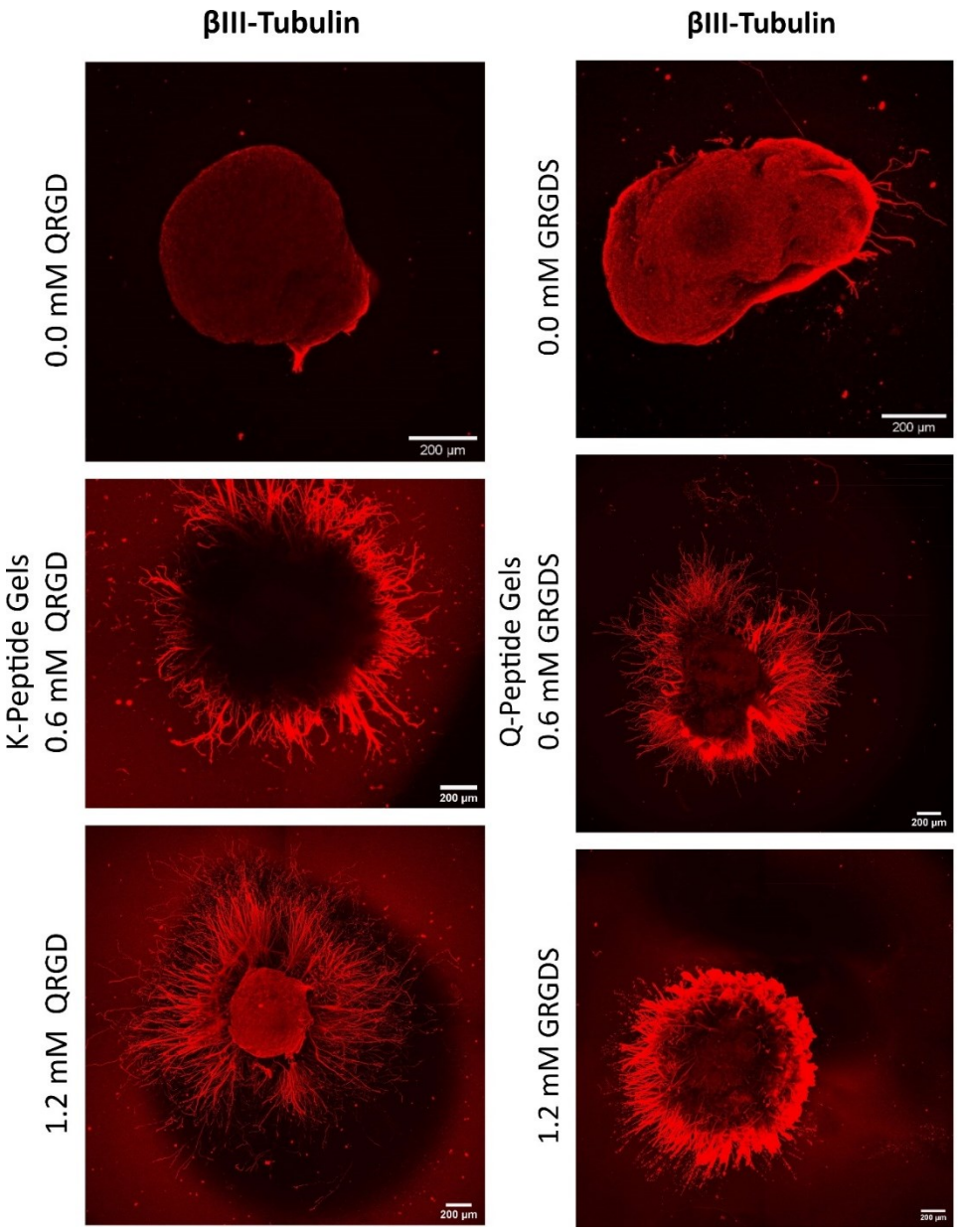

Figure 16. Z-stack projections of DRG in PEG VS-MAL hydrogels with different RGD concentrations via K- and Q-peptide linkers (βIII-Tubulin – 633 nm, stack size-variable)

Similar control experiments without FXIIIa were performed by encapsulating L929 cells with GRGDS and PEG networks with Q linker peptides. In the absence of FXIIIa, cells appear rounded due to the lack of bound GRGDS peptides to the hydrogel (**Figure 15**). In addition, very few cells are observed with filapodial sprouts; however, they do not contribute to the significant representation of cell behavior in such hydrogels. Hence, we conclude that the exclusivity of RGD tethering to the PEG backbone is an essential requirement for biofunctionalization. Furthermore, these results indicate

that it is both efficient and viable to translate from sequential biofunctionalization to single-step biofunctionalization for both K and Q peptide tethered hydrogels.

Photopatterning is vital for tissues that require complex architecture. Hence to test the applicability of this hydrogel platform, similar experiments with chicken dorsal root ganglion (DRG) in PEG hydrogels tethered with 0.0, 0.6, and 1.2 mM Q-RGD via K-peptide and GRGDS via Q-peptide were investigated. The hydrogel composition for DRG growth was favorable at all hydrogels tethered with Q-RGD or K-RGD (GRGDS) at both 0.6mM and 1.2 mM via uncaged K-peptide and Q-peptide linkers, respectively. The DRGs were stained for β-tubulin (red) to visualize the axon innervation in the PEG hydrogels (**Figure 16**). Further quantification is essential to compare the concentrations and tethering systems.

6.2.4 Photopatterning with caged K and Caged Q peptide tethered hydrogels

The photopatterning described by Mosiewicz et al. involves sequential steps after fabricating the in vitro PEG gel with caged peptides sensitive to light.[281] The hydrogels are irradiated using an optimized protocol, preventing any damage to the encapsulated cells. The gels are washed post patterning and labeled with the desired biomolecules of interest (BOI). Finally, the unbound BOI is removed by washing repeatedly. Though this protocol was optimized for controlled MSCs migration, re-optimization is required for the controlled growth of fibroblasts or nerve cells. I employed the PEG hydrogels described earlier for photopatterning using [K] peptides (**Figure 17a**). The photosensitive peptide is deprotected, revealing an active site that enables the binding of the biomolecule of interest (BOI) via an enzymatic transglutaminase reaction, as described in **chapter 4**. This allows spatial localization of the desired bio-molecules such as RGD (Linear/ Cyclic / Bicyclic), IKVAV, YIGSR, and fibronectin fragments FN 9*-10/12-14 as screened in previous sections and chapters through mild and highly specific reaction mechanism. BOI design requires a specific transglutaminase

sequence that is sensitive to FXIIIa crosslinking, and for shorter peptides, this is relatively easy to fabricate by peptide synthesis. However, larger protein fragments like FN 9*-10/12-14 require special plasmid engineering and production in E. coli.[31] The novelty of PEG and its applications with integrin-specific binding biomolecules for controlled cell adhesion and migration have been discussed thoroughly in **Chapters 1 and 2**.

I observed that the ability of cells to bind to the BOI with transglutaminase sequence is lower than the BOI alone. Hence, I also explored the feasibility of using the chemistry where the hydrogel is tethered to a caged Q or [Q] peptide, and the BOI can be tethered directly by decaging the [Q] peptide and binding to a simple amine bearing BOI. This chemistry does not require an additional NQEQVSPL sequence to the BOI. Thus, reducing the need for designing BOI with a transglutaminase sequence and allowing using peptides bearing only amines, improving cell adhesion drastically.

This inverse caging mechanism was developed in collaboration with PEPSCAN, Lelystad to develop caged glutamine with an o-NB group, which protects the carboxyl group of the glutamine. On exposure to UV light, the carboxyl group is made available from the photo-protective group, facilitating the transglutaminase reaction with peptides bearing an amine group (**Figure 17c**). The caging groups nvoc and oNB had their absorption maxima at ~350 nm and ~265 nm, respectively. While both are caged groups are UV-sensitive, the former cleave between 350 - 405 nm while the latter cleaves between 265 - 365 nm, respectively (**Figure 17 b,d**). The absorption spectrum was measured with 1mM of Caged peptides and exposed with an 8 mW UV lamp instead of laser to decap volumes larger than 500 µL. The spectra are measured at different time intervals. Decaging is significantly observed in nvoc and o-NB peptides after 120 min and 60 min, respectively.

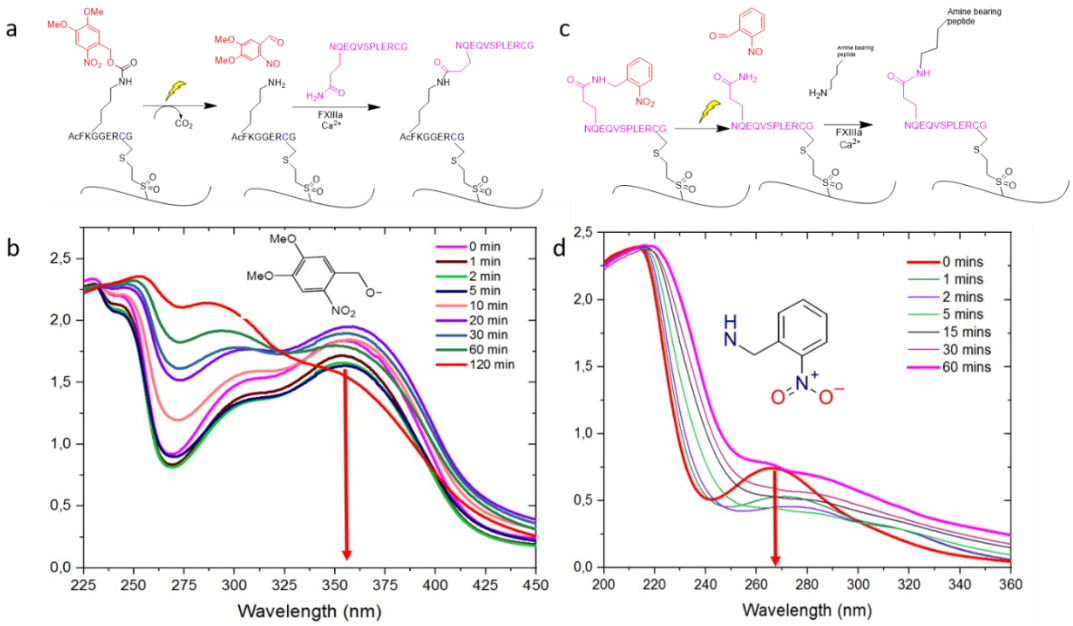

Figure 17. a) De-protection of the photo-protected lysine-based peptide by exposing UV light. The caged group nvoc is cleaved off the K peptide, thus exposing free amine groups of lysine. This free amine reacts to the carboxylic group of the glutamine to form an isopeptide bond via an enzymatic pathway facilitated by FXIIIa. b) UV-Vis absorption spectrum of [K] peptides at different UV exposure durations. c) De-protection of the photo-protected glutamine-based peptide by exposing UV light. The caged group is cleaved off the peptide, thus exposing free carboxyl groups of glutamine. This free carboxyl group reacts with any biofunctional amine-bearing peptide to form an iso-peptide bond via an enzymatic pathway facilitated by FXIIIa. d) UV-Vis absorption spectrum of [K] peptides at different UV exposure durations.

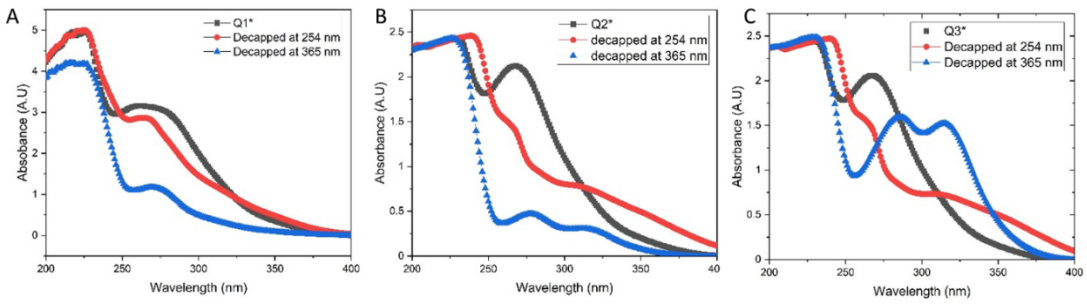

Figure 18. UV-Vis spectra of light-sensitive Q-peptides [Q1], [Q2], and [Q3] after 10 min exposure to UV light

In the case of caged Q peptides, the NQEQVSPL sequence bears two glutamines. Hence three variants were developed. These peptides are Q1 with both the glutamine caged: NQ(**o-NB**)EQ(**o-NB**)VSPLERCG-NH_2, Q2 with the first glutamine caged:

NQ(**o-NB**) EQVSPLERCG-NH_2 and Q3 with the second glutamine caged: NQEQ(**o-NB**)VSPLERCG-NH_2. The caged Q peptides bear a broad peak at 270 nm. Decaging was measured using absorption measurements for all three variants using UV light at 254 nm and 365 nm. The absorption spectrum is compared after exposing the peptides to a light source at 254 nm, revealing a reduction in absorbance around 270 nm for all the caged Q peptides. A more significant decrease in absorption peaks is observed for all caged Q peptides after exposure to light at 365 nm (**Figure 18**). Hence the choice of wavelength to photo pattern the Q peptide is at 365 nm.

Further, the time required for decaging all three Q peptides were analyzed using individual absorption measurements after several intervals of light exposure at 356 nm. The light was exposed to all three peptides in solution for 30 minutes (**Figure 19**). A drastic decrease in the peak was observed after 5 minutes of light exposure. However, no significant change in the spectra was observed on extended light exposure after 5 minutes. Thus, photopatterning for 5 mins is the minimum requirement for Caged Q peptides.

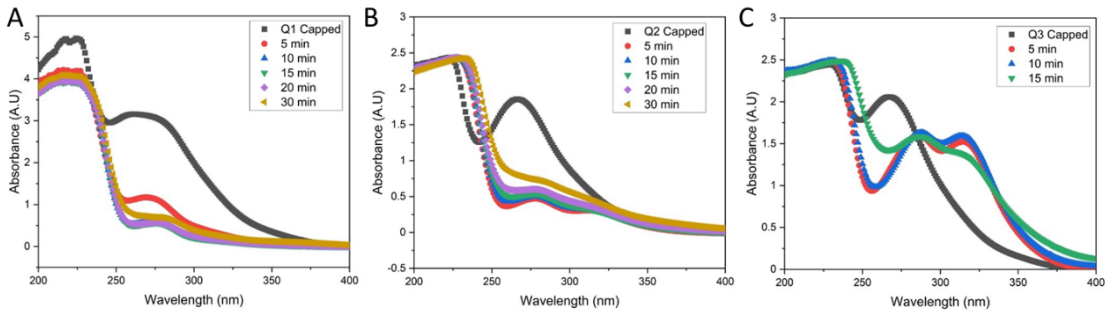

Figure 19 UV-Vis spectra of caged Q peptides ([Q1], [Q2], and [Q3]) at different time points after exposure to UV light at 365 nm UV light

In both the photopatterning systems, the desired spatial pattern must have a strong contrast between the patterned and the non-patterned regions for the cells to sense the biochemical contrast. Therefore, the photopatterning parameters, such as laser intensity, pixel dwell time, and pattern architecture, have been extensively optimized for the given laser system to enable localized biomolecule binding with a sufficiently

high concentration in the pattern. Using the Leica SP8 confocal (DWI, Aachen), a 100% intensity of the laser at 405 nm is irradiated into the hydrogel. The output power at the focal plane was 0.3 mW, measured using a photodetector (Thor Labs). For the entire photopatterning period, the gels are maintained in a closed incubating chamber at 37 °C. Since the gels were formulated with HEPES buffer, the pH was stable even without CO_2.

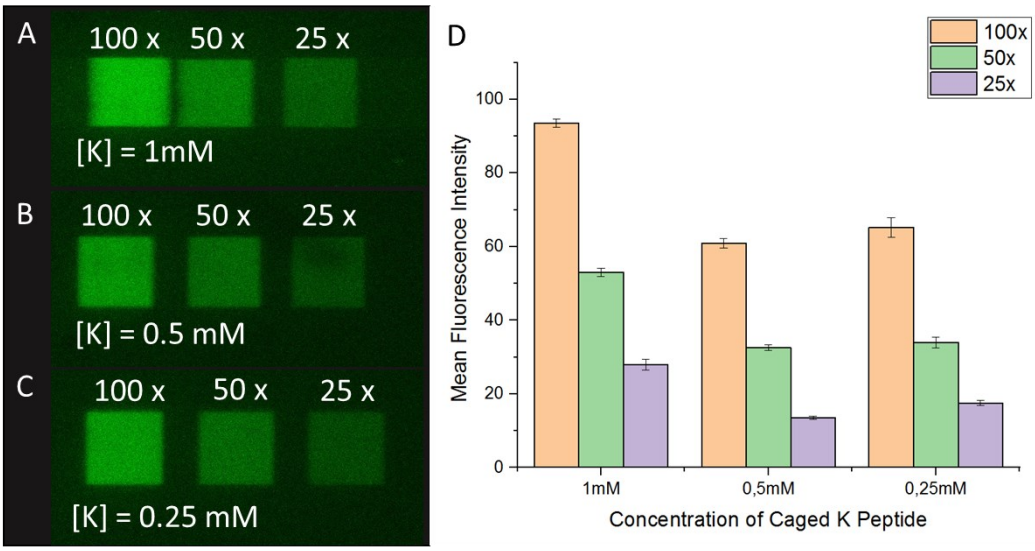

Figure 20. Screening parameters for different caged K peptide gels with a) 1mM b) 0.5 mM and c) 0.25 mM concentrations at 100x, 50x and 25x patterning iterations. d) The mean fluorescence intensity is quantified for the entire z stack is reported as (AU).

The laser intensity is a crucial factor for the decaging of caged K and Q peptides. The pixel dwell time is the duration of laser exposure per unit pixel area. Several parameters, including patterning speed, pattern size, and the number of scanning repetitions, determine the pixel dwell time. For most cell experiments, 48 µs was the optimized pixel dwell time. The influence of the concentration of caged peptides and the number of iterations was investigated (**Figure 20**). I observed that for a fixed hydrogel composition, an increase in iterations of laser in the ROI resulted in an increase in free amines (detected by CBQCA assay). 1mM, 0.5 mM and 0.25 mM concentrations of [K] were investigated with 100, 50 and 25 iterations of pattering in the ROI (**Figure 20 a,b,c**). The highest free amines were observed in the 1mM [K] with

100 iterations in the ROI. However, a similar decaging degree can be achieved by either altering the concentration of the [K] or the number of times the laser is exposed in the ROI. For example, the mean fluorescence intensity for 0.5mM with 100 iterations is similar to 1mM [K] with 50 laser iterations (**Figure 20d**).

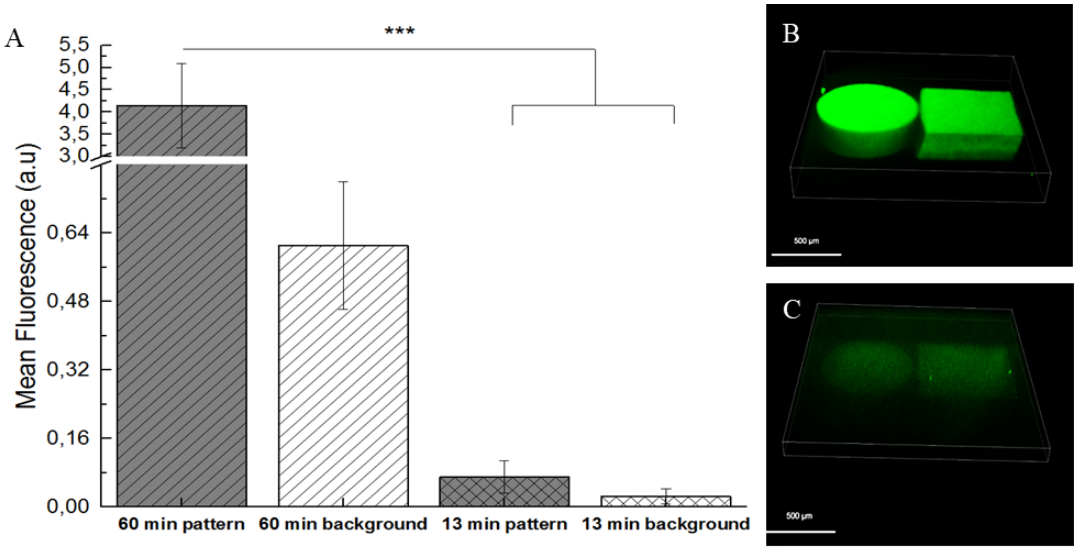

Figure 21. a) Quantification of free amine exposed after decaging inside a 3D photo patterned hydrogel CBQCA assay. b) 60mins pattern and c) 13-minute pattern for a fixed laser intensity.

Similarly, exposing the hydrogels for a more extended period with a fixed pixel dwell time in a defined region creates a contrast between the pattern and its surrounding (**Figure 21**). To achieve selective cell growth and migration into the pattern, it was essential to compare the biomolecular concentration at the region of the photo pattern compared to its background. After photopatterning, the decaged amines can be quantified by treating the gels with a CBQCA assay (Thermo Fisher). This assay is based on an ATTO-TAG bearing a non-fluorescent reagent, which becomes fluorescent on binding to a free amine. The fluorescent pattern after treatment with the CBQCA reagent for the gels with longer (60 mins) photo exposure showed higher fluorescence compared to the shorter duration patterned (13 mins) hydrogel (**Figure 21**). The contrast between the pattern and the background is also higher for the more extended irradiated photo pattern. With these results, it is clear that the duration of

laser exposure plays a vital role in the contrast of the photo pattern, thereby affecting the contrast of the biopattern.

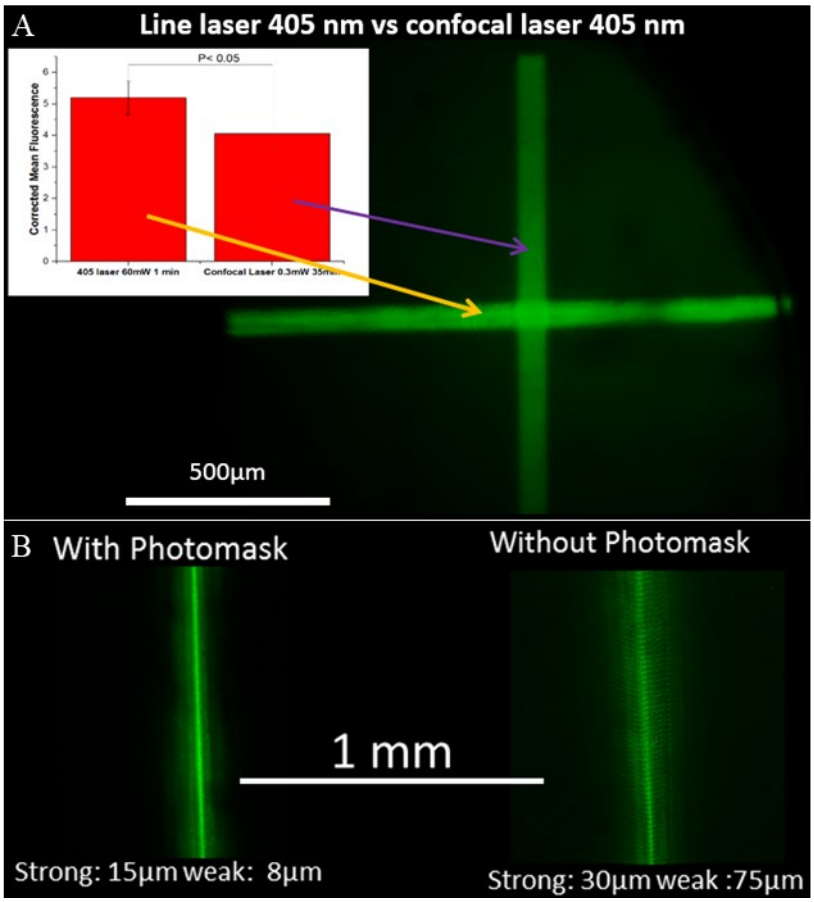

Figure 22. a) In-house-built laser diode showing higher intensity at shorter exposure time than the confocal microscope. b) Line laser with a photomask to prevent the light scattering and improve the contrast between pattern and background.

Although the cells initially responded to the biomolecular pattern, they failed to sense the contrast between the pattern and the background in more extended culture periods. Hence, we switched to a diode laser with higher laser power ranges (30-90 mW). However, the limitation of this diode laser was that it lacked the precision of a confocal microscope. The preliminary tests performed with the diode laser that was built in-house with Onur Bakirman (DWI, Aachen) revealed that the diode line laser at 60 mW for 60s exposure time has a significant ability to decap the caged peptides compared to the confocal laser at 0.35 mW for 35-minute exposure time (**Figure 22a**). The diode line laser was tested with different photomasks to improve its precision.

While the addition of a photomask drastically enhanced the width of the line laser from 30 μm wide to 15 μm wide at its strongest intensity, it could not remove the diffraction gradients created by the photomask, which contributed to 8 μm of additional pattern width (previously 75μm without photomask) (**Figure 22b**).

Similar to [K] peptides, [Q] peptides tethered to PEG hydrogels were decaged using light at 365 nm (Primovo Platform, FZ Jülich). [Q1]-peptide as the linker was employed and rendered biofunctional using GRGDS peptides labeled with fluorophores. The prelabelled biomolecules tethered via transglutaminase reaction PEG backbone can be easily measured using the mean fluorescence. The fluorescence intensity of gels exposed to and protected from UV light is measured using a photodetector (Leica, SP8). The difference between the pattern and the background, though not visually different, is statistically significant (**Figure 23a**). We reason the high fluorescence from the non-photopatterned regions to be due to the unbound, unwashed fluorophores from labeled RGD peptides. The fluorescence intensity distribution along the Z stack reveals that the gel core (Z ~ 0 μm) has a higher fluorescence compared to the edges (Z~100 μm), which are closer to the gel-media interface (**Figure 23b**). The unbound fluoro-RGD must diffuse out of the gels to obtain a strong contrast between the biopattern and the non-patterned regions. The decrease in fluorescence intensity may be due to higher diffusion at interfaces than the core of the hydrogel. While it is essential to create a strong contrast between biopattern and background, an experiment comparing the cell invasion in the photopatterned gels with RGD in gel mixture and RGD incubated as a solution is performed. The hydrogels with caged [K] peptides were used to encapsulate fibroblast spheroids. The gels were photo patterned with similar patterning parameters with a focused laser at 405 nm and cultured for ten days (**Figure 24 a,d)**. The cells are fixed and stained for DAPI to visualize nuclear migration. For gels with Q-RGD in the precursor mixture, higher DAPI stained structures are observed in the biopattern. Some cell migration is observed in all directions from the spheroids; however, a higher concentration of nucleus stained by DAPI is observed exclusively in the 0.6 mM Q-RGD photo-

patterned region (**Figure 24 b,c**). However, in the case of RGD incubated as a solution (**Figure 24 d**), the exclusive nuclear migration was not observed may be due to the lack of contrast between the patterned region and the nonpatterend surrounding regions (**Figure 24 e,f**). RGD in gel mix is preferred over the RGD incubation solution, eliminating the effect of concentration-dependent diffusion of RGD peptides into the gel from the incubation solution.

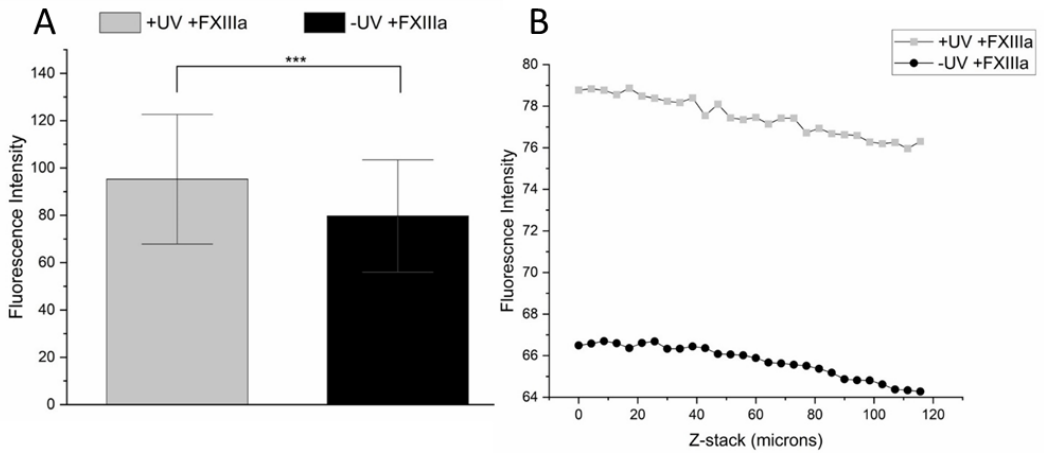

Figure 23. Fluorescence measurements for [Q1]-peptide hydrogels (a) Mean fluorescence intensity for photopatterned hydrogels and non-photopatterned hydrogels across 7 ROIs (n=2) (***p<0.01, error bars represent mean ± s.d) (b) Fluorescence vs Z-stack for photopatterned and non-photopatterned gels in ROI 01 (n=2)

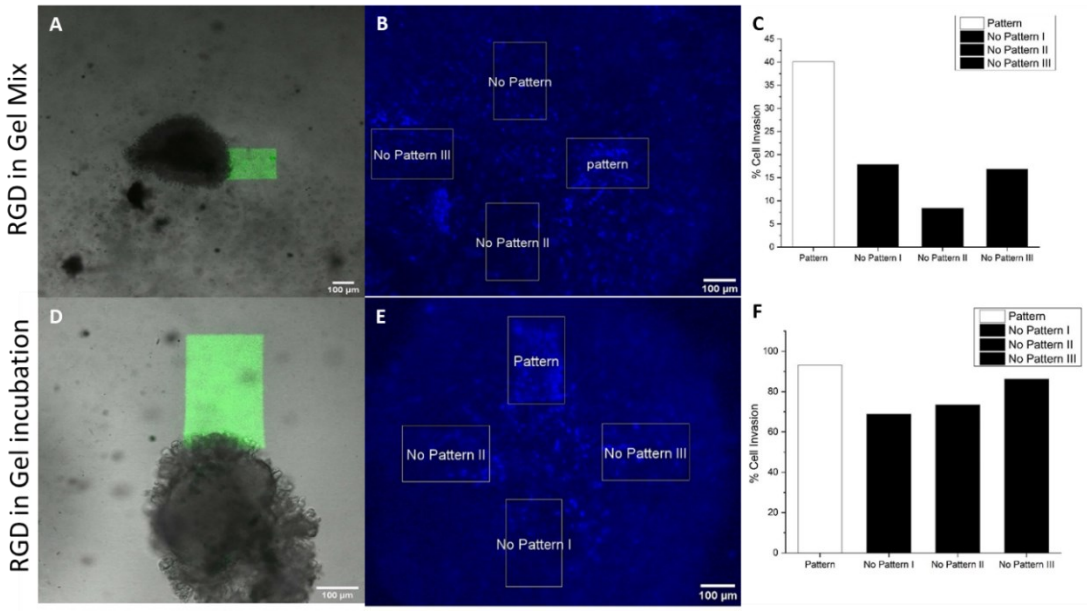

Figure 24. Invitro experiments comparing sequential photopatterning and single-step photopatterning. a) Bright-field images of photo-pattern adjacent to fibroblast spheroids for RGD in gel mix. b) Maximum intensity Z-stack projections of [K]-peptide hydrogels with 0.6 mM Q-RGD in the gel mix stained for DAPI. c) Cell invasion % computation using image analysis to determine increased DAPI levels in RGD in the mix. d) Bright-field images of photo-pattern adjacent to fibroblast spheroids for RGD in incubated solution. e) Maximum intensity Z-stack projections of [K]-peptide hydrogels with RGD in the incubated solution stained for DAPI. f) Cell invasion % computation using image analysis to determine increased DAPI levels in RGD in incubated solution (0.6 mM QRGD).

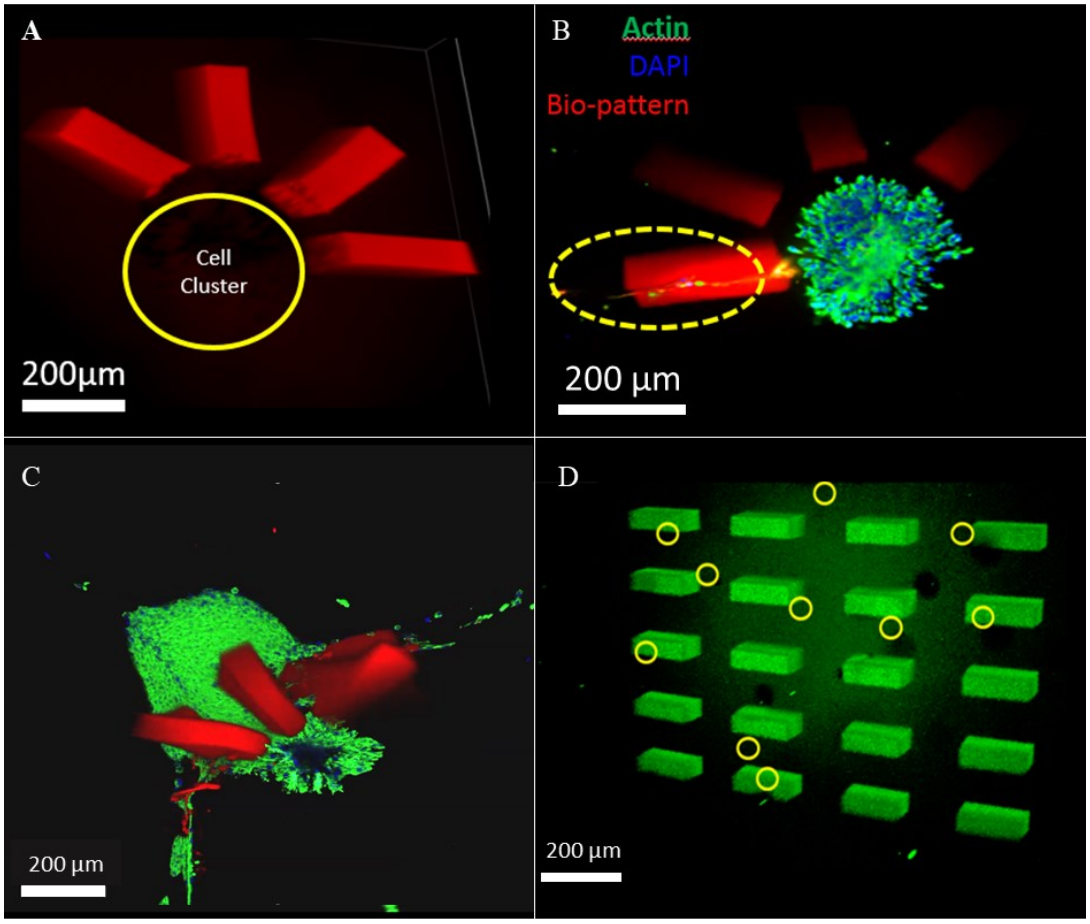

Figure 25. a) Radial RGD biopattern model without the cluster. b) Pattern with L929 cluster at day 4 showing selective migration into one of the arms of the radial pattern. c) L929 cell model remodeling the radial Q-RGD biopattern after 14 days. d) Single-cell grid model.

The pattern architecture was designed based on the cell model using a computer program that can specify the region of interest to be patterned. Several pattern architectures were tested on the nerve cell and DRG/fibroblast cluster models (**Figure 25**). Among the several tested, the radial pattern model for DRG/fibroblast cluster

showed cell migration on day 5 (**Figure 25b**). They remodeled the hydrogel around the cell cluster when the cells were cultured longer (14 days) (**Figure 25c**). The remodeling of the hydrogel is attributed to the local enzymatic degradation induced by the cells and the production of collective ECM by the cell clusters. As a result, the cells tend to stay together and grow out of the cluster together. To minimize the remodeling of the soft hydrogel due to collective cellular forces applied to the gel with a cluster model, a photo pattern model for single cells was designed, and the pattern architecture chosen was the grid model (**Figure 25d**). FN9*-10,12-14, an engineered fibronectin protein fragment, was selected as the biomolecule to pattern grids mimicking the ANISOGEL architecture. It is to be noted that some single cells in the grid model could be exposed to UV as cells are randomly mixed in the gel.

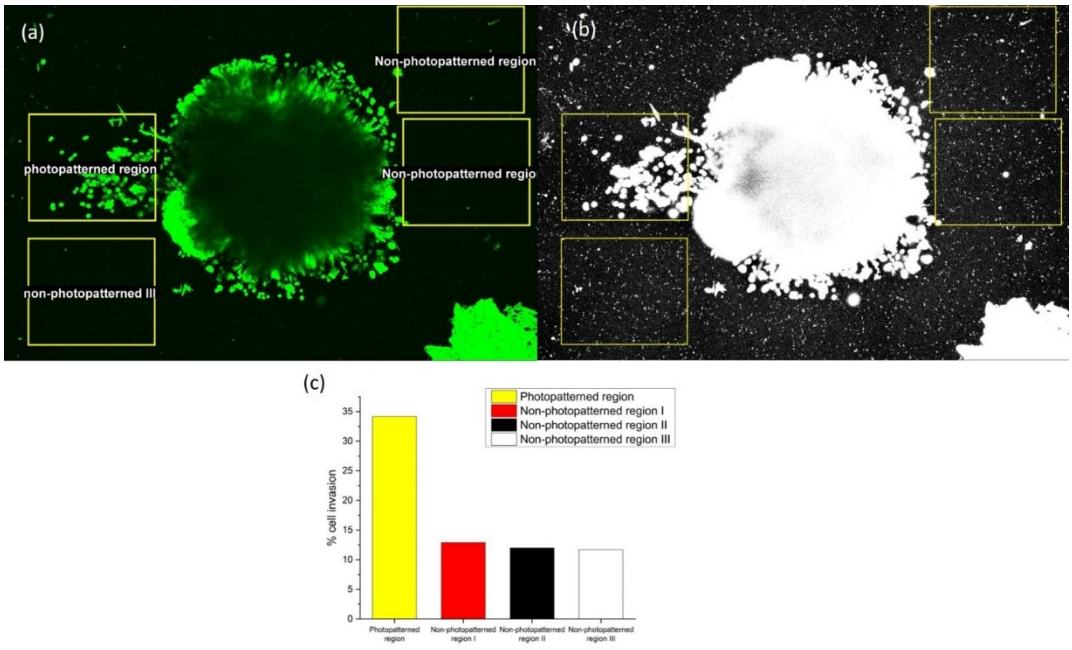

Figure 26. Fluorescent Z-stack images of RGD functionalized via [K]-peptide (a) Regions of interest defined for analysis (b) Image obtained after applying Otsu black & white filter on the fluorescent image (c) % cell invasion in each ROI.

PEG hydrogels made with a composition of 0.6 mM [K] peptide linker with QRGD were irradiated for 10 mins using a confocal laser at 405 nm, with a pixel dwell time of 100 μs and the non-exposed regions of the gels contributed to the negative control. We observed preferential cell migration along the pattern region compared to the

non-patterned regions (**Figure 26 a,b**). By analyzing the cell invasion (area % of actin stain) in 4 distinct the regions of interest (ROIs) around the cell spheroid bearing both light exposed and unexposed regions, a substantial difference in cell invasion in photo patterned regions was observed compared to the non-patterned regions (**Figure 26 c**). Additionally, the cells in the patterned region migrated 358.4±54 μm more than in the non-patterned regions. However, cells are minimally spread, unlike the uncaged K peptides described in previous sections, and inconsistent with the observations from earlier reports.[153,282]

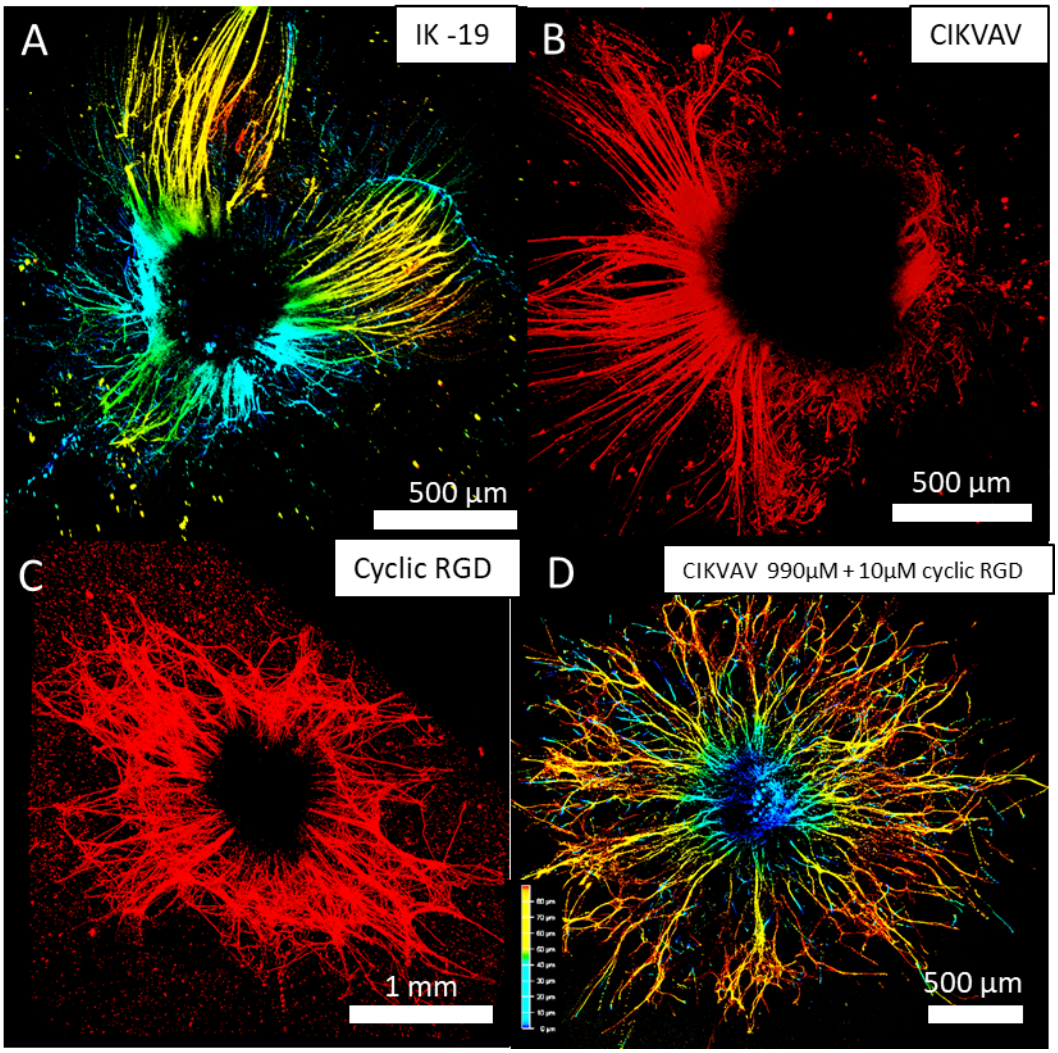

Figure 27. Neurite outgrowth from DRG explant encapsulated in PEG hydrogels with IKVAV-19, CIKVAV, Cyclic RGD peptides, and a combination of IKVAV and cyclic RGD peptides. The cells are stained for β-tubulin.

Uncaged IKVAV peptides (AG Del Campo) were tested in combination with RGD peptides (linear and cyclic) to screen for biomolecule concentrations. IK-19, a 19mer IKVAV peptide (200 µM), shows innervation along multiple planes in the PEG hydrogels (**Figure 27 a**). Since IK-19 is a commercially available product, this peptide cannot be modified with the photocaged groups. Hence, IKVAV bearing a cysteine is designed to bind the IKVAV to the PEG gels and also customized with a photolabile group. Neurite growth was screened in PEG hydrogels with uncaged CIKVAV at concentrations from 200 µM to 1mM (**Figure 27 b)**. Monocyclic RGD peptide was also employed at 200 µM concentrations to test for nerve growth (**Figure 27 b).** In both cases, neurites were able to invade the gel matrix in the presence of the desired biomolecules. Finally, the combination of CIKVAV at 990 µM and RGD peptide at 10 µM showed the most neurite growth in the IKVAV-tethered hydrogels (**Figure 27 d)**. Photopatterning experiments will be performed with this optimum concentration of IKVAV and RGD peptides for DRG growth. Control peptides, such as liner IKVAV, and caged scrambled IKVAV peptides, are tested to ensure the exclusivity of cell adhesion.

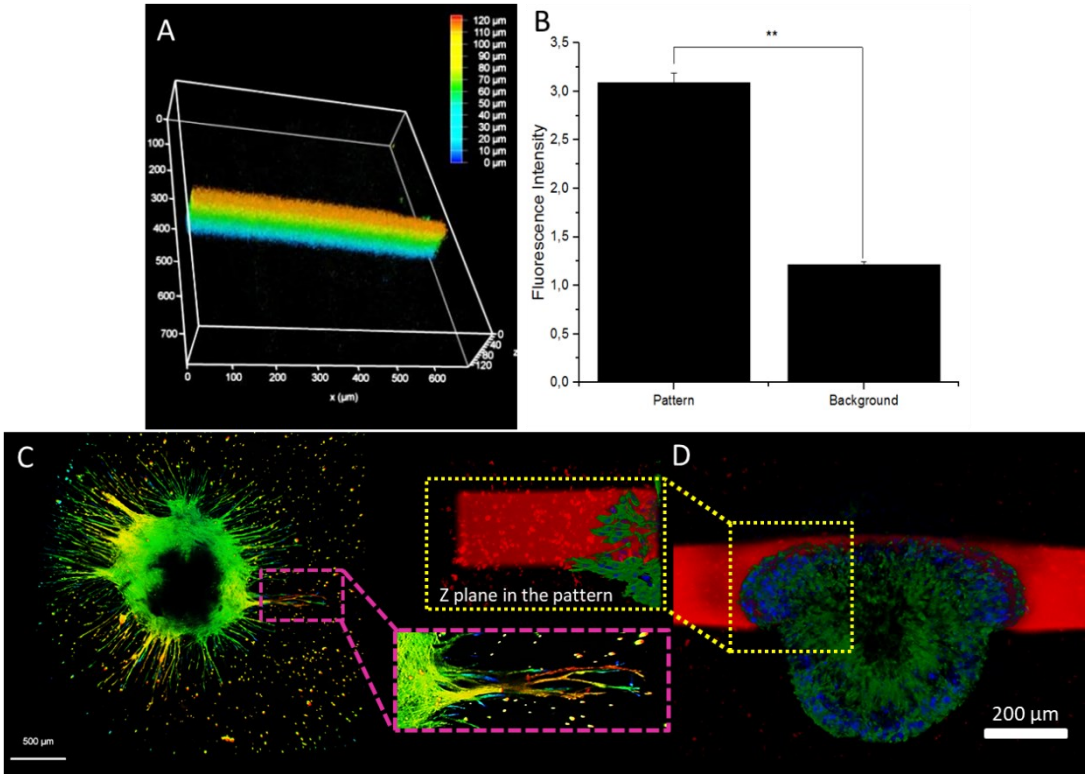

Figure 28. Caged cyclic RGD photo patterning with in vitro studies a) cyclic caged RGD peptide is patterned in 3D PEG hydrogel using 405 nm UV laser. The pattern is visualized with the help of caged fluorescein, which is coupled to the PEG backbone represented as a color-coded z stack pattern (120 µm). b) The mean fluorescence intensity quantified at the

pattern is much higher than its background. c) DRG explants are cultured in 1mM caged cyclic RGD tethered PEG hydrogels. Photodecapping next to the explant showed 3D cell invasion of the neurites; however, this invasion was not exclusive to the patterned region. D) fibroblast spheroids are encapsulated in PEG hydrogels with caged RGD peptides. The photopatterned region is visualized with the help of caged fluorescein. Selective cell migration is observed after 7 days of culture.

PEG hydrogels developed with caged motif on the IKVAV biomolecules like 3-(4,5-dimethoxy-2-nitrophenyl)butan-2-ol (DMNPB) or 2,2'-((3'-(1-hy droxypropan-2-yl)-4'-nitro-[1,1'-biphenyl]-4-yl)azanediyl)bis-(ethan-1-ol) (HANBP)[150] enable spatial patterning after exposure to UV light. These peptides are suitable for binding to the PEG backbone and releasing the caged groups on the trigger. The in vitro studies demonstrate that the cyclic caged RGD peptide, patterned in 3D PEG hydrogel shows statistically higher fluorescence intensity than its background (**Figure 28 a,b**). The DRG explants cultured in such caged peptides do not show preferential growth in the patterned region. This can be reasoned to the on cell demand degradable microenvironment that promotes cell growth in all directions (**Figure 28 c**). However, fibroblast spheroids encapsulated in similar gels responded to the decaged RGD peptides in the pattern and enabled controlled cell invasion and migration. (**Figure 28 d**)

A two-photon laser was used to enhance the biomolecular contrast between the pattern and the background as a promising alternative. The 2-photon laser system creates a voxel of 100 nm diameter, which is then focused inside the 3D hydrogel for high precision exclusive 3D patterns with better resolution in the z-direction. The concentrated laser voxel volume of the two-photon laser at 780 nm and 80 MHz enable successive electronic excitation, which mimics the energy level of a 390 nm UV laser. This allows the photo-labile group to be cleaved off, resulting in a free amine group for further biomolecule tethering. The optimized hydrogel was tested in the two-photon Nano scribe system (**Figure 29**) for different laser intensities/power scaling and slicing distances. Although the contrast with the background can still be improved, there is a great potential to use this system by further optimization.

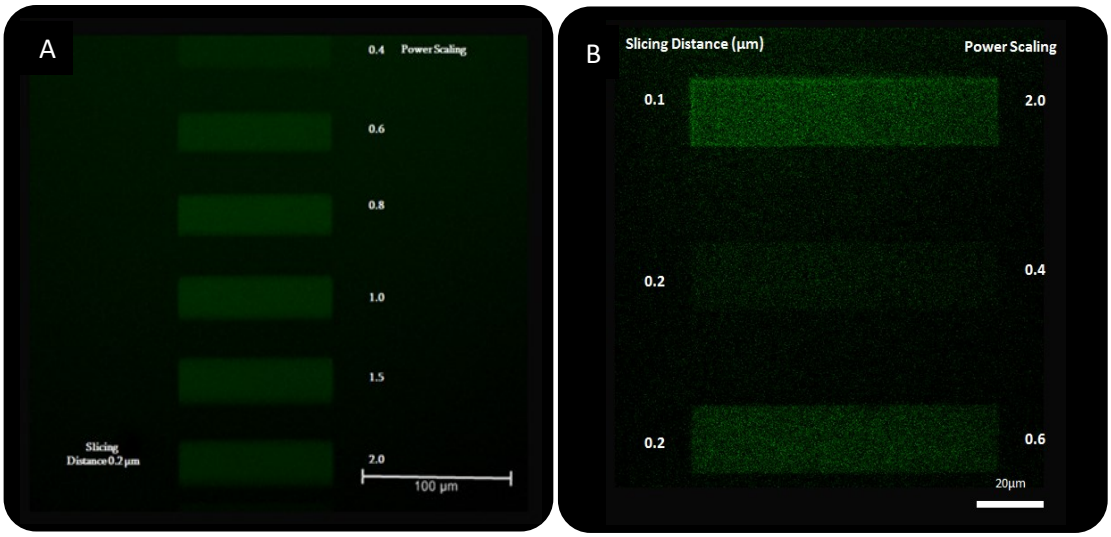

Figure 29. Pattern with two-photon laser system A) Pattern with increasing power scaling. b) Pattern with increased slicing distance with laser at 780nm at 80 MHz.

6.3 Conclusion

Spatial heterogeneities are fabricated in aECM to mimic hierarchical native ECM. While unmodified PEG hydrogels cannot recapitulate this dynamic microenvironment and resist protein absorption, powerful photopatterning strategies are essential to developing the 3D spatial distribution of biochemical cues inside a synthetic matrix. This chapter involves the fabrication of PEG hydrogels and tailoring them toward developing a robust photopatterning platform for 3D-controlled and directed cell growth. The hydrogels are optimized for their biomechanical properties like stiffness and degradability, suitable for fibroblasts and nerve cell growth. Biochemical cues are incorporated in the form of peptides and ECM fragments (Q-RGD, GRGDS YIGSR, IKVAV, and FN9*-10, 12-14) to support and stimulate the growth. Additionally, integrin-binding domains are screened on 2D PEG-NCO thin films. Optimal RGD, YIGSR, and IKVAV concentrations enable fibroblast cells to thrive inside the 3D aECM matrix. To render the gel photolabile, K and Q peptide linkers tethered to their respective biomolecules were screened at different concentrations. Later, these were caged to enable controlled spatial biopattern after exposure to light. Biopatterns in hydrogels with caged K residues were observed to

invade both pattern and non-patterned regions due to excessive ECM production. However, the RGD biopattern regions showed higher cell migration distances and more nuclei confinement. Biopatterns with caged Q peptides residues were able to tether biomolecules with any peptides or proteins with a free amine, translating enzymatic patterning to be a powerful tool in fabricating hierarchical scaffolds.

6.4 Experimental Section

Synthetic 3D PEG hydrogel formulation. 4 arm 20 kDa, with pentaerythritol core PEG-VS (Sunbrite, PTE-200VS, NOF Europe) and custom made (Biomatic, Pepscan, Caslo) linear crosslinker sequence was designed with di-thiol end groups to facilitate Michel type addition on both the ends. The middle part of the peptide sequence is the collagen-based MMP site which is readily cleavable in the presence of cellular protease at 37°C, pH 7.4. The sequence is GCREGPQG↓IWGQERCG (16W, 1717.93 Da) with purity > 95%. Stotiomeic functional ratios of PEG-VS and 16W are allowed to react to form bulk gels. The hydrogel is rendered photolabile by incorporating a caged lysine peptide F[K(Nvoc)]GGERCG ([K], Bachem, Germany), with nitroveratryloxycarbonyl (Nvoc) as the caging group and cysteine with which it binds to the backbone of the PEG. The hydrogels were prepared in a 10 µl angiogenesis µ-slide (ibidi®, Germany) with a glass bottom, and after gel formation, the gels were allowed to swell in 40 µl of cell cultivation media (DMEM).

Photo patterning of hydrogels. A confocal microscope (Leica, TCS SP8) equipped with a 405 nm diode laser (max. 7 mW at the focal plane, 0.3 mW measured with Thor Labs detector) was used to pattern the hydrogel. A 10 x/0.30 air objective was used to pattern the gels using the fluorescence recovery after photobleaching (FRAP) setting. The region of interest (ROI) facilitates controlled patterns in the x and y planes. The format of the bleach was varied based on the size of the photo pattern desired to start from 80 pixels to 1024 pixels. The control over the z-axis was satisfied due to the inverted positioning of the laser beam, which sufficed the decaging of [K], creating a

biochemical gradient along the z plane. The laser was irradiated for 300 iterations at 100 µs pixel dwell time. The speed of the pattern was set between 10 Hz to 200 Hz.

Incorporation of bio-functional proteins/peptides. The hydrogels after laser treatment were incubated in a solution mixture containing (2 U ml^{-1} of FXIIIa [Fibrogammin, CSL Behring, Germany, activated using thrombin in the presence of 10 mM TRIS, 150 mM NaCl and 25 mM of $CaCl_2$]), 10 mM $CaCl_2$, 90 mM of HEPES at pH 7.5 in cell cultivation media) 150 µM protein/peptide of interest (POI). The POI must bear an NQEQVSPL sequence that binds to the decaged lysine in the PEG gel in the presence of FXIIIa. To visually observe the patterned regions, the protein was fluorescently labeled using maleimide-functionalized Alexa Fluor dye. The solution mixture was incubated for 90 minutes at room temperature, gently shaking at 30 rpm. The solution mixture was washed with cell cultivation media overnight at 37 °C.

Two-Step Factor XIII linked biofunctionalization. 3.4 % PEG hydrogel precursor solutions were prepared, incorporating desired concentration of [K]-peptide or K -peptide, or [Q]-peptide or Q peptide, and allowed to crosslink for 1h in a humidified chamber. After photopatterning and washing with PBS to remove photodegradation products, the free K or Q-peptide linked hydrogels are incubated in a solution with the desired concentration of Q-RGD or K-RGD, 20 U ml-1 FXIIIa, 10 mM CaCl2 10 mM HEPES in Serum-free DMEM for 90 mins. Upon washing to remove unbound biomolecules, the hydrogels are cultured for 7 days at 37 °C, 5% CO_2 in media, with the medium being exchanged every 2-3 days.

One-Step Factor XIII linked biofunctionalization. A one-step biofunctionalization protocol was adapted from Broguiere et al.[154] Hydrogel precursor solutions now are altered by directly incorporating K- or Q-peptide with their complementary RGD peptides (QRGD or K-peptide hydrogels, respectively), 20 U/mL FXIIIa and Ehrbar 10X buffer. Cells were cultured for 7 days at 37 °C, with 5% CO2 in the culture medium, which is exchanged every 2-3 days.

sPEG-NCO films. Six arms, 12 kDa star PEG (sPEG), functionalized with isocyanate (NCO) groups, are used to dip-coat the bottom layer of an amine-functionalized 96 well plate (NH-covalink, Corning). Due to in situ gelation of terminal isocyanate (NCO) in aqueous solutions, the gels render surfaces ideal for immobilizing proteins. PEG-NCO stored in a nitrogen atmosphere is diluted to 100 mg/mL with tetrahydrofuran. Further, the sPEG-NCO is diluted with water to a final concentration of 10 mg/mL and pre-cured for 5 minutes at RT. The solution is then transferred and incubated on the amine covalink wells for 15 minutes at RT. The unbound sPEG-NCO is discarded and the NCO coated wells are further washed with sterile water and sterilized under UV for 30 minutes. The desired concentration of amine-bearing protein/peptide is incubated on the sPEG-NCO coated well plates for one hour at RT and 23 hours at 4 °C to covalently binding. Finally, desired cells such as dissociated primary nerve cells are seeded at 10,000 cells per well (96 well plate area) are cultured for 3-7 days.

Protein Fragment FNIII9*-10/12-14 production. FNIII9*-10/12-14 is a recombinant fragment of fibronectin (FN), engineered to comprise the 9th- 10th type III FN repeat (FNIII9-10), containing major integrin-binding domains and the FNIII12-14, which binds to nerve growth factors, such as NT-3 and BDNF. Such protein fragments offer a cell adhesion environment adjacent to the growth factors binding site proving a synergistic growth ambiance. These protein fragments are engineered and produced in E. Coli, and their production and purification are explained in detail in Chapter 4

YIGSR. The Laminin-derived short pentapeptide H-Tyr-Ile-Gly-Ser-Arg-NH_2 (YIGSR) of relative molecular mass of 593.68 [Bachem, Germany].

Chick embryo dissection. Fertilized chick eggs are obtained from a local farm and incubated at 37 °C with 40% - 50% relative humidity (RH) for 10 days. The egg was opened on the 10^{th} day and decapitated. The body is pinned to a pin-dish, and a vertical incision is made from the chest to the abdomen to remove all the organelle until the spinal cord is reached. The body is repeatedly flushed with Hank's Balanced

Salt Solution (HBSS) [Gibco, Germany] to remove blood traces. The DRG was removed with forceps, and it was detached from the spinal cord and finally stored in an HBSS solution until further use.

Dissociation of Dorsal root ganglion. The DRGs which were collected in the HBSS are treated with 10 vol % of 10x Trypsin (Sigma Aldrich) for 30 minutes at 37 °C. They are then transferred to a 50 ml falcon and triturated using a glass pipette along with 3 ml of fresh media. The supernatant of this triturated mixture is transferred to a new falcon tube while the sediment is re-triturated multiple times. Additionally, 3 ml of fresh media is added every time before the titration. The dissociated supernatant is transferred to a Petri dish for panning for 2 hours at 37 °C. Here the fibroblasts adhere to the cell culture dish while the nerve cells are still suspended. The supernatant after centrifugation is re-suspended with fresh cell cultivation media and 20 ng/ml of nerve growth factor (NGF). The dissociated cells were seeded at a cell density of 10000 cells/96 well plate area.

Preparation of L929 Spheroids. Fibroblast cell spheroids were made from a hanging drop model, where a master drop mix was prepared by mixing a defined amount of cells with 20% methylcellulose (Sigma) in media. Droplets (30µL) of the master mix were cast on 100 mm Petri dishes with low attachment surfaces and inverted. The bottom part is now supplemented with 3 mL PBS to create a humidity chamber for the hanging drops. The setup is incubated overnight at 37 °C and collected after washing once with media.

UV-Vis Spectra. 600 µL of 400 µM stock Caged peptide solution dispersed in HEPES buffer was placed in a quartz cuvette and set in front of a UV lamp and LEDs (λ = 254 nm, 365 nm) at a distance of 10 cm. UV-Vis spectra (V-780 Jasco) were measured after exposing the solutions to UV light for 10, 20, 30, 45, and 60 mins, respectively. LEDs emitting light at 365 nm were obtained from Dr. Rostislav Vinokur.

Culture Media. Dulbecco's Modified Eagle Medium (DMEM) supplemented with 10% Fetal Bovine Serum (FBS) and 1% antimycotic and antibiotic (AMB) as antibiotics for nerve cells and Roswell Park Memorial Institute (RPMI 1640) with 10% Fetal Bovine Serum (FBS) and 1% antimycotic and antibiotic (AMB) as antibiotics for L929 fibroblast.

Immunostaining. Nerve cells were stained with neural class III β-tubulin (TUJ1, BioLegend). This primary antibody is highly specific and does not even recognize β-tubulin in glial cells. L929 Cells are stained for Actin, Nucleus, and ECM proteins. Secondary antibody available commercially with a range of wavelengths is used. After 5-7 days of cultivation, the cells are washed thrice (30 minutes each) with phosphate buffer saline (PBS) (VRW, 1x) to remove media and other proteins adhering to the gel. The gels are then fixed for 30 minutes in paraformaldehyde, re-washed three times with PBS, and treated with 0.1% Triton X-100 for 40 mins. After this prep, the cells are stained with the primary antibody overnight at room temperature, followed by the secondary antibody for 4 hours. The cells are washed multiple times in between with PBS to remove unbound antibodies.

Ellman's Assay. The concentration of free thiols in solutions is quantified by measuring using Ellman's assay. We employ this technique to measure the thiols in the precursor solution. A solution comprising of 12.5 μL of Ellman's reagent (4 mg/mL of 5,5'-dithiobis-(2-nitrobenzoic acid), DTNB) in 1 mL 0.1 M phosphate buffer pH 8.0) is diluted in 625 μL 0.1 M phosphate buffer pH 8.0 to obtain the Ellman's reaction solution. The DTNB reacts with thiols, forming 2-nitro-5-thiobenzoate (absorbing at λ= 412 nm). A calibration curve based on the respective absorbance after reaction with cysteine in solution is used to determine the thiol concentrations.

MTS assay. Cell proliferation assay using Masson's trichrome staining (MTS) is performed with a starting cell concentration of 10,000 cells/ 96 well plate area. After 72h of cell culture on the substrates, media is replaced with MTS solution (diluted in

media) and incubated for 2 h at 37 °C. A tissue culture polystyrene (TCPS) dish with the same surface area is used as a control. Absorption is measured at λ = 490 nm using a microplate reader (Biotek® Synergy HT, USA).

Live Dead Assay. Live/Dead staining (Live/Dead kit for mammalian cells, Thermofischer) 2 µL of 2 mM Ethidium homodimer-1 in DMSO/H2O 1:4 (v/v) and 0.5 µL of 4 mM Calcein AM in anhydrous DMSO are dissolved in 1000 µL PBS H 7.4 and added to cells with cell media. Samples are incubated at 37 °C for 40 min and washed with PBS. Subsequently, cells are analyzed using fluorescence microscopy (λ=530 nm for live cells and λ=645 nm for dead cells).

Statistics. Statistical analysis was done using Origin 2020b for Windows. A one-way analysis of variants (ANOVA) was performed with Bonferroni and Tukey comparisons. p-values for significance were represented with star: $^{*}p<0.05$, $^{**}p<0.01$, $^{***}p<0.001$.

References

1. Hubbell, J. A. Biomaterials in tissue engineering. *Biotechnology. (N. Y).* **13**, 565–576 (1995).

2. Yannas, I. V., Burke, J. F., Orgill, D. P. & Skrabut, E. M. Wound tissue can utilize a polymeric template to synthesize a functional extension of skin. *Science (80-.).* **215**, 174–176 (1982).

3. Uhthoff, H. K., Poitras, P. & Backman, D. S. Internal plate fixation of fractures: Short history and recent developments. *J. Orthop. Sci.* **11**, 118–126 (2006).

4. Schwartz, A. B., Cui, X. T., Weber, D. J. J. & Moran, D. W. Brain-Controlled Interfaces: Movement Restoration with Neural Prosthetics. *Neuron* **52**, 205–220 (2006).

5. Hughes, D. L., Hughes, A., Soonawalla, Z., Mukherjee, S. & O'neill, E. Dynamic physiological culture of ex vivo human tissue: A systematic review. *Cancers (Basel).* **13**, (2021).

6. Kim, J., Koo, B. K. & Knoblich, J. A. Human organoids: model systems for human biology and medicine. *Nat. Rev. Mol. Cell Biol.* **21**, 571–584 (2020).

7. Bishehsari, F. Organ-Chip Models : Opportunities for Precision Medicine in Pancreatic Cancer. 1–14 (2021).

8. Siemionow, M., Bozkurt, M. & Zor, F. Regeneration and repair of peripheral nerves with different biomaterials: Review. *Microsurgery* **30**, 574–588 (2010).

9. Rice, J. J. *et al.* Engineering the Regenerative Microenvironment with Biomaterials. 57–71 (2013) doi:10.1002/adhm.201200197.

10. Jucker, M. The benefits and limitations of animal models for translational research in neurodegenerative diseases. *Nat. Med.* **16**, 1210–1214 (2010).

11. Duval, K. *et al.* Modeling Physiological Events in 2D vs. 3D Cell Culture. *Physiology* **32**, 266–277 (2017).

12. Catoira, M. C., Fusaro, L., Di Francesco, D., Ramella, M. & Boccafoschi, F. Overview of natural hydrogels for regenerative medicine applications. *J. Mater. Sci. Mater. Med.* **30**, (2019).

13. Frantz, C., Stewart, K. M. & Weaver, V. M. The extracellular matrix at a glance. *J. Cell Sci.* **123**, 4195–4200 (2010).

14. Yanagishita, M. Function of proteoglycans in the extracellular matrix. *Pathol. Int.* **43**, 283–293 (1993).

15. Watt, F. M. & Huck, W. T. S. Role of the extracellular matrix in regulating stem cell fate. *Nat. Rev. Mol. Cell Biol.* **14**, 467–473 (2013).

16. Bonnans, C., Chou, J. & Werb, Z. Remodelling the extracellular matrix in development and disease. *Nat. Rev. Mol. Cell Biol.* **15**, 786–801 (2014).

17. Yu, Y., Alkhawaji, A., Ding, Y. & Mei, J. Decellularized scaffolds in regenerative medicine. *Oncotarget; Vol 7, No 36* (2016).

18. Huang, G. *et al.* Functional and Biomimetic Materials for Engineering of the Three-Dimensional Cell Microenvironment. *Chem. Rev.* **117**, 12764–12850 (2017).

19. Drury, J. L. & Mooney, D. J. Hydrogels for tissue engineering: Scaffold design variables and applications. *Biomaterials* **24**, 4337–4351 (2003).

20. McKinnon, D. D., Domaille, D. W., Cha, J. N. & Anseth, K. S. Biophysically defined and cytocompatible covalently adaptable networks as viscoelastic 3d cell culture systems. *Adv. Mater.* **26**, 865–872 (2014).

21. Truong, V. X., Donderwinkel, I. & Frith, J. E. Bioorthogonal hydrogels by thiol–halide click crosslinking with fast gelation time and tunable stability in aqueous media. *J. Polym. Sci. Part A Polym. Chem.* **57**, 1872–1876 (2019).

22. Patterson, J. & Hubbell, J. A. Enhanced proteolytic degradation of molecularly engineered PEG hydrogels in response to MMP-1 and MMP-2. *Biomaterials* **31**, 7836–7845 (2010).

23. Sakai, T. *et al.* Design and fabrication of a high-strength hydrogel with ideally homogeneous network structure from tetrahedron-like macromonomers. *Macromolecules* **41**, 5379–5384 (2008).

24. Ehrbar, M. *et al.* Enzymatic formation of modular cell-instructive fibrin analogs for tissue engineering. *Biomaterials* **28**, 3856–3866 (2007).

25. Licht, C. *et al.* Synthetic 3D PEG-Anisogel Tailored with Fibronectin Fragments Induce Aligned Nerve Extension. *Biomacromolecules* **20**, 4075–4087 (2019).

26. Lutolf, M. P. *et al.* Synthetic matrix metalloproteinase-sensitive hydrogels for the conduction of tissue regeneration: Engineering cell-invasion characteristics. *Proc. Natl. Acad. Sci. U. S. A.* **100**, 5413–5418 (2003).

27. Seliktar, D., Zisch, A. H., Lutolf, M. P., Wrana, J. L. & Hubbel, J. A. MMP-2 sensitive, VEGF-bearing bioactive hydrogels for promotion of vascular healing. *J. Biomed. Mater. Res. - Part A* (2004) doi:10.1002/jbm.a.20091.

28. Mitchell, A. C., Briquez, P. S., Hubbell, J. A. & Cochran, J. R. Engineering growth factors for regenerative medicine applications. *Acta Biomater.* **30**, 1–12 (2016).

29. Martino, M. M. *et al.* Controlling integrin specificity and stem cell differentiation in 2D and 3D environments through regulation of fibronectin domain stability. *Biomaterials* **30**, 1089–1097 (2009).

30. Martino, M. M. & Hubbell, J. A. The 12th–14th type III repeats of fibronectin

function as a highly promiscuous growth factor-binding domain. *FASEB J.* **24**, 4711–4721 (2010).

31. Martino, M. M. *et al.* Engineering the growth factor microenvironment with fibronectin domains to promote wound and bone tissue healing. *Sci. Transl. Med.* **3**, (2011).

32. Hersel, U., Dahmen, C. & Kessler, H. RGD modified polymers: Biomaterials for stimulated cell adhesion and beyond. *Biomaterials* **24**, 4385–4415 (2003).

33. Massia, S. P., Rao, S. S. & Hubbell, J. A. Covalently immobilized laminin peptide Tyr-Ile-Gly-Ser-Arg (YIGSR) supports cell spreading and co-localization of the 67-kilodalton laminin receptor with alpha-actinin and vinculin. *J. Biol. Chem.* **268**, 8053–8059 (1993).

34. Tashiro, K.-I. *et al. A Synthetic Peptide Containing the IKVAV Sequence from the A Chain of Laminin Mediates Cell Attachment, Migration, and Neurite Outgrowth*.* *THE JOURNAL OF BIOLOGICAL CHEMISTRY* vol. 264 (1989).

35. Defined Substrates for Human Embryonic ARTICLE Stem Cell Growth Identified from Surface Arrays. *Am. J. Chem. Biol.* **2**, 337–346 (2007).

36. Benoit, D. S. W. & Anseth, K. S. The effect on osteoblast function of colocalized RGD and PHSRN epitopes on PEG surfaces. *Biomaterials* **26**, 5209–5220 (2005).

37. Ali, S., Saik, J. E., Gould, D. J., Dickinson, M. E. & West, J. L. Immobilization of Cell-Adhesive Laminin Peptides in Degradable PEGDA Hydrogels Influences Endothelial Cell Tubulogenesis. *Biores. Open Access* **2**, 241–249 (2013).

38. Schense, J. C., Bloch, J., Aebischer, P. & Hubbell, J. A. Enzymatic incorporation of bioactive peptides into fibrin matrices enhances neurite extension. *Nat. Biotechnol.* **18**, 415–419 (2000).

39. Mas-Moruno, C. *et al.* αvβ3- or α5β1-Integrin-Selective Peptidomimetics for Surface Coating. *Angew. Chemie - Int. Ed.* **55**, 7048–7067 (2016).

40. Vedaraman, S. *et al.* Bicyclic RGD peptides enhance nerve growth in synthetic PEG-based ANISOGELS. 3–5 (2021).

41. Kapp, T. G. *et al.* A comprehensive evaluation of the activity and selectivity profile of ligands for RGD-binding integrins. *Sci. Rep.* **7**, 1–13 (2017).

42. Babu, S., Albertino, F., Omidinia Anarkoli, A. & De Laporte, L. Controlling Structure with Injectable Biomaterials to Better Mimic Tissue Heterogeneity and Anisotropy. *Adv. Healthc. Mater.* **10**, 1–22 (2021).

43. Betsch, M. *et al.* Incorporating 4D into Bioprinting: Real-Time Magnetically Directed Collagen Fiber Alignment for Generating Complex Multilayered Tissues. *Adv. Healthc. Mater.* **7**, 1–9 (2018).

44. Nerger, B. A., Brun, P. T. & Nelson, C. M. Microextrusion printing cell-laden networks of type i collagen with patterned fiber alignment and geometry. *Soft Matter* **15**, 5728–5738 (2019).

45. Prendergast, M. E., Davidson, M. D. & Burdick, J. A. A biofabrication method to align cells within bioprinted photocrosslinkable and cell-degradable hydrogel constructs via embedded fibers A biofabrication method to align cells within bioprinted photocrosslinkable and cell-degradable hydrogel constructs via. (2021).

46. Sideris, E. *et al.* Particle Hydrogels Based on Hyaluronic Acid Building Blocks. *ACS Biomater. Sci. Eng.* **2**, 2034–2041 (2016).

47. Truong, N. F. *et al.* Microporous annealed particle hydrogel stiffness, void space size, and adhesion properties impact cell proliferation, cell spreading, and gene transfer. *Acta Biomater.* (2019) doi:10.1016/j.actbio.2019.02.054.

48. Richard, S. *et al.* 3D Magnetic Alignment of Cardiac Cells in Hydrogels. *ACS Appl. Bio Mater.* **3**, 6802–6810 (2020).

49. Feng, Q. *et al.* Uptake, distribution, clearance, and toxicity of iron oxide nanoparticles with different sizes and coatings. *Sci. Rep.* **8**, 1–13 (2018).

50. Antman-passig, M. Remote Magnetic Orientation of 3D Collagen Hydrogels for Directed Neuronal Regeneration. (2016) doi:10.1021/acs.nanolett.6b00131.

51. Rose, J. C. *et al.* Nerve Cells Decide to Orient inside an Injectable Hydrogel with Minimal Structural Guidance. *Nano Lett.* **17**, 3782–3791 (2017).

52. Omidinia-Anarkoli, A. *et al.* An Injectable Hybrid Hydrogel with Oriented Short Fibers Induces Unidirectional Growth of Functional Nerve Cells. *Small* **13**, 1–8 (2017).

53. Rose, J. C. *et al.* How Much Physical Guidance is Needed to Orient Growing Axons in 3D Hydrogels? *Adv. Healthc. Mater.* **2000886**, 2000886 (2020).

54. Rose, J. C. *et al.* Biofunctionalized aligned microgels provide 3D cell guidance to mimic complex tissue matrices. *Biomaterials* **163**, 128–141 (2018).

55. Dong, Y. *et al.* Engineering the Cell Microenvironment Using Novel Photoresponsive Hydrogels. *ACS Appl. Mater. Interfaces* **10**, 12374–12389 (2018).

56. DeForest, C. A. & Anseth, K. S. Cytocompatible click-based hydrogels with dynamically tunable properties through orthogonal photoconjugation and photocleavage reactions. *Nat. Chem.* **3**, 925–931 (2011).

57. Marcus, M. *et al.* Interactions of Neurons with Physical Environments. *Adv. Healthc. Mater.* **6**, (2017).

58. Pires, L. R. & Pêgo, A. P. Bridging the lesion-engineering a permissive substrate for nerve regeneration. *Regen. Biomater.* **2**, 203–214 (2015).

59. Kevin C. Flynn. The cytoskeleton and neurite initiation. *Bioarchitecture* **3**, 86–109 (2013).

60. Kamila Mohamed Om Alblazi*, C. H. S. ellular protrusions-Lamellipodia, Filopodia, Ivadopodia and Podosome. *Asian Pacific J. Cancer Prev. J Cancer Prev* **16**, 2187–2191 (2015).

61. Kahn, O. I. & Baas, P. W. Microtubules and Growth Cones: Motors Drive the Turn. *Trends Neurosci.* **39**, 433–440 (2016).

62. Miller, K. E. & Suter, D. M. An Integrated Cytoskeletal Model of Neurite Outgrowth. *Front. Cell. Neurosci.* **12**, 1–19 (2018).

63. Geraldo, S. & Gordon-Weeks, P. R. Cytoskeletal dynamics in growth-cone steering. *J. Cell Sci.* **122**, 3595–3604 (2009).

64. Kalil, K. & Dent, E. W. Touch and go: Guidance cues signal to the growth cone cytoskeleton. *Curr. Opin. Neurobiol.* **15**, 521–526 (2005).

65. Heckman, C. A. & Plummer, H. K. Filopodia as sensors. *Cell. Signal.* **25**, 2298–2311 (2013).

66. Jang, K. J. *et al.* Two distinct filopodia populations at the growth cone allow to sense nanotopographical extracellular matrix cues to guide neurite outgrowth. *PLoS One* **5**, (2010).

67. Maskery, S. M., Buettner, H. M. & Shinbrot, T. Growth cone pathfinding: A competition between deterministic and stochastic events. *BMC Neurosci.* **5**, 1–9 (2004).

68. Kerstein, P. C., Nichol IV, R. H. & Gomez, T. M. Mechanochemical regulation of growth cone motility. *Front. Cell. Neurosci.* **9**, 1–16 (2015).

69. Chua, J. S. *et al.* Extending neurites sense the depth of the underlying topography during neuronal differentiation and contact guidance. *Biomaterials* **35**, 7750–7761 (2014).

70. Hoffman-kim, D., Mitchel, J. A. & Bellamkonda, R. V. Topography, Cell Response, and Nerve Regeneration. *Annu. Rev. Biomed. Eng.* **12**, 203–231 (2010).

71. Thompson, D. M. & Buettner, H. M. Neurite outgrowth is directed by schwann cell alignment in the absence of other guidance cues. *Ann. Biomed. Eng.* **34**, 669–676 (2006).

72. Kilinc, D., Blasiak, A. & Lee, G. U. Microtechnologies for studying the role of mechanics in axon growth and guidance. *Front. Cell. Neurosci.* **9**, 1–8 (2015).

73. Simitzi, C., Ranella, A. & Stratakis, E. Controlling the morphology and outgrowth of nerve and neuroglial cells: The effect of surface topography. *Acta Biomater.* **51**, 21–52 (2017).

74. Koser, D. E. *et al.* Mechanosensing is critical for axon growth in the developing brain. *Nat. Neurosci.* **19**, 1592–1598 (2016).

75. Simitzi, C. *et al.* Laser fabricated discontinuous anisotropic microconical substrates as a new model scaffold to control the directionality of neuronal network outgrowth. *Biomaterials* **67**, 115–128 (2015).

76. Ballester-Beltrán, J., Biggs, M. J. P., Dalby, M. J., Salmerón-Sánchez, M. & Leal-Egaña, A. Sensing the Difference: The Influence of Anisotropic Cues on Cell Behavior. *Front. Mater.* **2**, 1–12 (2015).

77. Repic, T., Madirazza, K., Bektur, E. & Sapunar, D. Characterization of dorsal root ganglion neurons cultured on silicon micro-pillar substrates. *Sci. Rep.* **6**, 1–10 (2016).

78. Mattotti, M., Micholt, L., Braeken, D. & Kovačić, D. Characterization of spiral ganglion neurons cultured on silicon micro-pillar substrates for new auditory neuro-electronic interfaces. *J. Neural Eng.* **12**, (2015).

79. Kundu, A. *et al.* Superimposed topographic and chemical cues synergistically guide neurite outgrowth. *Lab Chip* **13**, 3070–3081 (2013).

80. Li, W. *et al.* Large-scale topographical screen for investigation of physical neural-guidance cues. *Sci. Rep.* **5**, 1–8 (2015).

81. Nguyen, A. T., Sathe, S. R. & Yim, E. K. F. From nano to micro: Topographical scale and its impact on cell adhesion, morphology and contact guidance. *J. Phys. Condens. Matter* **28**, (2016).

82. Rose, J. C. *et al.* Nerve Cells Decide to Orient inside an Injectable Hydrogel with Minimal Structural Guidance. *Nano Lett.* **17**, 3782–3791 (2017).

83. Rose, J. C. & De Laporte, L. Hierarchical Design of Tissue Regenerative Constructs. *Adv. Healthc. Mater.* **7**, 1–31 (2018).

84. Vedaraman, S. *et al.* Anisometric Microstructures to Determine Minimal Critical Physical Cues Required for Neurite Alignment. *Adv. Healthc. Mater.* **2100874**, 1–11 (2021).

85. Baker, B. M. & Chen, C. S. Deconstructing the third dimension – how 3D culture microenvironments alter cellular cues. *J. Cell Sci.* **125**, 3015 LP – 3024 (2012).

86. Kay, R. R., Langridge, P., Traynor, D. & Hoeller, O. Changing directions in the study of chemotaxis. **9**, (2008).

87. Trappmann, B. *et al.* Matrix degradability controls multicellularity of 3D cell migration. *Nat. Commun.* **8**, 1–8 (2017).

88. Mosiewicz, K. A. *et al.* In situ cell manipulation through enzymatic hydrogel photopatterning. *Nat. Mater.* (2013) doi:10.1038/nmat3766.

89. Hardy, T. A. Spinal Cord Anatomy and Localization. *Contin. Lifelong Learn. Neurol.* **27**, (2021).

90. Ahuja, C. S. *et al.* Traumatic spinal cord injury - Repair and regeneration. *Clin. Neurosurg.* **80**, S22–S90 (2017).

91. Anwar, M. A., Al Shehabi, T. S. & Eid, A. H. Inflammogenesis of Secondary Spinal Cord Injury. *Front. Cell. Neurosci.* **10**, 1–24 (2016).

92. Silva, N. A., Sousa, N., Reis, R. L. & Salgado, A. J. From basics to clinical: A comprehensive review on spinal cord injury. *Prog. Neurobiol.* **114**, 25–57 (2014).

93. Perale, G. *et al.* Hydrogels in spinal cord injury repair strategies. *ACS Chem. Neurosci.* **2**, 336–345 (2011).

94. Carballo-molina, O. A. & Velasco, I. Hydrogels as scaffolds and delivery systems to enhance axonal regeneration after injuries. **9**, 1–12 (2015).

95. Tabesh, H. *et al.* The role of biodegradable engineered scaffolds seeded with Schwann cells for spinal cord regeneration. *Neurochem. Int.* **54**, 73–83 (2009).

96. Zhang, N., Yan, H. & Wen, X. Tissue-engineering approaches for axonal guidance. *Brain Res. Rev.* **49**, 48–64 (2005).

97. Ji, W. *et al.* Tissue engineering is a promising method for the repair of spinal cord injuries (Review). *Exp. Ther. Med.* **7**, 523–528 (2014).

98. De Laporte, L. *et al.* Plasmid releasing multiple channel bridges for transgene expression after spinal cord injury. *Mol. Ther.* **17**, 318–326 (2009).

99. Geller, H. M. & Fawcett, J. W. Building a bridge: Engineering spinal cord repair. *Exp. Neurol.* **174**, 125–136 (2002).

100. Stoeckli, E. T. Understanding axon guidance: are we nearly there yet? *Development* **145**, dev151415 (2018).

101. Ji, W.-C., Zhang, X.-W. & Qiu, Y.-S. Selected suitable seed cell, scaffold and growth factor could maximize the repair effect using tissue engineering method in spinal cord injury. *World J. Exp. Med.* **6**, 58 (2016).

102. Geiger, B., Spatz, J. P. & Bershadsky, A. D. Environmental sensing through focal adhesions. *Nat. Rev. Mol. Cell Biol.* **10**, 21–33 (2009).

103. Giancotti, F. G. & Ruoslahti, E. Integrin Signaling. *Science (80-.).* **285**, 1028 LP – 1033 (1999).

104. Kapp, T. G. *et al.* A comprehensive evaluation of the activity and selectivity profile of ligands for RGD-binding integrins. *Sci. Rep.* **7**, 1–13 (2017).

105. Kantlehner, M. *et al.* Surface coating with cyclic RGD peptides stimulates osteoblast

adhesion and proliferation as well as bone formation. *Angew. Chemie (International Ed. English)* **39**, 107–114 (2000).

106. Pallarola, D. *et al.* Interface immobilization chemistry of cRGD-based peptides regulates integrin mediated cell adhesion. *Adv. Funct. Mater.* **24**, 943–956 (2014).

107. Neubauer, S. *et al.* Pharmacophoric modifications lead to superpotent αvβ3 integrin ligands with suppressed α5β1 activity. *J. Med. Chem.* **57**, 3410–3417 (2014).

108. Heckmann, D. *et al.* Rational design of highly active and selective ligands for the α5β1 integrin receptor. *ChemBioChem* **9**, 1397–1407 (2008).

109. Bernhagen, D. *et al.* High-Affinity α5β1-Integrin-Selective Bicyclic RGD Peptides Identified via Screening of Designed Random Libraries. *ACS Comb. Sci.* **21**, 598–607 (2019).

110. Bernhagen, D. *et al.* Bicyclic RGD Peptides with Exquisite Selectivity for the Integrin α v β 3 Receptor Using a 'random Design' Approach. *ACS Comb. Sci.* **21**, 198–206 (2019).

111. Rosales, A. M. & Anseth, K. S. The design of reversible hydrogels to capture extracellular matrix dynamics. *Nat. Rev. Mater.* **1**, 1–15 (2016).

112. Engler, A. J., Sen, S., Sweeney, H. L. & Discher, D. E. Matrix Elasticity Directs Stem Cell Lineage Specification. *Cell* **126**, 677–689 (2006).

113. Chaudhuri, O. *et al.* Hydrogels with tunable stress relaxation regulate stem cell fate and activity. *Nat. Mater.* **15**, 326–334 (2016).

114. Vining, K. H. & Mooney, D. J. Mechanical forces direct stem cell behaviour in development and regeneration. *Nat. Rev. Mol. Cell Biol.* **18**, 728–742 (2017).

115. Zustiak, S. P. & Leach, J. B. Hydrolytically Degradable Poly (Ethylene Glycol) Hydrogel Scaffolds with Tunable Degradation and Mechanical Properties. 1348–1357 (2010).

116. Bryant, S. J., Durand, K. L. & Anseth, K. S. Manipulations in hydrogel chemistry control photoencapsulated chondrocyte behavior and their extracellular matrix production. *J. Biomed. Mater. Res. - Part A* **67**, 1430–1436 (2003).

117. Schultz, K. M., Kyburz, K. A. & Anseth, K. S. Measuring dynamic cell-material interactions and remodeling during 3D human mesenchymal stem cell migration in hydrogels. *Proc. Natl. Acad. Sci. U. S. A.* **112**, E3757–E3764 (2015).

118. Liu, K., Mihaila, S. M., Rowan, A., Oosterwijk, E. & Kouwer, P. H. J. Synthetic Extracellular Matrices with Nonlinear Elasticity Regulate Cellular Organization. *Biomacromolecules* **20**, 826–834 (2019).

119. Taylor, D. L. & in het Panhuis, M. Self-Healing Hydrogels. *Adv. Mater.* **28**, 9060–9093 (2016).

120. Kouwer, P. H. J. *et al.* Responsive biomimetic networks from polyisocyanopeptide hydrogels. *Nature* **493**, 651–655 (2013).

121. Liu, K., Mihaila, S. M., Rowan, A., Oosterwijk, E. & Kouwer, P. H. J. Synthetic Extracellular Matrices with Nonlinear Elasticity Regulate Cellular Organization. *Biomacromolecules* **20**, 826–834 (2019).

122. de Almeida, P. *et al.* Cytoskeletal stiffening in synthetic hydrogels. *Nat. Commun.* **10**, 2–9 (2019).

123. Das, R. K., Gocheva, V., Hammink, R., Zouani, O. F. & Rowan, A. E. Stress-stiffening-mediated stem-cell commitment switch in soft responsive hydrogels. *Nat. Mater.* **15**, 318–325 (2016).

124. Sperling, L. H. & Hu, R. Interpenetrating Polymer Networks. in *Polymer Blends Handbook* (eds. Utracki, L. A. & Wilkie, C. A.) 677–724 (Springer Netherlands, 2014). doi:10.1007/978-94-007-6064-6_8.

125. Burdick, J. A. & Murphy, W. L. Moving from static to dynamic complexity in hydrogel design. *Nat. Commun.* **3**, 1–8 (2012).

126. DeForest, C. A. & Anseth, K. S. Photoreversible patterning of biomolecules within click-based hydrogels. *Angew. Chemie - Int. Ed.* **51**, 1816–1819 (2012).

127. Brown, T. E., Marozas, I. A. & Anseth, K. S. Amplified Photodegradation of Cell-Laden Hydrogels via an Addition–Fragmentation Chain Transfer Reaction. *Adv. Mater.* **29**, (2017).

128. Seidlits, S. K., Schmidt, C. E. & Shear, J. B. High-resolution patterning of hydrogels in three dimensions using direct-write photofabrication for cell guidance. *Adv. Funct. Mater.* **19**, 3543–3551 (2009).

129. Zheng, Y., Farrukh, A. & Del Campo, A. Optoregulated Biointerfaces to Trigger Cellular Responses. *Langmuir* **34**, 14459–14471 (2018).

130. Hahn, M. S., Miller, J. S. & West, J. L. Three-dimensional biochemical and biomechanical patterning of hydrogels for guiding cell behavior. *Adv. Mater.* **18**, 2679–2684 (2006).

131. Khetan, S., Katz, J. S. & Burdick, J. A. Sequential crosslinking to control cellular spreading in 3-dimensional hydrogels. *Soft Matter* **5**, 1601–1606 (2009).

132. Hansen, M. J., Velema, W. A., Lerch, M. M., Szymanski, W. & Feringa, B. L. Wavelength-selective cleavage of photoprotecting groups: Strategies and applications in dynamic systems. *Chem. Soc. Rev.* **44**, 3358–3377 (2015).

133. Azagarsamy, M. A., Mckinnon, D. D., Alge, D. L. & Anseth, K. S. Coumarin-Based Photodegradable Hydrogel: Design, Synthesis, Gelation, and Degradation Kinetics. (2014).

134. Azagarsamy, M. A., Marozas, I. A., Spaans, S. & Anseth, K. S. Photoregulated Hydrazone-Based Hydrogel Formation for Biochemically Patterning 3D Cellular Microenvironments. *ACS Macro Lett.* **5**, 19–23 (2016).

135. Marklein, R. A. & Burdick, J. A. Spatially controlled hydrogel mechanics to modulate stem cell interactions. *Soft Matter* **6**, 136–143 (2009).

136. Günay, K. A. *et al.* PEG–Anthracene Hydrogels as an On-Demand Stiffening Matrix To Study Mechanobiology. *Angew. Chemie - Int. Ed.* **58**, 9912–9916 (2019).

137. Mosiewicz, K. A., Kolb, L., Van Der Vlies, A. J. & Lutolf, M. P. Microscale patterning of hydrogel stiffness through light-triggered uncaging of thiols. *Biomater. Sci.* **2**, 1640–1651 (2014).

138. Farrukh, A. *et al.* In Situ, Light-Guided Axon Growth on Biomaterials via Photoactivatable Laminin Peptidomimetic IK(HANBP)VAV. *ACS Appl. Mater. Interfaces* **10**, 41129–41137 (2018).

139. Kloxin, A. M., Kasko, A. M., Salinas, C. N. & Anseth, K. S. and Chemical Properties. *Science (80-.).* **324**, 59–63 (2009).

140. Tibbitt, M. W., Kloxin, A. M., Dyamenahalli, K. U. & Anseth, K. S. Controlled two-photon photodegradation of PEG hydrogels to study and manipulate subcellular interactions on soft materials. *Soft Matter* **6**, 5100–5108 (2010).

141. Arakawa, C. K., Badeau, B. A., Zheng, Y. & DeForest, C. A. Multicellular Vascularized Engineered Tissues through User-Programmable Biomaterial Photodegradation. *Adv. Mater.* **29**, 1–9 (2017).

142. Arakawa, C. K., Badeau, B. A., Zheng, Y. & DeForest, C. A. Multicellular Vascularized Engineered Tissues through User-Programmable Biomaterial Photodegradation. *Adv. Mater.* **29**, 1–9 (2017).

143. Farahani, P. E., Adelmund, S. M., Shadish, J. A. & DeForest, C. A. Photomediated oxime ligation as a bioorthogonal tool for spatiotemporally-controlled hydrogel formation and modification. *J. Mater. Chem. B* **5**, 4435–4442 (2017).

144. DeForest, C. A. & Anseth, K. S. Cytocompatible click-based hydrogels with dynamically tunable properties through orthogonal photoconjugation and photocleavage reactions. *Nat. Chem.* **3**, 925–931 (2011).

145. Cui, J., Miguel, V. S. & Del Campo, A. Light-triggered multifunctionality at surfaces mediated by photolabile protecting groups. *Macromol. Rapid Commun.* **34**, 310–329 (2013).

146. Custódio, C. A. *et al.* Photopatterned antibodies for selective cell attachment. *Langmuir* **30**, 10066–10071 (2014).

147. Lee, T. T. *et al.* Light-triggered in vivo activation of adhesive peptides regulates cell adhesion, inflammation and vascularization of biomaterials. *Nat. Mater.* **14**, 352–360

(2015).

148. Farrukh, A., Paez, J. I. & del Campo, A. 4D Biomaterials for Light-Guided Angiogenesis. *Adv. Funct. Mater.* **29**, 1–11 (2019).

149. Nair, R. V., Farrukh, A. & del Campo, A. A Photoactivatable α5β1-Specific Integrin Ligand. *ChemBioChem* **19**, 1280–1287 (2018).

150. Farrukh, A. *et al.* Photoactivatable Adhesive Ligands for Light-Guided Neuronal Growth. *ChemBioChem* **19**, 1271–1279 (2018).

151. Luo, Y. & Shoichet, M. S. A photolabile hydrogel for guided three-dimensional cell growth and migration. *Nat. Mater.* (2004) doi:10.1038/nmat1092.

152. Broguiere, N., Isenmann, L. & Zenobi-Wong, M. Novel enzymatically cross-linked hyaluronan hydrogels support the formation of 3D neuronal networks. *Biomaterials* **99**, 47–55 (2016).

153. Mosiewicz, K. A. *et al.* In situ cell manipulation through enzymatic hydrogel photopatterning. *Nat. Mater.* **12**, 1072–1078 (2013).

154. Broguiere, N. *et al.* Morphogenesis Guided by 3D Patterning of Growth Factors in Biological Matrices. *Adv. Mater.* **32**, (2020).

155. Pénzes, K., Kövér, K. E., Fazakas, F., Haramura, G. & Muszbek, L. Molecular mechanism of the interaction between activated factor XIII and its glutamine donor peptide substrate. *J. Thromb. Haemost.* **7**, 627–633 (2009).

156. Lorand, L. & Graham, R. M. Transglutaminases: Crosslinking enzymes with pleiotropic functions. *Nat. Rev. Mol. Cell Biol.* **4**, 140–156 (2003).

157. Fiedler, J. *et al.* NCO-sP(EO-stat-PO) surface coatings preserve biochemical properties of RGD peptides. *Int. J. Mol. Med.* **27**, 139–145 (2011).

158. Huang, X. *et al.* Light-Patterned RNA Interference of 3D-Cultured Human Embryonic Stem Cells. *Adv. Mater.* **28**, 10732–10737 (2016).

159. Richter, B. *et al.* Guiding Cell Attachment in 3D Microscaffolds Selectively Functionalized with Two Distinct Adhesion Proteins. *Adv. Mater.* **29**, 1–6 (2017).

160. Mecham, R. P. Overview of extracellular matrix. *Curr. Protoc. Cell Biol.* **57**, (2012).

161. Özbek, S., Balasubramanian, P. G., Chiquet-Ehrismann, R., Tucker, R. P. & Adams, J. C. The evolution of extracellular matrix. *Mol. Biol. Cell* (2010) doi:10.1091/mbc.E10-03-0251.

162. Rozario, T. & DeSimone, D. W. The extracellular matrix in development and morphogenesis: A dynamic view. *Developmental Biology* (2010) doi:10.1016/j.ydbio.2009.10.026.

163. Escobedo-Lucea, C. *et al.* Development of a Human Extracellular Matrix for Applications Related with Stem Cells and Tissue Engineering. *Stem Cell Rev. Reports* (2012) doi:10.1007/s12015-011-9270-6.

164. Zhu, J. Bioactive modification of poly(ethylene glycol) hydrogels for tissue engineering. *Biomaterials* **31**, 4639–4656 (2010).

165. Hynes, R. O. The extracellular matrix: Not just pretty fibrils. *Science* (2009) doi:10.1126/science.1176009.

166. Saksela, O. & Laiho, M. Growth factors and the extracellular matrix. *Duodecim; lääketieteellinen aikakauskirja* (1990) doi:10.1096/fasebj.11.1.9034166.

167. Theocharis, A. D., Skandalis, S. S., Gialeli, C. & Karamanos, N. K. Extracellular matrix structure. *Advanced Drug Delivery Reviews* (2016) doi:10.1016/j.addr.2015.11.001.

168. Zollinger, A. J. & Smith, M. L. Fibronectin, the extracellular glue. *Matrix Biology* (2017) doi:10.1016/j.matbio.2016.07.011.

169. Aumailley, M. The laminin family. *Cell Adhesion and Migration* (2013) doi:10.4161/cam.22826.

170. Pierschbacher, M. D. & Ruoslahti, E. Cell attachment activity of fibronectin can be duplicated by small synthetic fragments of the molecule. *Nature* **309**, 30–33 (1984).

171. Li, X. *et al.* Short Laminin Peptide for Improved Neural Stem Cell Growth. *Stem Cells Transl. Med.* (2014) doi:10.5966/sctm.2013-0015.

172. Kanie, K. *et al.* Focused screening of ECM-selective adhesion peptides on cellulose-bound peptide microarrays. *Bioengineering* (2016) doi:10.3390/bioengineering3040031.

173. Boateng, S. Y. *et al.* RGD and YIGSR synthetic peptides facilitate cellular adhesion identical to that of laminin and fibronectin but alter the physiology of neonatal cardiac myocytes. *Am. J. Physiol. - Cell Physiol.* (2005) doi:10.1152/ajpcell.00199.2004.

174. Schneider-Barthold, C., Baganz, S., Wilhelmi, M., Scheper, T. & Pepelanova, I. Hydrogels based on collagen and fibrin - Frontiers and applications. *BioNanoMaterials* (2016) doi:10.1515/bnm-2015-0025.

175. Murphy, K. C., Whitehead, J., Zhou, D., Ho, S. S. & Leach, J. K. Engineering fibrin hydrogels to promote the wound healing potential of mesenchymal stem cell spheroids. *Acta Biomater.* (2017) doi:10.1016/j.actbio.2017.10.007.

176. Hussey, G. S., Dziki, J. L. & Badylak, S. F. Extracellular matrix-based materials for regenerative medicine. *Nat. Rev. Mater.* **3**, 159–173 (2018).

177. Berkovitch, Y. & Seliktar, D. Semi-synthetic hydrogel composition and stiffness regulate neuronal morphogenesis. *Int. J. Pharm.* **523**, 545–555 (2017).

178. Doyle, A. D., Carvajal, N., Jin, A., Matsumoto, K. & Yamada, K. M. Local 3D matrix microenvironment regulates cell migration through spatiotemporal dynamics of contractility-dependent adhesions. *Nat. Commun.* **6**, 8720 (2015).

179. Van Helvert, S. & Friedl, P. Strain Stiffening of Fibrillar Collagen during Individual and Collective Cell Migration Identified by AFM Nanoindentation. *ACS Appl. Mater. Interfaces* **8**, 21946–21955 (2016).

180. Weisel, J. W. & Litvinov, R. I. Fibrin Formation, Structure and Properties BT - Fibrous Proteins: Structures and Mechanisms. in (eds. Parry, D. A. D. & Squire, J. M.) 405–456 (Springer International Publishing, 2017). doi:10.1007/978-3-319-49674-0_13.

181. van Hinsbergh, V. W., Collen, A. & Koolwijk, P. Role of fibrin matrix in angiogenesis. *Ann. N. Y. Acad. Sci.* **936**, 426–437 (2001).

182. Gessmann, J., Seybold, D., Peter, E., Schildhauer, T. A. & Köller, M. Alignment of the Fibrin Network Within an Autologous Plasma Clot. *Tissue Eng. Part C Methods* **22**, 30–37 (2015).

183. Corral, M. *et al.* Clinician reported ease of use for a novel fibrin sealant patch for hemostasis: results from four randomized controlled trials. *Curr. Med. Res. Opin.* **32**, 367–375 (2016).

184. Mithieux, S. M. & Weiss, A. S. Elastin. *Adv. Protein Chem.* **70**, 437–461 (2005).

185. Alovskaya, a, Alekseeva, T., Phillips, J. B., King, V. & Brown, R. Fibronectin, Collagen, Fibrin-Components of Extracellular Matrix for Nerve regeneration. *Top. Tissue Eng.* **3**, 1–27 (2007).

186. Kleinman, H. K. & Martin, G. R. Matrigel: basement membrane matrix with biological activity. *Semin. Cancer Biol.* **15**, 378–386 (2005).

187. Hughes, C. S., Postovit, L. M. & Lajoie, G. A. Matrigel: a complex protein mixture required for optimal growth of cell culture. *Proteomics* **10**, 1886–1890 (2010).

188. Augst, A. D., Kong, H. J. & Mooney, D. J. Alginate Hydrogels as Biomaterials. *Macromol. Biosci.* **6**, 623–633 (2006).

189. Gwon, K., Kim, E. & Tae, G. Heparin-hyaluronic acid hydrogel in support of cellular activities of 3D encapsulated adipose derived stem cells. *Acta Biomater.* (2017) doi:10.1016/j.actbio.2016.12.001.

190. Burdick, J. A. & Prestwich, G. D. Hyaluronic acid hydrogels for biomedical applications. *Adv. Mater.* **23**, H41-56 (2011).

191. Nakamura, M., Mie, M., Mihara, H., Nakamura, M. & Kobatake, E. Construction of multi-functional extracellular matrix proteins that promote tube formation of endothelial cells. *Biomaterials* **29**, 2977–2986 (2008).

192. Massia, S. P., Rao, S. S. & Hubbell, J. A. Covalently immobilized laminin peptide Tyr-Ile-Gly-Ser-Arg (YIGSR) supports cell spreading and co-localization of the 67-kilodalton laminin receptor with α-actinin and vinculin. *J. Biol. Chem.* **268**, 8053–8059 (1993).

193. Van der Walle, C. F., Altroff, H. & Mardon, H. J. Novel mutant human fibronectin FIII9-10 domain pair with increased conformational stability and biological activity. *Protein Eng.* **15**, 1021–1024 (2002).

194. Repic, T., Madirazza, K., Bektur, E. & Sapunar, D. Characterization of dorsal root ganglion neurons cultured on silicon micro-pillar substrates. *Sci. Rep.* **6**, 1–10 (2016).

195. Omidinia-anarkoli, A. *et al.* Solvent-Induced Nanotopographies of Single Micro fi bers Regulate Cell Mechanotransduction. (2019) doi:10.1021/acsami.8b17955.

196. Tonazzini, I., Jacchetti, E., Meucci, S., Beltram, F. & Cecchini, M. Schwann Cell Contact Guidance versus Boundary -Interaction in Functional Wound Healing along Nano and Microstructured Membranes. *Adv. Healthc. Mater.* **4**, 1849–1860 (2015).

197. Hynd, M. R., Frampton, J. P., Dowell-Mesfin, N., Turner, J. N. & Shain, W. Directed cell growth on protein-functionalized hydrogel surfaces. *J. Neurosci. Methods* **162**, 255–263 (2007).

198. Tuft, B. W. *et al.* Photopolymerized microfeatures for directed spiral ganglion neurite and Schwann cell growth. *Biomaterials* **34**, 42–54 (2013).

199. Omidinia-Anarkoli, A., Ephraim, J. W., Rimal, R. & De Laporte, L. Hierarchical fibrous guiding cues at different scales influence linear neurite extension. *Acta Biomater.* **113**, 350–359 (2020).

200. Tran, K. T. M. & Nguyen, T. D. Lithography-based methods to manufacture biomaterials at small scales. *J. Sci. Adv. Mater. Devices* **2**, 1–14 (2017).

201. Bernal, P. N. *et al.* Volumetric Bioprinting of Complex Living-Tissue Constructs within Seconds. *Adv. Mater.* **31**, 1904209 (2019).

202. Béduer, A. *et al.* Engineering of adult human neural stem cells differentiation through surface micropatterning. *Biomaterials* **33**, 504–514 (2012).

203. Richardson, J. A., Rementer, C. W., Bruder, J. M. & Hoffman-Kim, D. Guidance of dorsal root ganglion neurites and Schwann cells by isolated Schwann cell topography on poly(dimethyl siloxane) conduits and films. *J. Neural Eng.* **8**, (2011).

204. Vincent, H. K., George, S. Z., Seay, A. N., Vincent, K. R. & Hurley, R. W. Resistance exercise, disability, and pain catastrophizing in obese adults with back pain. *Med. Sci. Sports Exerc.* **46**, 1693–1701 (2014).

205. Clarke, J. C. *et al.* Micropatterned methacrylate polymers direct spiral ganglion neurite and Schwann cell growth. *Hear. Res.* **278**, 96–105 (2011).

206. Xu, L. *et al.* Photopolymerized Microfeatures Guide Adult Spiral Ganglion and Dorsal Root Ganglion Neurite Growth. *Otol. Neurotol.* **39**, 119–126 (2018).

207. Tonazzini, I., Jacchetti, E., Meucci, S., Beltram, F. & Cecchini, M. Schwann Cell Contact Guidance versus Boundary -Interaction in Functional Wound Healing along Nano and Microstructured Membranes. *Adv. Healthc. Mater.* **4**, 1849–1860 (2015).

208. Huang, Y. A. *et al.* Nanoimprinted Anisotropic Topography Preferentially Guides Axons and Enhances Nerve Regeneration. *Macromol. Biosci.* **18**, 1–12 (2018).

209. Johansson, F., Carlberg, P., Danielsen, N., Montelius, L. & Kanje, M. Axonal outgrowth on nano-imprinted patterns. *Biomaterials* **27**, 1251–1258 (2006).

210. Tuft, B. W. *et al.* Photopolymerized micropatterns with high feature frequencies overcome chemorepulsive borders to direct neurite growth. *J. Tissue Eng. Regen. Med.* **12**, e1392–e1403 (2018).

211. Li, W. *et al.* Large-scale topographical screen for investigation of physical neural-guidance cues. *Sci. Rep.* **5**, 1–8 (2015).

212. Kundu, A. *et al.* Superimposed topographic and chemical cues synergistically guide neurite outgrowth. *Lab Chip* **13**, 3070–3081 (2013).

213. Park, M. *et al.* Control over Neurite Directionality and Neurite Elongation on Anisotropic Micropillar Arrays. *Small* **12**, 1148–1152 (2016).

214. Mantha, S. *et al.* Smart hydrogels in tissue engineering and regenerative medicine. *Materials* (2019) doi:10.3390/ma12203323.

215. Fan, C. & Wang, D. A. Macroporous Hydrogel Scaffolds for Three-Dimensional Cell Culture and Tissue Engineering. *Tissue Engineering - Part B: Reviews* (2017) doi:10.1089/ten.teb.2016.0465.

216. Jonker, A. M., Bode, S. A., Kusters, A. H., Van Hest, J. C. M. & Löwik, D. W. P. M. Soft PEG-Hydrogels with Independently Tunable Stiffness and RGDS-Content for Cell Adhesion Studies. *Macromol. Biosci.* **15**, 1338–1347 (2015).

217. Chan, B. P. & Leong, K. W. Scaffolding in tissue engineering: General approaches and tissue-specific considerations. in *European Spine Journal* (2008). doi:10.1007/s00586-008-0745-3.

218. Webber, M. J. *et al.* Development of bioactive peptide amphiphiles for therapeutic cell delivery. *Acta Biomater.* **6**, 3–11 (2010).

219. Webber, M. J. *et al.* Supramolecular nanostructures that mimic VEGF as a strategy for ischemic tissue repair. *Proc. Natl. Acad. Sci.* **108**, 13438 LP – 13443 (2011).

220. Zhang, N., He, L. & Wu, W. Self-assembling peptide nanofibrous hydrogel as a promising strategy in nerve repair after traumatic injury in the nervous system. *Neural Regen. Res.* **11**, 717–718 (2016).

221. Betre, H., Setton, L. A., Meyer, D. E. & Chilkoti, A. Characterization of a Genetically Engineered Elastin-like Polypeptide for Cartilaginous Tissue Repair. *Biomacromolecules* **3**, 910–916 (2002).

222. Meyer, D. E. & Chilkoti, A. Genetically encoded synthesis of protein-based polymers with precisely specified molecular weight and sequence by recursive directional ligation: Examples from the the elastin-like polypeptide system. *Biomacromolecules* **3**, 357–367 (2002).

223. Cipriani, F. *et al.* An elastin-like recombinamer-based bioactive hydrogel embedded with mesenchymal stromal cells as an injectable scaffold for osteochondral repair. *Regen. Biomater.* **6**, 335–347 (2019).

224. González de Torre, I. *et al.* Elastin-like recombinamer catalyst-free click gels: characterization of poroelastic and intrinsic viscoelastic properties. *Acta Biomater.* **10**, 2495–2505 (2014).

225. Wang, H., Cai, L., Paul, A., Enejder, A. & Heilshorn, S. C. Hybrid Elastin-like Polypeptide – Polyethylene Glycol (ELP-PEG) Hydrogels with Improved Transparency and Independent Control of Matrix Mechanics and Cell Ligand Density. (2014).

226. Liu, S. Q. *et al.* Synthetic hydrogels for controlled stem cell differentiation. *Soft Matter* (2009) doi:10.1039/b916705f.

227. Keys, K. B., Andreopoulos, F. M. & Peppas, N. A. Poly(ethylene glycol) star polymer hydrogels. *Macromolecules* **31**, 8149–8156 (1998).

228. Zacchigna, M., Cateni, F., Drioli, S. & Bonora, G. M. Multimeric, multifunctional derivatives of poly(ethylene glycol). *Polymers (Basel).* **3**, 1076–1090 (2011).

229. Liu, W. *et al.* Probing Sol-Gel Matrices and Dynamics of Star PEG Hydrogels near Overlap Concentration. *Macromolecules* **52**, 8956–8966 (2019).

230. Liu, M. *et al.* Injectable hydrogels for cartilage and bone tissue engineering. *Bone Research* (2017) doi:10.1038/boneres.2017.14.

231. Rokita, B., Rosiak, J. M. & Ulanski, P. Ultrasound-induced cross-linking and formation of macroscopic covalent hydrogels in aqueous polymer and monomer solutions. *Macromolecules* (2009) doi:10.1021/ma802565p.

232. Lutolf, M. P., Tirelli, N., Cerritelli, S., Cavalli, L. & Hubbell, J. A. Systematic modulation of Michael-type reactivity of thiols through the use of charged amino acids. *Bioconjug. Chem.* **12**, 1051–1056 (2001).

233. Echalier, C., Valot, L., Martinez, J., Mehdi, A. & Subra, G. Chemical cross-linking methods for cell encapsulation in hydrogels. *Mater. Today Commun.* (2019) doi:10.1016/j.mtcomm.2019.05.012.

234. Ehrbar, M. *et al.* Biomolecular hydrogels formed and degraded via site-specific

enzymatic reactions. *Biomacromolecules* **8**, 3000–3007 (2007).

235. Nimmo, C. M., Owen, S. C. & Shoichet, M. S. Diels-alder click cross-linked hyaluronic acid hydrogels for tissue engineering. *Biomacromolecules* (2011) doi:10.1021/bm101446k.

236. Smith, L. J. *et al.* Diels-Alder Click-Cross-Linked Hydrogels with Increased Reactivity Enable 3D Cell Encapsulation. *Biomacromolecules* (2018) doi:10.1021/acs.biomac.7b01715.

237. Freshney, R. I. *Culture of Animal Cells: A Manual of Basic Technique and Specialized Applications: Sixth Edition*. *Culture of Animal Cells: A Manual of Basic Technique and Specialized Applications: Sixth Edition* (2011). doi:10.1002/9780470649367.

238. Wu, S., Xu, R., Duan, B. & Jiang, P. Three-dimensional hyaluronic acid hydrogel-based models for in vitro human iPSC-derived NPC culture and differentiation. *J. Mater. Chem. B* (2017) doi:10.1039/c7tb00721c.

239. Mironi-Harpaz, I., Wang, D. Y., Venkatraman, S. & Seliktar, D. Photopolymerization of cell-encapsulating hydrogels: Crosslinking efficiency versus cytotoxicity. *Acta Biomater.* (2012) doi:10.1016/j.actbio.2011.12.034.

240. Su, J. Thiol-Mediated Chemoselective Strategies for In Situ Formation of Hydrogels. *Gels* (2018) doi:10.3390/gels4030072.

241. Jansen, L. E., Negrón-Piñeiro, L. J., Galarza, S. & Peyton, S. R. Control of thiol-maleimide reaction kinetics in PEG hydrogel networks. *Acta Biomater.* **70**, 120–128 (2018).

242. Elbert, D. L., Pratt, A. B., Lutolf, M. P., Halstenberg, S. & Hubbell, J. A. Protein delivery from materials formed by self-selective conjugate addition reactions. *J. Control. Release* (2001) doi:10.1016/S0168-3659(01)00398-4.

243. Lutolf, M. P. *et al.* Repair of bone defects using synthetic mimetics of collagenous extracellular matrices. *Nat. Biotechnol.* **21**, 513–518 (2003).

244. Elia, R. *et al.* Stimulation of in vivo angiogenesis by in situ crosslinked, dual growth factor-loaded, glycosaminoglycan hydrogels. *Biomaterials* (2010) doi:10.1016/j.biomaterials.2010.02.043.

245. Speidel, A. T. *et al.* Multimodal Hydrogel-Based Platform To Deliver and Monitor Cardiac Progenitor/Stem Cell Engraftment. *ACS Cent. Sci.* **3**, 338–348 (2017).

246. Phelps, E. A., Templeman, K. L., Thulé, P. M. & García, A. J. Engineered VEGF-releasing PEG–MAL hydrogel for pancreatic islet vascularization. *Drug Delivery and Translational Research* (2015) doi:10.1007/s13346-013-0142-2.

247. Hoyle, C. E. & Bowman, C. N. Thiol-ene click chemistry. *Angew. Chemie - Int. Ed.* **49**, 1540–1573 (2010).

248. Seidlits, S. K. *et al.* Peptide-modified, hyaluronic acid-based hydrogels as a 3D culture platform for neural stem/progenitor cell engineering. *J. Biomed. Mater. Res. A* **107**, 704–718 (2019).

249. Sperinde, Jeffery ; Griffith, L. Synthesis and Characterization of Enzymatically-Cross-Linked Poly(ethylene glycol) Hydrogels. *Macromolecules* **30**, 5255–5264 (1997).

250. Lorand, L. & Graham, R. Lorand L, Graham RM.. Transglutaminases: crosslinking enzymes with pleiotropic functions. Nat Rev Mol Cell Biol 4: 140-156. *Nat. Rev. Mol. Cell Biol.* (2003) doi:10.1038/nrm1014.

251. Arkenberg, M. R., Moore, D. M. & Lin, C.-C. Dynamic control of hydrogel crosslinking via sortase-mediated reversible transpeptidation. *Acta Biomater.* **83**, 83–95 (2019).

252. Broguiere, N., Formica, F., Barreto, G. & Zenobi-Wong, M. Sortase A as a cross-linking enzyme in tissue engineering. *Acta Biomater.* **77**, 182–190 (2018).

253. Munoz-Robles, B. G., Kopyeva, I. & DeForest, C. A. Surface Patterning of Hydrogel Biomaterials to Probe and Direct Cell–Matrix Interactions. *Adv. Mater. Interfaces* **7**, 1–25 (2020).

254. Qin, D., Xia, Y. & Whitesides, G. M. Soft lithography for micro- and nanoscale patterning. *Nat. Protoc.* **5**, 491–502 (2010).

255. Huffman, J. M., Shao, J., Hsu, C. H. & Folch, A. Elastomeric molds with tunable microtopography. *Adv. Mater.* **16**, 2201–2206 (2004).

256. Castaño, A. G. *et al.* Protein patterning on hydrogels by direct microcontact printing: application to cardiac differentiation. *RSC Adv.* **4**, 29120–29123 (2014).

257. Gobaa, S. *et al.* Artificial niche microarrays for probing single stem cell fate in high throughput. *Nat. Methods* **8**, 949–955 (2011).

258. Fedorovich, N. E., De Wijn, J. R., Verbout, A. J., Alblas, J. & Dhert, W. J. A. Three-dimensional fiber deposition of cell-laden, viable, patterned constructs for bone tissue printing. *Tissue Eng. - Part A.* **14**, 127–133 (2008).

259. Mateen, R., Ali, M. M. & Hoare, T. A printable hydrogel microarray for drug screening avoids false positives associated with promiscuous aggregating inhibitors. *Nat. Commun.* **9**, 1–9 (2018).

260. Gurkan, U. A. *et al.* Engineering anisotropic biomimetic fibrocartilage microenvironment by bioprinting mesenchymal stem cells in nanoliter gel droplets. *Mol. Pharm.* **11**, 2151–2159 (2014).

261. Pati, F. *et al.* Printing three-dimensional tissue analogues with decellularized extracellular matrix bioink. *Nat. Commun.* **5**, (2014).

262. Ronzoni, F. L. *et al.* Myoblast 3D bioprinting to burst in vitro skeletal muscle

differentiation. *J. Tissue Eng. Regen. Med.* 1–12 (2022) doi:10.1002/term.3293.

263. Kühn, S. *et al.* Cell-Instructive Multiphasic Gel-in-Gel Materials. *Adv. Funct. Mater.* **30**, (2020).

264. Parratt, K., Smerchansky, M., Stiggers, Q. & Roy, K. Effect of hydrogel material composition on hBMSC differentiation into zone-specific neo-cartilage: Engineering human articular cartilage-like tissue with spatially varying properties. *J. Mater. Chem. B* **5**, 6237–6248 (2017).

265. Darling, N. J., Sideris, E., Hamada, N., Carmichael, S. T. & Segura, T. Injectable and Spatially Patterned Microporous Annealed Particle (MAP) Hydrogels for Tissue Repair Applications. *Adv. Sci.* **5**, 1–8 (2018).

266. Rommel, D. *et al.* Functionalized Microgel Rods Interlinked into Soft Macroporous Structures for 3D Cell Culture. **2103554**, 1–15 (2022).

267. Husman, D. *et al.* Multiphasic microgel-in-gel materials to recapitulate cellular mesoenvironments in vitro. *Biomater. Sci.* **8**, 101–108 (2020).

268. Lam, J. & Segura, T. The modulation of MSC integrin expression by RGD presentation. *Biomaterials* (2013) doi:10.1016/j.biomaterials.2013.01.091.

269. Marozas, I. A., Cooper-White, J. J. & Anseth, K. S. Photo-induced viscoelasticity in cytocompatible hydrogel substrates. *New J. Phys.* (2019) doi:10.1088/1367-2630/ab1309.

270. Polizzotti, B. D., Fairbanks, B. D. & Anseth, K. S. Three-dimensional biochemical patterning of click-based composite hydrogels via thiolene photopolymerization. *Biomacromolecules* (2008) doi:10.1021/bm7012636.

271. Accardo, A. *et al.* Two-photon lithography and microscopy of 3D hydrogel scaffolds for neuronal cell growth Two-photon lithography and microscopy of 3D hydrogel scaffolds for neuronal cell growth. *Biomed. Phys. Eng. Express* **4**, 27009.

272. Katz, J. S. & Burdick, J. A. Light-responsive biomaterials: Development and applications. *Macromolecular Bioscience* (2010) doi:10.1002/mabi.200900297.

273. Broguiere, N. *et al.* Morphogenesis Guided by 3D Patterning of Growth Factors in Biological Matrices. *Adv. Mater.* **1908299**, 1–10 (2020).

274. Rapp, T. L. & DeForest, C. A. Visible Light-Responsive Dynamic Biomaterials: Going Deeper and Triggering More. *Adv. Healthc. Mater.* **1901553**, 1901553 (2020).

275. Wylie, R. G. *et al.* Spatially controlled simultaneous patterning of multiple growth factors in three-dimensional hydrogels. *Nat. Mater.* **10**, 799–806 (2011).

276. Kloxin, A. M., Kasko, A. M., Salinas, C. N. & Anseth, K. S. Photodegradable hydrogels for dynamic tuning of physical and chemical properties. *Science (80-.).* (2009) doi:10.1126/science.1169494.

277. Lee, S. H., Moon, J. J. & West, J. L. Three-dimensional micropatterning of bioactive hydrogels via two-photon laser scanning photolithography for guided 3D cell migration. *Biomaterials* **29**, 2962–2968 (2008).

278. Shadish, J. A., Benuska, G. M. & DeForest, C. A. Bioactive site-specifically modified proteins for 4D patterning of gel biomaterials. *Nat. Mater.* **18**, 1005–1014 (2019).

279. Nair, R. V., Farrukh, A. & del Campo, A. Light-Regulated Angiogenesis via a Phototriggerable VEGF Peptidomimetic. *Adv. Healthc. Mater.* **10**, 1–10 (2021).

280. Griffin, D. R. *et al.* Hybrid photopatterned enzymatic reaction (HyPER) for in situ cell manipulation. *ChemBioChem* **15**, 233–242 (2014).

281. Mosiewicz, K. A. *et al.* In situ cell manipulation through enzymatic hydrogel photopatterning. *Nat. Mater.* **12**, 1072–1078 (2013).

282. Griffin, D. R. *et al.* Hybrid photopatterned enzymatic reaction (HyPER) for in situ cell manipulation. *ChemBioChem* (2014) doi:10.1002/cbic.201300687.

283. Johnson, C. D. L. *et al.* Injectable, Magnetically Orienting Electrospun Fiber Conduits for Neuron Guidance. *ACS Appl. Mater. Interfaces* **11**, 356–372 (2019).

284. Pawar, K. *et al.* Biomaterial bridges enable regeneration and re-entry of corticospinal tract axons into the caudal spinal cord after SCI: Association with recovery of forelimb function. *Biomaterials* **65**, 1–12 (2015).

285. Chang, Y. C. *et al.* Multichanneled Nerve Guidance Conduit with Spatial Gradients of Neurotrophic Factors and Oriented Nanotopography for Repairing the Peripheral Nervous System. *ACS Appl. Mater. Interfaces* **9**, 37623–37636 (2017).

286. Hodde, D. *et al.* Characterisation of cell-substrate interactions between Schwann cells and three-dimensional fibrin hydrogels containing orientated nanofibre topographical cues. *Eur. J. Neurosci.* **43**, 376–387 (2016).

287. Wang, L. S., Chung, J. E., Pui-Yik Chan, P. & Kurisawa, M. Injectable biodegradable hydrogels with tunable mechanical properties for the stimulation of neurogenesic differentiation of human mesenchymal stem cells in 3D culture. *Biomaterials* **31**, 1148–1157 (2010).

288. Spedden, E., Wiens, M. R., Demirel, M. C. & Staii, C. Effects of surface asymmetry on neuronal growth. *PLoS One* **9**, (2014).

289. Piret, G., Perez, M. T. & Prinz, C. N. Support of Neuronal Growth Over Glial Growth and Guidance of Optic Nerve Axons by Vertical Nanowire Arrays. *ACS Appl. Mater. Interfaces* **7**, 18944–18948 (2015).

290. Wang, L., Wu, Y., Hu, T., Ma, P. X. & Guo, B. Aligned conductive core-shell biomimetic scaffolds based on nanofiber yarns/hydrogel for enhanced 3D neurite outgrowth alignment and elongation. *Acta Biomater.* **96**, 175–187 (2019).

291. Amin, H., Dipalo, M., De Angelis, F. & Berdondini, L. Biofunctionalized 3D Nanopillar Arrays Fostering Cell Guidance and Promoting Synapse Stability and Neuronal Activity in Networks. *ACS Appl. Mater. Interfaces* **10**, 15207–15215 (2018).

292. Leclech, C., Renner, M., Villard, C. & Métin, C. Topographical cues control the morphology and dynamics of migrating cortical interneurons. *Biomaterials* **214**, 119194 (2019).

293. Micholt, L. *et al.* Substrate Topography Determines Neuronal Polarization and Growth In Vitro. *PLoS One* **8**, 1–14 (2013).

294. Maria, A., Suarez, A., Rijn, P. Van & Harmsen, M. C. Directional topography gradients drive optimum alignment and differentiation of human myoblasts. 2234–2245 (2019) doi:10.1002/term.2976.

295. Xu, L. *et al.* Photopolymerized Microfeatures Guide Adult Spiral Ganglion and Dorsal Root Ganglion Neurite Growth. *Otol. Neurotol.* **39**, 119–126 (2018).

296. Liguori, G. R. *et al.* Directional topography influences adipose mesenchymal stromal cell plasticity: Prospects for tissue engineering and fibrosis. *Stem Cells Int.* **2019**, (2019).

297. Yang, L., Jurczak, K. M., Ge, L. & van Rijn, P. High-Throughput Screening and Hierarchical Topography-Mediated Neural Differentiation of Mesenchymal Stem Cells. *Adv. Healthc. Mater.* **9**, (2020).

298. Baranes, K., Chejanovsky, N., Alon, N., Sharoni, A. & Shefi, O. Topographic cues of nano-scale height direct neuronal growth pattern. *Biotechnol. Bioeng.* **109**, 1791–1797 (2012).

299. Baranes, K., Kollmar, D., Chejanovsky, N., Sharoni, A. & Shefi, O. Interactions of neurons with topographic nano cues affect branching morphology mimicking neuron-neuron interactions. *J. Mol. Histol.* **43**, 437–447 (2012).

300. Cecchini, M. *et al.* Nanotopographic Control of Neuronal Polarity. *Nano Lett.* **11**, 505–511 (2011).

301. Wang, K. *et al.* Nanotopographical Modulation of Cell Function through Nuclear Deformation. *ACS Appl. Mater. Interfaces* **8**, 5082–5092 (2016).

302. Orlowska, A. *et al.* The effect of coatings and nerve growth factor on attachment and differentiation of Pheochromocytoma Cells. *Materials (Basel).* **11**, 1–10 (2017).

303. Ciardelli, G. & Chiono, V. Materials for peripheral nerve regeneration. *Macromol. Biosci.* **6**, 13–26 (2006).

304. Mahoney, M. J., Chen, R. R., Tan, J. & Mark Saltzman, W. The influence of microchannels on neurite growth and architecture. *Biomaterials* **26**, 771–778 (2005).

305. Katz, M. J. How straight do axons grow? *J. Neurosci.* **5**, 589–595 (1985).

306. Béduer, A. *et al.* Engineering of adult human neural stem cells differentiation through surface micropatterning. *Biomaterials* **33**, 504–514 (2012).

307. Park, M. *et al.* Control over Neurite Directionality and Neurite Elongation on Anisotropic Micropillar Arrays. *Small* **12**, 1148–1152 (2016).

308. Kim, S. M. *et al.* Micropatterned nanolayers immobilized with nerve growth factor for neurite formation of PC12 cells . *Int. J. Nanomedicine* **Volume 14**, 7683–7694 (2019).

309. Lowery, L. A. & Vactor, D. Van. The trip of the tip: Understanding the growth cone machinery. *Nat. Rev. Mol. Cell Biol.* **10**, 332–343 (2009).

310. Denais, C. M. *et al.* Nuclear envelope rupture and repair during cancer cell migration. *Science (80-.).* **352**, 353–358 (2016).

311. Jähne, B. *Digital Image Processing*. (Springer, 2002).

312. Durande, M. *et al.* Fast determination of coarse-grained cell anisotropy and size in epithelial tissue images using Fourier transform. *Phys. Rev. E* **99**, 62401 (2019).

313. Cheng, S., Clarke, E. C. & Bilston, L. E. Rheological properties of the tissues of the central nervous system: A review. *Med. Eng. Phys.* **30**, 1318–1337 (2008).

314. Blewitt, M. J. & Willits, R. K. The effect of soluble peptide sequences on neurite extension on 2D collagen substrates and within 3D collagen gels. *Ann. Biomed. Eng.* **35**, 2159–2167 (2007).

315. Yamada, K. M. & Sixt, M. Mechanisms of 3D cell migration. *Nat. Rev. Mol. Cell Biol.* **20**, 738–752 (2019).

316. Nakaji-Hirabayashi, T., Kato, K. & Iwata, H. Improvement of neural stem cell survival in collagen hydrogels by incorporating laminin-derived cell adhesive polypeptides. *Bioconjug. Chem.* **23**, 212–221 (2012).

317. Bento, A. R., Quelhas, P., Oliveira, M. J., Pêgo, A. P. & Amaral, I. F. Three-dimensional culture of single embryonic stem-derived neural/stem progenitor cells in fibrin hydrogels: neuronal network formation and matrix remodelling. *J. Tissue Eng. Regen. Med.* **11**, 3494–3507 (2017).

318. Li, S. *et al.* Hydrogels with precisely controlled integrin activation dictate vascular patterning and permeability. *Nat. Mater.* **16**, 953–961 (2017).

319. Carriel, V. *et al.* Combination of fibrin-agarose hydrogels and adipose-derived mesenchymal stem cells for peripheral nerve regeneration. *J. Neural Eng.* **10**, (2013).

320. Chwalek, K. *et al.* Engineered 3D silk-collagen-based model of polarized neural tissue. *J. Vis. Exp.* **2015**, 1–7 (2015).

321. Zhu, J. & Marchant, R. E. Design properties of hydrogel tissue-engineering scaffolds.

Expert Rev. Med. Devices **8**, 607–626 (2011).

322. Plow, E. F., Haas, T. A., Zhang, L., Loftus, J. & Smith, J. W. Ligand binding to integrins. *J. Biol. Chem.* **275**, 21785–21788 (2000).

323. Lampe, K. J., Antaris, A. L. & Heilshorn, S. C. Design of three-dimensional engineered protein hydrogels for tailored control of neurite growth. *Acta Biomater.* **9**, 5590–5599 (2013).

324. dos Santos, B. P. *et al.* Development of a cell-free and growth factor-free hydrogel capable of inducing angiogenesis and innervation after subcutaneous implantation. *Acta Biomater.* **99**, 154–167 (2019).

325. Hopkins, A. M. *et al.* Silk hydrogels as soft substrates for neural tissue engineering. *Adv. Funct. Mater.* **23**, 5140–5149 (2013).

326. Palazzolo, G., Broguiere, N., Cenciarelli, O., Dermutz, H. & Zenobi-Wong, M. Ultrasoft Alginate Hydrogels Support Long-Term Three-Dimensional Functional Neuronal Networks. *Tissue Eng. - Part A* **21**, 2177–2185 (2015).

327. Boni, R., Ali, A., Shavandi, A. & Clarkson, A. N. Current and novel polymeric biomaterials for neural tissue engineering. *J. Biomed. Sci.* **25**, 1–21 (2018).

328. Naghdi, P. *et al.* Survival, proliferation and differentiation enhancement of neural stem cells cultured in three-dimensional polyethylene glycol–RGD hydrogel with tenascin. *J. Tissue Eng. Regen. Med.* **10**, 199–208 (2016).

329. Hsu, R. S. *et al.* Adaptable Microporous Hydrogels of Propagating NGF-Gradient by Injectable Building Blocks for Accelerated Axonal Outgrowth. *Adv. Sci.* **6**, (2019).

330. Li, X., Katsanevakis, E., Liu, X., Zhang, N. & Wen, X. Engineering neural stem cell fates with hydrogel design for central nervous system regeneration. *Prog. Polym. Sci.* **37**, 1105–1129 (2012).

331. Bott, K. *et al.* The effect of matrix characteristics on fibroblast proliferation in 3D gels. *Biomaterials* **31**, 8454–8464 (2010).

332. Truong, V., Blakey, I. & Whittaker, A. K. Hydrophilic and amphiphilic polyethylene glycol-based hydrogels with tunable degradability prepared by 'click' chemistry. *Biomacromolecules* **13**, 4012–4021 (2012).

333. Dechantsreiter, M. A. *et al.* N-methylated cyclic RGD peptides as highly active and selective α(v)β3 integrin antagonists. *J. Med. Chem.* **42**, 3033–3040 (1999).

334. Mas-moruno, C. *et al.* a v b 3- or a 5 b 1-Integrin-Selective Peptidomimetics for Surface Coating Angewandte. 7048–7067 (2016) doi:10.1002/anie.201509782.

335. Schiller, H. B. *et al.* β 1 - And α v -class integrins cooperate to regulate myosin II during rigidity sensing of fibronectin-based microenvironments. *Nat. Cell Biol.* **15**, 625–636 (2013).

336. Diaz, C., Neubauer, S., Rechenmacher, F., Kessler, H. & Missirlis, D. Recruitment of αvβ3 integrin to α5β1 integrin-induced clusters enables focal adhesion maturation and cell spreading. *J. Cell Sci.* **133**, (2020).

337. Cipriani, F. *et al.* Bicyclic RGD peptides with high integrin α v β 3 and α 5 β 1 affinity promote cell adhesion on elastin-like recombinamers. *Biomed. Mater.* **14**, (2019).

338. Hu, B. H. & Messersmith, P. B. Rational Design of Transglutaminase Substrate Peptides for Rapid Enzymatic Formation of Hydrogels. *J. Am. Chem. Soc.* **125**, 14298–14299 (2003).

339. Patterson, J. & Hubbell, J. A. SPARC-derived protease substrates to enhance the plasmin sensitivity of molecularly engineered PEG hydrogels. *Biomaterials* **32**, 1301–1310 (2011).

340. Bernhagen, D. *et al.* Bicyclic RGD Peptides with Exquisite Selectivity for the Integrin α v β 3 Receptor Using a 'random Design' Approach. *ACS Comb. Sci.* **21**, 198–206 (2019).

341. Danen, E. H. J. *et al.* Requirement for the synergy site for cell adhesion to fibronectin depends on the activation state of integrin α5β1. *J. Biol. Chem.* **270**, 21612–21618 (1995).

342. Zhao, X. K. *et al.* Focal adhesion kinase regulates fibroblast migration via integrin beta-1 and plays a central role in fibrosis. *Sci. Rep.* **6**, 1–12 (2016).

343. Yip, P. M., Zhao, X., Montgomery, A. M. P. & Siu, C. H. The Arg-gly-asp motif in the cell adhesion molecule L1 promotes neurite outgrowth via interaction with the α(v)β3 integrin. *Mol. Biol. Cell* **9**, 277–290 (1998).

344. Delannet, M. *et al.* Specific roles of the αVβ1, αVβ3 and αVβ5 integrins in avian neural crest cell adhesion and migration on vitronectin. *Development* **120**, 2687–2702 (1994).

345. Clegg, D. O., Wingerd, K. L., Hikita, S. T. & Tolhurst, E. C. Integrins in the development, function and dysfunction of the nervous system. *Front. Biosci.* **8**, (2003).

346. Fiorini, F. *et al.* Nanocomposite Hydrogels as Platform for Cells Growth, Proliferation, and Chemotaxis. *Small* **12**, 4881–4893 (2016).

347. Jessamine P Winer, S. O. and P. A. J. Non-Linear Elasticity of ECM enables contractile cells to communicate local position and orientation. (2009) doi:https://doi.org/10.1371/journal.pone.0006382.

348. Chaudhuri, O., Cooper-white, J., Janmey, P. A., Mooney, D. J. & Shenoy, V. B. Effects of extracellular matrix viscoelasticity on cellular behaviour. *Nature* **584**, 535–546 (2020).

349. Chaudhuri, O. *et al.* Substrate stress relaxation regulates cell spreading. *Nat. Commun.* **6**, 1–7 (2015).

350. Liu, K., Wiendels, M., Yuan, H., Ruan, C. & Kouwer, P. H. J. Cell-matrix reciprocity in 3D culture models with nonlinear elasticity. *Bioact. Mater.* (2021) doi:10.1016/j.bioactmat.2021.08.002.

351. Hall, M. S. *et al.* Fibrous nonlinear elasticity enables positive Mechanical feedback between cells and ECMs. *Proc. Natl. Acad. Sci. U. S. A.* **113**, 14043–14048 (2016).

352. Turner, C. E. Paxillin and Focal Adhesion Signalling. *Nature Cell Biology* vol. 2 231–236 (2000).

353. Han, Y. L. *et al.* Cell contraction induces long-ranged stress stiffening in the extracellular matrix. *Proc. Natl. Acad. Sci. U. S. A.* **115**, 4075–4080 (2018).

354. Pocaterra, A., Romani, P. & Dupont, S. YAP/TAZ functions and their regulation at a glance. *J. Cell Sci.* **133**, 1–9 (2020).

355. Chandorkar, Y. *et al.* Cellular responses to beating hydrogels to investigate mechanotransduction. *Nat. Commun.* 1–13 doi:10.1038/s41467-019-11475-4.

356. Jaspers, M. *et al.* Ultra-responsive soft matter from strain-stiffening hydrogels. *Nat. Commun.* (2014) doi:10.1038/ncomms6808.

357. Loebel, C., Rodell, C. B., Chen, M. H. & Burdick, J. A. Shear-thinning and self-healing hydrogels as injectable therapeutics and for 3D-printing. **12**, 1521–1541 (2017).

358. Torres-Rendon, J. G. *et al.* Cellulose Nanofibril Hydrogel Tubes as Sacrificial Templates for Freestanding Tubular Cell Constructs. *Biomacromolecules* **17**, 905–913 (2016).

359. Diba, M. *et al.* Engineering the Dynamics of Cell Adhesion Cues in Supramolecular Hydrogels for Facile Control over Cell Encapsulation and Behavior. **2008111**, (2021).

360. Madl, C. M. *et al.* Maintenance of neural progenitor cell stemness in 3D hydrogels requires matrix remodelling. *Nat. Mater.* **16**, 1233–1242 (2017).

361. Wang, H. & Heilshorn, S. C. Adaptable Hydrogel Networks with Reversible Linkages for Tissue Engineering. *Adv. Mater.* **27**, 3717–3736 (2015).

362. Strom, C., Pastore, J., MacKintosh, F. C., Lubensky, T. C. & Janmey, P. A. Nonlinear elasticity in biological gels. *Nature* **435**, 0–3 (2005).

363. Shi, N. *et al.* A 3D, Magnetically Actuated, Aligned Collagen Fiber Hydrogel Platform Recapitulates Physical Microenvironment of Myoblasts for Enhancing Myogenesis. *Small Methods* **5**, 1–12 (2021).

364. Matsumoto, T. *et al.* Three-Dimensional Cell and Tissue Patterning in a Strained

Fibrin Gel System. 1–6 (2007) doi:10.1371/journal.pone.0001211.

365. Sommerdijk, N. A. J. M. & Nolte, R. J. M. Conformational Analysis of Dipeptide-Derived Polyisocyanides. 1725–1736 (2003).

366. Kouwer, P. H. J. *et al.* Responsive biomimetic networks from polyisocyanopeptide hydrogels. *Nature* **493**, 651–655 (2013).

367. Koepf, M. *et al.* Preparation and characterization of non-linear poly(ethylene glycol) analogs from oligo(ethylene glycol) functionalized polyisocyanopeptides. *Eur. Polym. J.* **49**, 1510–1522 (2013).

368. Kouwer, P. H. J. *et al.* Controlling the gelation temperature of biomimetic polyisocyanides. *Chinese Chem. Lett.* **29**, 281–284 (2018).

369. Celikkin, N. *et al.* 3D printing of thermoresponsive polyisocyanide (PIC) hydrogels as bioink and fugitive material for tissue engineering. *Polymers (Basel).* **10**, (2018).

370. op 't Veld, R. C. *et al.* Thermosensitive biomimetic polyisocyanopeptide hydrogels may facilitate wound repair. *Biomaterials* **181**, 392–401 (2018).

371. Vandaele, J. *et al.* Structural characterization of fibrous synthetic hydrogels using fluorescence microscopy. *Soft Matter* **16**, 4210–4219 (2020).

372. Jaspers, M. *et al.* Nonlinear mechanics of hybrid polymer networks that mimic the complex mechanical environment of cells. *Nat. Commun.* **8**, 1–10 (2017).

373. Ward, J. H., Bashir, R. & Peppas, N. A. Micropatterning of biomedical polymer surfaces by novel UV polymerization techniques. *J. Biomed. Mater. Res.* **56**, 351–360 (2001).

374. Fernandes, R. *et al.* Electrochemically Induced Deposition of a Polysaccharide Hydrogel onto a Patterned Surface. *Langmuir* **19**, 4058–4062 (2003).

375. Parmar, P. A. *et al.* Temporally degradable collagen-mimetic hydrogels tuned to chondrogenesis of human mesenchymal stem cells. *Biomaterials* **99**, 56–71 (2016).

376. Brandenberg, N. & Lutolf, M. P. In Situ Patterning of Microfluidic Networks in 3D Cell-Laden Hydrogels. *Adv. Mater.* **28**, 7450–7456 (2016).

377. McKinnon, D. D., Brown, T. E., Kyburz, K. A., Kiyotake, E. & Anseth, K. S. Design and characterization of a synthetically accessible, photodegradable hydrogel for user-directed formation of neural networks. *Biomacromolecules* **15**, 2808–2816 (2014).

378. Kloxin, A. M. *et al.* Responsive culture platform to examine the influence of microenvironmental geometry on cell function in 3D. *Integr. Biol. (United Kingdom)* **4**, 1540–1549 (2012).

379. Mahoney, M. J. & Anseth, K. S. Three-dimensional growth and function of neural tissue in degradable polyethylene glycol hydrogels. *Biomaterials* **27**, 2265–2274

(2006).

380. Luo, Y. & Shoichet, M. S. A photolabile hydrogel for guided three-dimensional cell growth and migration. *Nat. Mater.* **3**, 249–254 (2004).

381. Nakajima, M. *et al.* Combinatorial protein display for the cell-based screening of biomaterials that direct neural stem cell differentiation. *Biomaterials* **28**, 1048–1060 (2007).

382. Yu, L. M. Y., Leipzig, N. D. & Shoichet, M. S. Promoting neuron adhesion and growth. *Advances* **11**, 36–43 (2008).

383. Berns, E. J. *et al.* Aligned neurite outgrowth and directed cell migration in self-assembled monodomain gels. *Biomaterials* **35**, 185–195 (2014).

384. Álvarez, Z. *et al.* Bioactive scaffolds with enhanced supramolecular motion promote recovery from spinal cord injury. **374**, (2021).

385. Farrukh, A. *et al.* Bifunctional Hydrogels Containing the Laminin Motif IKVAV Promote Neurogenesis. *Stem Cell Reports* **9**, 1432–1440 (2017).

386. Farrukh, A. *et al.* Photoactivatable Adhesive Ligands for Light-Guided Neuronal Growth. *ChemBioChem* (2018) doi:10.1002/cbic.201800118.

387. Martino, M. M. *et al.* Engineering the growth factor microenvironment with fibronectin domains to promote wound and bone tissue healing. *Sci. Transl. Med.* **3**, (2011).

388. Groll, J., Haubensak, W., Ameringer, T. & Moeller, M. Ultrathin coatings from isocyanate terminated star PEG prepolymers: Patterning of proteins on the layers. *Langmuir* **21**, 3076–3083 (2005).

389. Phelps, E. A. *et al.* Maleimide cross-linked bioactive PEG hydrogel exhibits improved reaction kinetics and cross-linking for cell encapsulation and in situ delivery. *Adv. Mater.* **24**, 64–70 (2012).

390. Paez, J. I., Farrukh, A., Valbuena-Mendoza, R., Włodarczyk-Biegun, M. K. & Del Campo, A. Thiol-Methylsulfone-Based Hydrogels for 3D Cell Encapsulation. *ACS Appl. Mater. Interfaces* **12**, 8062–8072 (2020).

Appendix A. Acknowledgement

I would like to convey my sincere gratitude to Prof. **Laura De Laporte**. Her immense support, consistent motivation, and guidance enabled me to ask the right scientific questions and seek great pleasure in finding its solutions. Her commitment and consistent participation in my projects with enthralling scientific discussions allowed me to overcome hurdles in this Ph.D. journey. Her perseverance, conviction, and passion for the sciences inspired me to work harder every day. Thank you, Laura, you are indeed an inspiration. I would like to Prof. Dr. **Martin Möller** for accepting me as his student and enabling me to start at DWI. Thank you, professor, for your timely advice and enlightening scientific discussions.

I would like to thank my friends and colleagues at DWI for the most enjoyable collaboration with similar scientific aptitude. Thank you, **Andreas**, **Arturo, Cedric, Chris, Daniel, David, Dirk, Luis, Luisa, Matthias, Omid, Onur, Sheila**, **Souad**, **Susan,** and **Yonca**, and for all the fruitful discussions and collaborations, addressing issues and finding meaningful solutions. Thank you for being such a great companion, I wouldn't have enjoyed my Ph.D. without you all. I would like to especially thank **Jose** and **Tamas** for training, mentoring, and motivating me to learn new concepts and tools, which greatly accelerated my project. Thank you, **Fred**, for being my friend in the lab and finding meaningful solutions to problems throughout. I also thank **Dr. Akihiro Nishiguchi**, **Dr Vinokur Rostislav**, **Christian Simons**, **Michaela Baulig** for supporting my project.

I would like to thank all my students for having provided me with a wonderful experience, learning and growing together. Thank you, **Winnie, Andrea, Julian, Amaury, Aron, Sabrina, Shreyas, Jonas, Marie, Max, Sinan, Ghazaleh,** and **Anna,** for your great scientific support. I wish you all the very best in your career. Being part of European Union projects such as **BIOGEL** and **ORGANTRANS** was an experience of a lifetime. I thank all my colleagues and friends, especially **Delphine, Jenny, Marcel,**

Max, and **Melanie,** for elevated scientific discussions and memorable relationships. I thank Dr. **Peter Timmerman** and **Dominik** for actively collaborating in the bicyclic peptide project and hosting me in PEPSCAN to develop caged glutamine peptides. I would like to thank external collaborators, **Prof. Del Campo** and **Dr. Aleeza Farrukh** from INM, Saarbrucken, for collaborating with the design and testing of caged Peptide systems; **Dr. Erik Noetzel-Reiss** and **Sven Gerlach**, Forschungszentrum Jülich for enabling me to use their laser system. I thank **Dr. Paul Kouwer** and **Dr. Kaizheng Liu** for their contribution in the PIC project.

I would like to thank the colleagues that assist in admin tasks, IT, purchasing, etc, especially **Angela, Corinna, Ewgeni, Lydia, Rebecca, Regina,** and **Silke,** for their support in making my tasks easier.

I received immense support from my family throughout my life, and especially during this phase, and I would like to thank them for being mine. 😊 Thank you, **Appa (Vedaraman)**, who showed me that there are no boundaries in life and encouraged me constantly to push the limits. Thank you, **Amma (Geetha),** for being there for me in both my difficult and good times and supporting me throughout. Thank you, **Karthik,** for your enormous support and technical assistance in this endeavor. My deepest gratitude towards your encouragement and patience in this commitment together. Thank you, **Paati (Vathsala),** for believing in me and being my pillar of support. I thank everyone who contributed to the success of this work by whatever means, especially those kind people I did not acknowledge personally.

Appendix B. List of Publications

1. **S.Vedaraman**, A. Perez-Tirado, T. Haraszti, J. Gerardo-Nava, L. De Laporte. Anisometric Microstructures to Determine Minimal Critical Physical Cues Required for Neurite Alignment. Adv. Healthcare Mater. 2021, 10, 2100874

2. **S.Vedaraman**, D. Bernhagen, T. Haraszti, C. Licht, A. Castro Nava, A. Omidinia Anarkoli P. Timmerman, L. De Laporte. Bicyclic RGD peptides enhance nerve growth in synthetic PEG-based ANISOGELS. Biomaterial Science, Biomater. Sci., 2021, 9, 4329-4342

3. D.Rommel, M.Mork, **S.Vedaraman**, C.Bastard, L. P. B. Guerzoni, Y. Kittel, R.Vinokur, N. Born, T. Haraszti, L. De Laporte. Functionalized Microgel Rods Interlinked into Soft Macroporous Structures for 3D Cell Culture. Adv. Sci. 2021, 202103554.

4. D. Rommel, **S. Vedaraman**, M. Mork, L. De Laporte. Interlinked Macroporous 3D Scaffolds from Microgel Rods. J. Vis. Exp. (184), e64010, doi:10.3791/64010 (2022).

5. S. Babu, I. Chen, **S. Vedaraman**, J. Gerardo-Nava, C. Licht, Y. Kittel, T. Haraszti, J. Di Russo, L. De Laporte. How do the local physical, biochemical, and mechanical properties of a synthetic Anisogel affect oriented nerve growth? Adv. Fun. Mat. adfm.202202468.